# PREDICTION OF PRESSURE DISTRIBUTION OVER A WING AT HIGH ANGLE OF ATTACK BY N-S EQUATIONS

A. Emarati, M.M. Haydari and M.M. Jafari

(YMA College, P. O. Box 19395-6618, Tehran –Iran)
Email: ahmademarati@hotmail.com

## ABSTRACT

*Consideration of flow over wings at high angle of attack is of considerable importance in aerodynamics. Hence, calculation of maximum lift coefficient and its corresponding angle of attack is one of the important problems in aerodynamics.*

*This problem can not be solved by the ordinary methods available, because of its complexity and three-dimensional nature with its separation over the wing. Hence, for analyzing this problem, we have to solve the Navier-Stokes equations in order to model the separation completely.*

*In this paper, the Navier-Stokes equation for incompressible flow have been discretized using finite difference and have been solved using SIMPLE (Semi Implicit Method for Pressure Linked Equations) method. The wing considered in this research is a rectangular one, with zero sweep, but the written computer program by the authors can be used for wings of different geometry, but limited to laminar flow. The flow over the wing have been considered for different aspect ratio and the calculated results show the dependency of the results on aspect ratio very well, and for high aspect ratio, the flow at mid-wing is quite two-dimensional. As the angle of attack is gradually increased, the thickness of the wake starts increasing and the point of separation moves forward. The results obtained from this research, compare rather well with the experimental results and the modeled flow is compatible with the physical flow.*

**KEYWORDS**: *Separation, High angle of attack, Wing, Navier-Stokes equations, SIMPLE method*

## 1. INTRODUCTION

Separation is an important subject in aerodynamics. The reason is due to separation phenomenon, the lift force decreases and the drag increases. In designing any kind of flying object, we have to know at what angle separation occurs. For analyzing separation flow, the viscosity of the flow cannot be ignored. Hence, the Navier-Stokes equations must be solved (it is necessary to mention that NASA have had many activities for solving separation phenomena by panel method and have had some good successes). As the angle of attack increases, the separation occurs suddenly and the lift decreases and the drag increases.

If angle of attack is kept increasing, the lift force gradually increases after separation, but never reaches the value of that before separation. References [3-7] consider this problem.

For analyzing the separation problem, the Navier-Stokes equations should be solved. For solving Navier-Stokes equations, the method of finite difference has been used together with SIMPLE algorithm. The SIMPLE algorithm is a semi-implicit method for solving the equations in which pressure and velocity are coupled together. In this method, the momentum equations have been solved by iterative method and at each step of iteration for each main node of the girds, the values of velocity and pressure are corrected by the principle of conservation of mass.
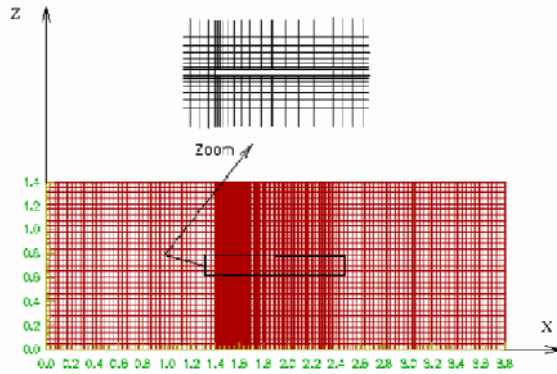
Fig.1 The cartesian grids in x-z plane
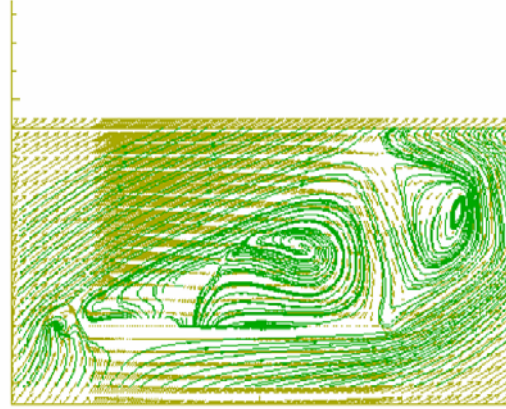


Fig.2 Separation phenomenon showing the reverse flow at high angle of attack

## 2. GOVERNING EQUATIONS

The governing equations for the system contain the conservation of mass and momentum that are known as Navier-Stokes equations:

Continuity equation:

$$\nabla \cdot \left(\rho \vec{V}\right) = 0 \tag{1}$$

X-momentum:

$$\rho \frac{Du}{Dt} = -\frac{\partial P}{\partial x} + \frac{\partial \tau_{xx}}{\partial x} + \frac{\partial \tau_{yx}}{\partial y} + \frac{\partial \tau_{zx}}{\partial z} \tag{2}$$

Y-momentum:

$$\rho \frac{Dv}{Dt} = -\frac{\partial P}{\partial y} + \frac{\partial \tau_{xy}}{\partial x} + \frac{\partial \tau_{yy}}{\partial y} + \frac{\partial \tau_{zy}}{\partial z} \tag{3}$$

Z-momentum:

$$\rho \frac{Dw}{Dt} = -\frac{\partial P}{\partial z} + \frac{\partial \tau_{xz}}{\partial x} + \frac{\partial \tau_{yz}}{\partial y} + \frac{\partial \tau_{zz}}{\partial z} \tag{4}$$

Where:

$$\tau_{xy} = \tau_{yx} = \mu \left(\frac{\partial v}{\partial x} + \frac{\partial u}{\partial y}\right) \tag{5}$$

$$\tau_{yz} = \tau_{zy} = \mu \left(\frac{\partial w}{\partial y} + \frac{\partial v}{\partial z}\right) \tag{6}$$

$$\tau_{zx} = \tau_{xz} = \mu \left(\frac{\partial u}{\partial z} + \frac{\partial w}{\partial x}\right) \tag{7}$$

$$\tau_{xx} = \lambda \left(\nabla \cdot \vec{V}\right) + 2\mu \frac{\partial u}{\partial x} \tag{8}$$

$$\tau_{yy} = \lambda \left(\nabla \cdot \vec{V}\right) + 2\mu \frac{\partial v}{\partial y} \tag{9}$$

$$\tau_{zz} = \lambda \left(\nabla \cdot \vec{V}\right) + 2\mu \frac{\partial w}{\partial z} \tag{10}$$

And by stokes hypothesis we have:

$$\lambda = -\frac{2}{3}\mu \tag{11}$$

And in the form of general transport equations for steady flow are written as below:

$$\frac{\partial}{\partial X_J}\left(\rho U_J \Phi\right) = \frac{\partial}{\partial X_J}\left(\Gamma_\Phi \frac{\partial \Phi}{\partial X_J}\right) + S_\Phi \tag{12}$$

Where the vector $U_J$ (for $J = 1,2,3$) Presents the three components of velocity.

## 3. SOLUTION METHOD

A finite difference method is used for solving the governing equations. For discretizing the diffusion terms, a central discretization is used and for discretizing the convection terms (considering the comparison between the ratio of convection to diffusion strength), a central discretization with combination of an upwind discretization is used[2], hence the coefficients of discretized equations are modified by an innovative method (improved and optimized power law) for solving difference method. The kind of grids used for solving this problem, are staggered ones, and SIMPLE algorithm is used for solving the equations. In every step of iteration, the system of equations is solved by ADI method, with applying the suitable under-relaxation factor. At the end, the corrected values of velocity and pressure are determined for each step and these iterative steps are continued till the point where the obtained values of velocity and pressure are satisfied in conservation equations. Finding a suitable and proper computational grid in three-dimension is not an easy task and for the points lying near the leading edge, special treatment (putting a great number of grids near leading edge by cosine spacing) should be applied, in order the peak suction at leading edge can be calculated exactly. A Cartesian grid has been used and the grids in x-z plane has been shown in FIG.1 also for reduction in cost and computer time, a combination of uniform and non-uniform grids are used. The range of CPU time for a grid of $145 \times 36 \times 17$ is about 3 hours on a Pentium 133.

To decide the right boundary conditions for the problem was not an easy task. The customary boundary condition is to put velocities known at six edges (far upstream and down stream, far above and below, and far to the left and right to the wing), but this boundary condition did not give the right pressure distribution over the wing. Therefore it was decided to use pressure boundary condition at six edges instead of velocity boundary condition. Putting pressure known at six edges also did not give the right pressure distribution over the wing. The alternative was to put a combination at six edges. Surprisingly, the combination boundary condition gave the right pressure distribution over the wing.

## 4. RESULTS AND DISCUSSION

A rectangular wing of aspect ratio 10 and thickness chord ratio of 0.1 at different angle of attack have been considered. For analyzing the behavior of flow over the wing and considering the separation which is a phenomena due to viscosity of the fluid is not an easy task to carry out in three-dimension, hence starting the research with a two-dimensional case is a sound decision to make. After considering a two-dimensional wing and finding the correct pressure distributions over the surfaces of the two-dimensional wing, the research for the three-dimensional wing started. The dimension of the field for this case along the chord was four times the length of the chord, in the direction perpendicular to chord was one and half times the length of the chord and in the direction of span was twelve times the length of the chord (the dimensions of the field for the three directions were doubled, but the changes occurred were negligible). For boundary conditions, where the pressure is known in downstream boundary (far away from the wing) and the velocity is known in all the other boundaries, the problem have been solved for different grid arrangements. When the number of grids are $145 \times 36 \times 17$ (145 along the chord, 36 along the thickness of the wing and 17 along the span) the best results were found independent of grids. For these mentioned conditions and an angle of attack of $10°$ for different aspect ratios (4,8,10,60) the pressure distribution over the wing was obtained and after analyzing the results, it was noticed that when the aspect ratio of the wing was increased, the pressure distribution at mid-span was very close to two-dimensional case (where analytical solution is available).

In FIG.2 the separation is shown and in FIG.3 and FIG.4 the comparison of pressure distribution along the chord between a two-dimensional wing and a three-dimensional wing with aspect ratios of 4 and 60 is made. These comparisons show that as the aspect ratio is increased, the results are getting closer to two-dimensional case. FIG.5, FIG.6 and FIG.7 show the pressure distribution along the chord for the wing with aspect ratio of 10 and angle of attack of $5°$, $10°$ and $15°$. These figures clearly show the effect of increasing angle of attack. It is obvious why in the above figure the comparison near leading edge is very poor. The reason is that the wing of analytical has zero thickness, but the wing for numerical calculation has some finite thickness.
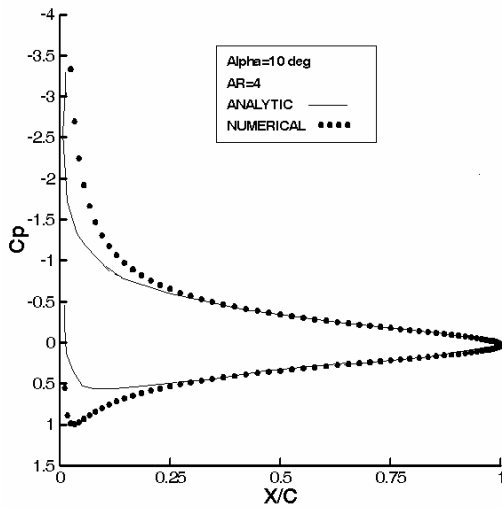
**Fig.3 Pressure distribution at**

$\alpha = 10°$ , $AR = 4$
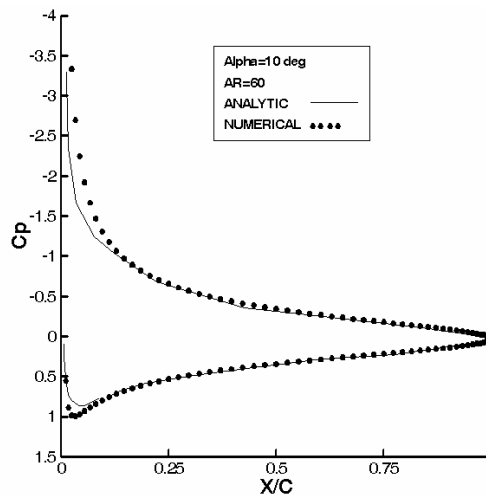


**Fig.4 Pressure distribution at**

$\alpha = 10°$ , $AR = 60$
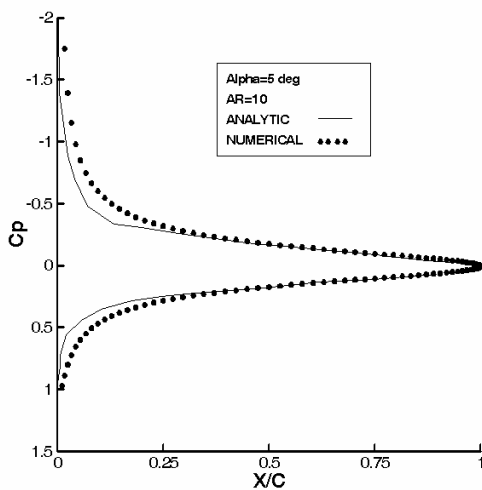


**Fig.5 Pressure distribution at**

$\alpha = 5°$ , $AR = 10$
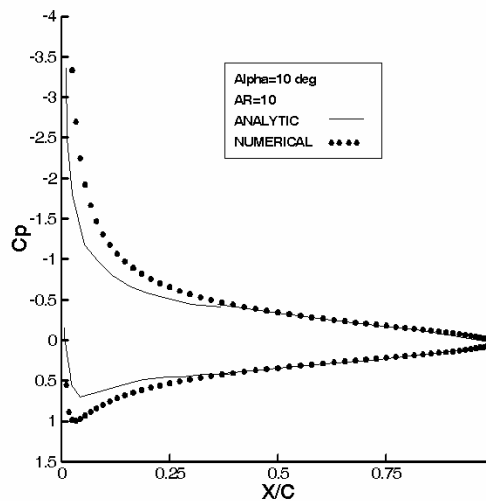


**Fig.6 Pressure distribution at**

$\alpha = 10°$ , $AR = 10$

Separation is a problem, which must be considered very carefully, hence different boundary conditions for this problem must be examined, in order to find the best boundary condition where separation is modeled properly. First the boundary condition of velocity known in all boundaries is considered. Then the pressure distributions and lift coefficient are obtained and the validity of the results were examined. Other boundary conditions (such as combinations of velocities and pressures known at different six edges of the field) were considered, and the best results for before separation were obtained when boundary conditions of velocity known on upstream and around the body, and pressure known on downstream. The results for this case were quite valid for different range of angle of attack $(5°,10°,12°)$.

As the angle of attack was increased, it was expected that the separation occurs about $15°$ and in return the lift coefficient decreases suddenly. But with the mentioned boundary conditions (known velocity at upstream and around the body, and known pressure at downstream) the separation did not occur about the right angle of attack, and the validity of the results were questionable above the angle of attack of $12°$. After considering all combinations of velocity and pressure known around the boundaries for separation region, the best boundary conditions were when pressure at upstream and downstream were known and the velocities at the rest of the

boundary around the body were known. For this case, the lift coefficient for different angle of attack is obtained for a rectangular wing and in figure (8) is compared with experimental results of reference [1]. The comparisons of obtained numerical results with experiment are quite promising.
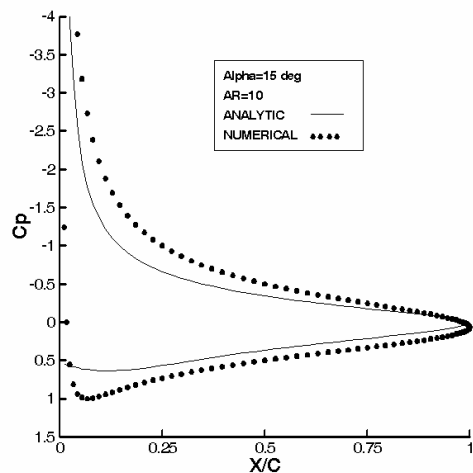


Fig.7 Pressure distribution at
$\alpha = 15°$ , $AR = 10$
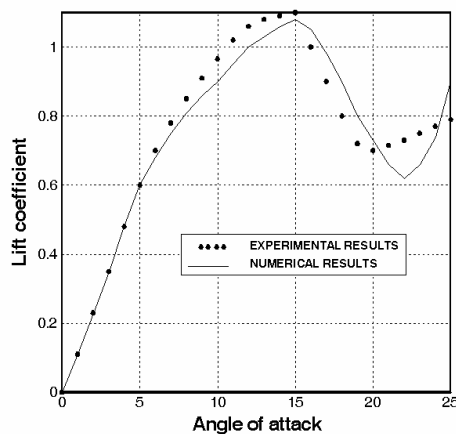


Fig.8 Lift coefficient against angle of attack

## 5. CONCLUSION

The problem of wing at high angle of attack was considered, and the aerodynamic coefficients were obtained for linear and non-linear range of angle of attack. The obtained results for both regions are valid, as long as the right boundary conditions are chosen for the right region. The reason why different boundary conditions must be used for different region must be worked on in more details.

## 6. NOTATIONS:

$\Delta CP$ : Pressure difference between the two surface of wing

$CP_L$ : Pressure distribution for wing lower surface

$CP_U$ : Pressure distribution for wing upper surface      $P$ : Pressure

$U_J$ : State of tensor in three components of velocity      $\alpha$ : Angel of attack

$\Phi$ : Transport quantity      $\rho$ : Density

$X_J$ : State of tensor in three directions      $\mu$ : Coefficient of viscosity

$u, v, w$ : Three components of velocity      $\lambda$ : Bulk viscosity coefficient

$\tau_{ij}$ : Shear and normal stresses      $S_\Phi$ : Source term

## 7. REFRENCES

[1] Winkelmann AE, Barlow JB, Agrawal S, Saini JK, Anderson TD, Jones JE. The effect of leading edge modifications on the post-stall characteristics of wings. AIAA Paper, No.80-0199 American Institute of Aeronautics & Astronautics, NewYork, 1980.
[2] Patankar SV. Numerical Heat Transfer and Fluid Flow. McGraw-hill Book Company, 1980.
[3] Katz J. Lateral aerodynamics of delta wings with leading edge separation. AIAA Journal, Vol. 22,No. 3, PP. 323-328, 1984.
[4] Levin D and Katz J. Vortex lattice method for the calculation of nonsteady separated flow over delta wings. J Aircraft, Vol. 18, No. 12, PP. 1032-1037, 1981.

[5] High angle of attack aerodynamics. AGARD-CP-247, Oct. 1978.

[6] Spalart PR and Leonard A. Computation of separated flows by a vortex tracing algorithm. AIAA paper 81-1246, June 1981.

[7] Winkelmann AE and Barlow JB. Flow field model for a rectangular planform wing beyond stall. AIAA Journal, Vol. 18, No. 8, PP. 1006-1008, 1980.

# THEORETICAL MODELING FOR PREDICTION OF NOISE LEVEL BY THE EXHAUST MUFFLER AND VALIDATION OF THESE ANALYTICAL RESULTS WITH THE EXPERIMENTAL RESULTS

**Bankim Bihari Ghosh,**
IEM, Kolkata and Research Consultant, IIT Kharagpur, India, bankimghosh@hotmail.com


Paritosh Bhattacharya, Rajsekhar Panua,
CEM, Kolaghat, East Midnapore, PIN 721171, India


Prabir Bose
Mechanical Engg. Dept. Jadavpur University, Kolkata-32, India


Satyajit Chakrabarty
Director, IEM, Kolkata, India

**ABSTRACT:**
A pollutant of concern to the mankind is the exhaust noise in the internal combustion engine. However this noise can be reduced sufficiently by means of a well designed muffler. The present paper aims the prediction of pressure drop an important factor for noise level by mathematical modeling in the exhaust muffler. The pressure drop in an exhaust muffler plays an important role for the design and development of a muffler. The prediction of pressure drop by mathematical modeling will be very useful for the design and development of muffler. The suitable design and development will help to reduce the noise level, but at the same time the performance of the engine should not be hampered by the back pressure caused by the muffler. This thought has implied the authors to predict pressure drop a very important tool for the design of muffler. The authors have solved one-dimensional wave equation by the method of separation variables using boundary conditions.
The author want to evaluate the pressure drop at the point x and at the time t along the muffler. The noise level by theoretical modeling was compared with the existing and the developed muffler and found 6.9 %less for developed muffler. The performance characteristics such as brake thermal efficiencies, brake specific fuel consumption of the existing and the developed mufflers was also compared and found parallel

**KEYWORD:**
Wave equation, Separable variable, Muffler, Decibel

**NOMENCLATURES**

BSFC      Brake Specific Fuel Consumption
BP      Brake Power
c      Speed of sound
db      Decibel
f      Frequency of sound wave
L      Length of the muffler
N      Speed of engine
SPL      Sound Pressure Level
t      Time
$u(x,t)$      Pressure Difference
$u_0$      Initial Sound pressure level
$\omega$      Angular Velocity

## INTRODUCTION:

Internal combustion engines are typically equipped with an exhaust muffler to suppress the acoustic pulse generated by the combustion process[3,4,5]. A high intensity pressure wave generated by combustion in the engine cylinder propagates along the exhaust pipe and radiates from the exhaust pipe termination. The pulse repeats at the firing frequency of the engine which is defined by $f$=(engine rpm x number of cylinders)/120 for a four stroke engine. The frequency of exhaust noise is dominated by a pulse at the firing frequency. In general, sound waves propagating along a pipe can be attenuated using either a resonative or a reactive muffler. Reactive and resonative silencers, which are commonly used in automotive applications, reflect the sound waves back towards the source and prevent sound from being transmitted along the pipe[1,2]. Reactive silencer design is based either on the principle of a Helmholtz resonator or an expansion chamber, and requires the use of acoustic transmission line theory.

## THEORETICAL MODELING

The one dimensional wave equation is

$$\frac{\delta^2 u}{\delta t^2} = c^2 \frac{\delta^2 u}{\delta x^2} \dots\dots\dots \quad \dots(1)$$

Using boundary conditions

$$u = 0 \dots\dots at \dots\dots x = L \dots and \dots for.all.t \dots\dots\dots(2)$$

$$u = u_0 \dots\dots at \dots\dots t = 0, \dots x = 0 \dots\dots\dots(3)$$

$$\frac{\delta u}{\delta x} = 0 \dots\dots \dots\dots at \dots\dots \dots x = 0 \dots\dots \dots\dots(4)$$

$$\frac{\delta u}{\delta t} = 0 \dots\dots at \dots t = 0 \dots (0 \leq x \leq L) \dots\dots \dots(5)$$

The solution of Equation (1) can be written in the form

$$u(x,t) = X(x)T(t) \dots\dots \dots\dots \dots(6)$$

Substituting this values of u(x,t) in (1) we get

$$X'' - \mu X = 0 \dots\dots \dots\dots .(7)$$

$$T'' - c^2 \mu T = 0 \dots\dots \dots\dots .(8)$$

Using (2) we get $X(L) = 0$

Using (4) we get $X'(0) = 0$

For the solution of equation (7) three cases arises

Case-I

Let $\mu = 0$ then the solution of equation (7) is $X(x) = Ax + B$ and we get A=0 and B=0. So we reject $\mu = 0$

Case-II

let $\mu = \lambda^2 (\lambda \neq 0)$ Then the solution of equation (7) is $X(x) = Ae^{\lambda x} + Be^{-\lambda x}$

we get A=B=0

So we again reject $\mu = \lambda^2 (\lambda \neq 0)$

Case-III

Let $\mu = -\lambda^2 (\lambda \neq 0)$

Then we get $X(x) = A \cos \lambda x + B \sin \lambda x$

554

By using the conditions $X(L) = 0$, $X'(0) = 0$ we obtain , $A \neq 0$ $B = 0$ and

$$L\lambda = \frac{1}{2}(2n-1)\pi \quad n = 1,2,3,\ldots \ldots \ldots$$

Hence non-zero solution of equation (7) becomes

$$X_n(x) = A_n \cos \frac{1}{2L}(2n-1)\pi x$$

Now equation (8) becomes $T'' + \frac{1}{4L^2}(2n-1)^2 \pi^2 c^2 T = 0$

Whose solution is

$$T_n(t) = C_n \cos \frac{1}{2L}(2n-1)\pi ct + D_n \sin \frac{1}{2L}(2n-1)\pi ct$$

The general solution for the equation (1) becomes

$$u(x,t) = \sum_{n=1}^{n=\infty} [E_n \cos \frac{1}{2L}(2n-1)\pi ct + F_n \sin \frac{1}{2L}(2n-1)\pi ct] \cos \frac{1}{2L}(2n-1)\pi x \text{ Applyin}$$

g boundary condition (3) we obtain $E_n = \dfrac{4u_0(-1)^{n-1}}{(2n-1)\pi}$

Again applying boundary condition (5) we obtain $F_n = 0$

Therefore the desired solution is

$$u(x,t) = \frac{4u_0}{\pi} \sum_{n=1}^{\infty} \frac{(-1)^{n-1}}{2n-1} \cos \frac{1}{2L}(2n-1)\pi ct . \cos \frac{1}{2L}(2n-1)\pi x$$

Now we have

$$u(x,t) = \frac{2u_0}{\pi} \sum_{n=1}^{\infty} \frac{(-1)^{n-1}}{2n-1}[\cos \frac{1}{2L}(2n-1)\pi(ct-x) + \cos \frac{1}{2L}(2n-1)\pi(ct+x)]$$

Therefore $u(x,t) = u_1(ct-x) + u_2(ct+x)$

Where $u_1(ct-x) = \dfrac{2u_0}{\pi} \sum\limits_{n=1}^{\infty} \dfrac{(-1)^{n-1}}{2n-1} \cos \dfrac{1}{2L}(2n-1)\pi(ct-x)$

$$u_2(ct+x) = \frac{2u_0}{\pi} \sum_{n=1}^{\infty} \frac{(-1)^{n-1}}{2n-1} \cos \frac{1}{2L}(2n-1)\pi(ct+x)]$$

$$u_2(ct+x) = 0$$

For positive going wave , we have

$$u(x,t) = u_1(ct-x) = \frac{2u_0}{\pi} \sum_{n=1}^{\infty} \frac{(-1)^{n-1}}{2n-1} \cos \frac{1}{2L}(2n-1)\pi(ct-x)$$

Here we have taken c = 368 m/s.

**DESIGN:**
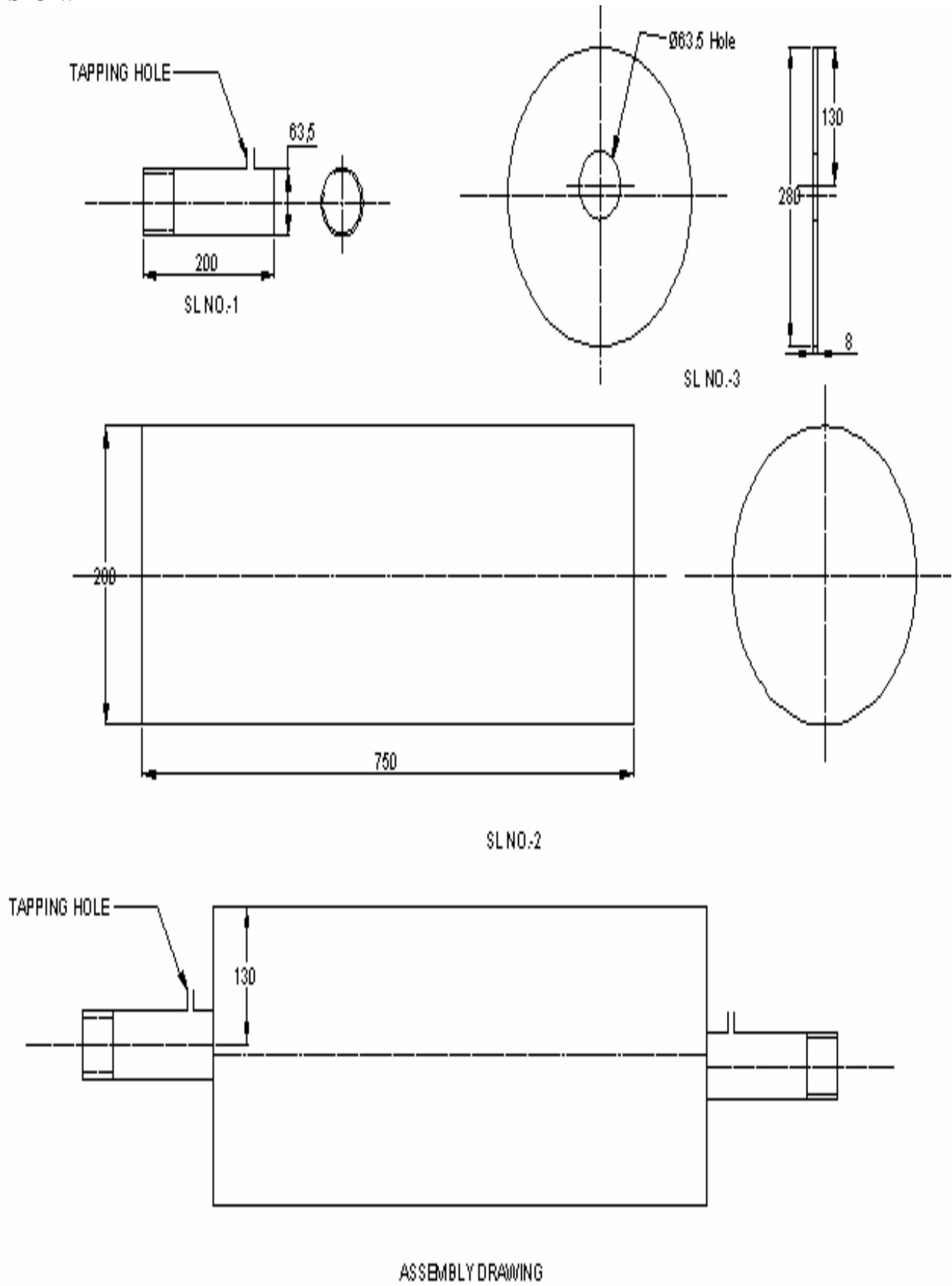


**Fig.1: Drawing of Developed Muffler**

**SIZE OF THE ASSEMBLY DRAWING**

| Sl. No. | Name | Quantity | Weight (Kg) | Thickness (mm) |
|---------|------|----------|-------------|----------------|
| 1 | Inlet pipe | 1 | 0.5 | 2 |
| 2 | Cylindrical drum | 1 | 3.4 | 3 |
| 3 | Side wall of drum | 2 | 2.2 | 3 |
| 4 | Exhaust pipe(same as Sl no. 1) | 1 | 0.5 | 2 |

**EXPERIMENTAL SETUP:**
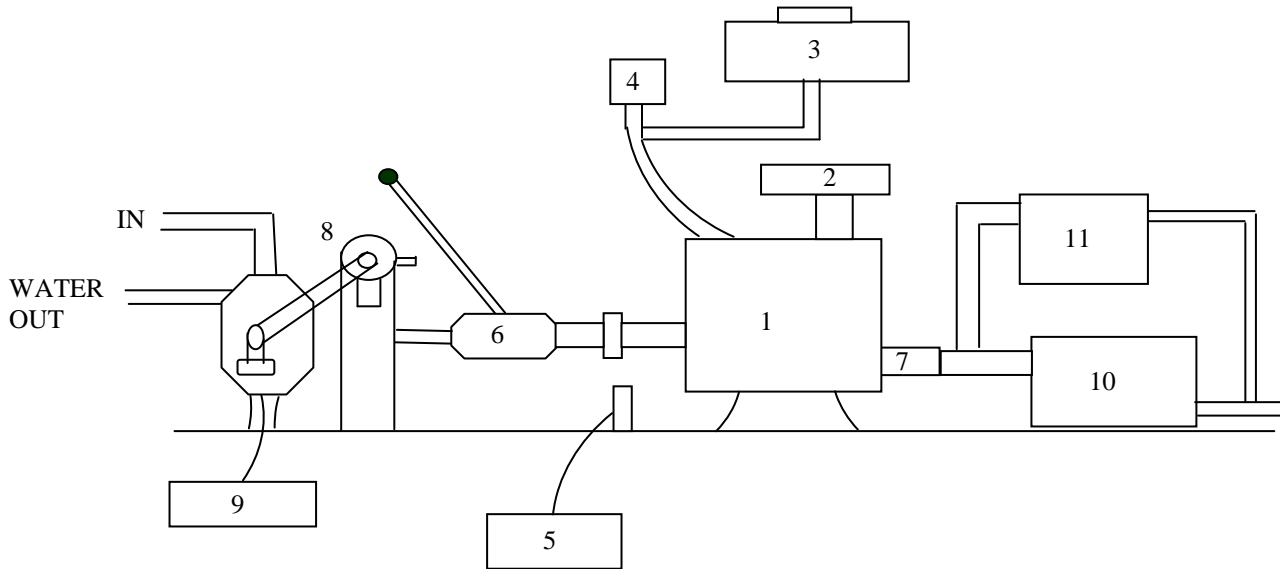


1.ENGINE                         2.AIR FILTER                         3.DIESEL TANK
4.DIESEL MEASURING BURRETT                         5.SPEED INDICATER
6.CLUTCH          7.EXHAUST PIPE          8.HYDRALIC DYNAMOMETER
9.TORQUE INDICATOR    10.REACTIVE MUFFLER      11.MANOMETER

**Fig 2  SCHEMATIC DIAGRAM OF EXPERIMENTAL SET UP**

**RESULTS AND DISCUSSIONS:**
Fig. 3 represents the sound level Vs BP (KW) at 1400 rpm. It is observed that that the sound level is 115.6 db, 95.9 db and 82.1 db by without muffler, existing muffler (supplied by the manufacturer) and developed muffler respectively. Where as 76.383 db by mathematical modeling.  It is interesting to note down the variations between the sound levels percentage variation measured by DEVELOPED and fabricated muffler & theoretical muffler is 6.9%. Since the variation of sound levels by mathematical modeling & DEVELOPED and fabricated muffler is of less order which justifies reasonable assumption taken in the mathematical modeling.

Fig.3: Comparison of sound Level among developed, existing and without muffler at 1400rpm
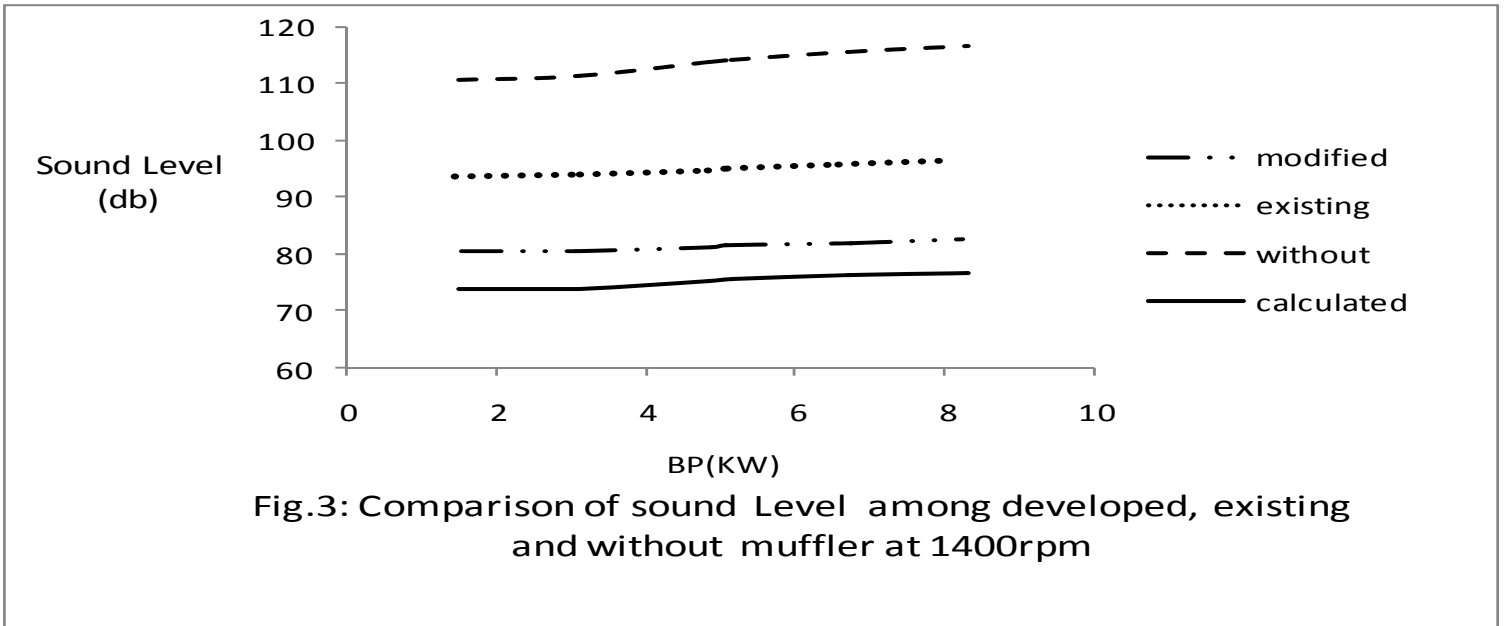
Fig.4 represents the Comparison of Brake Thermal efficiency among DEVELOPED, existing and without muffler at 1400 rpm. The maximum Brake Thermal efficiency without muffler, with existing muffler & with developed and fabricated mufflers are 26.63, 26.09 & 25.66 respectively. It is observed that Brake Thermal efficiencies without muffler and existing muffler are little higher than that of developed muffler. The Brake Thermal efficiency with developed muffler is little less than the without muffler, because of the higher pressure drop in case of developed muffler in comparison to without and existing mufflers.



Fig.4: Comparison of Brake Thermal Efficiency among developed, existing and without muffler at 1400 rpm
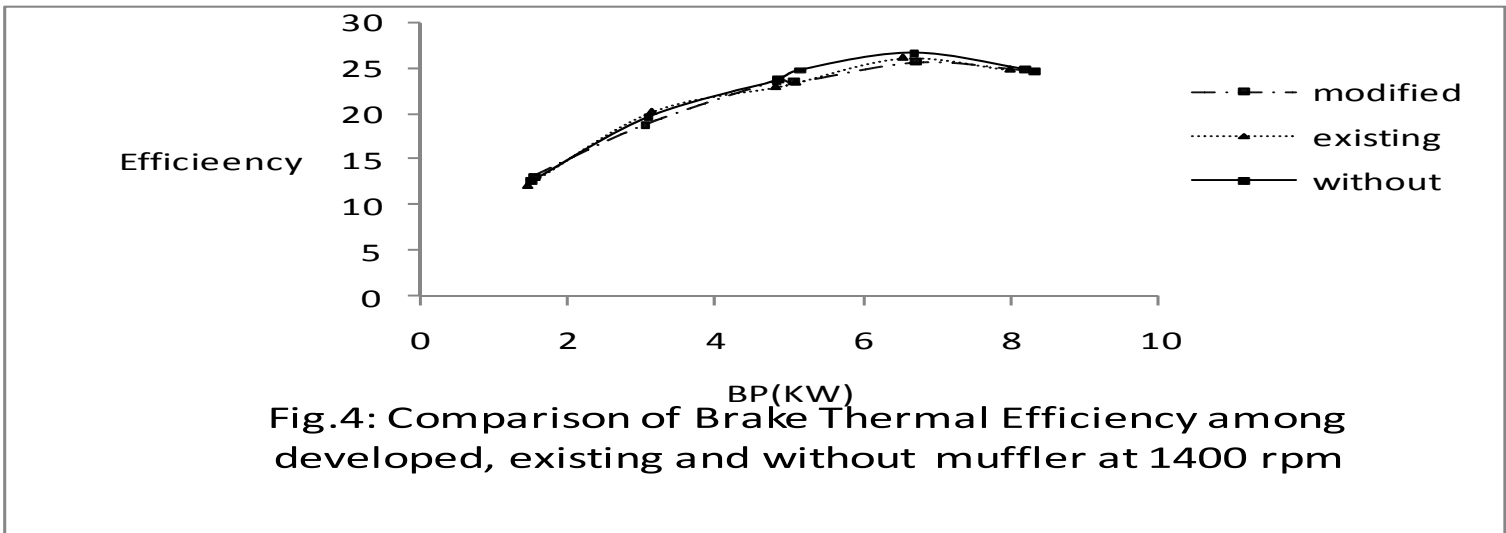
Fig.5 represents the comparison of BSFC among existing, developed and without muffler at 1400 rpm. Here it is observed that BSFC is 0.314 without muffler. In the case of existing muffler BSFC becomes 0.32. For developed and fabricated muffler BSFC is .326.

Fig.5: Comparison of BSFC among developed, existing and without muffler at 1400 rpm
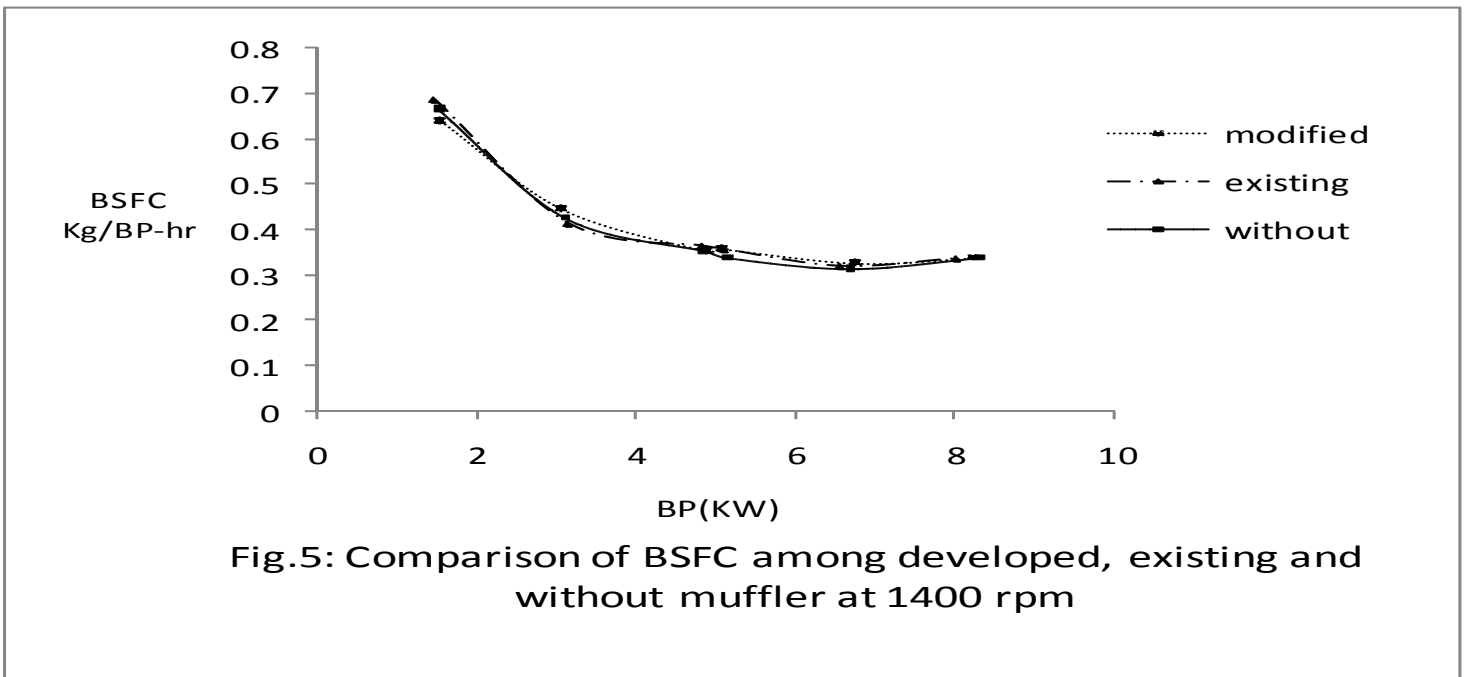
Fig. 6 represents the Drop of pressure at 1400 rpm with developed and existing muffler. It is interesting to note down that the pressure drop for developed fabricated muffler is higher than the existing muffler.



Fig.6: Drop of pressure Vs BP(KW) between developed and existing muffler at 1400 rpm
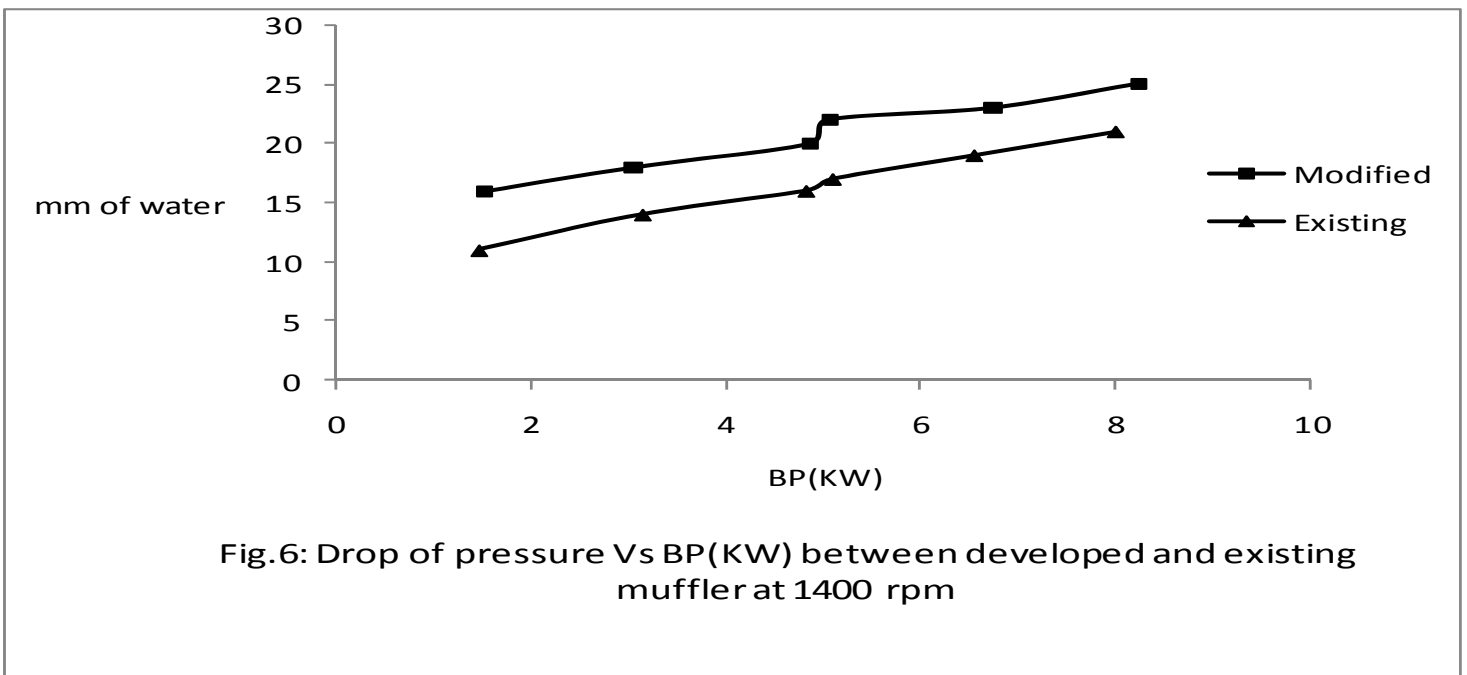
## CONCLUSION:

From results and discussions the following conclusions are drawn:
1. Reduction of noise level is around 14 db compared to existing muffler.
2. The Brake Thermal Efficiency of engine is 2% less for developed and fabricated muffler as compared to existing muffler.
3. The Brake Specific Fuel Consumption is at par compared to existing muffler.

**REFERNCE:**

[1]   Ghosh, B.B  and Bhattacharya, P , (2006), "Analytical and Experimental Study on Noise Attenuation of Multi-cylinder Diesel Engine with Existing and Modified Muffler " Noise and Vibration Worldwide,37, Number 9, pp 21-28(8).

[2]   Ghosh, B.B  and Bhattacharya, P , (2007), Analytical and Experimental Study on Noise Attenuation of Multi-cylinder Diesel Engine with Resonative Muffler, Journal of Applied Sciences Research, 3(7), pp-587-593.

[3]   Austen, A.E.W and Priede, T.(1986), "Noise of automotive diesel engine, its causes reduction, S.A.E. transaction", vol.74, paper 1000A.

[4]   Alfredson. R. J. and Davies, P.O.A.L. (1971). "The performance of exhaust silencer components, Journal of sound and vibration", 17, pp.175-196.

[5]   Belgaunkar, B. M, Somayajulu, K.D.S.R. and Mukherjee, Subrata (1969), "A Study of engine exhaust noise and silencer performance", N.V.R.L Report, I.I.T. Kharagpur.

[6]   Bender Erich, K and Brammer, A.J (1975), "Internal combustion engine intake and exhaust system noise, Journal of acoustical society of America", vol. 58, (1), pp. 22-30.

[7]   Blair, J.P and Spechko, J.A (1972), "Sound pressure level generated by internal combustion engine exhaust system ", S.A.E Transactions, paper 720155.

[8]   Crocker, M.J and price, A.R. Noise and Vibration Control vol-I, First edition, CRC Press Inc. Pp42-44 and 100-123.

[9]   Munjal, M.L. (1977), "Exhaust Noise And its Control- A review", Shock and Vibration Digest, 9, pp. 22-32.

## NUMERICAL SIMULATION OF BYPASS TRANSITION BY THE APPROACH OF INTERMITTENCY TRANSPORT EQUATION.

Most. Nasrin Akhter, Kazutoya YAMADA, Ken-ichi FUNAZAKI

Department of Mechanical Engineering
Iwate University, 4-3-5, Ueda, Morioka, Iwate 020-8551, Japan
E-mail: nasrin6092002@yahoo.com

### ABSTRACT

*This paper deals with the development of a numerical approach to predict freestream turbulence-induced (FST-induced) boundary layer bypass transition using an intermittency transport equation. An intermittency based transition model, which is critical for invoking transition onset according to Abu-Ghannam and Shaw correlation, is implemented into the proven Reynolds-Averaged N-S (RANS) solver. The intermittent behavior of the transitional flow is incorporated into the computation by modifying the eddy viscosity $\mu_t$, obtained from a turbulence model. Wilcox low Reynolds $k-\omega$ turbulence model is employed to calculate the eddy viscosity and others turbulent quantities. For validation, the current transition model is applied to the benchmark experiments of flat plate test cases of ERCOFTAC series and to predictions of a modern Low Pressure (LP) turbine flow analyses. It follows from the detail comparisons of the calculated results with the relevant experimental data and other researcher simulations that the present model is capable to make reasonable prediction of FST-induced bypass transition.*

**KEY WORDS:** *Boundary Layer, Bypass Transition, Numerical Prediction, Intermittency Factor*

### 1.  INTRODUCTION

Boundary layers developing on blades and vanes in turbomachines usually start as laminar boundary layer, and in most situations they eventually become turbulent. Since aerodynamic performance as well as reliability of turbomachines depend on the momentum and heat transfer characteristics of boundary layers and it is a widely accepted idea that the transition governed by the free stream turbulence or wake passing, which is called bypass transition, is a common mode in turbomachines. Therefore, proper prediction of the bypass transition is one of the most important and challenging tasks for turbomachine designers.

As the turbulence modeling makes steady progresses over the years, usually RANS based approach with low Reynolds version of two equation model. However, such prediction tended to predict too early transition onset, even for the simple flat plate case. One of the successful approaches was proposed by Schmidt and Patankar [1] using Production Term Modification (PTM) method. The approach of Schmidt and Patankar has failed to gain popularity even among the turbomachinery community probably because it requires two parameters in the differential equation to be determined empirically.

An alternative approach for predicting the bypass transition, which is nowadays being implemented into some of the commercial codes, is the usage of intermittency. The concept of intermittency, a measure of the probability of a given point to be inside the turbulent region, has evolved from the need to distinguish between the uniform and random behaviors of the flow in the intermittent region. Recently Suzen and Huang [5] proposed sophisticated intermittency-based transition model by combining two intermittency equations ( Stellant and Dick[2] and Cho and Chung [3] model). There transition model has turned out to be superior to the precedents in predicting the bypass transition , however some test cases identified that there still remained some discrepancies between the

prediction and experimental data. Very recently the present authors (N. Akhter & K.Funazaki, [4]) introduced a new intermittency based transition model, using Schmidt and Patankar [1] boundary layer analysis code. Their model exhibited a comparable or in some cases better predicting capability than that of Suzen and Huang.

In the present paper then tries to apply the same concept of the previous study from the boundary layer analysis code to the well-established highly accurate RANS code. Some adjustment should be made on the intermittency transport equation since this code employs Wilcox $k-\omega$ model. Section 2 provides the details of the turbulence model and numerical method. Section 3 shows the comparisons of the new transition model against T3 series of experiments of Savill [7], and the prediction of the $k-\varepsilon-\gamma$ model of Suzen and Huang [5], $k-\varepsilon$ model of Launder-Sharma [8], and base model of Wilcox $k-\omega$ [9]; Comparisons with the experiment of Simon et.al. [12] where Pratt and Whitney's modern low pressure turbine blade is studied. Section 4 provides the concluding remarks.

## 2. NEW TRANSITION MODEL

RANS based intermittency transport equations have been developed by modifying Cho and Chung [3] model. The proposed transport equation is coupled with Wilcox low Reynolds $k-\omega$ model with no modification.

### 2.1 Intermittency ($\gamma$) equation

The proposed intermittency equation is

$$\frac{\partial}{\partial x_j}(\rho u_j \gamma) = c_{g_1}\gamma(1-\gamma)\frac{P_k}{k} + \frac{cg2}{\beta^*}\rho\frac{k}{\omega}\frac{\partial \gamma}{\partial x_j}\frac{\partial \gamma}{\partial x_j} + \frac{\partial}{\partial x_j}\left[\sigma_\gamma(1-\gamma)(\mu+\mu_t)\frac{\partial \gamma}{\partial x_j}\right] \tag{1}$$

The first term of right hand side represents the production term, where $P_k = 2\mu_t' S^2$ represents the production of turbulent kinetic energy by the shear stress, where $\mu_t' = \dfrac{k}{\omega}$. This term expresses the generation of $\gamma$ owing to the production of the turbulent kinetic energy. The second term represents the increase of $\gamma$ by the spatial inhomogeneity or gradient of $\gamma$ itself. The last term represents the diffusion term. The role of diffusion term is to allow a gradual variation of $\gamma$ towards zero in the free stream.

Here presented intermittency transport equation is coupled with the turbulent kinetic energy $k$ and its dissipation equation $\omega$ where, the original Cho and Chung [3] model was coupled with the turbulent kinetic energy and its dissipation rate $\varepsilon$. The transform was done using $\varepsilon = \beta^* \omega k$, where $\beta^* = 0.09$ (details will appear later).

The present model also differs from the original version of Cho and Chung [3] in diffusion term and empirical constants. We have dropped the entrainment effect as this effect is found to be negligible for most flows. The proposed new diffusion term controls the gradual increase of intermittency in every streamwise location and proposed the best set up of model constants for wall bounded shear flows. Since the original Cho and Chung [3] model constants were selected based only on plane jet experiment but the present model deals with the wall bounded shear flows, so the retuning of model constants is significant.

Any sink term did not exists in original model of Cho and Chung and the destruction effect is embodied by decreasing the model constant $C_{g1}$ associated with the first source term ( Cho and Chung [3]). In the present model, the value of $C_{g1}$ was set to be 0.19 where the original constant was 1.6. The model constants $C_{g2}$, which is appear in second source term was set to be 1.0 instead of original constants, 0.15. As shown later, this constant controls the transition lengths in higher turbulence intensity cases. All constants are selected through some numerical experiments (not shown).

The intermittency concept was incorporated in to the computation through the eddy viscosity. The eddy viscosity relation then modifies

$$v_t^* = v_t\left[1+C_{\mu g}\frac{k}{\omega^2}\gamma^{-2}(1-\gamma)\frac{\partial \gamma}{\partial x_k}\frac{\partial \gamma}{\partial x_k}\right] \tag{2}$$

562

The above expression for the eddy viscosity was originally proposed by Cho and Chung [3] to account for the effect of outer irrotational fluid motion. The above relation Eq.(2) reduces to the fully turbulent flow, when $\gamma = 1.0$. $\nu_t$ is calculated from the Wilcox low Reynolds $k - \omega$ model,

Finally the model empirical constant are

$$c_{\mu g} = 0.001 \quad c_{g1} = 0.19 \quad c_{g2} = 1.0 \quad \sigma_\gamma = 1.0 \tag{3}$$

## 2.2 Baseline turbulence model and onset location.

As mentioned above, the two equation $k - \omega$ turbulence model of Wilcox [9] was chosen. The $k - \omega$ model is the model of choice in the sublayer of the boundary layer. Unlike any other model, the $k - \omega$ model does not involve damping functions and, of its simplicity, the $k - \omega$ model is superior to other models. Furthermore, it is as accurate as any other model in predicting the mean flow profiles and therefore it is used as a base line model to compute other turbulent quantities in the computations.

One of the important points associated with the intermittency-based turbulence model is to specify the transition onset point properly since the intermittency transport equation does not feature a capability to predict the transitional behavior of boundary layer. This study employed the well known Abu-Ghannam and Shaw [7] correlation for determining onset location, which is given as follows;

$$\mathrm{Re}_{\theta_t} = 163 + \exp(6.91 - Tu) \quad , \tag{4}$$

where $Tu$ is turbulence intensity and $\mathrm{Re}_{\theta_t}$ is the Reynolds number based on momentum thickness at onset location. Before the onset location, the production term of turbulent kinetic energy was set to be zero inside the boundary layer.

## 2.3 Numerical Method

Calculations have been done by the CFD code developed by Yamada et al [12]. The three dimensional Reynolds averaged Navier-Stokes equations are discretized spatially by a cell-centered finite volume formulation and in time using the Euler implicit method. The inviscid fluxes at cell interfaces are evaluated using a highly accurate upwind scheme based on a TVD formulation, where a Roe's approximate Riemann solver and third order accurate MUSCL- type approach with the Van Albada limiter were implemented. The viscous fluxes are determined in a central differencing manner with Gauss's theorem. Simultaneous equations linearized in time were solved by a point Gauss-Seidal relaxation method. To obtain a time accurate solution, inner iteration so called Newton iteration, is introduced at each time step. The code is able to deal with the multi-blocked computational grid system taking advantage of MPI.

## 3. RESULTS AND DISCUSSION

The test cases have been presented in this paper, including ERCOFTAC (Savill, [6]) T3 series of flat plate zero pressure gradient experiments, which are commonly used as a benchmark for validating any transition model. The second test case concern turbine cascade flow. In this study Pratt and Whitney's low pressure turbine, experiment of Simon et. al. [10] was chosen, this experiment covered the useful range for the Reynolds no. and FSTI values and it offers a good test case of bypass transition influence of free stream turbulence intensity and Reynolds number.

## 3.1 Test Cases of Flat plate

In T3 series the first two cases (T3A, T3B) are zero pressure gradient with free stream turbulence intensity (FSTI) 3% and 6% respectively. The grid sensitivity study was first performed of any CFD simulations. Grid sensitivity was checked by using four type of grid and $100 \times 100 \times 4$ was chosen in all cases, where the stream wise grid point number was 100 and crosstream grid point number also 100. The streamwise direction grid is clustered from the leading edge. The grid is expanded in cross stream direction with the first wall unit grid spacing $y^+$ approximately equal to one. In all computation, the inlet turbulent kinetic energy was fixed by the experimental freestream turbulence level. The onset of transition was specified according to the correlation of Abu-Ghannam and Shaw [7] for all cases. Comparisons are performed for these cases among the relevant experimental data and
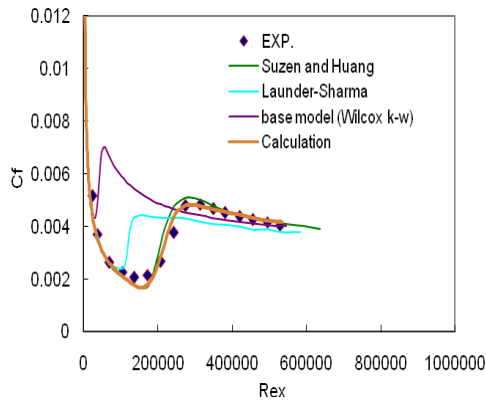
**Fig.1 Comparison of surface skin friction coefficient for T3A case**
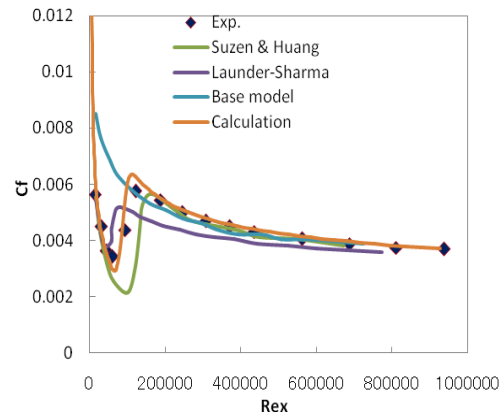


**Fig.2 Comparison of surface skin friction coefficient for T3B case**

the predictions using the new transition model, conventional turbulence models of Launder -Sharma $k-\varepsilon$ model [8], $k-\omega$ model of Wilcox [9] and Suzen-Huang $k-\varepsilon-\gamma$ model [5].

Figure1 shows the surface skin friction coefficients $C_f$ for T3A case. As can be seen in Figure 1, Launder-Sharma $k-\varepsilon$ model and Wilcox $k-\omega$ model predicted early transition, while Suzen-Huang $k-\varepsilon-\gamma$ model and the present model exhibited better performance in the prediction of the skin friction coefficients. It appears that the present model yielded an improved agreement with the experiment in comparison with that of the Suzen-Huang model.

The second test case of T3 series is the T3B case. This test case is also for flat plates zero pressure gradient flow with free stream turbulence intensity 6 % at the leading edge. Due to this higher free-stream turbulence intensity, the boundary layer experienced very early transition. Figure2 clearly demonstrates that the prediction by the present model matched the experimental skin friction coefficient more adequately than any other models employed in this study. Again the Wilcox model and Launder-Sharma model yielded much prompted transition and the model of Suzen and Huang predicted slightly delayed onset of transition.

### 3.2 Test Cases of LP Turbine blade

The intermittency transport model has been applied against the experiment of Simon et al. [10] where recent low pressure turbine blade of Pratt and Whitney (Pak-B blade) is studied. Measurement were made on the suction surface of the blade at locations from P2 to P13, and there exact positions in terms of the suction surface length are as follows: location 2, 4.5%, location 3, 17.8%, location 4, 29%; location 5, 35%; location 6 40.9%; location 7 47%; location 8, 52.9%; location 9, 59%; location 10, 67.9%; location 11, 73.8%; location 12, 82.1%; and location 13, 92.6%. These experiments were conducted in order to examine the effect of Reynolds numbers and free stream turbulence intensity. Four Reynolds number ; Re= 50,000, 100,000, 200,000, 300,000 and three levels of free stream turbulence intensity, 0.5%, 2.5%, 10% were studied.

The calculations were performed with H type of grid and the inlet boundary provided at one chord length upstream of the turbine blade and outlet also provided one chord downstream from trailing edge. A no slip boundary condition was applied to the blade surface and periodic boundary condition was applied along with the pitch wise direction. In the cross stream direction with the first wall unit grid spacing $y^+$ approximately equal to 0.5. The grid dependency study was first performed in a linear cascade and the sensitivity was checked. All results are reported here by the use of grid $400\times4\times100$ where the surface grid point number was 200 along stream wise direction and cross-stream wise grid point number was 100. In the present study two free stream turbulence intensity (FSTI=10% and =2.5%) and three Reynolds number were dealt. For the FSTI=10% case Reynolds number are considered $Re=1\times10^5$ and $Re=2\times10^5$ and for the case FSTI=2.5% the Reynolds number are $Re=2\times10^5, Re=3\times10^5$. Figure 3 shows the comparisons of pressure coefficients over the blade suction surface for $Re=2\times10^5$ and $Re=3\times10^5$ with FSTI=2.5%. Agreement between the calculations and the experiment was good, where the coefficient was defined as $2(p_{total}-p)/\rho U_{exit}^2$. As shown in Fig. 3(a), the measurement for
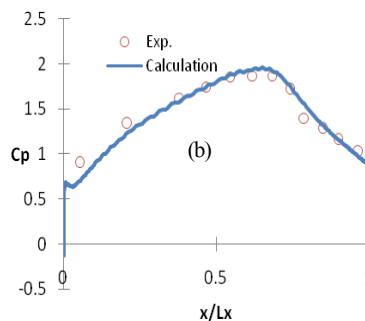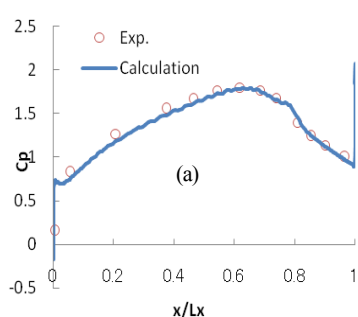
**Fig. 3 Comparisons of pressure coefficient for the case of (a)** $\mathrm{Re} = 2 \times 10^5$ **and FSTI=2.5% (b)** $\mathrm{Re} = 3 \times 10^5$ **and FSTI=2.5% .**
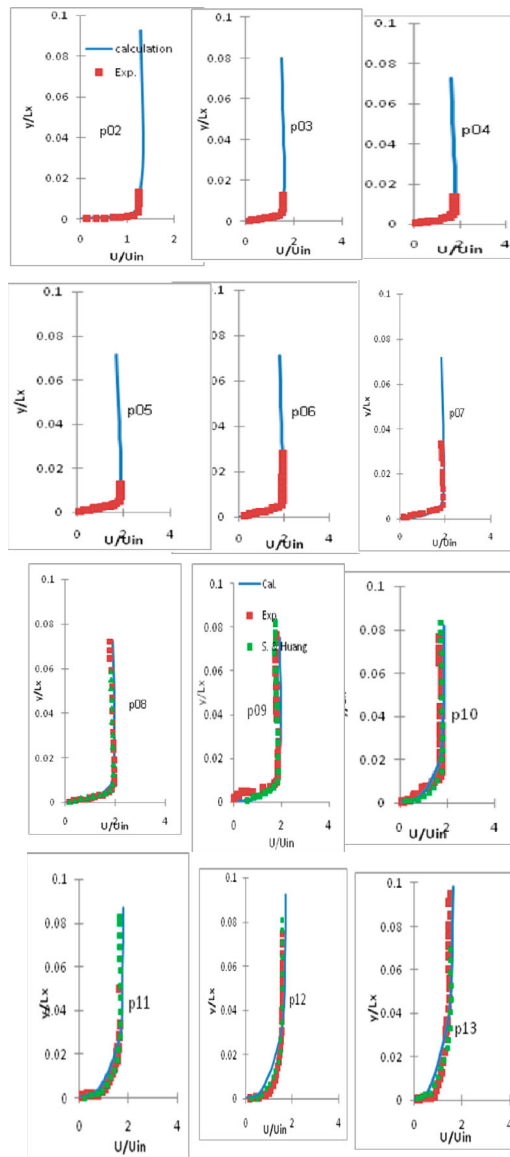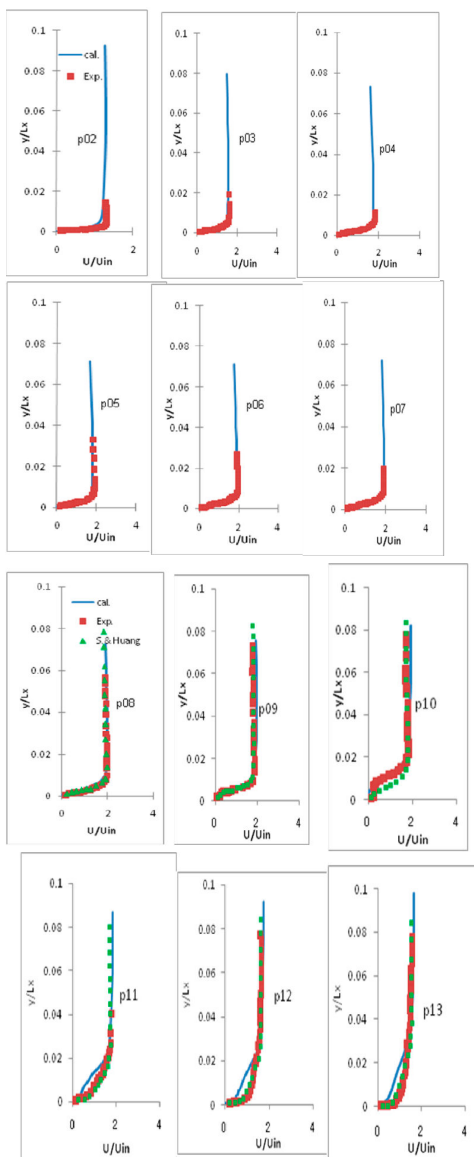


**Fig. 4 Comparisons of velocity profile from p02-p13, for the case of** $\mathrm{Re} = 2 \times 10^5$ **and FSTI=2.5%**

**Fig. 5 Comparisons of velocity profile from p02-p13, for the case of** $\mathrm{Re} = 3 \times 10^5$ **and FSTI=2.5%**

$Re = 2 \times 10^5$ indicate the existence of Separation and reattachment around $x/L_x$=0.7-0.8. The corresponding calculation reasonably reproduced those phenomena. For higher Reynolds number i.e. $Re = 3 \times 10^5$ it is clear from the measurement and calculations that the separation was substantially suppressed.

In figure 4 shows calculated and measured velocity profiles for the case of FSTI 2.5% and $Re = 2 \times 10^5$. It seems from the comparison that the velocity profiles calculated in this study agree with the measurements on the upstream portion (p02-p07). From the comparisons of the data on the aft portion (p08-p13), reasonable prediction of separation bubble was identified. Note that Suzen and Huang model showed little earlier reattachment of the separation bubble at position p10, while the present model almost reproduced the experiment. Unfortunately the present model fail to capture the transitional behavior of the separation bubble, which can be attributed to the lack of a function in the model to invoke separation induced transition. The present authors are now underway to cope with this task. The next case was FSTI=2.5% and $Re = 3 \times 10^5$, as shown in fig.5. The comparisons of velocity profile in front portion of the blade shows that good agreement was observed over the region from p02-p07. The experiment also suggested that there appeared a separated region around p09 station, which was so tiny that not only the present model but also Suzen and Huang model did not reproduce the reverse flow. Apart from this discrepancy, it can be concluded that reasonable agreement was observed in this rather higher Reynolds number case.

## 4. CONCLUDING REMARKS

A transition model, based on a dynamic transport equation for the intermittency factor, has been presented. For validation, the new model is tested against transitional boundary layer of flat plate zero pressure gradient case and the transitional boundary layer of low pressure turbine. In all flat plate cases the model shows good transitional behavior. The low pressure turbine cascade cases are generally believed to be difficult cases for any model. Multiple points of separation, transition, relaminarization provide a severe test case for transition model. Although the present transition model is not designated for separation induced transition but the performance of current model is good and also there is a scope for improvement, spatially separation correction. Further study is being continued to investigate the predicting capability of the current model in different kinds of flow fields.

## 5. NOMENCLATURE

$C_f$ : skin friction coefficient
$C_p$ : pressure coefficient
$L_x$ : axial chord length
$L_{ss}$ : suction surface length
$Re_x$ : Reynolds number based on $x$
$x$ : axial distance from the leading edge
$y^+$ : non-dimensional distance from the wall
$Re_\theta$ : Reynolds number based on momentum thickness

$p$ : static pressure
$p_{total}$ : total pressure
$Tu$ : turbulence intensity
$U_e$ : free stream velocity
$U_{in}$ : inlet velocity
$U_{exit}$ : exit velocity
$\mu_t$ : eddy viscosity

## 6. REFERENCES

[1] Schmidt R.C. and Patanker, S.V. , Two equation Low Reynolds number turbulence modeling of transitional boundary Layer flows characteristic of Gas turbine, NASA contractor report 4145, 1988

[2] Steelant, J., and Dick, E., , Modelling of bypass transition with conditioned NS equations coupled to an intermittency transport equation," *Int. J. Numer. Methods Fluids,* 23,1996, pp.193-220

[3] Cho, J.R., and Chung, M.K., A $k - \varepsilon - \gamma$ equation turbulence model, *J. Fluid Mech.,* 237, 1992, pp. 301-322

[4] Akhter, M.N., Funazaki, K., Development of Prediction Method of Boundary Layer Bypass Transition using Intermittency Transport Equation, International Journal of Gas Turbine, Propulsion and Power Systemes, Vol. 1, 2007, pp 30-37.

[5] Suzen, Y. B., and Huang, P. G, Modelling of flow transition using an intermittency transport equation for modeling flow transition, *J. Fluid Engg.* Vol.122, 2000, pp.273-284

[6] Savill, A. M., Some recent progress in the turbulence modeling of bypass transition," In: R.M.C. So, C.G. Speziale and B.E. Launder, Eds.: Near wall turbulent flows, *Elsevier Science*, 1993, p. 829-848

[7] Abu-Ghannam, B. J., and Shaw, R., Natural transition of boundary layer the effect of turbulent pressure gradient and flow history, *J. Mech. Engg.Sci.* 22, no.5 , 1980, pp. 213-228

[8] Launder, B. E., and Sharma, B. I, Application of the energy dissipation model of turbulence to the calculation of flow near a Spinning Disc, *Lett. Heat mass transfer,* 1, 1974 pp. 131-138

[9] Wilcox, D. C., turbulence modeling for CFD, DCW Industry, La Canada., 1993

[10] Simon, T. W., Qiu, S., and Yuan, K., Measurement in a Transitional Boundary Layer Under Low-Pressure Turbine Airfoil Conditions, NASA CR 2000-209957, March 2000

[11] Suzen, Y.B., Xiong, G, and Huang, P.G., Predictions of Transitional Flow in Low-Pressure Turbines Using Intermittency Transport Equation, AIAA Journal Vol. 40, No. 2 pp. 254-266, 2002.

[12] Yamada, K., Furukawa, M., Nakano, T., Inoue, M., Funazaki, K., "Unsteady Three-Dimensional Flow Phenomena Due to breakdown of Tip Leakage Vortex in a Transonic Axial Compressor Rotor," ASME Turbo Expo 2004, June 14-17 2004, Vienna Austria., GT 2004-53745

# NUMERICAL STUDIES ON THE EFFECT OF IMPELLER BLADE SKEW ON CENTRIFUGAL COMPRESSOR PERFORMANCE

**V.C. Arunachalam, Q.H. Nagpurwala, M.D. Deshpande, S.R. Shankapal**

Centre for Rotating Machinery Design
Department of Mechanical and Automotive Engineering
M. S. Ramaiah School of Advanced Studies, Bangalore 560054 India
nagpurwala@msrsas.org

## ABSTRACT

*The need to maintain reasonably high levels of efficiency and stall margin in a centrifugal compressor under off-design conditions makes its design more challenging and calls for improvement in the through flow quality by incorporating suitable changes in the impeller vane shape. This paper examines the effect of introducing tangential skew near the trailing end of a high pressure ratio, back-swept, centrifugal compressor impeller. The blade skew was introduced in such a way that the blade angle distribution varied from hub to shroud near the trailing end only. Steady state numerical simulations were performed on the baseline impeller with zero skew and four modified impellers with tangential skew of –45°, -30°, +30° and +45° using a commercially available code, FLUENT. It is observed that the impellers with positive skew produced higher pressure ratio with reduced stall margin compared to baseline 0° skew impeller. On the contrary, the impellers with negative skew produced lower pressure ratio with increased stall margin compared to the baseline 0° skew impeller. It is concluded that a proper skew to the impeller blade needs to be imparted based on the requirement of higher pressure ratio or higher stall margin. The results have also suggested a need for further optimisation of skew angle at the impeller trailing edge.*

**KEYWORDS:** *Centrifugal Compressor, Impeller, Blade Skew, Lean, Stall Margin*

## 1. INTRODUCTION

Centrifugal compressors are widely used in various industries like, aviation, oil & gas, refrigeration, etc. There have been continuous efforts to improve the performance of these machines. Since the impeller is an active part that adds energy to the fluid, its geometry plays a major role in the performance of a centrifugal compressor. Performance improvements have been reported by introducing splitter blades [1,2], tandem blades [3], three-dimensional impeller design [4,5], etc. A detailed study by Elder and Gill [6] showed that the parameters, like slope of pressure rise characteristic; inducer incidence; impeller back-sweep angle; number of impeller and diffuser vanes; and diffusion rate in rotor and stator, have significant effect on the compressor stability limit. Hildebrandt and Genrup [7] investigated the effect of different back sweep angles and exducer widths on the steady-state impeller outlet flow pattern of a centrifugal compressor with vaneless diffuser through CFD simulations. It is shown that the impeller with increased back sweep provides more uniform flow pattern with better potential for diffusion process inside the diffuser. The differences between a conventional and an inverse designed impeller were compared in detail by Zangeneh et al [8].

Numerical simulations confirmed that the inverse designed impeller had more uniform exit flow, better control of tip leakage flow and higher efficiency than the conventional impeller. The results also showed that the shape of the trailing edge geometry had appreciable effect on the impeller performance.

In the context of three-dimensional impeller design, the blade skew means introduction of variation in the blade angle from hub to shroud at the trailing end (Fig. 1). Blade skew is considered to redistribute the flow and move the high loss fluid from the suction side to the hub, resulting in significant reduction of the blade-to-blade flow variation at the impeller exit. Work reported by Moore and Moore [9] has shown improvement in the compressor performance by introducing skew / lean to the impeller blades. Similarly, Moore et al [10] have also shown the use of impeller blade skew to improve the uniformity of the exit flow. A patent by Harada and Shin [11] has disclosed the blade skewing techniques to improve the performance of the centrifugal compressors. It is claimed that the secondary flows can be suppressed by reducing the pressure gradient across the hub and the shroud by introducing blade skew in an impeller.
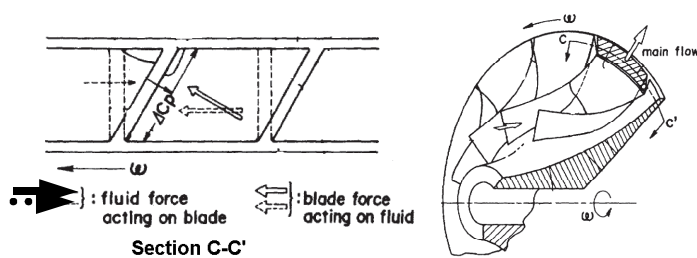


Fig. 1 Typical centrifugal compressor impeller with skew at the vane exit
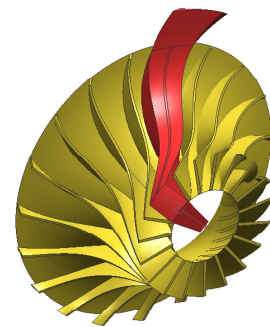
Fig. 2 CAD model of the impeller and the extracted fluid domain

The published literature, as discussed above, reveals that the overall performance and the stability margin of the centrifugal compressors are improved by introducing tangential skew at the impeller blade exit. However, there is no clear understanding of the changes in the impeller passage flow, brought about by the blade skew, which are responsible for these improvements. To address this issue, detailed CFD simulations of a high pressure ratio backswept centrifugal compressor were carried out with five different exit skew angles, including the baseline zero skew case. Following sections explain the CFD modeling of the selected impeller with and without skew; validation of the CFD simulation using experimental data; and detailed discussion on the overall performance and on the flow behaviour through different impeller builds.

## 2. IMPELLER DESIGN SPECIFICATIONS AND GEOMETRIC MODEL

A centrifugal compressor having design pressure ratio of 4:1 and design rotational speed of 30000 rpm was chosen for the present study. The CAD model of the compressor impeller is shown in Fig.2 and the geometric data is given in Table-1. It must be noted that the compressor impeller was originally designed with a skew angle of +45° and the experimental performance data for this impeller was available at 50% design speed only. Hence, the validation of the CFD simulations was limited to 50% design speed on the impeller with +45° skew. For subsequent CFD simulations at 100% design speed, the impeller was remodeled with 0° skew and that was considered as the baseline impeller. To investigate the effect of skew, the new baseline geometry was imparted different skew angles without violating other geometrical constraints and CFD analyses were performed at the design rotational speed.

**Table-1 Geometric details of the centrifugal compressor impeller**

| Parameters | Values |
|---|---|
| Type of impeller | Open Impeller |
| Number of blades | 19 |
| Impeller inlet eye dia | 160mm |
| Impeller inlet root dia | 80mm |
| Impeller tip dia | 300mm |
| Back sweep angle | 25-35° |
| Blade width at tip | 9.63mm |
| Tip clearance | 0.5mm |
| Operating speed | 30,000 rpm |
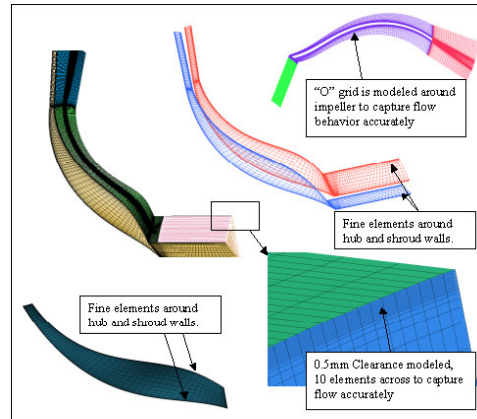


**Fig. 3 Details of computational grid**

## 3. DETAILS OF NUMERICAL MODEL

Since the geometry of the impeller was cyclic symmetric, the CFD simulations were performed on one impeller passage only by applying periodic boundary condition, resulting in considerable saving in the computational time. The impeller had 19 blades; hence an 18.95° sector model was created. The fluid domain was extracted for one impeller blade passage with the blade itself in the middle of the domain, as shown in Fig.2. The computational grid, comprising structured hexahedral elements in multi-block environment, was generated using ICEM CFD. Sufficiently fine elements were created in the impeller tip clearance region, around the impeller, and at the hub and shroud walls, as shown in Fig.3. Adequate mesh quality checks were also performed by keeping the parameters like mesh angle and determinants within acceptable limits.

The impeller hub and the blades were defined as rotating components with reference to the stationary domain. The shroud was defined as non-rotating domain. The periodic cutting planes were defined as periodic boundaries, on which the flow properties were computed by taking average on either side of them. The working fluid was air and the computations were performed using steady state segregated solver (FLUENT), with standard wall function to solve the boundary layer, and also standard $k$-$\varepsilon$ turbulence model. Based on the grid independence study, a grid size of about 498000 elements was used in the CFD simulations.

## 4. CONSTRUCTION OF SKEWED IMPELLERS

The baseline zero skew impeller geometry was modified with 4 different exit skew (lean) angles of +45°, +30°, -30° and –45°. Figure 4 shows the impellers with skew angles of +45° and –45° along with the baseline impeller. In case of positive skew, the impeller tip makes an acute angle with the direction of rotation and the point at the shroud of the tip section would *lead* in relation to the point at the hub. In case of negative skew, the impeller tip makes an obtuse angle with the direction of rotation and the point at the hub of the tip section would *lead* in relation to the point at the shroud. In the present study, the skew was limited to a fraction of the impeller length near the trailing end, based on the energy addition rate along the impeller. Sufficient care was taken so that the geometrical features, like tangency and profile smoothness, were not disturbed. This was considered important in order to bring out the effect of skew angle alone. Presence of the skew indirectly affects the blade angle distribution from hub to shroud, as shown in Fig.5. Hence, introduction of the skew in this way was to ensure that the impeller flow profile did not change too much, thus making the comparison of the baseline and the skewed impellers more meaningful.

45° Skew        0° Skew        -45° Skew



a) Blade angle variation – pictorial representation



b) Blade angle variation along impeller height at exit plane
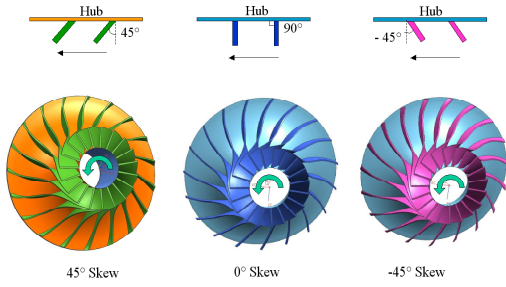
**Fig. 4  Impellers with positive, zero and negative exit skew**
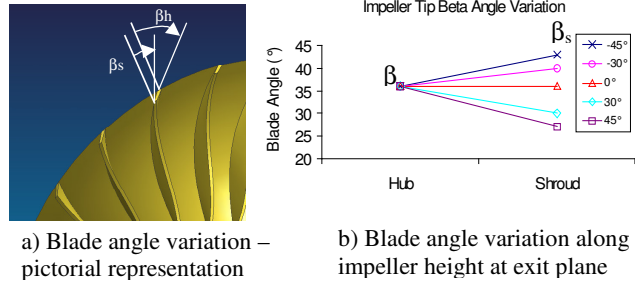
**Fig. 5  Modified skew geometries**

## 5.  RESULTS AND DISCUSSION

The CFD simulations of the five impeller builds having different exit skew angles of +45°, +30°, 0°, -30° and –45° were performed at 100% design speed of 30000 rpm. Referring to Fig.6, there is significant increase in pressure ratio of about 2.2%, when the impeller has positive skew. On the contrary, for negative skew, the compressor pressure ratio is reduced by almost 3.5% compared to the baseline skew case. Also, there is an appreciable difference in the compressor stall point pressure ratio and stalling mass flow rate owing to impeller skew.
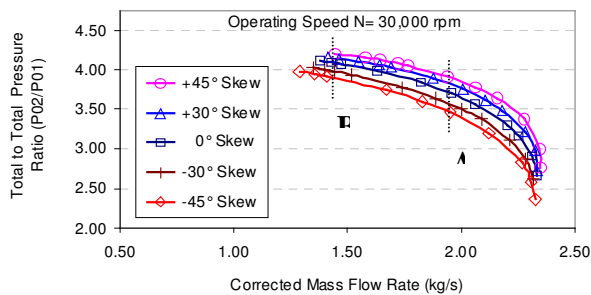


**Fig. 6  Compressor performance map (total pressure ratio) for different skew angles**
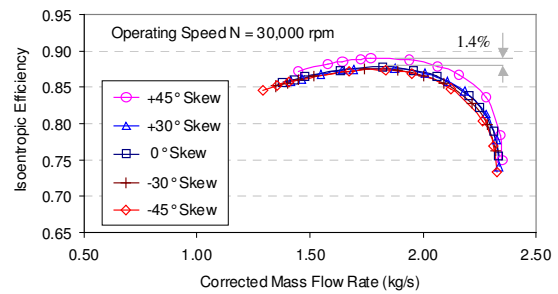


**Fig. 7  Compressor performance map (isentropic efficiency) for different skew angles**

Introduction of skew gives rise to a new performance map for each skew angle. The stall point pressure ratio increases when the skew angle is increased from negative to positive and the stall point mass flow rate decreases when the skew angle is changed from positive to negative.  For a skew angle of +45°, the compressor stalls at a relatively higher mass flow rate compared to 0° skew



**Fig. 8  Total pressure rise along the impeller**

and the reduction in stall margin is ~4.7%.  On the other hand, at a skew angle of –45°, the stall margin improves by ~6.5%.  There is significant effect of skew on the impeller efficiency also (Fig.7).  The peak efficiency improves by 1.4% at +45° skew, which can be attributed to improved energy adding capability of the impeller. The efficiency levels for other skew angles are comparable to the baseline impeller.

The pressure ratio curves (Fig.6) of the compressor with different skew angles diverge at low mass flow rates near the stall region. Effect of skew is more pronounced at high pressure ratios. On the other hand, near the choke limit, there is not much variation in the pressure ratio between skewed and unskewed cases. Figure 8 explains the variation in energy addition to the

fluid by impellers with different skew. The impeller with +45° skew is able to add higher energy from 75% of the merdional distance, thus producing more pressure ratio and also higher efficiency for the entire mass flow range.

Due to blade skew, the mass averaged relative flow angle $\beta_2$ varies at the impeller exit. For +45° and –45° skew cases, the variation, compared to 0° skew, is about –2° and +3° respectively. Referring to the velocity triangles in Fig.9, the change in $\beta_2$ is from 41° to 39° for +45° skew and the exit relative flow velocity is reduced. Consequently, the absolute flow velocity is higher with higher tangential component, leading to higher work coefficient. Hence, the impeller with +45° skew is able to generate more pressure for the given work input. On the contrary, for -45° skew, the relative velocity increases due to increased $\beta_2$, with consequent reduction in the exit absolute and tangential velocities. The work addition is less, resulting in lower pressure rise. The variation of $\beta_2$ in the blade-to-blade tangential plane is shown in Fig.10. It appears that, for +45° skew, an acute angle between the blade suction surface and impeller shroud reduces slip with consequent lowering of $\beta_2$. The converse is true for -45° skew wherein the slip is increased due to an obtuse angle between the blade suction surface and impeller shroud, resulting in higher $\beta_2$.

The relative Mach number variation in the blade-to-blade plane at impeller exit is shown in Fig.11a, corresponding to the near design point flow rate, and Fig.11b corresponding to the stall mass flow rate of the +45° skew impeller. There is relatively larger low momentum fluid region at the shroud (Fig.11a) for +45° skew impeller, which is responsible for lower average relative velocity. At the stall point of the impeller with +45° skew (Fig.11b), this low momentum fluid zone becomes larger, compared to the other two cases of 0° and -45° skew. It must be noted that although the +45° skew impeller is operating at near stall, the other two impeller builds, with 0° and –45° skew, are away from their corresponding stall points. The low momentum fluid regions are relatively smaller in extent, allowing further reduction in the compressor mass flow rate and hence higher stall margin. The larger low-momentum zone in the +45° skew impeller is created due to higher diffusion near the stall point.
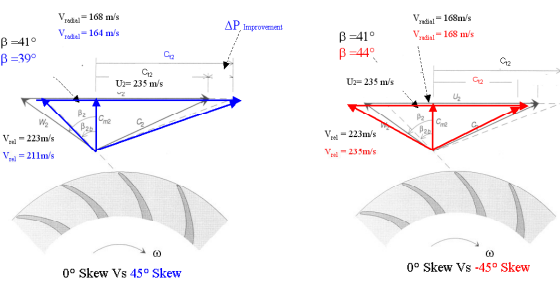


**Fig. 9  Exit velocity triangles – effect of relative flow angle variation**
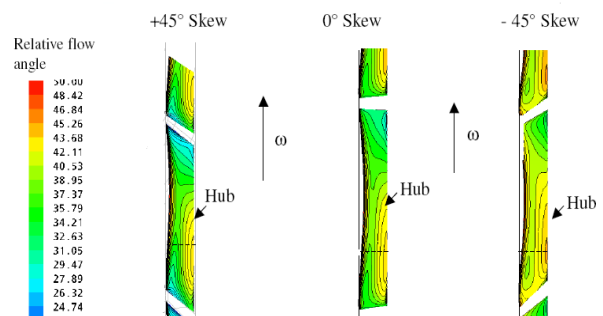


**Fig. 10  Relative flow angle distribution at impeller exit for three skew cases at near design mass flow rate**
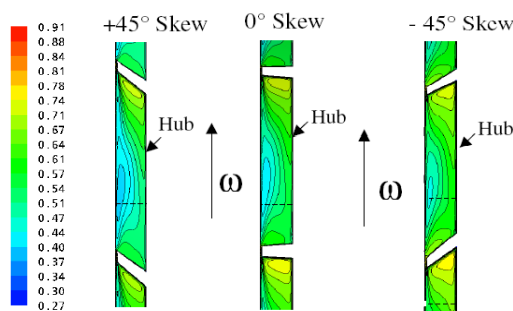


**a) At near-design mass flow rate**
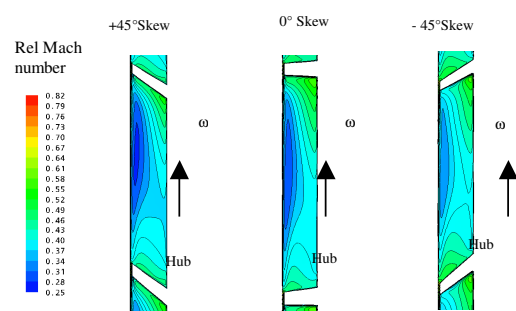


**b) At stall mass flow rate of impeller with +45º skew**

**Fig. 11  Relative Mach number distribution at impeller exit for three skew cases**

It can be argued that the factors responsible for reduced stall mass flow rate for –45° skew impeller are: a) lower pressure rise characteristic; b) less aggressive work addition; and c) lower diffusion rate within the impeller passage. From the above discussions, it is apparent that the impeller with +45° skew is capable of generating higher pressure ratio with higher efficiency, but the stall initiation is at a higher mass flow rate than that for +0° and -45° skew impellers.

## 6. CONCLUSIONS

Introduction of skew at the impeller trailing edge significantly changes the work addition to the fluid.  Introduction of positive skew produces lesser back-sweep angle at the impeller hub, resulting in higher work addition. Hence, the efficiency and pressure ratios are higher than those for 0° and –45° skew.  For the +45° skew case, the pressure ratio improvement is ~2% compared to 0° skew impeller. With negative skew, the compressor performance in terms of stall margin improves.  For the -45° skew case, the stall margin is improved by ~6% compared to the 0° skew case. Due to negative skew at the impeller exit, energy addition to the fluid becomes less aggressive with lower diffusion in the impeller passage, leading to safe compressor operation even at reduced flow rates.

## 7. REFERENCES

[1]    Hirotaka Higashimori, Kiyoshi Hasagawa, Kunio Sumida and Tooru Suita, Detailed Flow Study of Mach Number 1.6 High Transonic Flow with a Shock Wave in a Pressure Ratio 11 Centrifugal Compressor Impeller, *Trans. ASME Journal of Turbomachinery*, (2004), Vol. 126, pp. 473-481.
[2]    Larosiliere L.M., Skoch G.J. and Prahst P.S., Aerodynamic Synthesis of a Centrifugal Impeller Using CFD and Measurements, 33rd Joint Propulsion Conference and Exhibit AIAA–97–2878, Technical Report ARL–TR–1461, 1997.
[3]    Robert D. A. and Kacker S.C., Numerical Investigation of Tandem Impeller Designs for a Gas Turbine Compressor, *Trans. ASME Journal of Turbomachinery*, (1992), Vol.124, No.1, pp. 36-44.
[4]    Zangeneh M., A Compressible 3D Design Method for Radial and Mixed Flow Turbomachinery Blades, *Int. Journal of Numerical Methods in Fluids*, (1991), Vol. 13, pp. 599-624.
[5]    Zangeneh M., On 3D Inverse Design of Centrifugal Compressor Impellers with Splitter Blades, *43rd ASME International Gas Turbine and Aeroengine Congress and Exposition*, Stockholm, Sweden, (ASME paper 98-GT-507), 1998.
[6]    Elder R.L. and Gill M.E., A Discussion on the Factors Affecting Surge in Centrifugal compressors, *Trans. ASME Journal of Engineering for Gas Turbines and Power*, (1985), Vol. 107, p. 499.
[7]    Hildebrandt A. and Genrup M., Numerical Investigation of the Effect of Different Back Sweep Angle and Exducer Width on the Impeller Outlet Flow Pattern of a Centrifugal Compressor with Vaneless Diffuser, *Trans. ASME Journal of Turbomachinary*, (2007), Vol. 129, p. 433.
[8]    Zangeneh M., Schleer M., Hildebrandt A. and Genrup M., Investigation of an Inversely Designed Centrifugal Compressor Stage-Part I: Design and Numerical Verification, *Trans. ASME, Journal of Turbomachinary*, (2004), Vol. 126, p. 73.
[9]    Moore J. and Moore J. G., Use of Blade Lean in Turbomachinery Redesign, *NASA Marshall Space Flight Center, Eleventh Workshop for Computational Fluid Dynamic Applications in Rocket Propulsion*, 1994.
[10]   Moore J., Moore J.G. and Timmis P.H., Performance Evaluation of Centrifugal Compressor Impeller using 3D Viscous Flow, *Trans. ASME, Journal of Engineering for Gas Turbines and Power*, (1984).
[11]   Harada H. and Shin Konomi, Centrifugal Turbomachinery, United States Patent No. 6,338,610 B1, 2002.

# NUMERICAL ANALYSIS OF THE AUTOMOBILE HVAC SYSTEM THROUGH DEFROST MODE

Lee KUMBAE, Jun YONG-DU, Kader Md. FAISAL & Kang HYU GOO

Department of Mechanical Engineering, Kongju National University,
275 Boodae-Dong, Cheonan 330-717, Republic of Korea
e-mail: mfaisaliut@yahoo.com

## ABSTRACT

*Understanding the fluid flow and heat transfer characteristics within a vehicle compartment is very important for controlling the effect of major design parameters. Also, adequate visibility through the vehicle windshield over the entire driving period is of paramount practical significance. The unsteady flow field data which was used in temperature solver is analyzed by using an operation friendly, fast and accurate CFD code – SC/Tetra. Turbulence was modeled by the standard k-ε equation. Numerical analysis of the three-dimensional model predicts a detailed description of fluid flow and temperature distribution in the passenger compartment and on the inside windshield screen. During the cooling period, the lowest temperature is observed in the lower part of the windshield and in the vicinity of the defroster griller. It was found that the temperature come down to a comfortable range almost linearly at the initial stage. The numerical predictions are in good agreement with the experimental results.*

**KEYWORDS**: CFD, Defroster Griller, Automobile HVAC

## 1. INTRODUCTION

The substantial advancement in the field of CFD encouraged a number of researchers to investigate the various studies in the field of automobile Heating, Ventilating, and Air-Conditioning (HVAC) system. Numerical simulations of a two-dimensional, and a three-dimensional airflow in a passenger compartment were performed by Hara *et al.* [5]. Also, the effect of four HVAC design parameters on passenger thermal comfort was analyzed in a simplified passenger compartment using CFD [Lin *et al.*, 10]. They found that the location of the vents and the air flow rate were the most important parameters which influenced the thermal comfort of the passengers. The position of the outlet in the rear of the car was equally important for the thermal comfort of rear passenger. A study by Ishihara *et al.* [6] examined the airflow inside a one-fourth scale three-dimensional model. Lee *et al.* [7] utilized a CFD code, namely ICEM-CFD, to simulate the mechanism of windshield de-icing. The complete vehicle configuration was transformed from CAD and the mesh was created and assembled using a multi-domain approach. The authors demonstrated the capability of the developed module in simulating cold room de-icing tests to supplement the experimental work. Recently, Brewster *et al.* [4] used the CFD code STAR-CD to simulate mechanism of ice building on the windshield in three-dimensional form. The authors used a non-linear enthalpy-temperature relationship to simulate the ice/water layer. Melting contours were predicted every 5 minutes. Aroussi and

Aghile [2] used a one-fifth scaled Perspex model of a passenger compartment for experiment by Particle Image Velocimetry (PIV) technique. A further study by Aroussi *et al.* [3] concentrated to simulate the turbulent fluid flow over and heat transfer through a model of vehicle windshield defrosting and demisting system. Lee *et al.* [8, 9] stressed on temperature distribution characteristics of automobile interior both numerically and experimentally when operating the HVAC system in the summer. In the present study, the flow field and temperature distribution within a 3D full scale model of a vehicle compartment and on the windshield are investigated using CFD to determine the capability of the method. Thermo-graphy and temperature measurements by K-type probe are presented and evaluated.

## 2. EXPERIMENTAL SETUP

The HVAC system is used in automobiles to control the thermal environments of passenger compartment and to defrost/demist. The present experiment was performed on a 2006 SM3 model vehicle of Samsung Automobile Company with a 1,500 cc gasoline engine. The automobile was instrumented with sensors in the passenger compartment to measure the air temperature on the locations shown in the Figure 1. The horizontal line L1 represents the vertical cross section where the velocity vector has been observed. A series of tests and measurements were performed in the automobile while parked in sunny and hot summer conditions. The fully opened defrost registers were used to supply the flow at a velocity of 7 m/s with 35° injection angle. The experimental period was 30 minutes from 11:10 am to 11:40 am on 27 August, 2008. Since a large number of sensors (K-type probe) were used for temperature measurements during the cooling period, and the data were automatically saved to the hard drive every 3 seconds, a data acquisition system integrated with a PC was employed to control the complicated task. Outside ambient conditions were approximately 28 °C dry bulb temperature. Thermography was used to determine the temperature contours and examine the mechanism of condensation during the cooling period. The system consists of a thermal image camera, which records the thermal evolution of the windshield and a video recorder together with a PC, to capture, analyze and process the images obtained. The lens was perpendicular to the plane of the windshield. The thermal image camera was positioned on a tripod at a distance of about 3m in the front of the windshield. After turning on the blower of the HVAC system and setting up the thermographic equipment, thermal maps were recorded, at intervals of thirty seconds, starting from the time at which the cooling is switched on.
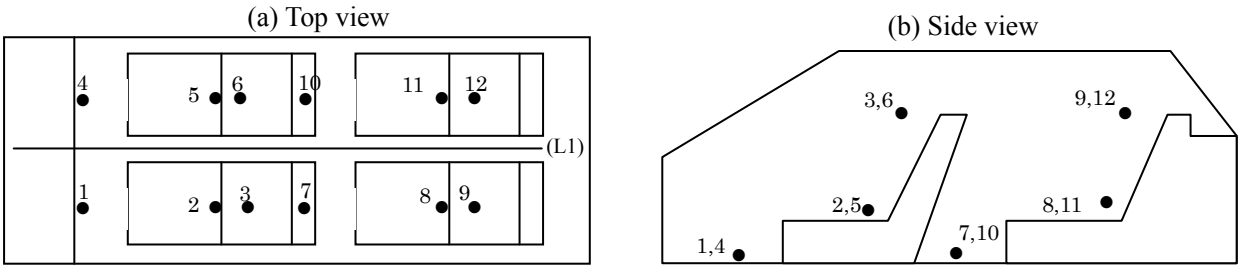


Figure 1: Temperature measurement locations inside an automobile compartment.

## 3. NUMERICAL INVESTIGATION:

The numerical code used in this study is the finite volume CFD code Scryu Tetra (SC/Tetra) version 7 [1]. SC/Tetra is equipped with an automatic hybrid mesh generator, a high-speed unsteady flow solver and a state of the art postprocessor. The three dimensional geometry of the model was imported to the pre-processor of the SC/ Tetra and a computational mesh of fluid cells

(2078571 tetrahedral elements) are generated by using the automatic mesh generator. To increase the accuracy of numerical analysis the defroster nozzle, frost and windshield were meshed closely. The flow inside the compartment was unsteady and incompressible turbulent flow. The numerical solution was done in SC/Tetra solver. The solution involves splitting the geometry into many sub-volumes and then integrating the differential equations over these volumes to produce a set of coupled algebraic equations at the centroid of each volume. The solver guesses the pressure field and then solves the discretized form of momentum equations to find new values of pressure and velocity components. This process carries on an iterative manner, until the convergence criterion is satisfied. The turbulence was modeled by using the standard k-ε turbulence equations.

## 3.1 Numerical Model

The simplified three dimensional geometry of an automobile compartment was generated in CATIA (Computer-graphics Aided Three dimensional Interactive Application) version 5. The numerical model is shown in Figure 2. The simplified geometry represents the actual dimensions of a SM3 2006 car (manufactured by Renault and Samsung) compartment and windshield, with accurate locations of the nozzles and vents including the seating arrangements. The tetrahedral volume mesh of the model is illustrated in Figure 3.
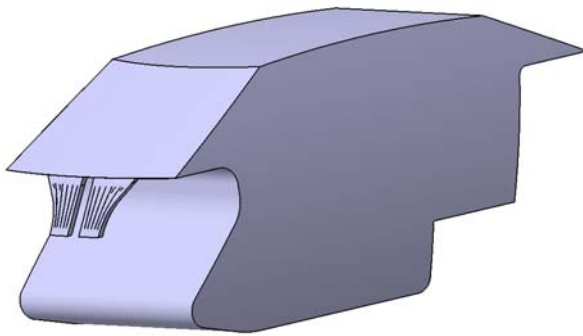


**Fig. 2 Numerical model of an automobile compartment along with the defroster nozzle.**
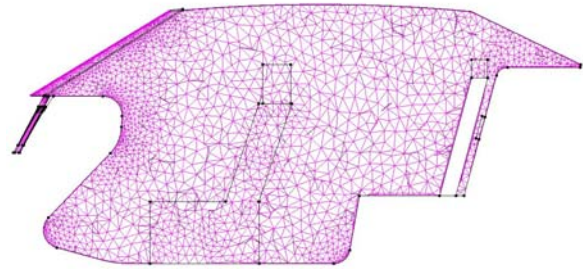


**Fig. 3 Overall computational mesh (2078571 elements) of the model.**

## 3.2 Governing Equation:

The Governing Equations involved for the numerical simulation are Momentum conservation equations (the Navier-Stokes equation), continuity equation, and energy conservation equation. Let us consider the vehicle compartment as an incompressible fluid.

Mass Conservation Equation:
$$\frac{\partial u}{\partial x} + \frac{\partial v}{\partial y} + \frac{\partial w}{\partial z} = 0 \qquad (1)$$

Momentum Conservation Equation:
$$\frac{\partial \rho u_i}{\partial t} + \frac{\partial u_j \rho u_i}{\partial x_j} = -\frac{\partial p}{\partial x_i} + \frac{\partial}{\partial x_j}\mu(\frac{\partial u_i}{\partial x_j} + \frac{\partial u_j}{\partial x_i}) - \rho g_i \beta(T - T_0) \qquad (2)$$

Here, $\mu = \mu_1 + \mu_2$ $\qquad \mu_1 = $ Laminar coefficient of viscosity

$$\mu_2 = C_t \rho \frac{k^2}{\varepsilon} = \text{Turbulent coefficient of viscosity}$$

Energy Conservation Equation:
$$\frac{\partial \rho C_p T}{\partial t} + \frac{\partial u_j \rho C_p T}{\partial x_j} = \frac{\partial}{\partial x_j} K \frac{\partial T}{\partial x_j} + \dot{q} \qquad (3)$$

The standard k-ε equation has been considered to represent the intensity of turbulence and the rate of energy dissipation.

Turbulent energy equation: $\dfrac{\partial \rho k}{\partial t} + \dfrac{\partial u_i \rho k}{\partial x_i} = \dfrac{\partial}{\partial x_i}(\dfrac{\mu_t}{\sigma_k}\dfrac{\partial K}{\partial x_i}) + G_S + G_T - \rho\varepsilon$  (4)

Here, $G_S = \mu_t(\dfrac{\partial u_i}{\partial x_j} + \dfrac{\partial u_j}{\partial x_i})\dfrac{\partial u_i}{\partial s_j}$ and $G_T = \rho_j \beta \dfrac{\mu_t}{\sigma_t}\dfrac{\partial T}{\partial x_i}$

$k$ - Turbulence energy $[\dfrac{m^2}{S^2}]$ and $\varepsilon$ – Turbulence dissipation rate $[\dfrac{m^2}{S^3}]$

Turbulent energy dissipation equation: $\dfrac{\partial \rho\varepsilon}{\partial t} + \dfrac{\partial u_i \rho\varepsilon}{\partial x_i} = \dfrac{\partial}{\partial x_i}(\dfrac{\mu_t}{\sigma_\varepsilon}\dfrac{\partial\varepsilon}{\partial x_i}) + C_1\dfrac{\varepsilon}{k}(G_S + G_T)(1 + C_3 R_f) - C_2\dfrac{\rho\varepsilon^2}{k}$  (5)

Here, $R_f = -\dfrac{G_T}{G_S + G_T}$, $\mu_t = C_t\rho\dfrac{k^2}{\varepsilon}$, $\sigma_k = 1$, $\sigma_\varepsilon = 1.3$, $\sigma_t = 0.9$, $C_{\varepsilon1} = 1.44$, $C_{\varepsilon2} = 1.92$, $C_t = 0.009$

The finite volume method is used in SC/Tsolver to solve the equations listed above on a computer. A finite volume method solves the governing equations by converting them into an integral conservation from that is expressed on each fractional unit of decomposed elements, or control volume.

### 3.3 Boundary/Initial condition:

The initial temperature of the compartment was 35°C. Only the defroster grillers were employed to inject the air at a velocity of 7 m/s. The unsteady inlet temperature varies from 23°C to 12°C as the first and final temperature respectively over a period of 30 minutes. Fixed static pressure was selected for outflow condition. The wall of the compartment was considered as adiabetic. The ambient temperature was considered as 28°C and isothermal.

### 4. RESULTS AND DISCUSSION

The study concentrates on the actual air distributions through the windshield vents including the complete HVAC system, operating in the defroster mode only.
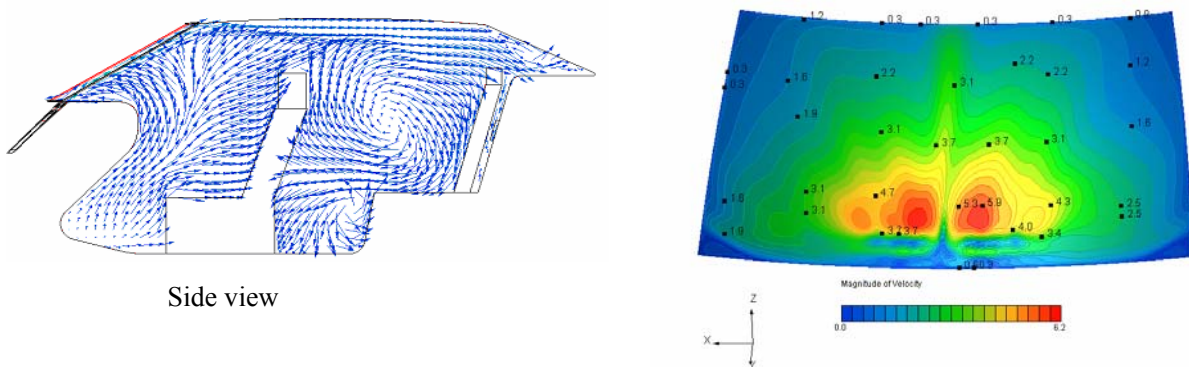


**Fig. 4 (a) Velocity vector and (b) Velocity distribution, in the vicinity of windshield.**

A general observation of the flow behavior inside and around the windshield model through the plane L1, have been shown in Figure 4(a), which is characterized by the flow discharged from the defroster grillers. The flow from defroster grillers impinges on the windshield,

and then moves forward according to the windshield angle to the top and over the front seats to impinge on the back seats resulting in a stagnation region. Finally the flow returning from the rear is joining to the main stream. Figure 4(b) illustrates the velocity distribution in the vicinity of windshield. It can be seen that the magnitude of velocity varied from 0.0 m/s to 6.2 m/s, the airflow does not cover the whole windshield area at the same magnitude due to the geometric complexity of the windshield and the defrosting system. A lack of flow has been observed near the corners and the lower part of the windshield due to the obstructions caused by the windshield, the front side windows and the dashboard. Consequently, a critical dead zone occurs, most perpetually at the corners and at the bottom most part of the windshield.
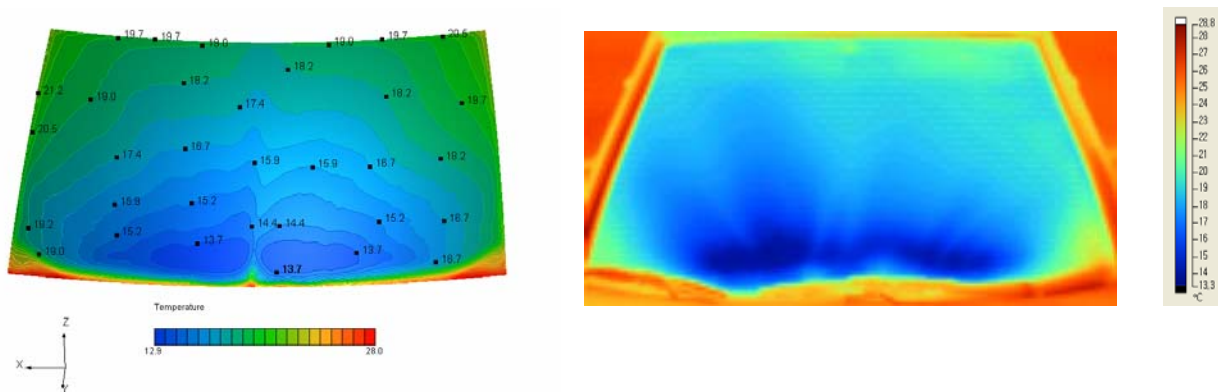


**Fig. 5 Comparison of the condensation formation pattern and temperature contours on the windshield (a) calculated temperature contour and (b) Measured temperature contour**

To illustrate the effect of velocity vector on the temperature distribution in the vicinity of the windshield glass, a front view is presented in the Figure 5(a). The local temperature on the windshield is evident from the front view. It can be seen that the lowest temperature region is in the lower part of the windshield near the defroster nozzle, over a value of 13.7°C. In the upper part of the windshield, the temperature magnitude increase up to 21°C. This temperature gradient is the effect of velocity magnitude, deflected from the defroster nozzle on the dashboard. The highest temperature was observed at two bottom corners and the bottom most part of the windshield. The thermographic temperature contour has been presented in Figure 5(b). The numerical predictions and the measured temperature contour are in good agreement.
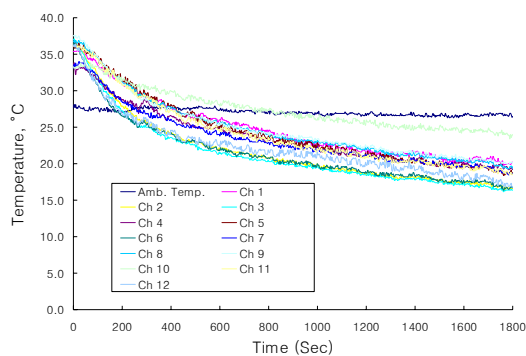


**Fig. 6 Experimental temperature distribution inside the compartment.**
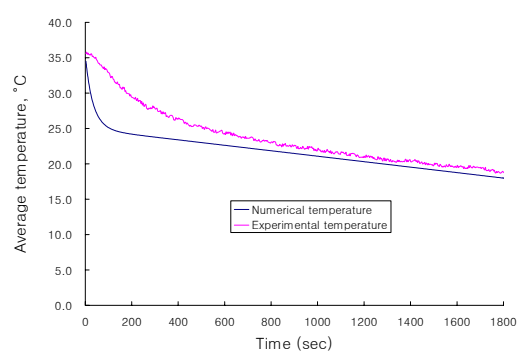


**Fig. 7 Variation on average temperature inside the compartment**

The experimental temperature distribution inside the compartment has been presented in the Figure 6. The temperature at 12 different locations inside the vehicle decreased almost linearly up to 400 seconds during the cooling period, while the ambient temperature remains constant throughout the whole experiment. After that slight decrease has been noticed up to 1800 seconds.

One important observation is that the temperature at the bottom part of the compartment remained lower than the top side of the compartment because of the roof of the vehicle achieving higher temperature and the radiation through the windshield and other glasses. In addition, it must be mentioned that measurements were taken in a parked automobile. The automobile in motion or in an automobile with passengers may affect the measurements. The numerical predictions of average temperature inside the compartment have been illustrated in Figure 7. The initial period of temperature drop is a bit different than the experimental result. In the numerical analysis the whole compartment was considered as adiabatic, but during experiment the radiation through the windshield and other glasses may cause this difference. Otherwise a good agreement has been found between the numerical predictions and experimental results.

## 5. CONCLUSION

The fluid flow pattern, velocity contour and temperature distribution adjacent to a vehicle windshield and inside the compartment were determined by using a new CFD code. Comparison with the experimental results obtained by the thermographic technique and K-type probe temperature measurements showed that the CFD code can be a very useful design tool for an automobile HVAC system. The standard k-ε turbulence model and a properly refined grid were found acceptable for the analysis of an automobile HVAC system.

## 7. REFERENCES

[1] Anon, (2005). SC/ Tetra User's Guide. Software Cradle Co., Ltd.

[2] Aroussi, A. and Aghil, S. (2000). Characterisation of the flow field in a passenger car model. *Optical Diagnostics in Engineering* 4 ,1, 1–15.

[3] Aroussi, A.; Hassan, A. and Morsi, Y.S. (2003). Numerical simulation of the airflow over and heat transfer through a vehicle windshield defrosting and demisting system. *Heat and Mass Transfer* 39, 401–405.

[4] Brewster, R. A. ; Frik, S. and Werner, F. (1997). Computational analysis of automotive windshield de-icing with comparison to test data. *SAE paper No. 971833*. London & New York.

[5] Hara, J. ; Fujitani, K. and Kuwahara, K. (1988). Computer simulation of passenger compartment airflow. *SAE Paper No.881749.*

[6] Ishihara, Y. ; Hara, J. ; Sakamoto, H. ; Kamemoto, K. and Okamoto, H. (1991). Determination of flow velocity distribution in a vehicle interior using a visualization and computation techniques. *SAE paper No. 910310.*

[7] Lee, J.-G. ; Jiang, Y. ; Przekwas, J. and Sioshansi, M. (1994). Validation of Computational Vehicle Windshield De-icing Process. *SAE paper No. 940600.*

[8] Lee, K. B. ; Jean, H. H. ; Youn, Y. M. (2006). Temperature Distribution Characteristics of Automobile Interior When Operating the HVAC System in the Summer. Proc. KSME Autumn Annual Conference, 1763-1768.

[9] Lee, K. B. ; Kader, M. F. and and Youn, Y. M, (2008*).* Numerical Analysis Of Automobile Environment During The Cooling Period In Summer. Proc. Micro/Nanoscale Heat Transfer Int. Conference, ASME Conference, January 6-9, 2008, Tainan, Taiwan. MNHT2008-52344

[10] Lin, C. H. ; Han, T. and Koromilas, C. A. (1992). Effects of HVAC design parameters on passenger thermal comfort, *SAE paper No. 920264.*

# NUMERICAL INVESTIGATION ON EFFECT OF VANE CROSS SECTION ON A VENTILATED DISC BRAKE ROTOR FOR COOLING CHARACTERISTICS

Adityakumar[1], S.N. Sridhara[2], Abdul Nassar[3]

[1]Student, M.Sc. (Engg.), [2]Head of Mech. and AE Dept, [3]Course Manager, MCAD
Automotive Engineering Centre, M. S. Ramaiah School of Advanced Studies, Bangalore, INDIA
Contact e-mail: sns@msrsas.org, sridharasn1964@gmail.com

## ABSTRACT

*The energy absorption requirement in automobile brakes is becoming a critical issue due to the limiting size of brake pads and increasing speed capability of automobiles. An improperly ventilated brake system may lead to thermal failures such as hot spots and cracking of brake material. Several attempts have been reported in the literature towards analyzing the heat transfer capabilities of the brake system, however, these are limited to only analyzing the existing brake systems and do not explore the possibilities of designing new brakes.*

*In the present study, the cooling characteristics of a baseline disk brake rotor used in automobiles have been studied. Further, the disk rotor has been modified and numerically studied for enhanced cooling characteristics. Three dimensional CAD models were generated using software tool CATIA V5, and the meshing was done using ANSA as a pre-processor and STAR CD, a commercial CFD tool, was used as solver and post processor tool. The analysis was carried out on existing brake system and modified designs of ventilated disc rotor. By introducing cylindrical structures between the straight vanes (Model-4, Model-5) in the air-flow channel of the baseline configuration, a reduction of wall temperature of rotor by around 9.5% and 9% respectively for single and multiple struts was observed. With airfoil shaped structures between the straight vanes (Model-10, Model-11) a reduction of wall temperature of rotor by around 11% is observed. Hence, it is concluded that vanes with airfoil structures between straight vanes in the disk brake rotor may be effectively used to reduce the thermal loading and increase the life.*

**Key words:** *Automotive brake, disk brake heat transfer, CFD*

## 1. INTRODUCTION

The modern automobiles are designed to race at high speeds which in turn require the equally matching braking system for stopping the vehicle witin the shortest distanse possible, without affecting the stability of the vehicle. The requirement of driving the vehicle in sharp corners at reasonable safe speed and reduced un-sprung mass of the vehicle demand low centre of gravity of the automobile with respect to the road surface. This necessitates the size of the brakes to be smaller and lighter, yet   they are expected to absorb high kinetic energy.

During this process of braking, large amount of heat is generated due to direct conversion of kinetic energy into heat energy which must be promptly dissipated. The disc temperature can exceed 450K for normal cars and 1100K for race cars. The air flowing

1

through the internal passages in the disk rotor carry the heat from the brake shoes (Fig. 1) and the heat transfer characteristics depend on many factors including the geometry of the passages.

Many investigations of analysis of heat flow through the ventilated disk brakes are reported in the literature. Michael and Roland [1] discussed the airflow patterns in the disk rotors. Wallis et al [2] carried out a numerical study using Fluent on disc rotor blades to examine the effects of local heat and mass transfer of the axial gap distances for a single and co-rotating disk. The study of single rotating disk showed that heat and mass transfer coefficient are enhanced considerably by decreasing the hub height.

Schmidt and Krusemann [3] designed a brake disk and its surrounding components for optimal air flow, restricted by the functional requirement of the vehicle for reduced drag coefficient, weight and cost of the brake system. According to the authors [3], the most significant way to achieve thermal cooling efficiency is to make the rotor act as an air pump by largely increasing the airflow velocity. Anwar [4] conducted numerical study on a disc rotor operating at 800 rpm with 72 curved fins of $45^o$ air inlet angle and $105^o$ for the outlet angles on the fins with an air direction which will increase the airflow velocity by 37.2% compared to the current production rotors. Effect of vane shape on flow and heat transfer characteristics of brake disc has been discussed by Mallikarjun et al [5]. Although the published literature throw light on the analysis of heat transfer through the ventilated brake system, very few efforts have been reported towards exploring the possibilities of designing new types of brakes.

The present work is an effort to fill this gap by exploring different configurations of disk brake vanes towards enhanced heat transfer capabilities. The cooling characteristic of the disk brake rotor studied by Wallis et al [2] has been used for the validation studies. Further, the geometry of disk rotor vane passage has been modified and numerically studied for enhanced cooling characteristics.

## 2. NUMERICAL PROCEDURE

The disk rotor vane passage and a sector chosen for the numerical analysis are shown in Fig. 2. The dimension for the baseline study is taken from Wallis et al [2] with an outer diameter of 295 mm and inner diameter of 180 mm and 36 vanes. The geometric model was created using CATIAV5.
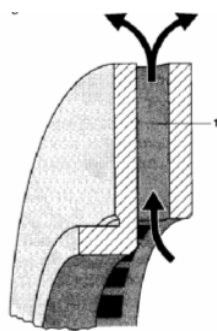


**Fig 1 Section of a disk rotor of a disk brake showing the airflow through the ventilation channels**
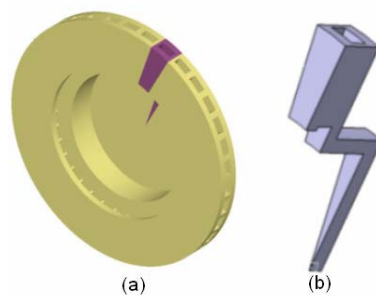
**Fig 2 (a) Disc rotor (b) 10 degree sector modeled in CATIA**
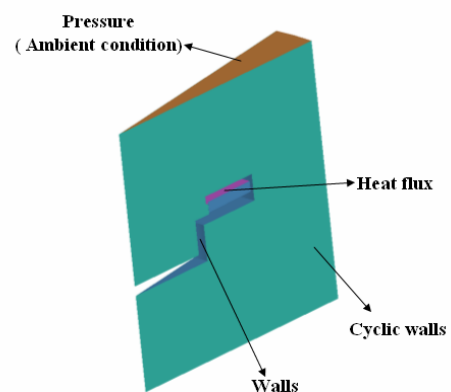
**Fig 3 Boundary conditions**

2

The rotor considered for the analysis has 36 passages and hence a 10 degree sector of the rotor has been modelled using a rotating frame of reference with cyclic boundaries using Star CD software. The rotors are considered as spinning in an infinite environment; hence pressure boundary of 1 atm was applied at domain boundary. The heat flux is applied at the passage walls, considering heat getting transferred from the walls of rotor. No slip condition is imposed at the rotor walls and conduction heat flow within the rotors is not investigated. The rotor is assumed to be rotating in anti-clockwise direction at speed of 1227 rpm.

The conduction within the rotor is not investigated, so the rotor is treated as hollow within the domain. The element type used is hexahedral and pentahedral elements. The number of cells for each of the models model is about 0.8 to 0.9 million.

The heat flux on the brake surface (28.06 kW/m$^2$) is computed with the assumption that the complete kinetic energy of vehicle traveling at 80 km/h is absorbed and converted into heat at the brake shoes, when the brakes are applied. The rotor is considered to be rotating in anti-clockwise direction at 1227 rpm. Periodic boundaries conditions are applied as only a $10^0$ sector is modeled. Boundary conditions applied on the flow domain are shown in Fig. 3. k-ω turbulence model used for the analysis.

## 3. RESULTS AND DISCUSSIONS

### 3.1 Baseline Studies:

The results obtained from the analysis on the baseline rotor are compared with those reported in ref [2]. Although the heat flux conditions are different in ref [2] to the one reported in this study (Fig. 4), the profiles of temperatures at the midline are alike and show similar trends. The velocity profiles at the midsection of the rotor (Fig. 5) show a relatively lower velocity region at the left-side of exit of the vane section. This is the indication of the separated flow at this region which might increase the local temperature in these regions due to lowered heat transfer characteristics.

One to one mapping of velocity to temperature profile can be seen in these to plots (Figs. 4 and 5) with higher velocity region experiencing higher heat flow rates and therefore resulting in reduced temperatures.
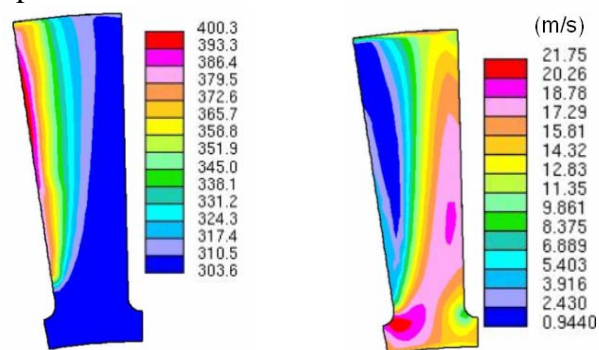


**Fig. 4 and 5 Temperature and velocity profiles at the midsection of the cavity of the rotor for baseline model. The temperature shown is in Kelvin**

### 3.2 Modifications to Vanes of the Rotor:

Based on this argument, several modifications with flow deviators in the flow passage as shown in Fig 6 were made and the flow and heat transfer characteristics were computed.

3

Model-1 represents baseline configuration, in model-2 a spike at the entry vane is introduced. Model-3 posses many such spikes along the channel.
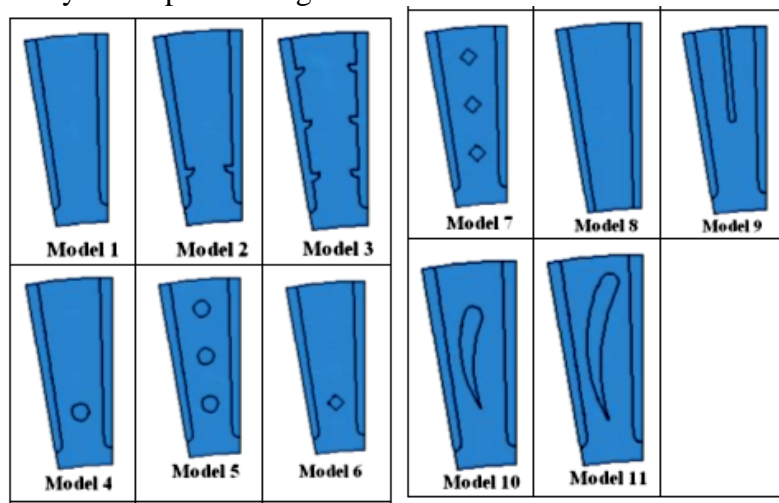


**Fig 6 Configurations of disc rotor and cross section of different vane designs**

These configurations were expected to deflect the flow so as to distribute the flow around the walls along the channel for maximized heat transfer. Model-4 consists of a cylindrical structure across the passage of flow of air in the vane. In Model-5 a row of such structures are introduced in the flow passage. Model-6 and model-7 are similar to model-4 and model-5 but the cross section of the structure is rhombus instead of circular shape.

Model 8 is modified to have a varying channel cross section area and different from the baseline configuration in terms of overall geometry. Model-9 has a split vane at the exit. Model-10 and model-11 have reversed aerofoil shape structures. These were expected to divert the flow of air close to the walls on both sides and enhanced heat transfer rates were expected from these configurations.

In all such cases, the air flow pattern, the temperature profile along the mid section of the vane and the wall temperature of vane are computed and compared for better cooling characteristics. However, only a few important cases are discussed in this section to avoid redundancy. The velocity and temperature profiles in the mid section of the vane for model-5 are shown in Fig 7.
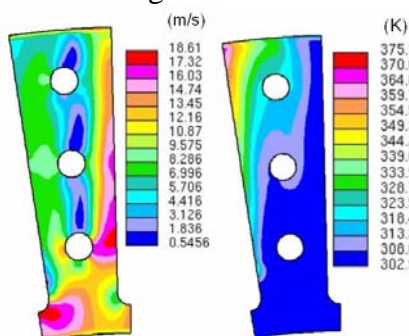


**Fig. 7 - Velocity and temperature profiles at the midsection of the cavity of the rotor for model - 5.**
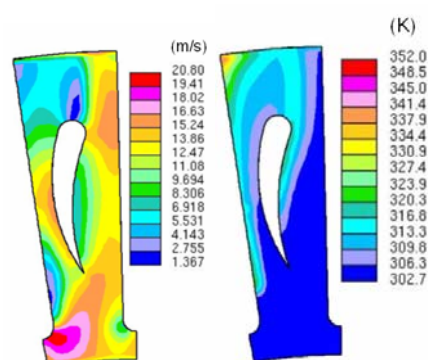
**Fig 8 Velocity and temperature profiles at the midsection of the cavity of the rotor for model-10.**

The cylindrical sections introduce recirculations around these sections resulting in a longer stay of the air in the vane. This results in cooler regions in the vane passage as shown. When compared to the baseline configuration with no modification in the geometry of the vane, (see Fig. 4 and 7) the overall temperature level is found decreased and the region of

4

hot-spots has also been reduced in size. The maximum temperature observed in this case is about 375 K, whereas the maximum temperature with the baseline configuration is around 400 K.

In case of configurations shown in model-10 and model-11, reversed aerofoil shaped splitter vanes are introduced in the air-flow channel; the aerofoil being small in case of model-10 and relatively large in case of model-11. As expected the temperature levels further reduce (see Fig 8) due to bettered air flow distribution around the vane channel due to the aerofoil shaped structure.
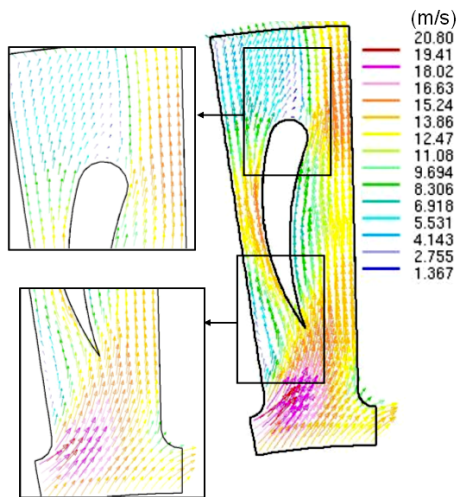


**Fig 9 Velocity vectors at the midsection of the cavity of the rotor for model-10.**
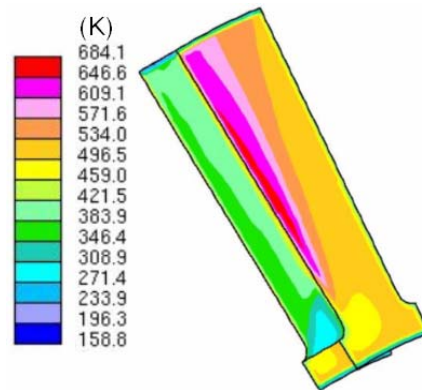


**Fig 10 Wall temperature distribution for the baseline model-1**

The velocity vectors around the aerofoil in model-10 (see Fig. 9) show smooth diversion of air around the aerofoil, making the air to flow close to the walls of the channel, due to which the heat transfer characteristics have been enhanced. The maximum temperature recorded at the midsection of the vane is found to be about 350 K which is lesser than that observed in model-5 (375 K) and baseline Model-1 (400 K)
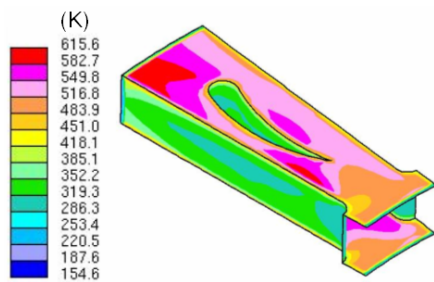


**Fig 11 Wall temperature distribution for the baseline model-10**
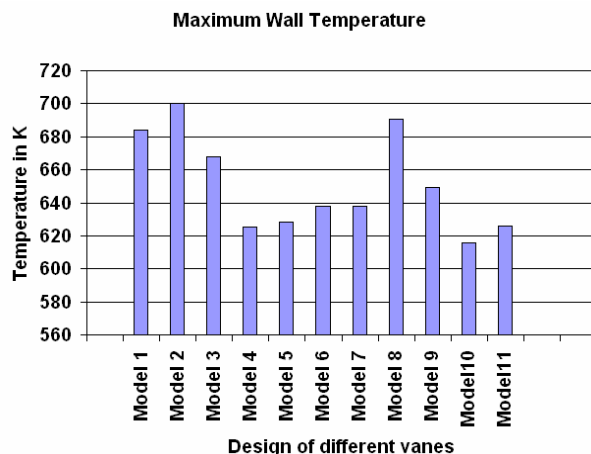


**Fig 12 Maximum wall temperature observed with various configuration of vane geometry in the disk rotor brake drum.**

The wall temperature profiles along the vane for baseline model-1 and the model with aerofoil splitter vane, model-10 are shown in Fig. 10 and Fig. 11 respectively. The maximum

5

temperature observed in model-1 is 684 K whereas it is about 615 K in model-10. In the present study, the convective heat transfer in the flowing air carrying the heat generated at the walls of the disk brake rotor has been considered ignoring the conduction heat transfer along the walls of the rotor

For this reason the predicted temperature levels near the walls are seen to be high. Nevertheless, conjugate heat transfer would give appropriate results; the heat transfer prediction with conjugate heat transfer involves greater numerical complexity. For simplified analysis, the results obtained in this study considering only the convective heat transfer mode would be sufficient to understand the trend of heat transfer in the disk rotor.

Further, it is also observed that the overall temperature levels in all regions near the walls of the rotor with the aerofoil shaped splitter vane have been decreased when compared to the baseline configuration (see Fig. 10 and 11). For a comparative study of heat transfer characteristics in all the models tested, the maximum wall temperature levels observed in all such cases have been compared and shown in Fig. 12. Fig 12 show that the aerofoil shaped splitter vane inside the air flow channel in the disk rotor brake drum will result in the lowest levels of maximum wall temperature. Hence this geometry can be considered to be the best configuration among the other configurations tested.

## 4. CONCLUSIONS

In the present study, cooling characteristics of a disk brake rortor used in automobiles has been studied numerically and the airflow channel in the vane are modified and tested for enhanced heat transfer characteristics. The following observations were made with the heat transfer characteristics in the modified disk brake rotor vane.

- With cylindrical structures between the straight vanes (Model-4, Model-5), a reduction in wall temperature of rotor by around 9.42% and 8.84% is observed respectively when compared with the baseline model (Model-1).
- With airfoil structures between the straight vanes (Model-10, Model-11), a reduction of wall temperature of rotor by around 11.12% and 9.24% respectively is observed when compared with the baseline model (Model-1).
- Hence, for modern high speed vehicles aerofoil shaped splitter blades are recommended in the vanes of brake disk rotor.

## 5. REFERENCES

[1]   Michael D. Hudson and Roland L. Ruhl, (1997), "Ventilated Brake Rotor Air Flow Investigation"  SAE 1997-97-1033

[2]   Lisa Wallis, Eddie Leonardi, and Brian Milton, (2002), "Air Flow and Heat Transfer in Ventilated Disc Brake Rotors with Diamond and Tear-Drop Pillars", Proceedings of International Symposium on Advances in Computational Heat Transfer, Australia, vol. 41, pp. 643-655.

[3]   Krusemann R., & Schmidt G., (1995), "Analysis and optimization of disk brake cooling via computational fluid dynamics", SAE transactions Society of Automotive Engineers, New York,  vol. 104 (1),  no6,  pp. 1475-1481

[4]   Anwar R. Daudi., (1999), "72 Curved Fins Rotor Design for Reduced Maximum Rotor Temperature" SAE 1999-01-3395

[5]   J M Mallikarjun, S Manohar Reddy and Ganeshan V., (2006), "Effect of Vane Shape on Flow and Heat Transfer Characteristics of Brake Disc". Proceedings of 3rd BSME-ASME International conference on thermal engineering 20 -22 December 2006, Dhaka Bangladesh.

6

# MODELING AND SIMULATION OF A REGENERATIVE DOWNDRAFT GASIFIER

P. C. Roy

Department of Mechanical Engineering,
National Institute of Technology Silchar
Silchar, Assam, India
E-mail:prokash@nits.ac.in or prokash.roy@gmail.com

## ABSTRACT

*A mathematical thermodynamic model of downdraft gasifier has been developed with regenerative air pre-heating effect to analyze the performance with respect to its operating parameter to obtain optimal performance parameters. The model has been formulated based on chemical equilibrium and thermodynamic equilibrium considering the effect of non-linear variable specific heats with temperature. The developed model has been well validated with the experimental data in available literature. Effects of equivalence ratio and moisture content of biomass on product gas composition as well calorific value have been obtained for wood waste (low ash content) and municipal solid waste (high ash content). Regenerated air-preheating effect has been analyzed for both. It has been found that regenerated preheating effect is not that much important for wood waste but it is significantly affects on the performance of gasifier handling municipal solid waste. It shows that gasification temperature falls sufficiently in case of municipal solid waste. But gasification temperature can be raised by regenerated air-preheating by the product gas subsequently improves product gas compositions and calorific value in case of municipal solid waste.*

**Key words:** *Biomass gasification, Downdraft gasifier, Chemical equilibrium, equivalence ratio and Regenerated air-preheating, Gasifier performance.*

## 1. INTRODUCTION

Biomass energy plays a pivotal role in the filed of renewable energy due to its availability and suitability for distributed power generation for the sustainable development of developing countries like India, Bangladesh etc. Energy can be recovered from biomass either by direct combustion or initial gasification and subsequent combustion. Out of these, second method is favoured as it is more efficient and less polluting to the environment. Biomass gasification is a thermo-chemical process by which solid biomass is converted into combustible gaseous fuel and this conversion is due to partial combustion of solid biomass [1-3]. In the present study, a complete gasification system for distributed power generation has been shown in figure 1. Inlet air has been preheated by the product gas which is coming from the cyclone separator where dusts are collected to clean the product gas.
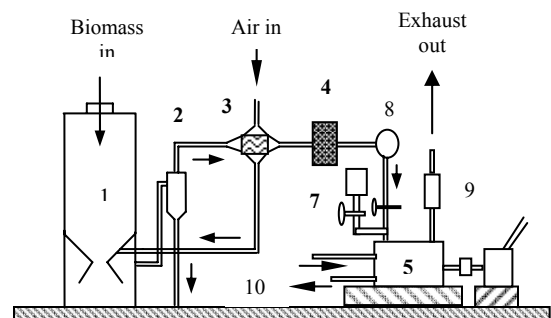


Figure 1. Biomass gasification system for distributed power generation.
( 1- Gasifier, 2-Cyclone Separator, 3-Air preheater, 4- Filter, 5-Producer gas engine, 6-Generator, 7- Air Filter, 8-Blower, 9- Muffler and 10- Water in and out)

The thermo-chemical processes occur inside the gasifier is very complex not only due to pyrolysis, partial oxidation and successive gasification at different elevated temperatures but also dependent on biomass composition, moisture content, ash content, reactivity of biomass and also gasifier design. Therefore, it is very necessary to understand the working behaviour of gasifier with respect to its operating parameters to obtain optimal performances such as calorific value of product gas. A thermodynamic model of down-draft gasifier has been developed based on the chemical equilibrium and the thermodynamic equilibrium of the global reaction predicting the final gas composition of the product gas ($H_2$, $CO$, $CO_2$, $CH_4$ and $N_2$) as well as its reaction temperature. The effect of variation of specific heat with temperature has been considered during the analysis. In the present model effect of ash content has been taken care of during the analysis. Predicted results have been well validated with the available experimental results in available literature. Effects of moisture content and equivalence ratio have been depicted with the abundantly available biomass wastes such as wood waste (WW) and municipal solid waste (MSW). Based on the composition of MSW and WW shown in table 1, have been treated as biomass fuel [5].

**Ruggiero et al. (1999) [4]** developed an equilibrium model considering the Gibbs free energy and predicted producer gas composition and the corresponding heating value but not well validated due to the simplicity in their model. And later on, the biomass gasification process was modeled by **Zainal et al. (2001) [5]** based on thermodynamic equilibrium by calculating equilibrium constant based on mean temperature. They investigated the influence of the moisture content and reaction temperature on the producer gas composition and its calorific value. **Khadse et al. (2006) [6]** developed an equilibrium model for biomass gasification for predicting gas composition and gross calorific value which is main criteria for engine application at different reaction temperature for four different available biomasses in India. Gross calorific value increases with reaction temperature and remains same at higher reaction temperature. **Jarungthammachote et al. (2007) [7]** studied a thermodynamic equilibrium model and second law analysis of a downdraft waste gasifier which was based on equilibrium constant for predicting the composition of producer gas and further modification was made by multiplying the equilibrium constants with coefficients to enhance the performance of the model. **Melgar et al. (2007) [8]** developed a mathematical model for the thermo-chemical processes in a downdraft biomass gasifier combining the chemical equilibrium and the thermodynamic equilibrium of the global reaction, predicting the final composition of the producer gas as well as its reaction temperature. The model has been validated experimentally. **Sharma (2008) [9]** proposed a full equilibrium model of global reduction reactions for a downdraft biomass gasifier in order to predict the accurate distribution of various gas species, unconverted char and reaction temperature. Full equilibrium of the global reduction reactions have been described using the principles of thermodynamics based on the stoichiometric approach. Model predictions for equilibrium constants for reduction reactions and dry gas composition have been validated by comparing the data collected from various sources. But the accuracy of the prediction of the equilibrium model depends on the correctness of the initial conditions of temperature and reactants concentrations.

With the above literature reviews, it shows that lots of works covered based parametric study such as moisture content, equivalence ratio etc. using different type of biomass fuels. Present study deals with the study of effect of ash content, moisture content, equivalence ratio, regenerated preheated air on the product gas composition, gasification temperature and calorific value. A regenerator has been used to preheat inlet air by the product gas.

## 2. FORMULATION OF THE MODEL
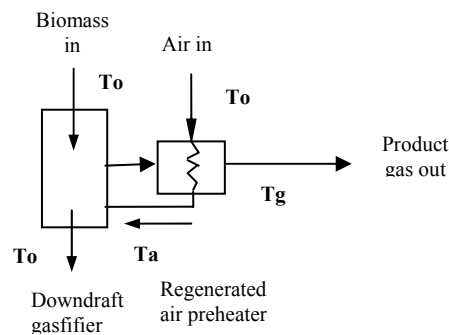


Figure 2. Schematic of the developed model.

In the present model it has been assumed that all the reactions are in thermodynamic equilibrium. It is considered that the pyrolysis product burns and achieves equilibrium in the reduction zone before leaving gasifier; hence an equilibrium model can be used for downdraft gasifier [5]. The reactions are as follows:

$$C + CO_2 = 2CO \qquad (1)$$

$$C + H_2O = CO + H_2 \qquad (2)$$

$$C + H_2 = CH_4 \qquad (3)$$
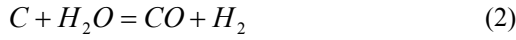
The equilibrium constant for methane formation eq. (3)

$$k_1 = \frac{P_{CH_4}}{\left(P_{H_2}\right)^2} \qquad (4)$$

Eqs. (1) and (2) are combined to get shift reaction and equilibrium constant for shift reaction.

$$CO + H_2O = CO_2 + H_2$$
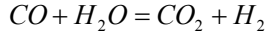
$$k_2 = \frac{P_{CO_2} P_{H_2}}{P_{CO} P_{H_2O}} \qquad (5)$$

The equilibrium constants $k_1$ and $k_2$ are obtained from the change in Gibbs function between the gaseous constituents in the products and reactants at the temperature of the zone ($T$)

$$k_1 = \exp\left(-\frac{\overline{g}^o_{CO_2}}{\overline{R}T} - \frac{\overline{g}^o_{H_2}}{\overline{R}T} + \frac{\overline{g}^o_{CO}}{\overline{R}T} + \frac{\overline{g}^o_{H_2O}}{\overline{R}T}\right) \qquad (6)$$

$$k_2 = \exp\left(-\frac{\overline{g}^o_{CH_4}}{\overline{R}T} + 2\frac{\overline{g}^o_{H_2}}{\overline{R}T}\right) \qquad (7)$$

The values of the Gibbs function for the different species have been obtained from the JANAF tables available in the literature [11].

The global reaction of gasification process can be written as follows:

$$CH_mO_n + aO_2 + 3.76aN_2 + wH_2O = x_1H_2 + x_2CO + x_3CO_2 + x_4H_2O + x_5CH_4 + 3.76aN_2 \qquad (8)$$
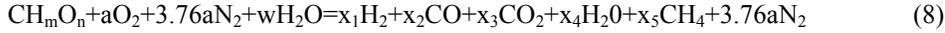
Where, $CH_mO_n$ = Formula of Biomass, a = the amount of oxygen per mol of wood, w= the amount of water per mol of wood, $x_1, x_2, x_3, x_4, x_5$ = the coefficients of constituents of the products

Table 1
Ultimate analysis of the biomass (dry basis, % weight)[13]

| Biomass | C | H | N | S | O | Ash | HHV(J/mol) |
|---------|------|-----|-----|-----|------|------|------------|
| Wood | 50.0 | 6.0 | 0.0 | 0.0 | 44.0 | 0.0 | 449568 |
| MSW | 47.6 | 6.0 | 1.2 | 0.3 | 32.9 | 12.0 | 433034 |

Moisture content per mol of wood can be defined as

$$w = \frac{(12 + m + 16n)MC}{18w(1 - MC)} X100\%, \text{ where MC is the moisture content by mass.}$$

From C balance of eq. (8), $1 = x_1 + x_3 + x_5 \qquad (9)$

From H balance of eq. (8), $m + 2w = 2x_1 + 2x_4 + 4x_5 \qquad (10)$

By O balance of eq. (8), $n + 2a + w = x_2 + 2x_3 + x_4 \qquad (11)$

From eq. (8) $x_5 = k_1 x_1^2 \qquad (12)$

From eqn. (8) $\quad x_1 x_3 = k_2 x_2 x_4 \qquad (13)$

In the global reaction eq. (8) we have five unknowns ($x_1$ to $x_5$). So we have five eqs. (9-13) and two of them are non-linear equations to form a polynomial of forth order. It has been solved by Newton Rapson iterative method to obtain the unknowns.

The gasification temperature ($T$) has been obtained by heat balance assuming the adiabatic flame temperature,

$$H_{fwood} + w\left(H_{fH_2O} + Hvap\right) + a\left(H_{fO2} + \int_{T_o}^{T_a} C_{P_{O_2}} dT\right) + 3.76a\left(H_{fN_2} + \int_{T_o}^{T_a} C_{P_{N_2}} dT\right)$$

$$= x_1\left(H_{fH_2} + \int_{T_O}^{T} C_{P_{H_2}} dT\right) + x_2\left(H_{fCO} + \int_{T_O}^{T} C_{P_{CO}} dT\right) + x_3\left(H_{fCO_2} + \int_{T_o}^{T} C_{P_{CO_2}} dT\right) +$$

$$x_4\left(H_{fH_2O(vap)} + \int_{T_O}^{T} C_{pH_2O} dT\right) + x_5\left(H_{fCH_4} + \int_{T_O}^{T} C_{pCH_4} dT\right) + 3.76a\left(H_{fN2} + \int_{T_O}^{T} C_{pN_2} dT\right)$$

(19)

where $H_{fwood}$, $H_{fO2}$, $H_{fN2}$, $H_{fH2}$, $H_{fCO}$, $H_{fCO2}$, $H_{fCH4}$ represent enthalpy of formation of wood, oxygen, nitrogen, hydrogen, carbon monoxide, carbon dioxide and methane in J/mol respectively. $H_{fH2O}$, $Hvap$, $H_{fH2O(vap)}$ stand for the enthalpy of formation of water, enthalpy of vaporization and enthalpy of formation of water vapor in J/mol respectively obtained from [11]. The gasification temperature has obtained by heat balance eq. (19) by Newton Rapson iterative method by coupling the eqs. (9-13).

### Regenerated Air pre-heater:
It has considered as a heat exchanger where air will be heated before entering to the gasifier by the product gas. Exhaust heat will be further utilized by this heat exchanger.
Heat gained by air= Heat loss by gas

$$Ma.Cpa(Ta - To) = \sum (x_i Cp_i) \int_{T}^{T_g} dT$$

(20)

Ma=4.76*a   where, number of moles of air entering to the gasifier per mol of biomass

Where $x_i$ are mole fraction $i^{th}$ of composition of the product gas, $Cp_i$ (in J/mol) has been assumed as a function of temperature and calculated by the polynomial [11]. ($Cp_i = a_i + b_i T + c_i T^2 + d_i T^3$),

Specific heat of air, Cpa is calculated from the relation by Moran and Shapiro [12].

$$Cpa = 8.314(3.653 - T*1.337e-3 + T^2*3.294e-6 - T^3*1.91e-9). \quad (21)$$

Product gas temperature at the outlet of the heat exchanger can be obtained by proper setting the value of Ta.

## 3. MODEL VALIDATION
The present model has been compared with the experimental and predicted gas composition by Jayah et al. [10] considering same biomass composition and operating conditions, which has been shown in figure 3. It has been found that gas compositions predicted in the present model are well matched with the experimental results and predicted by Jayah model and Melgar model.
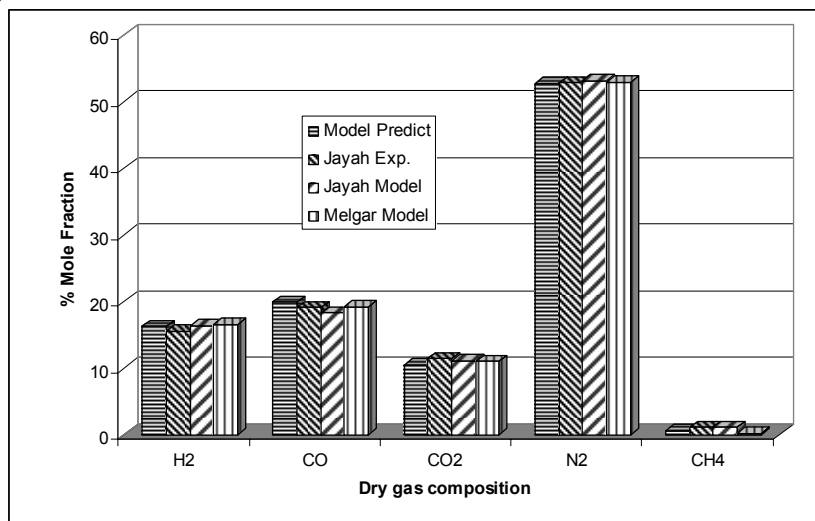


Fig. 3. Model Validation with experimental data and model by Jayah et al. [10] and Melgar Model [8]

## 4. RESULTS AND DISCUSSIONS

After the validation of present model, parametric study such as effect of equivalence ratio and moisture content on the product gas and heating value as well as gasification temperature has been depicted and discussed for both biomasses with without preheating and at different preheating air temperature.

### 4.1 Effect of equivalence ratio

Equivalence ratio is vital operating parameter is gasification. As per the literature, equivalence ratio varies between (2.0 to 3.5) to obtain good quality of product gas. The effects of equivalent ratio in the gasifier have shown on the dry gas compositions as well as heating value of the product gas shown in figure 4 for (a) wood waste and (b) municipal solid waste. For wood waste, $H_2$ composition has increased by 40% where as CO composition increases 4.5% with the increase of eq. ratio froo 2.2 to 3.2. Similar trends of results are obtained by experimentally Melgar et al. [8]. $N_2$ gas composition decreases with increase of $H_2$, CO, $CH_4$ composition in the product gas. Heating value of the product gas increases with the increase in equivalence ratio. Similar patterns have been found for the municipal solid waste up to the equivalence ratio 2.5 and after that gasification temperature falls below such that it is unable to perform the thermo-chemical conversion of biomasses.



(a)                                                         (b)
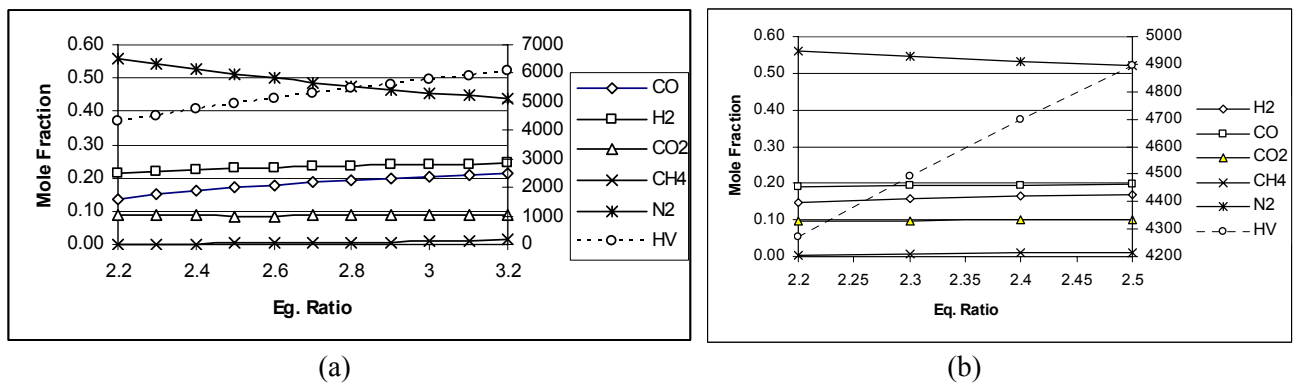
Fig. 4. Effect of equivalence ratio on gas composition at moisture content 14.7% by mass for (a) wood waste and (b) municipal solid waste.

### 4.2 Effect of moisture content

Figure 5. (a,b ) show the effect of moisture content on dry gas composition and heating value of the gas. For both biomasses, $H_2$ gas composition has increased by nearly 30% and at the same time CO composition decreased by nearly 25% with the increase in moisture content from 0 to 40%. $H_2$ composition increases due to the water shift reaction to form H2 from $H_2$0. $CO_2$ gas composition has also been increased by 20%. Where as $N_2$ gas composition is remain unchanged as inert gas. The heating value of the product gas decreases with the increase in moisture content.



(a)                                                         (b)
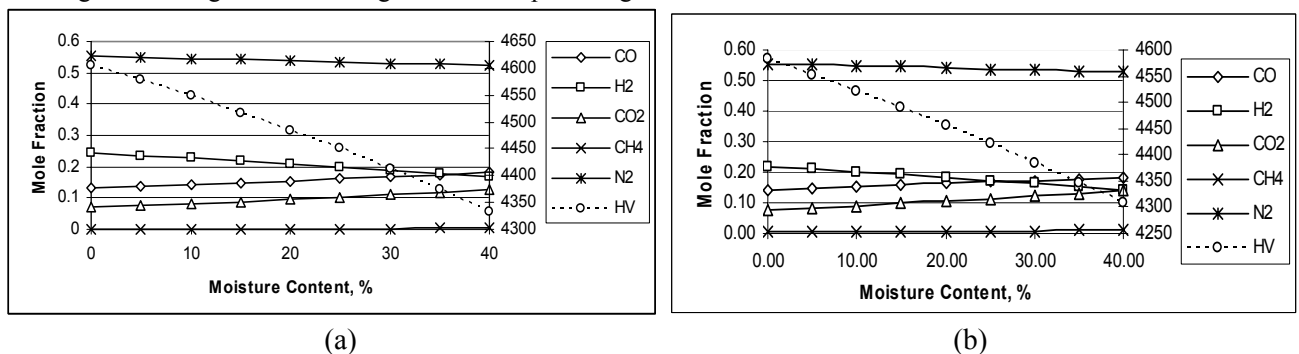
Fig. 5. Effect of moisture content in % mass on gas composition at equivalence ratio 2.2 for (a) wood waste and (b) municipal solid waste.

### 4.3 Effect of regenerative heating

In the figure 6(a), effect of equivalence ratio on gasification temperatures and corresponding calorific values been shown for wood waste. It has been found that gasification temperature decreases with the increase of equivalence ratio and which increases the calorific value of the product gas. But with the increase of air temperature by preheating, increases the gasification temperature but not improving the heating value of gases because of high gasification temperature

reported by **Khadse et al. (2006)** [6]. It has been found that with the regenerative preheating gasification temperature increases from 1180K to 1400K when equivalence ratio changes from 2.2 to 3.2, but there is not much improvement on calorific value of the product gas which was mentioned by **Khadse et al. (2006) [6]**. In case of municipal solid waste, effect of preheating of air on the gasification temperature as well calorific values have been shown in the figure 6. (b). It has been found that maximum attainable calorific value of product gas is nearly 4980 kJ/m$^3$ without doing any regenerative preheating. Calorific value of the product gas can be improved with the adequate regenerative air heating this is because that a certain amount of heat can be extracted from product gas and utilized to enhance the gasification temperature.   It has been found that heating value of the product gas can be raised up to nearly 5900 kJ/m$^3$ with the preheated air temperature 998K.



<div style="text-align:center">(a)</div> <div style="text-align:center">(b)</div>
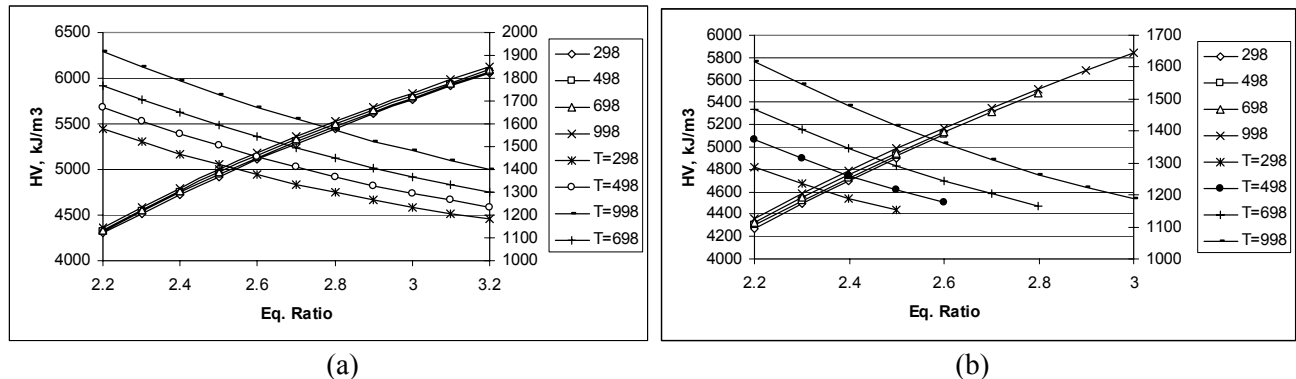
Fig. 6. Effect of equivalence ratio on gasification temperature and heating value at moisture content 14.7% by mass for (a) wood waste and (b) municipal solid waste.

## 5. CONCLUSIONS

A thermodynamic model of down-draft gasifier has been developed based on the chemical equilibrium and the thermodynamic equilibrium with regenerative air preheating effect. The effects of variation of specific heat with temperature and ash content have been considered during the analysis. Predicted results have been well validated with the available experimental results in available literature. Effects of moisture content and equivalence ratio have been depicted with the abundantly available biomass wastes such as wood waste (WW) and municipal solid waste (MSW).  It has been found that regenerated preheating effect is not that much important for wood waste but it is significantly affected on the performance of gasifier handling municipal solid waste. It shows that gasification temperature falls sufficiently in case of municipal solid waste. But gasification temperature can be raised by regenerative air-preheating by the product gas subsequently improves product gas composition and calorific value in case of municipal solid waste. The present study may be utilized in the design of gasifiers for gasifying of high ash and low heating value biomasses and in that case preheating of air will improve the gasification performance.

## References

[1]   McKendry, P., Energy production from biomass (part 1): overview of biomass, *Bioresource Technology* 83 (2002) 37–46.
[2]   McKendry, P., Energy production from biomass (part 3): gasification technologies, *Bioresource Technology* 83 (2002) 55–63.
[3]   Dasappa, S., Paul, P. J., Mukunda, H. S., Rajan, N. K. S., Sridhar, G., Sridhar, H. V., Biomass gasification technology – a route to meet energy needs, *Current Science*, 87(7), 908-916, 2004.
[4]    Ruggiero, M. and Manfrida, G., An equilibrium model for Biomass Gasification process, *Renewable Energy* 16 (1999) 11&1109
[5]   Zainal ZA, Ali R, Lean CH, Seetharamu KN. Prediction of performance of a downdraft gasifier using equilibrium modeling for different biomass materials. *Energy Conversion and Management* 2001;42:1499–515.
[6]   Khadse Anil, Parulekar Prasad, Aghalayam Preeti and Ganesh Anuradda, Equilibrium model for biomass gasification, *Advances in Energy Research* (AER – 2006)pp 106-112
[7]   Jarungthammachote S., Dutta A., Thermodynamic equilibrium model and second law analysis, of a downdraft waste gasifier, *Journal of Energy*.2007

[8]  Melgar Andres,  Juan F. Perez , Hannes Laget, Alfonso Horillo, Thermochemical equilibrium modelling of a gasifying process *Energy Conversion and Management* 48 (2007) 59–67

[9]  Sharma, Avdhesh Kr. Equilibrium modeling of global reduction reactions for a downdraft (biomass) gasifier *Energy Conversion and Management*, Volume 49, Issue 4, April 2008, Pages 832-842

[10] Jayah, T.H., Aye, Lu, Fuller, R.J., Stewart, D.F., 2003. Computer simulation of a downdraft wood gasifier for tea drying. Biomass and Bioenergy 25, 459–469. (8)

[11] Turns, S.R., 2000. Introduction to Combustion, second ed. McGraw Hill. (14)

[12] Moran, M. J and Shapiro, H. N, Fundamentals of Engineering Thermodynamics, Second edition, 1993, John Wiley & sons.

[13] Robert, H. P., Don WG., Perry's Chemical Hand Book, Sixth Ed. New York, McGraw Hill, 1984.

# FLOW INSTABILITY WITH CONVECTIVE HEAT TRANSFER THROUGH A CURVED DUCT

Rabindra Nath MONDAL, Molla Ahammad ALI and Anup Kumar DATTA

Mathematics Discipline; Science, Engineering and Technology School,
Khulna University, Khulna-9208, Bangladesh.
E-mail: rnmondal71@yahoo.com

## ABSTRACT

*Flow instability with convective heat transfer through a curved duct with square cross section is studied numerically by using the spectral method, and covering a wide range of the Dean number, $0 \leq Dn \leq 6000$, the Grashof number, $100 \leq Gr \leq 1000$, and the curvature, $0 < \delta \leq 0.5$. The outer wall of the duct is heated while the inner one is cooled. First, steady solutions and their linear stability is investigated. Then, for the unsteady solutions, we perform time evolution calculations and it is found that typical transition occurs from steady flow to chaos through various flow instabilities, if $Dn$ is increased, no matter what $\delta$ is. Nusselt numbers are calculated as an index of horizontal heat transfer and it is found that convective heat transfer is significantly enhanced by the secondary flow. If the flow becomes periodic and then chaotic, as $Dn$ increases, the rate of heat transfer increases remarkably compared to that of a straight channel.*

**KEY WORDS:** *Curved duct, Secondary flow, Curvature, Dean number, Chaos*

## 1. INTRODUCTION

The study of flows and heat transfer in curved ducts and channels is of fundamental interest because of their ample applications in fluids engineering, such as in fluid transportation, air conditioning systems, refrigeration, heat exchangers and gas turbines, not to mention applications in other areas, such as blood flow in veins and arteries. A number of studies has been performed concerning curved duct flows, here the review articles by Berger et al. [1] and Ito [2] may be referred.

One of the interesting phenomena of the flow through a curved duct is the bifurcation of the flow because generally there exist many steady solutions due to channel curvature. Winters [5] and Yanase et al. [6] performed numerical investigations of flows through a curved rectangular duct. Very recently, Mondal et al. [3] performed a comprehensive numerical study of the flow through a curved duct with square cross section, and found a close relationship between the unsteady solutions and the bifurcation diagram of steady solutions. A remarkable characteristic of the flow through a curved duct is the enhancement of thermal exchange between two sidewalls. Recently, Mondal et al. [4] performed numerical prediction of non-isothermal flows through a curved square duct for small Grashof number ($Gr = 100$). From the scientific as well as engineering point of view, it is, however, quite interesting to study curved duct flows by varying curvature for large Grashof numbers, because this type of flow is often encountered in engineering applications.

In the present paper, a numerical study is presented for the curved square duct flows for large Grashof numbers. Studying the effects of curvature on the flow instability is an important objective of the present study.

## 2. BASIC EQUATIONS

Consider a hydrodynamically and thermally fully developed 2-D flow of viscous incompressible fluid through a curved square duct. The coordinate system with the relevant notations are shown in Fig. 1. It is assumed that the outer wall of the duct is heated while the inner one is cooled. The temperature of the outer wall is $T_0 + \Delta T$ and that of the inner wall is $T_0 - \Delta T$ where $\Delta T > 0$, $\delta$ being the curvature of the duct. Velocity components in the $x$, $y$ and $z$ directions are $u$, $v$ and $w$, respectively. All the variables are non-dimensionalized. The sectional stream function $\psi$ is introduced as

$$u = \frac{1}{1 + \delta x}\frac{\partial \psi}{\partial y}, \quad v = -\frac{1}{1 + \delta x}\frac{\partial \psi}{\partial x}. \tag{1}$$
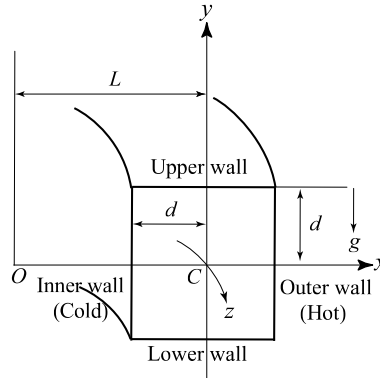


**Fig. 1 Coordinate system**

The basic equations for $w$, $\psi$ and $T$ are derived from the Navier-Stokes equations and the energy equation under the *Boussinesq approximation* as,

$$(1 + \delta x)\frac{\partial w}{\partial t} + \frac{\partial(w, \psi)}{\partial(x, y)} - Dn + \frac{\delta^2 w}{1 + \delta x} =$$
$$(1 + \delta x)\Delta_2 w - \frac{\delta}{(1 + \delta x)}\frac{\partial \psi}{\partial y}w + \delta\frac{\partial w}{\partial x}, \tag{2}$$

$$\left(\Delta_2 - \frac{\delta}{1 + \delta x}\frac{\partial}{\partial x}\right)\frac{\partial \psi}{\partial t} = -\frac{1}{(1 + \delta x)}\frac{\partial(\Delta_2 \psi, \psi)}{\partial(x, y)}$$
$$+\frac{\delta}{(1 + \delta x)^2}\left[\frac{\partial \psi}{\partial y}\left(2\Delta_2 \psi - \frac{3\delta}{1 + \delta x}\frac{\partial \psi}{\partial x} + \frac{\partial^2 \psi}{\partial x^2}\right) - \frac{\partial \psi}{\partial x}\frac{\partial^2 \psi}{\partial x \partial y}\right]$$
$$+\frac{\delta}{(1 + \delta x)^2}\left[3\delta\frac{\partial^2 \psi}{\partial x^2} - \frac{3\delta^2}{1 + \delta x}\frac{\partial \psi}{\partial x}\right] - \frac{2\delta}{1 + \delta x}\frac{\partial}{\partial x}\Delta_2 \psi + w\frac{\partial w}{\partial y}$$
$$+\Delta_2^2 \psi - Gr(1 + \delta x)\frac{\partial T}{\partial x}, \tag{3}$$

$$\frac{\partial T}{\partial t} + \frac{1}{(1 + \delta x)}\frac{\partial(T, \psi)}{\partial(x, y)} = \frac{1}{Pr}\left(\Delta_2 T + \frac{\delta}{1 + \delta x}\frac{\partial T}{\partial x}\right) \tag{4}$$

where

$$\Delta_2 \equiv \frac{\partial^2}{\partial x^2} + \frac{\partial^2}{\partial y^2}, \quad \frac{\partial(f, g)}{\partial(x, y)} \equiv \frac{\partial f}{\partial x}\frac{\partial g}{\partial y} - \frac{\partial f}{\partial y}\frac{\partial g}{\partial x}. \tag{5}$$

The Dean number, $Dn$, the Grashof number, $Gr$, and the Prandtl number, $Pr$, which appear in Eqs. (2) to (4) are defined as $Dn = \frac{Gd^3}{\mu\nu}\sqrt{\frac{2d}{L}}$, $Gr = \frac{\gamma g \Delta T d^3}{\nu^2}$ and $Pr = \frac{\nu}{\kappa}$, respectively. The rigid boundary conditions for $w$ and $\psi$ are used as

$$\left.\begin{array}{l} w(\pm 1, y) = w(x, \pm 1) = \psi(\pm 1, y) = \psi(x, \pm 1) \\ = \frac{\partial \psi}{\partial x}(\pm 1, y) = \frac{\partial \psi}{\partial y}(x, \pm 1) = 0, \end{array}\right\} \tag{6}$$

and the temperature $T$ is assumed to be constant on the walls as

$$T(1, y) = 1, \quad T(-1, y) = -1, \quad T(x, \pm 1) = x. \tag{7}$$

## 3. NUMERICAL METHOD

In order to solve Eqs. (2) to (4) numerically, the spectral method is used. By this method the expansion functions $\Phi_n(x)$ and $\Psi_n(x)$ are expressed as

$$\Phi_n(x) = (1 - x^2)C_n(x), \quad \Psi_n(x) = (1 - x^2)^2 C_n(x) \tag{8}$$

where $C_n(x) = \cos(n \cos^{-1}(x))$ is the $n$-th order Chebyshev polynomial. $w(x, y, t)$, $\psi(x, y, t)$ and $T(x, y, t)$ are expanded in terms of $\Phi_n(x)$ and $\Psi_n(x)$ as

$$\left.\begin{array}{l} w(x, y, t) = \sum_{m=0}^{M} \sum_{n=0}^{N} w_{mn}(t)\Phi_m(x)\Phi_n(y), \\ \Psi(x, y, t) = \sum_{m=0}^{M} \sum_{n=0}^{N} \psi_{mn}(t)\Psi_m(x)\Psi_n(y), \\ T(x, y, t) = \sum_{m=0}^{M} \sum_{n=0}^{N} T_{mn}(t)\Phi_m(x)\Phi_n(y) + x, \end{array}\right\} \tag{9}$$

where $M$ and $N$ are the truncation numbers in the $x$ and $y$ directions respectively.

## 4. RESISTANCE COEFFICIENT AND THE NUSSELT NUMBER

In this study, the resistance coefficient $\lambda$ is used as the representative quantity of the flow state and is defined as

$$\frac{P_1^* - P_2^*}{\Delta z^*} = \frac{\lambda}{4d}\rho\langle w^*\rangle^2 \tag{10}$$

where quantities with an asterisk denote dimensional ones. Since $(P_1^* - P_2^*)/\Delta z^* = G$, $\lambda$ is related to the mean nondimensional axial velocity $\langle w \rangle$ as

$$\lambda = \frac{4\sqrt{2\delta}Dn}{\langle w\rangle^2}, \tag{11}$$

where $\langle w \rangle = \sqrt{2\delta}d\langle w^*\rangle/\nu$. The Nusselt number, $Nu$, is defined as

$$Nu_c = \frac{1}{2}\int_{-1}^{1}\left[\frac{\partial T}{\partial x}\right]_{x=-1} dy, \quad Nu_h = \frac{1}{2}\int_{-1}^{1}\left[\frac{\partial T}{\partial x}\right]_{x=1} dy \tag{12}$$

for steady solutions. For unsteady solutions, on the other hand, it is defined as

$$Nu_{\tau_c} = \frac{1}{2}\int_{-1}^{1}\left\langle\!\!\left\langle\frac{\partial T}{\partial x}\bigg|_{x=-1}\right\rangle\!\!\right\rangle dy, \quad Nu_{\tau_h} = \frac{1}{2}\int_{-1}^{1}\left\langle\!\!\left\langle\frac{\partial T}{\partial x}\bigg|_{x=1}\right\rangle\!\!\right\rangle dy. \tag{13}$$

## 5. RESULTS AND DISCUSSION
### 5.1 Steady solutions and linear stability analysis

Two branches of asymmetric steady solutions are obtained for the Grashof number $100 \leq Gr \leq 1000$, curvature $0 < \delta \leq 0.5$, and the Dean number $0 \leq Dn \leq 6000$. In the present study, however, a single case $Gr = 500$ at $\delta = 0.1$ is mainly discussed, and the diagrams for the distribution of steady and unsteady solutions are presented in the $Dn - \delta$ plane for $0 \leq Dn \leq 6000$ and $0 < \delta \leq 0.5$, and in the $Dn - Gr$ plane for $0 \leq Dn \leq 6000$ and $100 \leq Gr \leq 1000$.



(a)                                           (b)
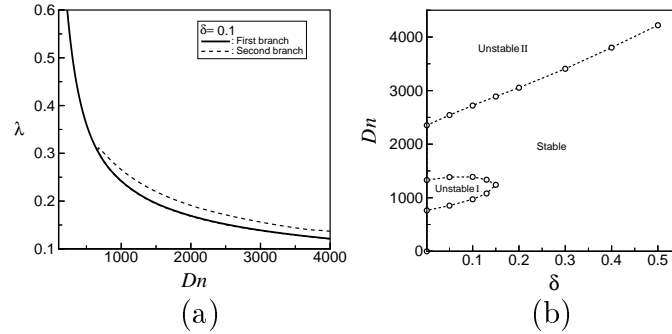
**Fig. 2 (a) Solution structure for Gr = 500 at $\delta$ = 0.1. (b) Stability results for Gr = 500.**

A bifurcation diagram of the two steady solution branches, obtained for $Gr = 500$ at $\delta = 0.1$, is shown in Fig. 2(a). The two steady solution branches are named the *first steady solution branch* (solid line) and the *second steady solution branch* (dashed line), respectively. The first steady solution branch consists of asymmetric two-vortex solutions, while the second branch two- and four-vortex solutions.

Linear stability of the steady solutions shows that only the first branch is linearly stable in two distinct intervals of $Dn$ for small $\delta$; for large $\delta$, on the other hand, the steady solution is stable in a single but wide interval of $Dn$. The stability characteristics are illustrated in Fig. 2(b) for $Gr = 500$. As seen in Fig. 2(b), there exist two unstable regions. One unstable region, say region I, exists for small $Dn$'s which vanishes suddenly as $Dn$ increases. The other unstable region, say region II, on the other hand, exists for large $Dn$'s and is not stabilized any more as $Dn$ or $\delta$ is increased. It is found that the stability region increases with an increase of $\delta$.

### 5.2 Time evolution

In order to study the nonlinear behavior of the unsteady solutions, time evolution calculations are performed covering a wide range of $Dn$ and $Gr$. Time evolutions of $\lambda$ for $Dn \leq 981$ at $\delta = 0.1$ show that the flow is stable while those for $982 \leq Dn \leq 1388$ show that the flow is unstable, and in this unstable region the flow possesses periodic first and then multi-periodic oscillation. Time evolution of $\lambda$ for $Dn = 1200$ is shown in Fig. 3(a), where it is seen that the flow oscillates multi-periodically. Contours of secondary flow and temperature profile are shown in Fig. 3(b), and it is found that the flow oscillates between asymmetric two- and four-vortex solution.

Time evolutions of $\lambda$ for $1389 \leq Dn \leq 2721$ at $\delta = 0.1$ show that the flow becomes stable again, but those for $Dn \geq 2722$ show that the flow is periodic first, then multi-periodic and then chaotic, if $Dn$ is increased. Figure 4(a) shows time evolution of $\lambda$ for
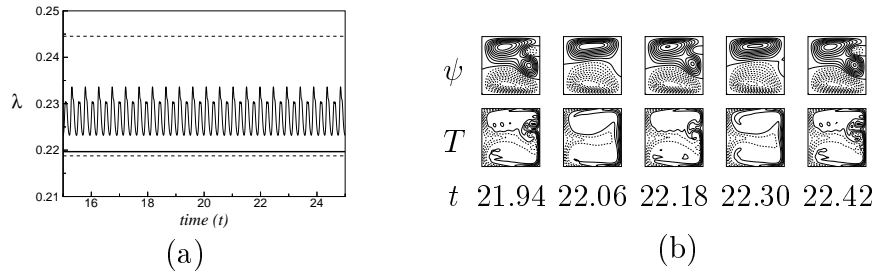
Fig. 3 (a) Time evolution of $\lambda$ for Dn = 1200 and Gr = 500 at $\delta$ = 0.1, (b) contours of secondary flow (top) and temperature profile (bottom) for one period of oscillation.
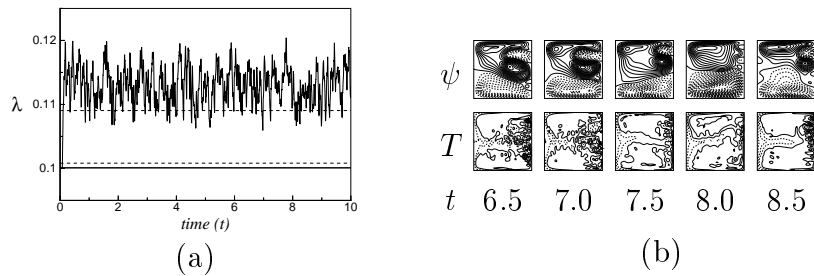


Fig. 4 (a) Time evolution of $\lambda$ for Dn = 6000 and Gr = 500 at $\delta$ = 0.1, (b) contours of secondary flow (top) and temperature profile (bottom).

$Dn = 6000$, which shows that the flow is chaotic. Typical contours of secondary flow and temperature profile for $Dn = 6000$ are shown in Fig. 4(b), where it is seen that the chaotic solution at $Dn = 6000$ is an asymmetric two- and multi-vortex solution.
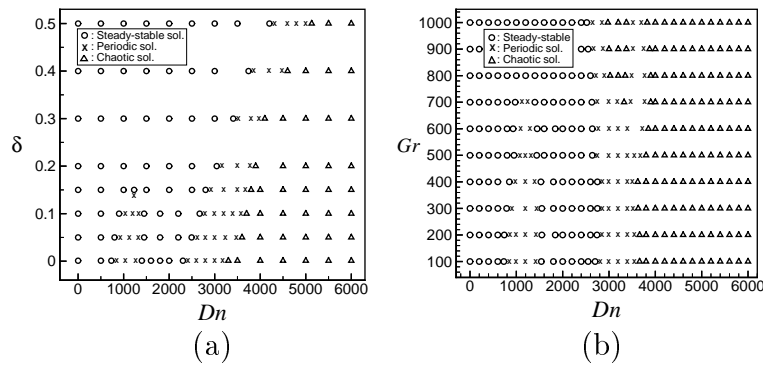


Fig. 5 (a) Unsteady solutions for Gr = 500, (b) Unsteady solutions for $\delta = 0.1$.

## 5.3 Phase diagram

Here, the distribution of steady, periodic and chaotic solutions, obtained by the time evolution calculations, are presented in Fig. 5(a) in the $Dn - \delta$ plane for $Gr = 500$, and in Fig. 5(b) in the $Dn - Gr$ plane. In this picture, the circles denote stable steady solutions, the crosses periodic solutions and the triangles chaotic solutions. As seen in Fig. 5(a), steady flows turn into chaos through periodic (or multi-periodic) flows if $Dn$ is increased no matter what $\delta$ is. If $\delta$ is increased ($\delta \geq 0.15$), the region of the stable steady solution increases and consequently the occurence of the periodic state and hence the chaotic state is delayed. As seen in Fig. 5(b), stable steady flows turn into chaotic flows through various flow instabilities depending on $Gr$, if $Dn$ is increased.

596
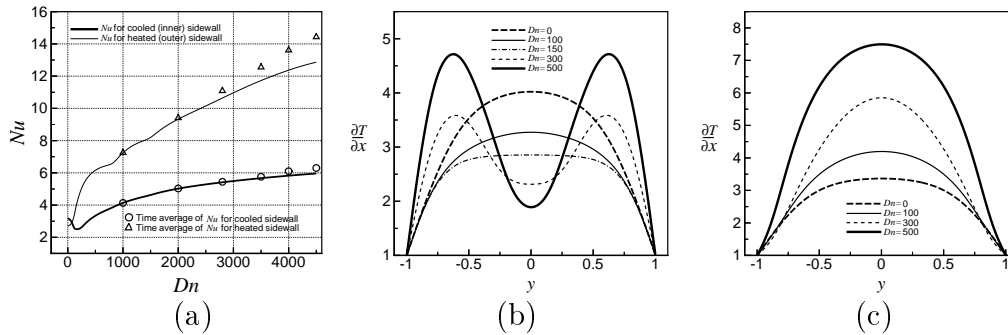
Fig. 6 (a) Variation of **Nu** with **Dn** for Gr = 500 at **δ** = 0.1, (b) Temperature gradient at the cooled sidewall, (c) Temperature gradient at the heated sidewall.

## 5.4 Nusselt number

In order to study the convective heat transfer for differentially heated vertical sidewalls, variation $Nu$ with $Dn$ is shown in Fig. 6(a), where a thick solid line denotes $Nu_c$ on the cooled sidewall and a thin solid line $Nu_h$ on the heated sidewall. Temperature gradients on both the sidewalls are also calculated and shown in Figs. 6(b) and 6(c), respectively. Time-average of $Nu$, obtained by the time evolution computation of $Nu$, is calculated at several values of $Dn$ for both the periodic and chaotic solutions and plotted with the steady values of $Nu$ in Fig. 6(a). As seen in Fig. 6(a), the time-averaged values of $Nu$ are larger than the steady values of $Nu$, which suggests that the occurence of the periodic or chaotic flow enhances heat transfer more significantly in the flow. To compare the convective heat transfer in a curved duct with that in a straight channel, an additional calculation of $Nu$ for a straight channel is conducted and it is found that convective heat transfer is significantly enhanced by the curved duct than that in a straight channel.

# References

[1] Berger, S. A., Talbot, L. and Yao, L. S. Flow in curved pipes, *Annu. Rev. Fluid. Mech.*, 35(1983), pp. 461–512.

[2] Ito, H. Flow in curved pipes, *JSME Int. J.*, 30(1987), pp. 543-552.

[3] Mondal, R. N., Kaga, Y., Hyakutake, T. and Yanase, S. Bifurcation diagram for two-dimensional steady flow and unsteady solutions in a curved square duct, *Fluid Dyn. Res.*, 39(2007), pp. 413–446.

[4] Mondal, R. N., Kaga, Y., Hyakutake, T. and Yanase, S. Effects of curvature and convective heat transfer in curved square duct flows, *Trans. ASME, Journal of Fluids engineering*, 128(9), 2006, pp. 1013–1022.

[5] Winters, K. H. A bifurcation study of laminar flow in a curved tube of rectangular cross-section, *J. Fluid Mech.*, 180(1987), pp. 343–369.

[6] Yanase, S., Mondal, R. N., Kaga, Y. and Yamamoto, K. Transition from steady to chaotic states of isothermal and non-isothermal flows through a curved rectangular duct, *J. Phys. Soc. Japan*, 74(1), 2005, pp. 345–358.

# NUMERICAL STUDY ON OPTIMUM WIRE SCREEN COMBINATIONS FOR USE IN A FAN TEST CHAMBER

K.S. Niaki, F. Farhani, A. Anvari

Iranian Research Organization for Science and Technology (I.R.O.S.T),
P.O. Box 15815 – 3538, Tehran, Iran.
ffarhani@yahoo.com

## ABSTRACT

*A fan test chamber has been designed and constructed by the authors for providing experimental data on energy evaluation of ventilation fans manufactured in Iran. To obtain reliable experimental data, wire screens had to be used to ensure a substantially uniform airflow ahead of the measurement plane. However, the wire screens also introduced pressure drop, which had to be minimized to reduce the power requirement of the auxiliary fan in the test chamber. In this paper we present the results of our numerical simulations to investigate the optimum combinations of wire screens of 40%, 50% and 60% open area ratios to produce the required uniform airflow profile for the minimum pressure drop in the test chamber. The variables considered are the open area ratios of the wire screens, and the screens layout (screens arrangement). The results show that the 50-50-40% combination presents the optimum flow conditions at upstream of the measurement plane, and produces the minimum pressure drop in the chamber. The results of this analytical study were used in the design and construction of the fan test chamber with acceptable results.*

**KEYWORDS:** *Ventilation fans, Ventilation Efficiency Ratio (VER), Airflow measurement, Airflow profile, Settling means, Screens, Open area ratio*

## 1. INTRODUCTION

The residential ventilation fans consume a significant portion of energy in the residential ventilation sector. Hence, performance evaluation of residential ventilation fans is an important consideration in the optimum design and production of fans, having high Ventilation Efficiency Ratios (VER). A standard test chamber will be a very useful facility for this purpose. The test chamber not only provides a platform for performance evaluation of commercially available fans, but also assists the researches in their quest for development of new and more energy efficient fans.

To obtain reliable experimental data, a difficulty is to obtain uniform air velocity profile with minimum pressure drop, ahead of the measurement plane. The reduced pressure drop decreases the power requirement of the auxiliary fan in the test chamber. Figure 1 shows the velocity profile of the air exiting from a centrifugal fan in the test chamber, when no screens are used.

According to ANSI/AMCA210-99/ASREA 51-99 standard [1], the problem may be alleviated by using one or more screens in the flow path such that the maximum flow velocity at a section, at a distance, 0.1 times the hydrodynamic diameter, $D_h$, from the last screen, exceeds the average velocity at that section by only 25%. Positioning of the screens to achieve

this flow velocity and minimum pressure drop must be done by trial and error, and the results validated experimentally. This procedure can be time consuming and expensive. Therefore, during our preliminary design of the fan test chamber, we used numerical simulations to have an estimate of the appropriate positions of the screens in the chamber to produce the required uniform flow and the minimum pressure drop. Although the test chamber dimensions were real, the simulation needed a fine solution grid (about 0.1 mm). Simplifying assumptions such as symmetrical geometry have been used in this study.

In this paper we present the results of our numerical simulations to investigate the optimum combinations of wire screens of 40%, 50% and 60% open area ratios to produce the required uniform airflow profile for the minimum pressure drop in the test chamber. Variables such as the open area ratios of the wire screens, and the screens layout (screens arrangement) were considered. Three arrangements of wire screens namely 50-50-40%, 50-50-50% and 60-60-60% have been considered in this numerical study. The results have been used in the design and construction of the fan test bed [2], being used for compilation of standards for energy consumption and labeling of residential exhaust fans in Iran.

## 2. THE MODELING PROCESS

Figure 1 presents the computational domain, showing the flow geometry in the model under consideration. As shown, the geometrical model is a rectangular chamber, having 0.5 m width (1 m for symmetrical condition), and 1.5 m length. An opening of 0.125 m length (0.25 m for symmetrical condition) has been considered in the middle of the left surface of the chamber model as the air entrance. As the main aim of this study is to analyze the air profile at a small distance from the last screen, the right surface of the chamber has been considered to be the flow exit.
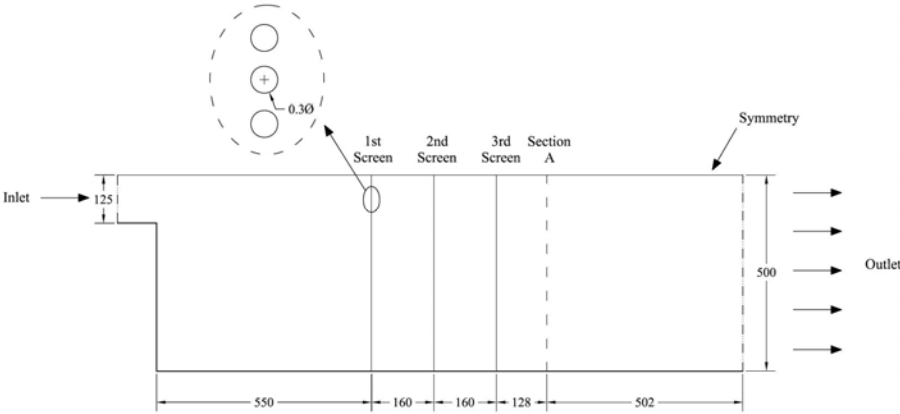


**Fig.1 Computational domain, showing the flow geometry considered in this study**

In order to perform the two dimensional simulation, the screens have been assumed to be a vertical chain of circular openings of 0.3 mm (screens of 0.3 mm openings are the most prevalent) in a direction perpendicular to the flow direction.
The acceptable distance between screens used for obtaining uniform flow in a wind tunnel is $500d$, where $d$ is the diameter of the screen wire [3]. Therefore, in all the simulations in this study, the distance between the screens factor has been considered to be the fixed value of 0.16 m. According to the reference standard [1], the minimum distance between the first screen and the entering flow is determined to be 0.55 m.

The non-uniformity of the entering flow will increase the distribution of the flow through the screens, which will result in more uniform flow through the screens into the test chamber. However, in order to simulate the worst case for the entering flow, the conditions at

the entrance have been considered to be uniform flow of incompressible air, having a velocity of 8 m/s.

The boundary condition for the screens is considered to be insulated walls and no-slip condition. To define the flow output, the "Out Flow" boundary condition in FLUENT software has been used.

As the air flow in the chamber is turbulent, it becomes necessary to select a suitable turbulence model from FLUENT for analyzing this flow. In these simulations, the turbulence model selected is a widely used model for numerical simulations, namely; the $k - \varepsilon$ two-equation model. The model has three classifications, and we have used the standard model for this analysis.

In order to cope up with the resulting big numerical grid with many cells, the solver used for the flow equations is *segregated* type. The SIMPLE algorithm has been used to couple pressure and velocity in the solver. The *Second-Order Upwind* algorithm has been used for discretization of the momentum and turbulence equations. The triangular unstructured grid has been selected for discretization of the solution field.

## 3. RESULTS

Figure 2 presents the velocity profile of the air exiting from a centrifugal fan in the test chamber, when no screens are used.
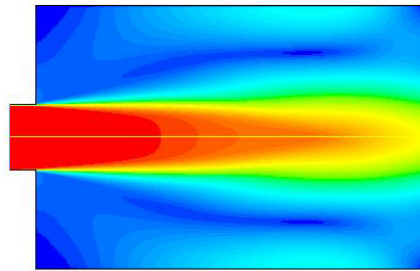


**Fig.2 Velocity profile of the air exiting from a centrifugal fan in the test chamber (no screens)**

As the first step for understanding the effect of insertion of a single screen on the flow conditions, a screen having a 60% open area ratio has been considered. The result of the analysis for a single screen is shown in fig. 3. As seen, a single screen does not affect the flow profile significantly.
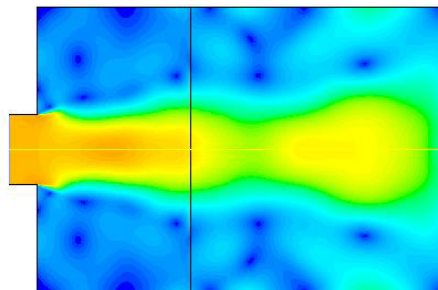


**Fig.3 The velocity contours due to the insertion of a single screen of 60% open area ratio**

In the next step, 3 screens, separated by a distance of 0.16 m, were inserted and the flow profile was studied. As shown in fig. 4, insertion of 3 screens has had greater effect on the flow profile, compared to a single screen. However, further analysis of the velocity values, at a section located $0.1D_h$ (0.128 m for this study) from the last screen [1] (designated as

section A from now on), shows that the maximum velocity is about 75% of the corresponding average velocity at this section (2 m/s) (see fig. 5).

The same procedure was used to simulate other screen combinations such as 40-60-60% and 50-50-50-50%. In the case of 40-60-60% screen combination, the maximum velocity was reduced to about 45% of the corresponding average velocity at section A. For 50-50-50-50% screen combination, the maximum velocity was reduced to about 25% of the corresponding average velocity at section A.
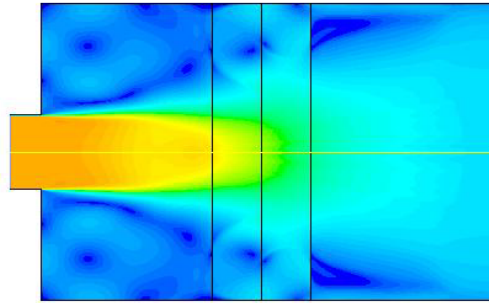


**Fig.4 The velocity contours due to the insertion of 3 screens of 60% open area ratios**
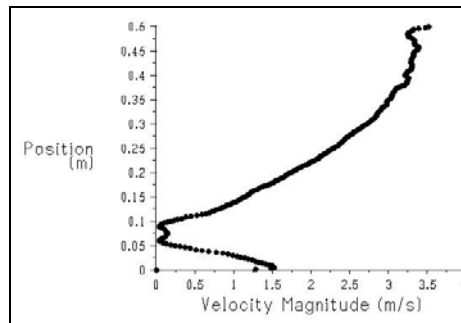


**Fig.5 The air velocity curve at section A: the screens arrangement and open area ratios are 60-60-60%**

The next choice was to consider the 40-50-50% screen combination. The results for this screen combination, presented in figs. 6 and 7, show that the maximum velocity has been reduced to about 13% of the corresponding average velocity at section A. However, for this combination of screens, a study of the static pressure contours indicates that due to the impact of the fan exit air on the first screen, which has the least open area ratio, a considerable pressure drop has occurred (see fig. 8). Therefore, to reduce the pressure drop in the test bed, the order in which the screens are arranged has been reversed, the new screen arrangement being 50-50-40%. Figures 9 through 11 show the results for this new arrangement of screens, representing the results when the screens are inserted, from the entrance to exit, in the order of 50-50-40% open area ratios. As expected, reversing of the order has resulted in decreased pressure drop in comparison with the previous arrangement.
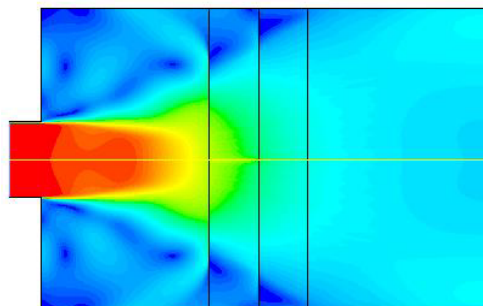


**Fig.6 The velocity contours due to the insertion of 3 screens of 40-50-50% open area ratios**
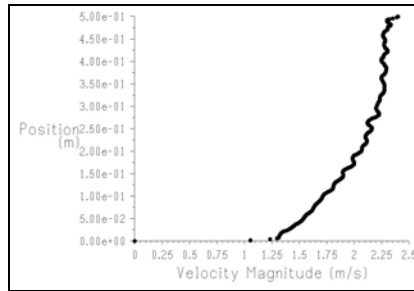
**Fig.7 The air velocity curve at section A for screens arrangement and open area ratios of 40-50-50%**
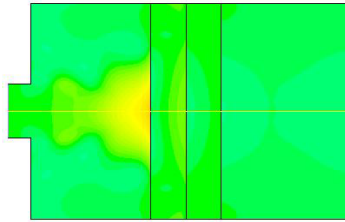


**Fig.8 The static pressure contours due to the insertion of 3 screens of 40-50-50% open area ratios**
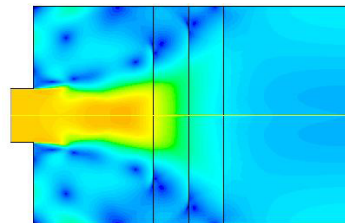


**Fig.9 The static pressure contours due to the insertion of 3 screens of 50-50-40% open area ratios**
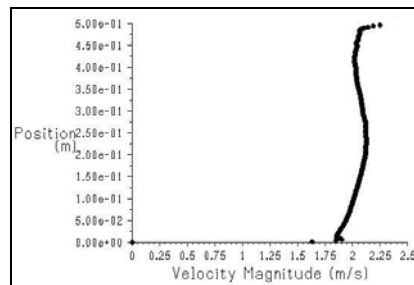


**Fig.10 The air velocity curve at section A for screens arrangement and open area ratios of 50-50-40%**
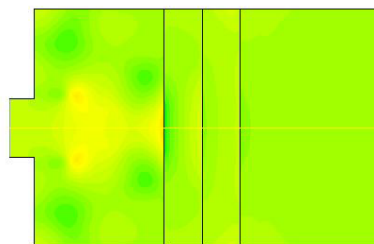


**Fig. 11: The static pressure contours due to the insertion of 3 screens of 40-50-50% open area ratios**

## 4. CONCLUSIONS

Parameters such as the number of screens, distance between the screens, the screens open area ratio, and the positional order of the screens with respect to one another have been identified as important factors, affecting the flow profile after the flow settling means.

Comparison of results shows that reversing of the screens arrangement from 40-50-50% to 50-50-40% results in reduced pressure drop in the chamber, and a more uniform velocity profile, compared to other screens combinations studied in this work. However, for this screens arrangement, the maximum velocity at a section located 0.128 m from the last screen (section A) is still about 13% of the corresponding average velocity at this section, which shows the importance of selection of right arrangement of screens, to obtain uniform airflow in a fan test chamber. Although the results show that the settling means with 50-50-40% open area ratios combination, presents acceptable flow conditions at the upstream of the measuring plane in the fan test chamber, the results are not unique, and other optimum conditions may be obtained by varying the above mentioned parameters.

Results of this study have been used in the design and construction of a bed for testing of fans [4]. Figures 12 and 13 show the constructed test bed, presently in use at Mechanical Engineering Department (IROST). Evaluation of experimental data obtained from the constructed chamber, using a pitot-tube traverse at section A, shows good agreement with the numerical results for the screens with 50-50-40% open area ratios arrangement.



**Fig.12 Photograph of the fan test chamber [4]**



**Fig.13 Photograph showing another view of the fan test chamber [4]**

## 5. ACKNOWLEDGEMENT

## 6. REFERENCES

[1]  ANSI/AMCA210-99/ANSI/ASHRAE 51-1999, "Laboratory Methods of Testing Fans for Aerodynamic Performance Rating", (1999).

[2]  Niaki, K.S., et al., "Design and Construction of a Test Bed for Performance Evaluation of Fans", Proceedings of the International Conference on Mechanical Engineering (ICME2007), Dhaka, Bangladesh, (Dec. 2007).

[3]  Barlow, E.B., W.H., Rae and Pope, A.J., "Low-Speed Wind Tunnel Design Testing", McGraw Hill, (1998).

[4]  Niaki, K.S., et al., "Compilation of Energy Consumption Standard, and Energy Labeling of Fans up to 3500 m³/hr (2100 cfm)", Final Project Report (In Persian), Tehran, Iran, (2007).

# NUMERICAL SIMULATION OF GAS FLOW IN POLYMER ELECTROLYTE FUEL CELL AND DEFORMATION EFFECT OF POROUS MEDIA

Litan Kumar Saha, Eru Kurihara, Nobuyuki Oshima

Laboratory of Space Physical Fluid Dynamics, Division of Mechanical and Space Engineering, Graduate School of Engineering, Hokkaido University, Kita-13, Nishi-8, Kita-Ku, Sapporo, 060-8628, JAPAN
E-mail: saha@mech-me.eng.hokudai.ac.jp

## ABSTRACT

*Gas flow in the separator channel and the deformation effect of gas diffusion layer (GDL) of a polymer electrolyte fuel cell (PEFC) has been investigated by using a transient, non-isothermal and three-dimensional numerical model. In order to seal the PEFC against any gas leakages a suitable compression force is applied between the gas diffusion layer and bipolar plate which results the deformation of GDL. In this present investigation, non-uniform deformations of GDL are taken into consideration and chosen as in the experimental data. Numerical simulations are performed for a wide range of porosity and permeability values and the effects of these parameters on the pressure distribution are measured. The results obtained by numerical simulation are also compared with the experimental as well as theoretical solution. It is revealed that the increase of porosity and permeability parameter caused the decrease of pressure drop (difference of pressure from inlet and outlet) but the decreasing rate is not uniform. It is also found that there is an effective range of porosity and permeability values for which these parameters have a very strong effect on the pressure drop. The results obtained by numerical simulation are also compared with the experimental as well as theoretical solution.*

**Key words:** *Gas diffusion layer, Pressure drop, Deformation thickness, separator channel, Numerical simulation.*

## 1. INTRODUCTION

Polymer electrolyte fuel cell (PEFC) is considered as the prime candidature among the fuel cell under development because of its high power density, low operating temperature, low emissions and environmentally friendly nature. This recognizes PEFC as a suitable and alternative power source for the next generation vehicular application and portable power plants. Performance improvement of PEFC is necessary for large scale market penetration. The operating parameters such as pressure, temperature and flow distribution in the flow channel and GDL has a great influence on the performance of polymer electrolyte fuel cell. The effects of different operating parameters on the performance of proton exchange membrane (PEM) fuel cell have been studied experimentally by Wang et. al. [1]. Hydrogen is used as a fuel in the anode side where as oxygen is used as fuel in the cathode side and produces water and heat as a by-product. Since both the reactants and the byproduct passes through the channel and GDL this are considered as an important parts of PEFC.

Barbir et al. [2] investigated the relationship between pressure drop and cell resistance as a diagnostic tool for PEM fuel cells. They observed that an increase in pressure drop is a reliable indicator of polymer electrolyte fuel cell flooding. Also by monitoring both pressure drop and cell resistance they were able to diagnose either flooding or drying.

The gas diffusion layer in a polymer electrolyte fuel cell consists of a thin layer of carbon black mixed with polytetrafluoroethylene (PTFE) [3] that is coated onto a sheet of macro-porous carbon backing cloth. GDL permits the gaseous reactants to move towards the catalyst layer. Flow of electron between catalyst layers and bipolar plates also have been maintained by the GDL. The diffusion layer also plays a critical role in water management within the cell. The effect of diffusion layer parameter on the performance of PEFC [4, 5] has been considered a great research interest till now. Characteristic of the diffusion layer thickness and porosity of the proton exchange membrane fuel cell has been studied by Lee et. al. [6].

In order to seal the fuel cell against any gas leakages and reduce the interfacial contact resistance the gas diffusion layers and bipolar plates are usually clamped together under a suitable pressure. The influence of clamping force on the performance of polymer electrolyte fuel cell with interdigitated gas distribution has been investigated by Zhou [7, 8]. They found that the clamping force affects the permeability and diffusion of the reactant gas transport of the liquid water due to GDL deformation and the porosity variation. Chang et. al. [9] investigated experimentally that the external clamping pressure not only change the thickness but also the porosity and permeability of the GDL. Roshandel et. al. [10] examined the variation of porosity distribution considering both the effect of compression of the electrodes on the solid landing area and the water generated at the cathode side of GDL. Nitta et. al. [11] investigated experimentally the effect of inhomogeneous compression of GDL caused by the channel/rib structure of flow field plate. They observed that GDL under the channel remained almost at the initial thickness regardless of the width of the channel. On the other hand GDL under the bipolar plate is compressed to gasket thickness.

The objective of the present work is to study the influence of GDL properties on the pressure drop in the channel. The pressure drop between the inlet and outlet channel and the velocity distribution of the channel and GDL will be treated as a diagnostic tool to monitor the performance of PEFC. Also we will analyze the effect of GDL deformation on the physical property of the diffusion layer qualitatively.

## 2. PHYSICAL AND MATHEMATICAL MODEL

We want to concentrate our attention to observe the physical properties of the GDL which can be obtained by observing the flow behavior inside the channel and GDL. For symmetry considerations separator of same width is distributed on both sides of the channel. GDL of same size is taken under the channel and separator region. Deformation of GDL is considered in our present investigation and is taken form the experimental results of the GDL deformation conducted by Saito [12]. Figure 1 shows the numerical grid used for the system. For simplification, the following assumptions will be considered: (1) ideal gas mixture; (2) incompressible and laminar flow due to small Reynolds number; (3) the GDL is considered to be isotropic porous media. Here we investigate the gas flow only.

The flow field in the separator channel and GDL can be obtained by solving the conservation equations of mass and momentum. A single set of governing equations valid for the sub regions (1) gas channel and (2) porous GDL is used. Therefore interfacial conditions of the internal boundaries between gas channel and GDL need not to be specified. Considering the assumptions the governing equations can be written as:

Mass conservation:

$$\frac{\partial(\varepsilon\rho)}{\partial t}+\nabla\cdot(\varepsilon\rho\mathbf{u})=0 \tag{1}$$

Momentum conservation:

$$\frac{\partial\varepsilon\rho\mathbf{u}}{\partial t}+\nabla\cdot(\varepsilon\rho\mathbf{u}\mathbf{u})=-\nabla(\varepsilon p)+\nabla\cdot(\varepsilon\mu\nabla\mathbf{u})+\varepsilon\rho g-\frac{\mu}{K}\varepsilon^{2}\mathbf{u} \tag{2}$$

where $u$ is the velocity vector, $\mu$ the viscosity, $\rho$ the density, $\varepsilon$ the porosity of the GDL and K is the permeability of the GDL. Porosity, $\varepsilon$ is defined by the ratio of the volume occupied by the pore to the total volume of the porous media where as permeability, K is defined by the square of the effective volume to surface area ratio of the porous matrix as in Mazumder and Cole [13]. The last term of equation (2) represents the Darcy's drag force in the porous media. In the gas channel, $\varepsilon \to 1$ and $K \to \infty$, so equation (2) becomes the original Navier-Stokes equation.

A constant velocity is given to the inlet boundary of the channel. All wall boundary conditions are considered as no slip. Constant pressure condition is used at the outlet of the flow channel.
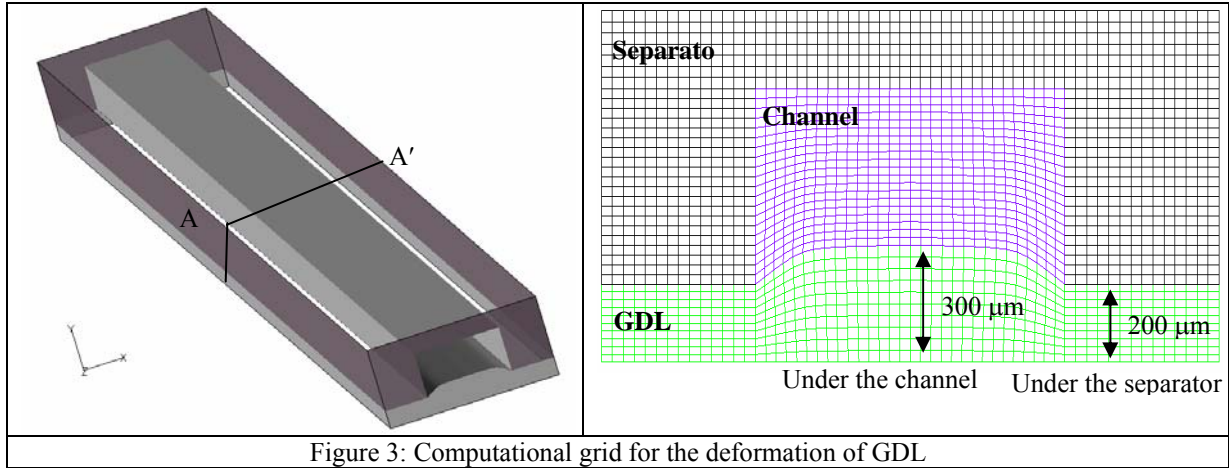


Figure 3: Computational grid for the deformation of GDL

## 3. NUMERICAL PROCEDURE

The conservation equation of mass and momentum, together with the boundary condition are discretized by finite volume method and solved by the software ForntFlow/PEFC which is a general purpose numerical simulator. Euler implicit scheme has been used for time integration. The first order upwind scheme has been applied to discretize the convection terms in the governing equations. The SIMPLE algorithm is used to update the pressure and velocity fields from the solutions of pressure correction equation.

## 4. RESULTS AND DISCUSSION

Pressure drop is a result of frictional loss and bending loss in the gas flow channel. In the anode side, loss coefficient can be approximated only by the friction loss coefficient. The pressure drop between inlet and outlet of a rectangular channel can be calculated by using the following formula [14]:

$$Q = \frac{4ab^3(p_1 - p_2)}{3\mu l}\left[1 - \frac{192b}{\pi^5 a} \sum_{n=1,3,..}^{\infty} \frac{1}{n^5} \tanh\left(\frac{n\pi a}{2b}\right)\right] \tag{3}$$

where Q is the flow rate, $\mu$ the viscosity, $(p_1 - p_2)$ the pressure drop, l the length of the channel and 2a, 2b is the sides of the rectangular channel.

Here $Q = 3.54 \times 10^{-6}$ m$^3$/s, $\mu = 1.98 \times 10^{-5}$, $a = 0.25 \times 10^{-3}$ m and $b = 0.5 \times 10^{-3}$ m is used both for the theoretical and numerical solution. Using the formula (3) pressure drop in the anode channel becomes: $\Delta p = p_1 - p_2 = 712$ Pa.

The pressure drop of anode channel, obtained by the numerical simulation is shown in the Fig. 2. Pressure drop is calculated by subtracting the channel outlet pressure from the channel inlet pressure. It is found that pressure drop obtained by the numerical simulation is 711 Pa.

Now the pressure drop obtained by the numerical simulation has been compared with the theoretical solution and we found an excellent agreement between these two results which also shows the validation of our code.
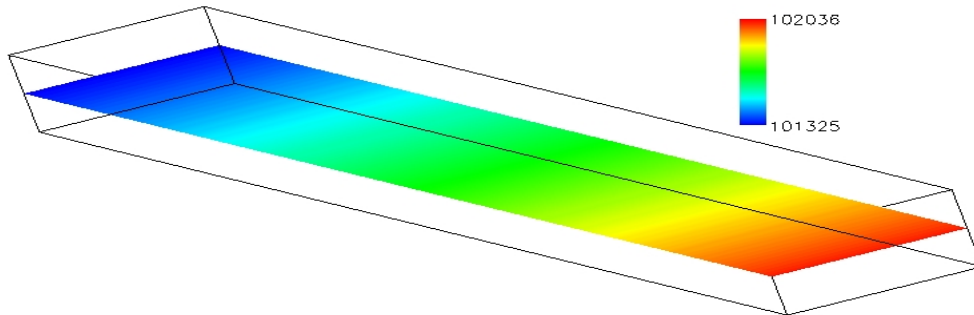


Figure 2: Pressure distribution along the channel

The physical conditions and the operational parameters used for the numerical simulation are listed in Table 1.

**Table 1: Physical properties and operational parameters**

| | | |
|---|---|---|
| Porosity, $\varepsilon$ | | 0.1 to 0.9 |
| Permeability, K (m$^2$) | | $10^{-15}$ to $10^{-1}$ |
| Density, $\rho$ (kg/m$^3$) | Nitrogen | 1.251 |
| Viscosity, $\mu$ (kg/m s) | Nitrogen | $1.98 \times 10^{-5}$ |
| Operational temperature, T (K) | | 333 |
| Operational pressure, P (pa) | | 202650 |
| Inlet gas velocity (m/s) (without deformation) | | 4.72 |
| Inlet gas velocity (m/s) (with deformation) | | 5.62 |
| Gas composition | | $N_2$:72% |
| Channel length, $l$ (m) | | 0.11 |
| Channel width, $b$ (m) | | 0.001 |
| Channel height, $a$ (m) | | 0.0005 |
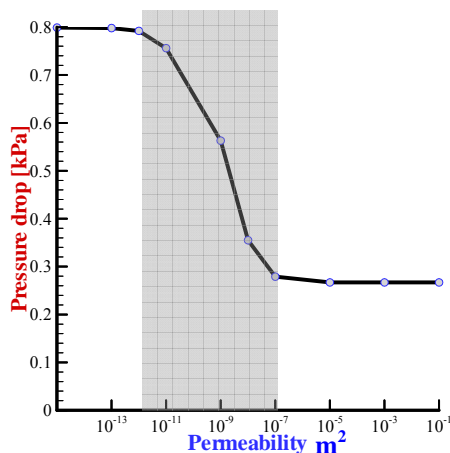


Fig. 3: pressure drop for a wide range of permeability values
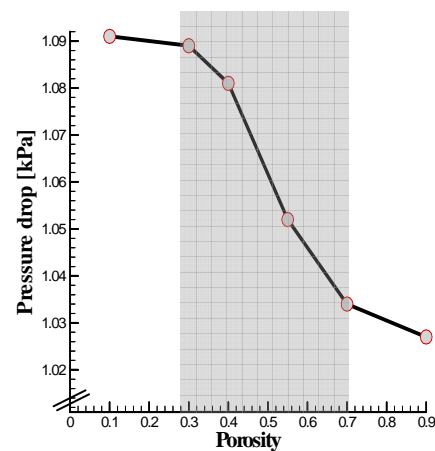
Fig. 4: Pressure drop for different values of porosity

The pressure drop for various values of permeability parameter is shown in Fig. 3. Here

the values of porosity parameter are chosen to be 0.4. We see that permeability parameter has a very strong effect on the pressure drop. The values of the pressure drop decreases with the increasing values of permeability. Now from Fig. 6 representative effect found for a range of permeability values between $10^{-8}$ and $10^{-12}$ m$^2$. GDL behaves like an impermeable wall for the values of permeability smaller than $10^{-13}$ m$^2$. The values pressure drop remains same for the permeability values grater than $10^{-7}$ m$^2$.
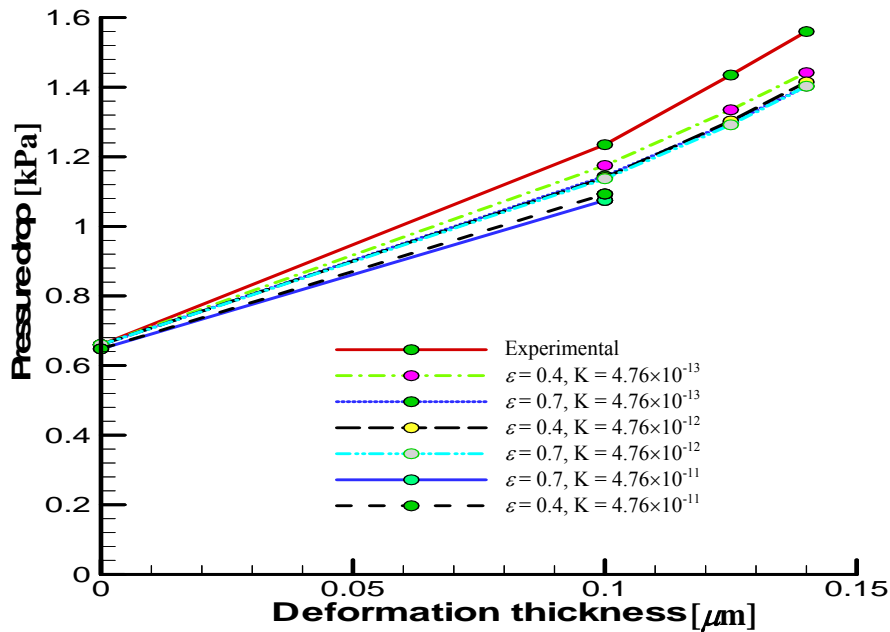


Figure 5: Compare the numerical result and experimental result for different physical parameters

The pressure drop in the GDL for different values of porosity parameter is shown in Fig. 4. We see that pressure drop decreasing with the increasing values of porosity. We also observe from Fig. 4 that even though the effect is not strong, there is a range of porosity parameter for which pressure drop is mostly affected. The range of the porosity parameter which has comparatively large effect approximately lies between 0.3 and 0.7.

Now the results obtained by the numerical simulation are compared with the experimental result. From the experimental result we do not have the information about porosity and permeability parameter. For this reason taking other parameter same we observed several cases and find the values of porosity and permeability for which we get the same pressure drop as in the experimental result by Saito [12]. We see that for the values of porosity =0.4 and permeability =4.76×$10^{-12}$ m$^2$ has the same pressure drop as in the experimental result without considering deformation of GDL. First we considered that the values of porosity and permeability of the GDL with deformation case is same as in the without deformation case. To observe the effect of physical parameters of the GDL we consider change of porosity without change of permeability, change of permeability without change of porosity and change of both the porosity and permeability. By observing the tendency of the fig. 5 we can say clamping force not only deformed the structure of the GDL but also change its physical property such as porosity and permeability.

## 6. CONCLUSIONS

The flow behavior in the gas channel and porous GDL of a proton exchange membrane fuel cells has been investigated by a transient, isothermal three-dimensional numerical

simulation. It has been observed that permeability parameter has a strong effect on the pressure drop. Also it is shown that the major effect occurs for the permeability values between $10^{-8}$ to $10^{-12}$ m$^2$. Though the effect porosity on the pressure drop is not so strong but the porosity values between 0.3 and 0.7 have major influence. Deformation of GDL has a very strong effect on the pressure drop and it changes the physical parameter of the porous GDL.

## 7. REFERENCES

[1] Wang, L., Husar, A., Zhou, T. and Liu, H., 2003, "A Parametric Study of PEM Fuel Cell Performances", International Journal of Hydrogen Energy, 28, pp.1263 – 1272.

[2] Barbir F., Gorgun H., Wang X., 2005, "Relationship between Pressure Drop and Cell Resistance as a Diagnostic Tool for PEM Fuel Cells", Journal of Power Sources, 141, pp. 96–101.

[3] Passalacqua1 E., Squadrito G., Lufrano F., Patti A. and Giorgi L, 2001, "Effects of the Diffusion Layer Characteristics on the Performance of Polymer Electrolyte Fuel Cell Electrodes", Journal of Applied Electrochemistry, 31, pp. 449-454.

[4] Jordan, L. R., Shukla, A. K., Behrsing, T., Avery, N. R., Muddle, B. C. and Forsyth, M., 2000, "Diffusion Layer Parameters Influencing Optimal Fuel Cell Performance", Journal of Power Sources, 86, pp. 250-254.

[5] Passalacqua, E., squadrito, G., lufrano, F., patti, A. and giorgi, L., 2001, "Effects of the Diffusion Layer Characteristics on the Performance of Polymer Electrolyte Fuel Cell Electrodes", Journal of Applied Electrochemistry, 31, pp. 449-454.

[6] Lee, H-K., Park, J-H., Kim, D-Y. and Lee, T-H., 2004, "A Study on the Characteristics of the Diffusion Layer Thickness and Porosity of the PEMFC", Journal of Power Sources, 131, pp. 200-206.

[7] Zhou, P., Wu, C.W. and Ma, G.J., 2006, "Contact Resistance Prediction and Structure Optimization of Bipolar Plates", Journal of Power Sources, 159(2), pp. 1115-1122.

[8] Zhou, P., Wu, C.W. and Ma, G.J., 2007, "Influence of Clamping Force on the Performance of PEMFCs", Journal of Power Sources, 163(2), pp. 874-881.

[9] Chang, W.R., Hwang, J.J., Weng, F.B. and Chan, S.H., 2007, "Effect of Clamping Pressure on the Performance of a PEM Fuel Cell", Journal of Power Sources, 166(1), pp. 149-154.

[10] Roshandel, R., Farhanieh, B. and Saievar-Iranizad, E., 2005, "The Effects of Porosity Distribution Variation on PEM Fuel Cell Performance", Renewable Energy, 30(10), pp. 1557-1572.

[11] Nitta, I., Hottinen, T., Himanen, O. and Mikkola, M., 2007, "Inhomogeneous compression of PEMFC gas diffusion layer: Part I. Experimental", Journal of Power Sources, 171(1), pp. 26-36.

[12] Saito, M., 2008, "Experimental Data Acquisition for Numerical Simulation of PEM Fuel Cell, and Analysis of Flooding Phenomenon by Electrochemical Measurement", Under graduate thesis, Laboratory of Energy Conversion System, Hokkaido University, Japan.

[13] Mazumder, S. and Vernon, C. J., 2003, "Rigorous 3-D Mathematical Modeling of PEM Fuel Cells", Journal of the Electrochemical Society, 150, pp.A1503-1509.

[14] Irvine Jr. T. F. and Hartnett J.P., 1978, Advances in heat transfer, supplement 1, 196, academic press.

# LES OF PHYSIOLOGICAL PULSATILE FLOW IN A MODEL ARTERIAL STENOSIS

## Md. Mamun Molla and <u>Manosh C. Paul</u>

Department of Mechanical Engineering, University of Glasgow, Glasgow G12 8QQ, UK
e-mail: <u>m.paul@mech.gla.ac.uk</u>

## ABSTRACT

*Physiological pulsatile flow in a 3D model of arterial stenosis is investigated by applying Large Eddy Simulation (LES) technique. The computational domain has been chosen is a simple channel with a biological type stenosis formed eccentrically on the top wall. The physiological pulsation is generated at the inlet of the model using the fourth harmonic of the Fourier series of the physiological pressure pulse. The flow Reynolds numbers which are typical of those found in human large artery are chosen in the present work. Transitions to turbulent of the pulsatile flow in the post stenosis are examined through the various numerical results and explained physically along with the relevant medical concerns.*

**KEYWORDS:** *Arterial stenosis, LES, Physiological flow, Turbulent flow*

## 1 INTRODUCTION

The term arterial stenosis refers the narrowing of an artery where the cross-sectional area of blood vessel reduces. The most common cause is the atherosclerosis where cholesterol and other lipids are deposited beneath the intima (inner lining) of the arterial wall. As the amount of this fatty material increases there is an accompanying proliferation of connective tissue and the whole forms a thickened area in the vessel wall called plaque. The vessel wall remodels to accommodate this varying degrees but with marked plaque deposition then this will reduce the effective cross-section of the vessel and retard the blood flow. When the reduction in vessel calibre is severe the result is that blood flow transient to turbulent and there will be a pressure drop across the stenotic region.

The alteration in flow dynamics in turn produces abnormal wall shear stress both at the plaque and at the post stenotic area such that the plaque may fissure and rupture exposing the lipid plaque core to the blood stream with potential for thrombosis (blood clotting) at the site of rupture. This development of atherothrombosis may dangerously acutely occlude the vessels with in critical territories such as the coronary arteries and cerebral vessels catastrophic results. Non-occlusive atherotrhombosis is also clinically important as the thrombotic material deposited is often unstable and a source of distal combolism, this is particularly important in the extracranial carotid arteries as a source of stroke.

The blood flow through arteries is inherently unsteady due to the cyclic nature of heart pump. These disturbed flows may either be laminar or transition to turbulent and the pulsatile character of the flow has a significant effect on the transition to turbulence which represents an abnormal flow nature in the circulation, and the development of transition to turbulence flow in the arteries has a clinical interest as outlined above. From the point of an accurate computational modelling, such flow can be challenging.
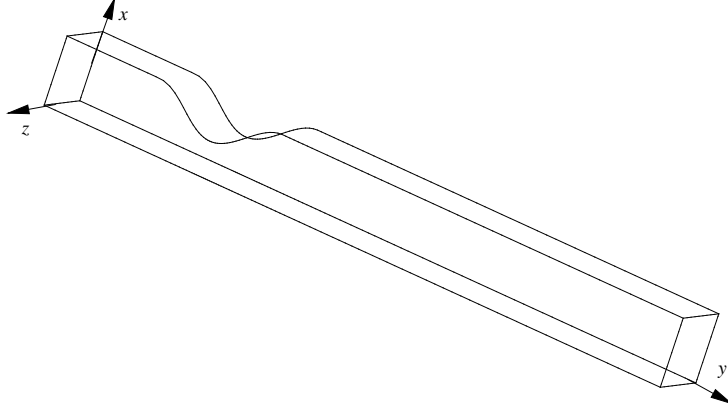
Figure 1: A schematic of the model with coordinate system.

Very recently Paul *et al.* [1] have investigated the non-additive pulsatile turbulent blood flow through a model of arterial stenosis applying the LES technique. Using the first harmonic of the Fourier series of the pressure pulse, a Large-eddy simulation of the physiological pulsatile flow in the same model is performed by Molla *et al.* [2]. In the present paper, the aim is to use more accurate pulsatile inflow and investigate the turbulent flow downstream of the stenosis applying the LES. In this regard, the fourth harmonic of the Fourier series of the physiological pressure pulse (Womersley [3]) is used in the model. The results obtained by LES are compared with those of Direct Numerical Simulation (DNS). The fluid in the model is treated as Newtonian and incompressible according to Pedley [4].

## 2 FORMATION OF THE PROBLEM

### 2.1 Model geometry

The geometry shown in Fig. 1 consists of a 3D channel with one sided cosine shape stenosis on the upper wall centred at $y/L = 0.0$, where $y$ is the horizontal distance or the distance along the flow and $L$ is the height of the channel. In the model the height $(x)$ and its width $(z)$ are kept same, which gives a square cross-section at the upstream and downstream of the stenosis. The length of the stenosis is equal to twice of the channel height. Before the stenosis the channel length is $5L$, and $15L$ is the downstream region of the stenosis.

### 2.2 Governing equations for LES

The equations of motion for Large Eddy Simulation are obtained by applying a spatial filter, namely *grid*-filter, to the Navier-Stokes equations and written in the following filtered forms:

$$\frac{\partial \bar{u}_j}{\partial x_j} = 0, \tag{1}$$

$$\frac{\partial \bar{u}_j}{\partial t} + \frac{\partial \bar{u}_i \bar{u}_j}{\partial x_j} = -\frac{1}{\rho}\frac{\partial \bar{P}}{\partial x_i} + \frac{\partial}{\partial x_j}\left[\nu\left(\frac{\partial \bar{u}_i}{\partial x_j} + \frac{\partial \bar{u}_j}{\partial x_i}\right)\right] - \frac{\partial \tau_{ij}}{\partial x_j}, \tag{2}$$

where $\bar{u}_i$ is the velocity vector along $x_i = (x, y, z)$, $\bar{P}$ is pressure, $t$ is time, $\rho$ is the fluid density, and $\nu$ is the kinematic viscosity of the fluid. The effects of the small scale appear in the subgrid-scale stress (SGS) term as

$$\tau_{ij} = \overline{u_i u_j} - \bar{u}_i \bar{u}_j, \tag{3}$$

which is modelled as (Smagorinsky [5]),

$$\tau_{ij} - \frac{1}{3}\delta_{ij}\tau_{kk} = -2(C_s\triangle)^2|\bar{S}|\bar{S}_{ij}, \tag{4}$$

where $\triangle = \sqrt[3]{\triangle x \triangle y \triangle z}$ is the filter width and $|\bar{S}| = \sqrt{2\bar{S}_{ij}\bar{S}_{ij}}$ is the magnitude of the large scale strain rate tensors defined as $\bar{S}_{ij} = \frac{1}{2}\left(\frac{\partial \bar{u}_i}{\partial x_j} + \frac{\partial \bar{u}_j}{\partial x_i}\right)$. The unknown Smagorinsky constant, $C_s$, is calculated using the localized dynamic model of Piomelli and Liu [6].

## 2.3 Boundary conditions

To generate the physiological pulsatile flow at the inlet of the model artery, one-dimensional form of the Navier-Stokes equation (2) for the streamwise velocity is solved first taking the pressure gradient as a Fourier series in time (Womersley [3], Loudon and Tordesillas [7]),

$$-\rho\frac{\partial \bar{v}}{\partial t} + \mu\frac{\partial^2 \bar{v}}{\partial x^2} = \frac{2}{3}A_0 + A\sum_{n=1}^{N} M_n e^{i(n\omega t + \phi_n)}, \tag{5}$$

where $A_0$ and $A$ are the constants corresponding to the steady and oscillatory pressure gradient respectively; $M_n$ and $\phi_n$ are the respective coefficients and the phase angle of the different harmonics, which are known from Womersley [3]; $N$ is the number of harmonics of the Fourier series; and $\omega = \frac{2\pi}{T}$ is the frequency of the unsteady flow. The solution of Eq. (5) takes the following form:

$$\bar{v}(x,t) = 4\bar{V}\frac{x}{L}\left(1 - \frac{x}{L}\right) + A\sum_{n=1}^{N}\frac{iM_n L^2}{\mu\omega_0^2 n}$$

$$\left[\cosh(\omega_0\sqrt{in}\frac{x}{L}) - \frac{\cosh(\omega_0\sqrt{in}) - 1}{\sinh(\omega_0\sqrt{in})}\sinh(\omega_0\sqrt{in}\frac{x}{L}) - 1\right]e^{i(n\omega t + \phi_n)}. \tag{6}$$

The real part of this solution is used as the inlet condition to generate the physiological velocity profiles. We have used $N = 4$ (fourth harmonic) in the simulation. In Eq. (6), the bulk velocity $\bar{V}$ relates to the flow Reynolds number defined as $Re = \frac{\bar{V}L}{\nu}$, and $\omega_0 = L\sqrt{\frac{\rho\omega}{\mu}}$ is the Womersley number. In Fig. 2, the inlet velocity profile is presented for one pulsation for $Re = 2000$ and $\omega_0 = 10.5$, note that the velocity in frame (a) is recorded at very close to the bottom wall. The choice of the Womersley number of 10.5 in the simulation indicates that the unsteady part of the velocity dominates the flow, see Ku [8]. In addition, the maximum streamwise velocity at the inlet is controlled by taking the value of the amplitude of oscillation as $A = 0.4$.

No slip boundary conditions are used for both the lower and upper walls of the model, and at the outlet a convective boundary condition is used. For the spanwise boundaries, periodic boundary conditions are applied for modelling the spanwise homogeneous flow.

## 2.4 Overview of the numerical procedures

The governing filtered equations (1-2) in Cartesian coordinates are transformed into curvilinear coordinates system and the finite volume approaches are used to discretise the partial differential equations to yield a system of linear algebraic equations. To discretise the spatial derivatives in eqns. (1-2), the standard second order accurate central difference scheme is used, except for the convective terms in the momentum equations (2) for which an energy conserving discretisation scheme is used.
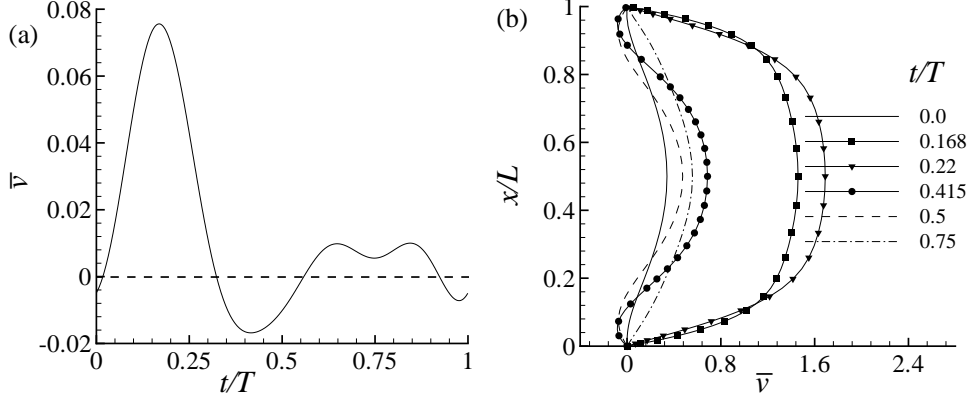
Figure 2: Streamwise velocity at the inlet for $Re = 2000$ and $\omega_0 = 10.5$.

Time derivatives are discretised by a three point backward difference scheme with a constant timestep of $\delta t = 10^{-3}$. A pressure correction algorithm is applied to couple pressure with the velocity components where the results are stored at the centre of a control volume according to the collocated grid arrangement. The Poisson like pressure correction equation is discretised by using the pressure smoothing approach of Rhie and Chow [9], which prevents the even-odd node uncoupling in the pressure and velocity fields.

A BI-CGSTAB [10] solver is used for solving the matrix of velocity vectors, while for the Poisson like pressure correction equation a ICCG [11] solver is applied due to its symmetric and positive definite nature. Overall the code is second order accurate in both time and space and fully implicit, which is in-house developed and has been applied extensively in other engineering flows.

The methods of data processing for the random turbulent fluctuations and the spanwise average quantities are summarised in Molla and Paul [12].

## 3   RESULTS AND DISCUSSION

In the present study the Reynolds numbers ranging from 1000 to 2000 are chosen for simulation, and the area reduction of the channel due to the stenosis is fixed at 50%. The numerical grid employed in the LES consists of a total of $5 \times 10^5$ control volumes with $50 \times 200 \times 50$ grid nodes in the $x$ and $y$ and $z$ directions respectively. A finer grid of $70 \times 350 \times 50$ has been employed in the DNS for $Re = 2000$ and the results are compared with those of LES. The statistics for mean quantities have been gathered after finishing the ten cycles of the pulsation, where the mean flow eventually becomes stationary.

The streamwise mean streamlines based on the mean velocity components, $< \bar{u} >$ and $< \bar{v} >$, are depicted in Fig. 3 while $Re = 2000$. It is seen that a re-circulating region is created after the stenosis near the upper wall owing to the experience of the adverse pressure gradient in this region. The blood flow in this recirculation region stays for a long time, and this prolonging staying time is known to be an important factor for causing the heart attack or brain stroke to a patient suffering from a disease related to arterial stenosis. Figure 4 shows the contours of the spanwise-averaged vorticity, $\omega_z = \frac{\partial \bar{u}}{\partial y} - \frac{\partial \bar{v}}{\partial x}$, for $Re = 2000$ when the pulsation attains its peak position. It can be seen in this figure that the two shear layers, one of which separating from the nose of the stenosis generates an anticlockwise (dashed lines) vortex close to the lip region, while the other one separating from the bottom wall induces a clockwise (solid lines) vortex in the post-stenosis. These pair vortices then interact and create highly oscillating flow at the downstream of the
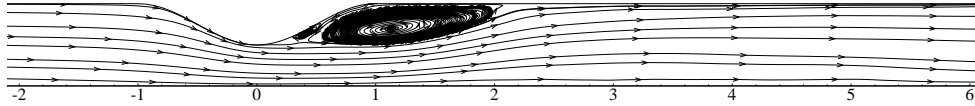
Figure 3: Mean streamlines while $Re = 2000$.
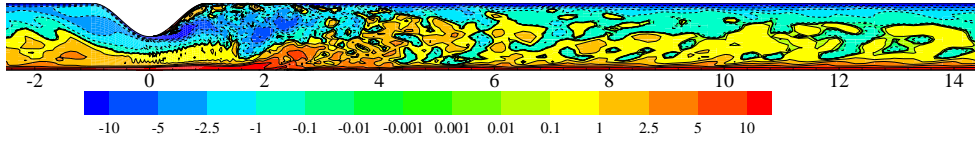


Figure 4: Spanwise-averaged vorticity while $Re = 2000$.

stenosis. The instantaneous shear stress distributions, $\tau_{xy} = \mu \left( \frac{\partial \bar{u}}{\partial y} + \frac{\partial \bar{v}}{\partial x} \right)$, at the upper wall is shown in Figure 5 for the different Reynolds numbers. Just prior to the centre of the stenosis, an acute stress drop happens due to the flow separation. This low shear stress usually stimulates the growth of tissue proliferation at the throat of the stenosis, and as a result the reduction of the arterial area increases, which might be a severe condition for a patient. The oscillatory stresses in the post-stenosis are also a concerned matter in the point of pathological view as these could smash up the material of the blood cells as well as the inner lining of an artery.

Figure 6 shows the mean pressure, $< \bar{p} >$, at the upper wall. It is very much clear in this figure that the maximum pressure drop occurs at the centre of the stenosis, which is located at the region $0 \leq y/L \leq 2.0$ and this is the region where the flow re-circulating region was found (see Fig. 3). Finally, Fig. 7 illustrates the normalised turbulent kinetic energy (TKE) for the different Reynolds numbers. Before the stenosis the TKE is very small, which is expected, as the pulsatile flow is laminar; but after the centre of stenosis in the post-stenosis region, $0 < y/L < 5$, the high levels of TKE usually play a significant role in the formation of thrombosis by inducing platelet aggregation in blood.

## 4 CONCLUSION

Large Eddy Simulation with a localized dynamic sub-grid model has been applied to study the physiological pulsatile flow through a 3D model of arterial stenosis. In the model, the stenosis was placed eccentrically at the upper wall of the channel, which reduces the cross-sectional area of the channel of 50%. The different Reynolds numbers, 1000, 1400, 1700 and 2000, based on the bulk velocity, were chosen for this study – the
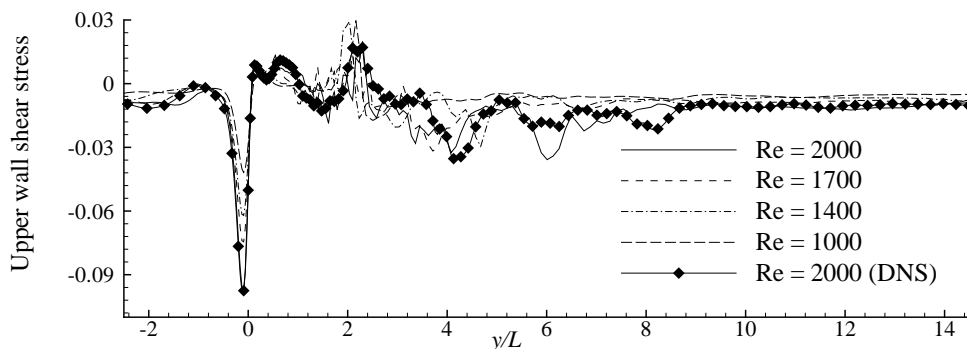


Figure 5: Instantaneous shear stress at the upper wall for the different Reynolds numbers.
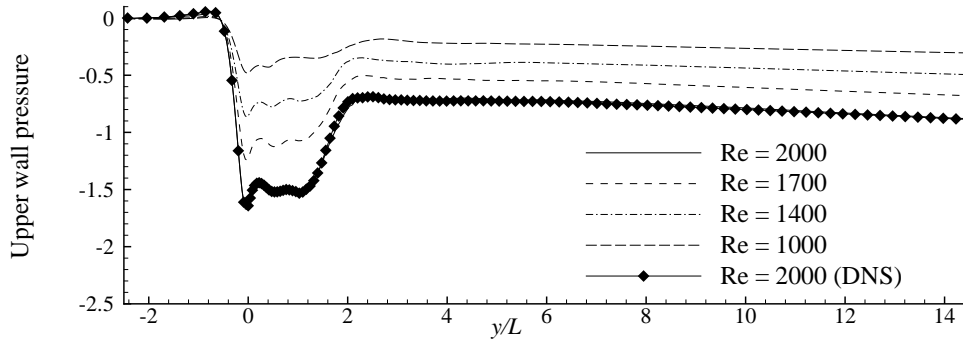
Figure 6: Mean pressure at the upper wall for the different Reynolds numbers.
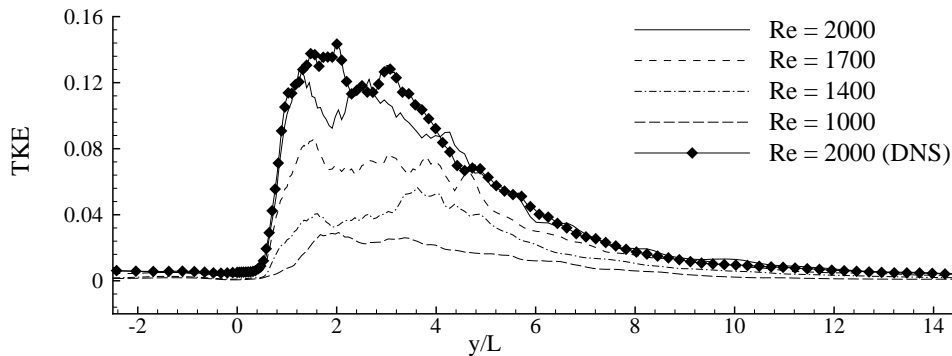


Figure 7: Turbulent kinetic energy for the different Reynolds numbers.

choice of these Reynolds numbers is realistic for human arteries, see Ku [8]. The results obtained by the LES have also been compared with those of the DNS for $Re = 2000$ and the agreement we found is quite satisfactory.

The turbulent kinetic energy is found high in the downstream of the stenosis because of the highly oscillating nature of the transient flow and the shear stresses in that region. As reported, the level of this turbulence has an impact in causing damage to the materials of blood cells and activate the blood platelets and, consequently, these could create many pathological diseases. Although a simple model is considered here, we believe that the results presented in the paper would give a better insight and in-depth knowledge to understand the important fluid dynamics roles of atherosclerosis. Future extension of this work is to consider a more biological realistic domain, e.g. circular domain, and investigate the turbulent flow coupling the fluid with structure.

**REFERENCES**

[1] M. C. Paul, M. M. Molla, G. Roditi, Large-eddy simulation of pulsatile blood flow, Med. Eng. Phys. (in press) doi:10.1016/j.medengphy.2008.04.014.

[2] M. M. Molla, M. C. Paul, G. Roditi, Physiological flow in a model of arterial stenosis, J. Biomech. 41(S1) (2008) S243.

[3] J. R. Womersley, Method for the calculation of velocity, rate of flow and viscous drag in arteris when the pressure gradient is known, J. Physiol. 155 (1955) 553–563.

[4] T. J. Pedley, The fluid mechanics of large blood vessels, Cambridge University Press, 1980.

[5] J. Smagorinsky, General circulation experiment with the primitive equations. i. the basic experiment, Monthly Weather Rev. 91 (1963) 99–164.

[6] U. Piomelli, J. Liu, Large-eddy simulation of rotating channels flows using a localized dynamic model, Phys. Fluids 7 (4) (1994) 839–847.

[7] C. Loudon, A. Tordesillas, The use of the dimensionless Womersley number to characterize the unsteady nature of internal flow, J. Theo. Biol. 191 (1998) 63–78.

[8] D. N. Ku, Blood flows in arteries, Annu. Rev. Fluid Mech. 29 (1997) 399–434.

[9] C. M. Rhie, W. L. Chow, Numerical study of the turbulent flow past an airfoil with trailing edge separation, AIAA J. 21(11) (1983) 1525–1532.

[10] H. A. D. Vorst, BI-CGSTAB: a first and smoothly converging variant of BI-CG for the solution of the non-symmetric linear systems, SIAM J. Sci. Stat. Comput. 13 (2) (1992) 631–644.

[11] D. S. Kershaw, The Incomplete Cholesky-Cojugate Gradient method for the iterative solution of systems, J. Com. Phys. 26 (1978) 43–65.

[12] M. M. Molla, M. C. Paul, A study of transition to turbulent pulsatile flow in a model arterial stenosis using large eddy simulation, Comp. and Fluids. (2008) submitted.

# COMPOUND WALL TREATMENT FOR RANS COMPUTATION

M. M. Rahman[1], A. K. M. Sadrul Islam[2] and T. Siikonen[1]
[1]Helsinki University of Technology, Department of Applied Mechanics,
Sähkömiehentie 4, FIN-02015 HUT
Finland
[2]Department of Mechanical & Chemical Engineering,
Islamic University of Technology, Board Bazar,
Gazipur 1704, Bangladesh
[1]E-mail: Mizanur.Rahman@tkk.fi

## ABSTRACT

*A generalised treatment for the wall boundary conditions of RANS computation relating to turbulent flows is developed. The blending function ensures a smooth transition between the viscous and turbulent regions. An improved low-Reynolds number $k$–$\epsilon$ model is coupled with the proposed compound wall treatment to determined the turbulence field. Computations with fine and coarse meshes of a few flow cases yield appreciably good agreement with the direct numerical simulation and experimental data. The method is recommended for computing the industrial flows in complex domains.*

**KEYWORDS:** *$k$–$\epsilon$ turbulence model, wall integration, wall function, nonequilibrium flow.*

## 1. INTRODUCTION

The wall effect on a turbulent flow is inherently difficult to model, since the flow includes strong inhomogeneity and anisotropy in the viscous sublayer adjacent to the wall. Two different methods, referred to as the wall integration (WI) and the wall function (WF), are commonly employed in evaluating the near-wall behavior of complex flows. The WI method requires a low-Reynolds number (LRN) turbulence model in which near-wall modifications are introduced to account for wall-vicinity and viscous effects. The LRN model necessitates that the near-wall flow region must be sufficiently resolved (i.e., the first near-wall grid node is located roughly at $y^+O(1)$ where $y^+ = u_\tau y/\nu$, $u_\tau$ is the friction velocity and $y$ implies the normal distance from a wall) to capture the steep gradients usually found there. The ultimate result is enhanced predictions for the near-wall sensitive parameters such as the skin friction and heat transfer coefficients. However, the computational effort is substantially higher than that of using the alternative WF approach.

With the WF strategy, a high-Reynolds number turbulence model is employed, utilizing algebraic functions to bridge the near-wall viscous layer that substantially relax the mesh requirements. In this case, the first near-wall nodal point must lie outside the viscosity affected region, approximately at $y^+ \geq$ 30, which is in practice cumbersome to ensure in all regions of complex flows. Admittedly, the falling of the first grid point in the buffer layer (i.e., $5 \leq y^+ < 30$ in wall attached flows) makes neither WI nor WF applicable in a consistent manner.

Several proposals are available in the literature that aim at improving and generalising the wall treatment. Chieng and Launder [1] attempt to improve the WF by allowing a linear variation in both the shear

stress and the turbulent kinetic energy across the near-wall cell. A more general variant of this approach is developed by Craft et al. [2] who abandon most of the traditional near-equilibrium assumptions and derive the wall functions on the basis of assumed eddy viscosity distributions across the first near-wall cell. In a more sophisticated approach, Craft et al. [3] propose to integrate the parabolised transport equations over an embedded fine grid within the first grid cell. Despite obvious improvements demonstrated in several test cases, the resulting scheme is unfortunately too cumbersome to be implemented due to its apparent complexity. Another approach is to employ a blending between the wall-limiting and fully turbulent expressions for various flow properties in question. The blending functions ensure a smooth transition between the two layers that provides adequate conditions for the first near-wall node even it lies in the buffer region. For instance, Esch and Menter [4] propose a quadratic blending of the wall-limiting (viscous) and the outer (turbulent) values of the shear stress and $\omega$ to provide wall functions (boundary conditions) with the $k$–$\omega$ model. Popovac and Hanjalic [5] develop a compound wall treatment (CWT) that reduces either to the WI or the appropriate WF depending on the location (viscous sublayer/turbulent region) of the first near-wall cell. When the first gride node lies in the buffer zone, the boundary conditions are provided from blending the viscous and fully turbulent limits using exponential blending functions. This blending is based on the generalised expressions for the mean velocity and temperature profiles of Kader [6] that reasonably approximates the whole wall region of a boundary layer, including viscous/conductive and logarithmic layers. In an attempt to improve the CWT, Basara [7] uses a similar blending for the wall shear stress $\tau_w$ and the production $P$ of turbulent kinetic energy $k$, but a different scaling (blending) for the dissipation rate $\epsilon$.

The present study concentrates on the coupling of CWT with an improved LRN $k$–$\epsilon$ model that permits integration up to the wall. The Kader blending [6] is adopted to ensure a smooth transition between the viscous and turbulent boundary conditions. As mentioned by Popovac and Hanjalic [5], this blending makes the model insensitive to the precise positioning of the first grid point and within a reasonable limit, to the quality of the mesh in the near-wall region. The blending formula of Basara [7] adhering to $\epsilon$ is further improved by introducing a new function with the fully turbulent quantity. The model performance is demonstrated through the comparisons with experimental and direct numerical simulation (DNS) data of well-documented flows, consisting of a fully developed flow, a backward facing step flow and an asymmetric plane diffuser flow.

## 2. LRN $k$–$\epsilon$ MODEL

In collaboration with the Reynolds-averaged Navier-Stokes (RANS) equations, the proposed model determines the turbulence kinetic energy $k$ and its dissipation rate $\epsilon$ by the following transport relations:

$$\frac{\partial \rho k}{\partial t} + \frac{\partial \rho u_j k}{\partial x_j} = \frac{\partial}{\partial x_j}\left[\left(\mu + \frac{\mu_T}{\sigma_k}\right)\frac{\partial k}{\partial x_j}\right] + \rho P - \rho \epsilon \tag{1}$$

$$\frac{\partial \rho \epsilon}{\partial t} + \frac{\partial \rho u_j \epsilon}{\partial x_j} = \frac{\partial}{\partial x_j}\left[\left(\mu + \frac{\mu_T}{\sigma_\epsilon}\right)\frac{\partial \epsilon}{\partial x_j}\right] + (C_{\epsilon 1}\,\rho\,P - C_{\epsilon 2}\,\rho\,\epsilon)/T_t \tag{2}$$

where $\mu$ implies the molecular viscosity, $\sigma_{(k,\epsilon)}$ are the appropriate turbulent Prandtl numbers and the production term $P = -\overline{u_i u_j}(\partial u_i/\partial x_j)$. The Reynolds stresses $\rho\overline{u_i u_j}$ are related to the mean strain-rate tensor $S_{ij}$ through the Boussinesq approximation:

$$-\rho\overline{u_i u_j} = 2\,\mu_T\left(S_{ij} - \frac{1}{3}\,S_{kk}\,\delta_{ij}\right) - \frac{2}{3}\,\rho\,k\,\delta_{ij}, \qquad S_{ij} = \frac{1}{2}\left(\frac{\partial u_i}{\partial x_j} + \frac{\partial u_j}{\partial x_i}\right) \tag{3}$$

Since the viscous dissipation presumably dominates near the wall, the turbulent viscosity is evaluated from

$$\mu_T = f_\mu C_\mu \rho\,k\,T_t \tag{4}$$
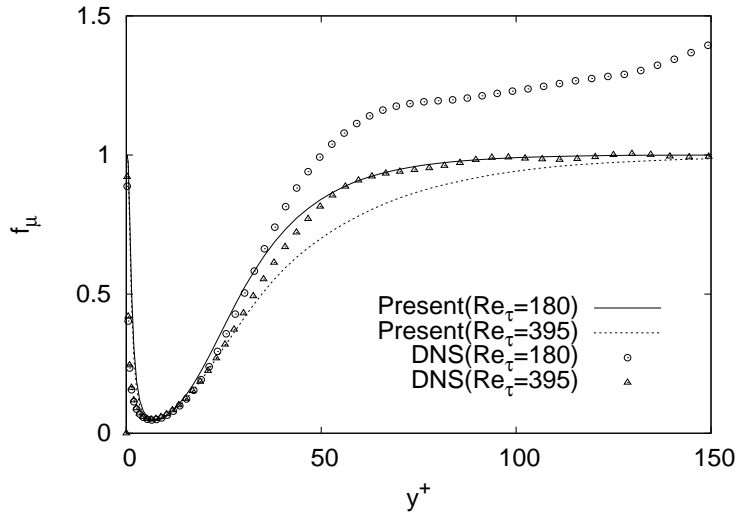
Figure 1: **Variations of eddy viscosity damping function with wall distance in channel flows.**

where $C_\mu = 0.09$. The dynamic time scale $k/\epsilon$ is replaced by a realizable time scale $T_t$ and can simply be defined as

$$T_t = \sqrt{\frac{k^2}{\epsilon^2} + C_T^2 \frac{\nu}{\epsilon}} = \frac{k}{\epsilon} \sqrt{1 + \frac{C_T^2}{Re_T}}, \qquad Re_T = \frac{k^2}{\nu \epsilon} \tag{5}$$

where $\nu = \mu/\rho$ denotes the kinematic viscosity and $Re_T$ is the turbulence Reynolds number. Equation (5) warrants that the eddy time scale never falls below the Kolmogorov time scale $C_T\sqrt{\nu/\epsilon}$, dominant in the immediate neighborhood of the solid wall. It prevents the singularity in the dissipation equation down to the wall. Alternatively, the turbulence time scale is $k/\epsilon$ at large $Re_T$ but approaches the Kolmogorov limit $C_T\sqrt{\nu/\epsilon}$ for $Re_T \ll 1$. The empirical constant $C_T = \sqrt{2}$ associated with the Kolmogorov time scale is estimated from the behavior of $k$ in the viscous sublayer [8]. Obviously, the inclusion of $T_t$ in the $\epsilon$ equation guarantees the near-wall asymptotic consistency without resorting to *ad hoc* damping functions employed in many $k$–$\epsilon$ models [9].

The eddy viscosity damping function included in Equation (4) is chosen pragmatically as

$$f_\mu = \tanh\left(\frac{Re_y^{1.5}}{3\,Re_T}\right)^2, \qquad Re_y = \frac{\sqrt{k}y}{\nu} \tag{6}$$

where $Re_y$ is another Reynolds number associated with the turbulence modeling. A plot of $f_\mu$ against the DNS data [10] for fully developed turbulent channel flows is shown in Fig. 1 and a good correlation is obtained. The empirical function $f_\mu$ is valid in the whole flow field, including the viscous sublayer and the logarithmic layer. As evinced by Fig. 1 in comparison with the DNS data, the adopted form of $f_\mu$ reproduces the asymptotic limit involving the distinct effects of LRN and wall proximity. The proposed $f_\mu = 1$ remote from the wall to ensure that the model is compatible with the standard $k$-$\epsilon$ turbulence model. The use of ($Re_y$ & $Re_T$) confronts the singularity at neither the separating nor the reattaching point in contrast to the adoption of $y^+$. Consequently, the model is applicable to separated and reattaching flows.

Near-wall flows show a tendency to underestimate the dissipation rate $\epsilon$ due to the local anisotropy of turbulence, adhering to the non-dimensional parameter $P/\epsilon$ [11]. Researchers allow the coefficient $C_{\epsilon 1}$ to be a function of $P/\epsilon$ with a view to enhancing dissipation in such a situation [12, 13]. However, in some of the more complex flows that have been calculated, the dependence on $P/\epsilon$ prevents numerical convergence to a steady state [14]. One possible approach to counteracting this adverse situation is to
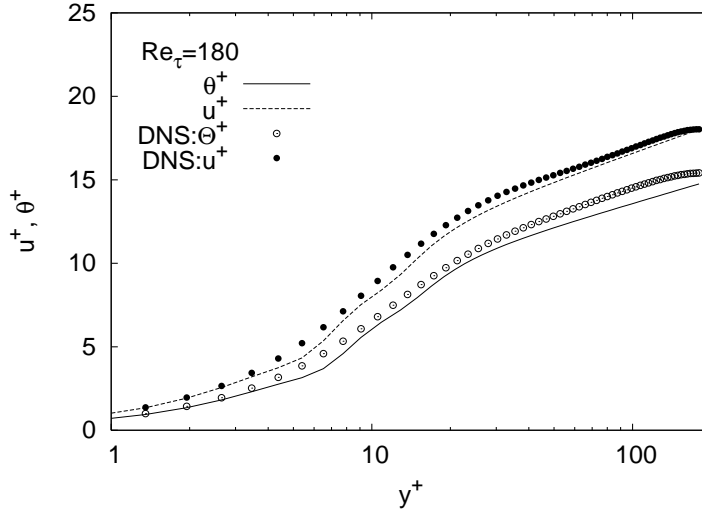
Figure 2: **Variations of mean velocity and temperature with wall distance in channel flow.**

explore alternative elements with relevance to $P/\epsilon$:

$$f = 1 + \left(\frac{C_\mu}{2f_\mu}\right)^3, \quad C_{\epsilon 1} = \min(1.44\,f,\,C_{\epsilon 2}), \quad C_{\epsilon 2} = 1.92 \tag{7}$$

As $f_\mu < 1$ in the near-wall region, the difference $(C_{\epsilon 2} - C_{\epsilon 1})$ becomes smaller that accounts for the additional production of dissipation by the anisotropy of turbulence. The parameter $P/\epsilon$ is supposed to serve the same purpose when included with $C_{\epsilon 1}$.

The budgets of $k$ and $\epsilon$ from the DNS data suggest that the role of turbulent diffusion in the near-wall region is substantial. Accordingly, the coefficients $\sigma_{(k,\epsilon)}$ are modeled, rather than being assigned constant values (unlike the commonly adopted practice with $\sigma_k = 1.0$, and $\sigma_\epsilon = 1.3$):

$$\sigma_k = \sqrt{C_\mu} + f_\mu \left(1 - \sqrt{C_\mu}\right), \qquad \sigma_\epsilon = C_\mu^{2/3} + f_\mu, \tag{8}$$

The model coefficients $\sigma_{(k,\epsilon)}$ are developed such that sufficient diffusion is obtained in the vicinity of the wall. This contrivance tends to successfully predict the kinetic energy and dissipation rate profiles [15].

The transport equations for $k$ and $\epsilon$ are subjected to the following boundary conditions at solid walls:

$$k_w = 0, \qquad \epsilon_w = 2\,\nu \left(\frac{\partial \sqrt{k}}{\partial y}\right)^2 \approx 2\,\nu\frac{k}{y^2} \tag{9}$$

To avoid numerical instability, the approximation for $\epsilon_w$ is applied at the first grid node neighboring the wall, rather than on the wall itself. This requires normal distance from a wall to the nearest grid point, which is unambiguous and readily available. The validity of Eq. (9) necessitates that the grid system is fine enough to produce the near-wall limiting behavior.

## 3. WALL FUNCTION APPROACH

The LRN model predicts the relevant wall parameters (i.e., wall shear and heat flux) reasonably well when the first node is located within the viscous sublayer ($y^+ \leq 5$). However, when the first grid point is in the fully turbulent region ($y^+ > 30$), it is inevitable to apply WF in order to provide the wall shear stress and other variables at the near-wall grid nodes. The WF relates the values of the variables in the cell centers with those at the wall through pre-integrated simplified expressions, thus providing indirectly the wall boundary conditions. In principle, the WF boundary conditions are established on the idea that

620
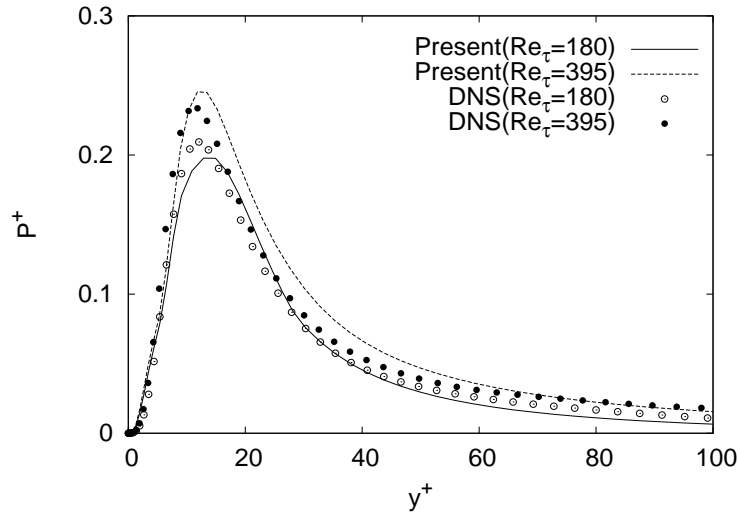
Figure 3: **Variations of kinetic energy production $P$ with wall distance in channel flows.**

equilibrium flow conditions exist in a region of the flow close to the wall. The standard wall functions exercise the universal law of the wall that implies the following assumptions [5]: Semi-logarithmic velocity (and temperature) distribution $u^+ = u/u_\tau = \ln(Ey^+)/\kappa$, constant turbulent shear stress (wall shear stress) $\tau = -\rho\overline{uv} = \tau_w = \rho u_\tau^2$, constant structure parameter $\overline{uv}/k = \sqrt{C_\mu} = 0.3$, turbulent kinetic energy equilibrium (convection and diffusion are negligible) $P = \epsilon = u_\tau^3/(\kappa y) = k^{2/3}/(C_l y)$, and a universal length scale distribution $l = C_l y$. The associated constants with the standard wall functions are the surface roughness parameter (dependent upon the flow structure over the viscosity affected sublayer) $E = 9.0$ for a smooth wall, the von Karman constant (reflecting the structure of turbulence in the fully turbulent region) $\kappa = 0.41$ and $C_l = 2.5$.

In particular, the largest error is introduced with the turbulence model when the first computational cell falls in the buffer region. The usual remedy is to combine the integration up to the wall with wall functions [4, 5, 16]. This signifies that a blending of the two formulations into a unified approach, providing the wall boundary conditions irrespective of whether the first near-wall grid node lies in the viscous sublayer, turbulent zone or in the buffer region. The procedure reduces to either the LRN or WF method depending on the appropriate position of the near-wall node. However, if the near-wall node lies in the buffer zone, the boundary conditions are provided in the form of wall functions, but modified to account for the viscous and other (inviscid) wall effects. These smoothing functions which blend two schemes together are known as automatic wall treatment, hybrid, or CWT.

Alike the conventional WF approach, the quantities for which the boundary conditions have to be specified depend on the turbulence model used. The primary variables are the wall shear stress $\tau_w$ and its relation with the mean velocity, wall heat flux $q_w$ and its relation with the mean temperature, the production $P$ and dissipation $\epsilon$ of the turbulence kinetic energy $k$. For the LRN $k$–$\epsilon$ model considered herein, the near-wall value of $k$ needs to be modified to enforce zero flux (i.e., $\partial k/\partial y \approx 0$) at the wall for the high-Reynolds number condition [17].

In principle, the physical requirement of the CWT method is to reproduce the relevant quantities in the buffer region. This can be achieved by combining the viscous and fully turbulent values with a compatible blending function in terms of some local flow variables. As suggested by Popovac and Hanjalic [5], the blending of the wall-limiting and fully turbulent properties in the manner of Kader [6] is considered, who proposed a single expression for the temperature profile throughout the whole wall boundary layer:

$$\Theta^+ = \rho c_p u_\tau \frac{T_w - T}{q_w} = Pry^+ e^{-\Gamma_\theta} + \left[2\ln(Pry^+) + \beta(Pr)\right]e^{-1/\Gamma_\theta} \tag{10}$$
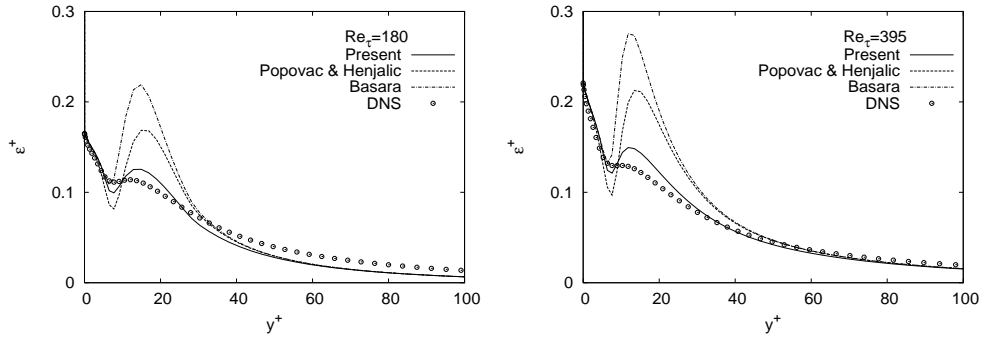
Figure 4: **Variations of dissipation rate $\epsilon$ with wall distance in channel flows.**

Where $c_p$ is the specific heat at constant pressure, $Pr$ denotes the molecular Prandtl number and $T$ implies the temperature. The thermal boundary layer parameter $\beta(Pr)$ and the blending coefficient are given by

$$\beta(Pr) = \left(4Pr^{1/3} - 1.3\right)^2, \qquad \Gamma_\theta = \frac{0.01\,(Pr\,y^+)^4}{1 + 5Pr^3 y^+} \tag{11}$$

Note that the associated constants are slightly modified to reproduce the data of DNS and experiments. By simply inserting $Pr = 1$, Equations (10) and (11) can be applied to the velocity profile:

$$u^+ = y^+ e^{-\Gamma} + \left[\frac{1}{\kappa} \ln\left(E y^+\right)\right] e^{-1/\Gamma}, \qquad \Gamma = \frac{0.01\,(y^+)^4}{1 + 5y^+} \tag{12}$$

Relations (10–12) represent the blending of the viscous and the fully turbulent definitions of $\Theta^+$ and $u^+$ through the blending functions $e^{-\Gamma_\Theta}$ and $e^{-\Gamma}$, respectively. The blending formula for the flow properties specified at the cell $p$ next to the wall can be generalised as

$$\phi_p = \phi_\nu e^{-\Gamma} + \phi_t e^{-1/\Gamma} \tag{13}$$

where $\nu$ and $t$ are respectively, the viscous (wall-limiting) and fully turbulent values of the wall shear stress $\tau_w$, production $P$ and dissipation $\epsilon$ of the turbulence kinetic energy $k$.

In some nonequilibrium conditions such as separation and reattachment, the physical argument behind the WF no longer applies (i.e., singularity occurs when $u_\tau$ tends to zero), and it is important to ensure a robust boundary condition [18]. Consequently, one should follow the conventional practice and replace $u_\tau$ by $u_k = C_\mu^{1/4} k_p^{1/2}$ for the velocity scale to characterize the turbulence intensity in the vicinity of $y$. The issue of the replacement deserves further attention: $u_\tau$ is constant throughout the layer (for instance, fully developed channel flows), whereas $u_k$ changes with $k$ from the wall. Numerical experiments based on developed channel flows show that $y^* = u_k y / \nu$ used in equations (10) and (12) underestimate the velocity/temperature profile to the full length of $y^+ = u_\tau y / \nu$. To avoid this situation, $y^*$ is approximated as

$$y_p^* = \frac{y_p}{\nu_p} \left(k_p^2 + \nu_p \epsilon_p\right)^{1/4} \tag{14}$$

where $(\nu\epsilon)^{1/4}$ is the Kolmogorov velocity scale and $y^+$ is replaced from the velocity/temperature profile and blending functions by $y^*$. Craft et al. [2] have used the velocity scale $\sqrt{k}$ in their analytical WF model to identify the edge of the viscous sublayer. However, $u_k$ is used in practice to evaluate $P$ and $\epsilon$ in the fully turbulent region [17].

The CWT simplified as Equation (13) can be adopted for the wall boundary of the momentum and temperature equations (wall turbulent eddy viscosity and thermal conductivity) as

$$\mu_w = \mu \frac{y_p^*}{u_p^+}, \qquad \gamma_w = \gamma \frac{Pr\, y_p^*}{\Theta_p^+} \tag{15}$$

where $\Theta^+$ and $u^+$ are given by Equations (10) and (12), respectively. Using DNS data [10, 19], they are plotted in Figure 2 showing acceptable agreement with DNS results for a developed channel across the whole flow field.

Having an analytical solution for the velocity distribution across the near-wall region, an expression for $P$ can be derived by taking $(\partial u/\partial y)$ from Equation (12) in combination with the near-wall and fully turbulent values for the turbulent stress. In principle, this reduces to the blending of relation (13), where $\phi_\nu$ is the fine-resolution $P$ value from the wall integration and $\phi_t$ is the coarse-mesh $P$ from the WF approach:

$$P_p = -\rho \overline{uv} \frac{\partial u}{\partial y} = (\mu_T)_p \left(\frac{\partial u}{\partial y}\right)_p^2 e^{-\Gamma} + \frac{\rho u_k^3}{\kappa y_p} e^{-1/\Gamma} \tag{16}$$

where $\mu_T$ is given by Equation (4). Figure 3 shows $P$ from (16), compared with the DNS data [10]. It seems likely that the WF for $P$ is more sensitive and deviates somewhat in the buffer region. However, compared with DNS, it can be considered as acceptable.

Recalling that the dissipation rate $\epsilon$ satisfies the following expressions in the viscous sublayer and in the fully turbulent wall region, respectively:

$$\epsilon_\nu = \frac{2\nu k}{y^2}, \qquad \epsilon_t = \frac{C_\mu^{3/4} k^{3/2}}{\kappa y} \tag{17}$$

One can use the blending (13) to express $\epsilon$ in the whole wall region. However, due to a very steep and specific (non-monotonic) variation of $\epsilon$ in the near-wall region, Popovac and Hanjalic [5] found it beneficial to modify slightly the coefficient in the exponent of the blending function $\Gamma$, so that the recommended expression for the complete near-wall region becomes:

$$\epsilon_p = \frac{2\nu_p k_p}{y_p^2} e^{-\Gamma_\epsilon} + \frac{u_k^3}{\kappa y_p} e^{-1/\Gamma_\epsilon} \tag{18}$$

where $\Gamma_\epsilon = 0.001 \, (y^+)^4 / (1 + y^+)$. Basara [7] found that a better agreement with the measurements is reached if (13) is used for the wall shear stress and the production rate, but not for the dissipation rate which is scaled as

$$\epsilon_p = (1 - \alpha) \frac{2\nu_p k_p}{y_p^2} + \alpha \frac{u_k^3}{\kappa y_p}, \qquad \alpha = \frac{u_k^3}{\kappa y_p P_p} e^{-1/\Gamma} \tag{19}$$

where $P_p$ is given by Equation (16). Equations (18) and (19) are plotted in Figure 4. Despite satisfying the wall-limit and the fully turbulent phenomena, the blended curve exhibits a large discrepancy from the DNS data in the buffer region. Popovac and Hanjalic [5] suggest that the agreement can be improved by further tuning of the blending functions, or even simply by reducing the value of the coefficient $C_\mu$. In the present study, the blending formula of Basara [7] adhering to $\epsilon_p$ is further improved by introducing a new function with the fully turbulent quantity:

$$\epsilon_p = (1 - \alpha) \frac{2\nu_p k_p}{y_p^2} + \alpha f_p \frac{u_k^3}{\kappa y_p}, \qquad f_p = \sqrt{\tanh\left(\sqrt{C_\mu} \frac{Re_y^{1.5}}{Re_T}\right)} \tag{20}$$

Equation (20) is also included in Figure 4. Evidently, the present approach provides significant improvement over (18) and (19), particularly in the buffer region.
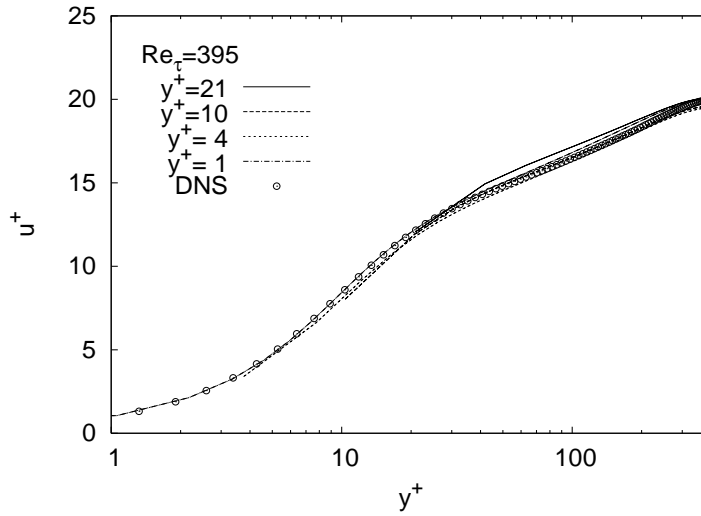
Figure 5: **Mean velocity profile of a channel flow.**

The present LRN $k$–$\epsilon$ model is subjected to have $k_w = 0$ at the wall and with a cell-centered finite-volume scheme, $(\partial k/\partial y)_w$ is approximated as

$$\left(\frac{\partial k}{\partial y}\right)_w = \frac{8k_w - 9k_p + k_{p+1}}{6y_p} \tag{21}$$

in order to evaluate the viscous flux for the $k$ equation. However, as the model tends to preserve the characteristics of a high-Reynolds number model, a common practice is to dissolve the flux of $k$ at the wall [17], a condition simply enforced by setting the appropriate finite-difference coefficients to zero, i.e., $(\partial k/\partial y)_w = 0$. This situation is explored by modifying the near-wall value of $k$ in collaboration with the blending (13) after the updating stage (i.e., at the beginning of each iteration phase):

$$k_p^* = k_p\,(1-\alpha) + \alpha\,\frac{k_{p+1}}{9} \tag{22}$$

where the asterisk denotes the modified value. Intuitively, this technique induces a smooth transition between two boundary conditions.

To this end, it must be emphasized that the LRN model coupled with the CWT adopts a simpler formulation for the distribution of turbulent viscosity over the near-wall cell:

$$\mu_T^* = \mu_T\,\left(e^{-\Gamma} + \kappa\,e^{-1/\Gamma}\right) \tag{23}$$

where $\mu_T^*$ represents a near-wall nodal value. This relation holds around singularities such as stagnation, separation and attachment. The discontinuity in $\mu_T$ as introduced by Craft et al. [2] and Popovac & Henjalic [5], is smoothed out using the blending functions associated with the CWT.

## 4. MODEL VALIDATION

As an illustration of the CWT performance, some computational results from a few generic flows with near-wall computational grids placed in the buffer region, are presented. These computations are compared with the fine grid integration up to the wall. Considered test cases include a fully developed channel flow, a backward facing step flow and an asymmetric plane diffuser flow. The objective herein is to validate the CWT insensibility to the location of the first interior node through a comprehensive mesh study.
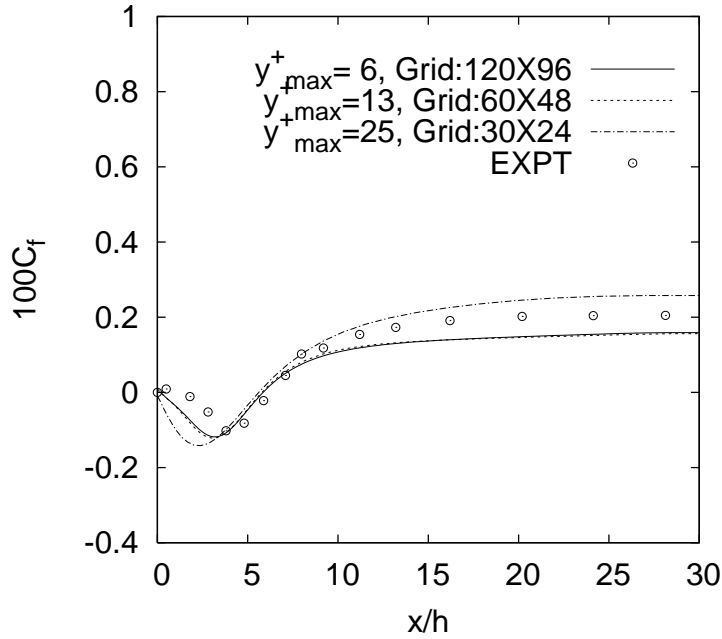
Figure 6: **Skin friction coefficient along the step-side bottom wall.**

### 4.1. Fully Developed Channel Flow

The computation is carried out for a fully developed turbulent channel flow at $Re_\tau = 395$ for which turbulence quantities are attainable from DNS data [10]. It is attractive to include this test case in spite of its simplicity, since the important wall effects are present in the flow. Only half of the channel needs to be simulated with symmetric condition applied along the centerline of the channel. The number of nodes in the wall normal direction range from $N = 20$ (uniformly distributed) to a near-wall clustered 100–node mesh. The log law considering velocity distribution for different locations of the first interior node is well captured as shown in Figure 5. It seems likely that the CWT is used for the interpolation in buffer layer.

### 4.2. Backward Facing Step Flow

To ascertain the performance in a complex flow, the present model is applied to the flow over a backward facing step. The step flow undergoes separation, recirculation and reattachment followed by a redeveloping boundary layer. In addition, this case involves a shear-layer mixing process and an adverse pressure gradient. The step flow is thus an attractive flow for evaluating the turbulence models. The computations are conducted corresponding to the experimental case with zero deflection of the wall opposite to the step, as investigated by Driver and Seegmiller [20]. The reference velocity $U_{ref} = 44.2$ $m/s$ and the step height $h = 0.0127\ m$. The ratio between the channel height and the step height is 9, and the step height Reynolds number is $Re = 3.75 \times 10^4$. At the channel inlet, the Reynolds number based on the momentum thickness is $Re_\theta = 5.0 \times 10^4$. The computed skin friction coefficient $C_f = 2\tau_w / \rho U_{ref}^2$, using different meshes is shown in Figure 6. The experimental data are also included for comparison. The computed $C_f$ with the CWT gives analogous results for the two meshes ($120 \times 96$ and $60 \times 48$). Coarsening the mesh further to a first node location at $y^+ = 25$ gives a small deviation in the predicted $C_f$ and a slight re-location of the reattachment point.

### 4.3. Asymmetric Plane Diffuser Flow

To further validate the performance in complex separated and reattaching turbulent flows, the present model is applied to the flow in an asymmetric diffuser with an opening angle of $10^o$, for which mea-
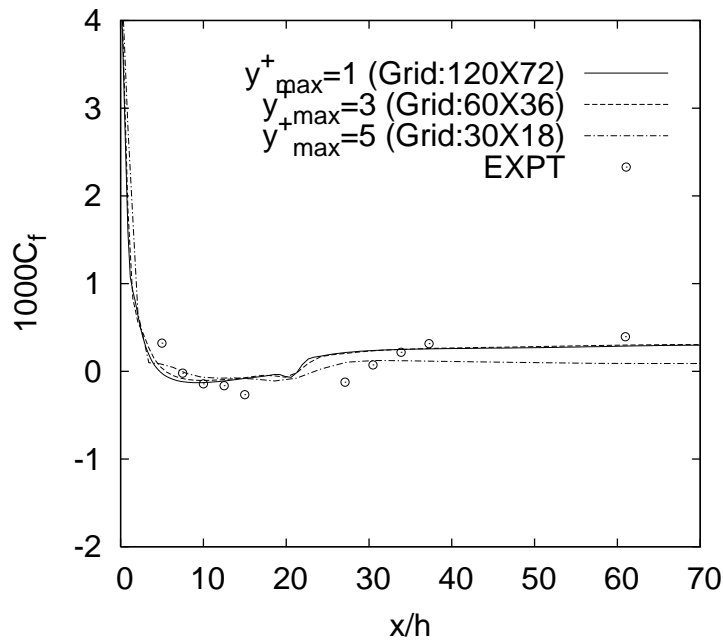
Figure 7: **Skin friction coefficient of diffuser flow along deflected bottom wall.**

surements are available [21]. The expansion ratio of $4.7$ is sufficient to produce a separation bubble on the deflected wall. Hence the configuration provides a test case for smooth, adverse pressure driven separation. The entrance to the diffuser consists of a plane channel to invoke fully developed flow with $Re = 2.0 \times 10^4$ based on the centerline velocity $U_{ref}$ and the inlet channel height $h$. Figure 7 portrays the predicted skin friction coefficients $C_f$ with different meshes. The performance of the present model evinces an encouraging qualitative agreement with measurements for two meshes ($120 \times 72$ and $60 \times 36$). Further Coarsening of the mesh provides less satisfactory results compared with the experiment.

## 5. CONCLUSIONS

A compound wall treatment (CWT) is developed that provides adequate boundary conditions in complex flows irrespective of whether the near-wall grid point lies in the viscous sublayer or in the buffer/fully turbulent region. The CWT combines the LRN $k$–$\epsilon$ model to devise the wall integration with the wall function (WF) approach. Contrasting the predictions with the reference data demonstrates that the present model offers acceptable results with relatively coarse meshes. However, it can be stressed that a coarse mesh gives less accurate calculation of gradients and this can deteriorate the computational accuracy. In some cases it can also lead to numerical instabilities. Therefore, the WF approach sometimes needs lower under-relaxation factors and more stable preconditioners/solvers. On the other hand, finer mesh computations will certainly give better results since the CWT approaches the full wall integration.

## 6. REFERENCES

1. Chieng CC, Launder BE. On the calculation of turbulent heat transport downstream from an abrupt pipe expansion. *Numerical Heat Transfer* 1980; 3: 189-207.
2. Craft TJ, Gerasimov AV, Iacovides H, Launder BE. Progress in the generalisation of wall function treatments. *International Journal of Heat and Fluid Flow* 2002; 23: 148-160.
3. Craft TJ, Gant SE, Iacovides H, Launder BE. A new wall function strategy for complex turbulent flows. *Numerical Heat Transfer Part B* 2004; 45: 301-317.
4. Esch T, Menter RF. Heat transfer predictions based on two-equation turbulence model with advanced wall treatment. *Proceedings of the 4th International Symposium on Turbulence, Heat and Mass Transfer*, edited by K. Hanjalic,Y. Nagano and M. Tummers, Begell House, 2003; 4: 633-640.

5. Popovac M, Hanjalic K. Compound wall treatment for RANS computation of complex turbulent flows and heat transfer. *Flow turbulence and Combustion* 2007; 78: 177-202.

6. Kader BA. Temperature and concentration profiles in fully turbulent boundary layers. *international Journal of Heat and Mass Transfer*, 1981; 24: 1541-1544.

7. Basara B. Eddy viscosity transport model based on elliptic relaxation approach. *AIAA Journal* 2006; 44: 1686-1690.

8. Rahman MM, Siikonen T. Near-wall turbulence modeling with enhanced dissipation. *International Journal for Numerical Methods in Fluids* 2003; 42: 979-997.

9. Patel VC, Rodi W, Scheuerer G. Turbulence models for near-wall and low Reynolds number flow: A review. *AIAA Journal* 1985; 23:1308-1319.

10. Mansour NN, Kim J, Moin P. Reynolds-stress and dissipation-rate budgets in a turbulent channel flow. *Journal of Fluid Mechanics* 1988; 194: 15-44.

11. Durbin PA, Speziale CG. Local anisotropy in strained at high Reynolds numbers. *Journal of Fluids Engineering* 1991; 113: 707-709.

12. Ahn JW, Park TS, Sung HJ. Application of a near-wall turbulence model to the flows over a step with inclined wall. *International Journal of Heat and Fluid Flow* 1997; 18: 209-217.

13. Durbin PA. A Reynolds-stress model for near-wall turbulence. *Journal of Fluid Mechanics* 1993; 249: 465-498.

14. Durbin PA. Separated flow computations with $k$–$\epsilon$– $v^2$ model. *AIAA Journal* 1995; 33: 659-664.

15. Abe K, Kondoh T, Nagano Y. On Reynolds-stress expression and near-wall scaling parameters for predicting wall and homogeneous turbulent shear flows. *International Journal of Heat and Fluid Flow* 1997; 18: 266-282.

16. Bredberg J, Davidson L. Low-Reynolds number turbulence models: an approach for reducing mesh sensitivity. *Journal of Fluids Engineering* 2004; 126: 14-21.

17. Launder BE, Spalding DB. The numerical computation of turbulent flows. *Computer methods in Applied Mechanics and Engineering* 1974; 3: 269-289.

18. Launder BE. Numerical computation of convective heat transfer in complex turbulent heat transfer in complex turbulent flows: time to abandon wall function? *International Journal of Heat and Mass Transfer*, 1984; 27: 1485-1490.

19. Kim J, Moin P. Transport of passive scalars in a turbulent channel flow. *Turbulent Shear Flows* 1989; 6: 85-96.

20. Driver DM, Seegmiller HL. Features of a reattaching turbulent shear layer in divergent channel flow. *AIAA Journal* 1985; 23: 163-171.

21. Buice C, Eaton JK. Experimental investigation of flow through an asymmetric plane diffuser. *Dept. of Mechanical Engineering, Thermoscience Div.* 1997; Rept. TSD-107, Stanford University, California, CA.

# NUMERICAL SIMULATION ON MIXING FIELD FLOW FIELD WITH DIFFERENT MACH NUMBERS

M. Rafiqul Hoque[1] and Mohammad Ali[2]

[1]Institute of Information and Communication Technology
[2]Department of Mechanical Engineering
Bangladesh University of Engineering and Technology (BUET)
Dhaka 1000, Bangladesh.
e-mail: rafiqul@iict.buet.ac.bd

## ABSTRACT

*The present study involves the investigations of the performance of fuel combustion with the help of computer based simulation system. The simulation is carried out using huge volume of data analysis. A numerical study on mixing of hydrogen injected into a supersonic air stream has been performed by solving Two-Dimensional full Navier-Stokes equations. An explicit Harten-Yee Non-MUSCL Modified-flux-type TVD scheme has been used to solve the system of equations, and a zero-equation algebraic turbulence model to calculate the eddy viscosity coefficient. The main objectives of this study are to increase the mixing efficiency and the flame holding capability of a supersonic combustor. The performance of combustor has been investigated by varying the air stream Mach number, keeping constant the backward-facing step height and other calculation parameters. The results show that small Mach number causes good mixng of hydrogen and oxygen in upstream recirculation region, but penetration height is low in downstream. In moderate Mach number large and elongated upstream recirculation causes high prenetration dominated by convection of recirculation. The increase of Mach number causes higher penetration of hydrogen. High Mach number increases both the mixing efficiency and flame holding capability.*

**KEYWORDS:** *Mach Number, Navier-Stokes equations, Combustor, Flame, Mixing efficiency*

## 1. INTRODUCTION

Mixing of fuel with oxidizer and their combustion are encountered in many engineering applications. Particularly, the fuel injection in both supersonic and hypersonic streams requires special attention for efficient mixing and stable combustion. Though a considerable number of researches have been carried out on mixing and combustion of fuel with supersonic air stream, still it faces many unresolved problems. The main problems that arise in this regard, concern mixing of reactants, ignition, flame holding, and completion of combustion. More investigations are required to overcome these problems. In fact, in supersonic combustion, high penetration and mixing of injectant with main stream is difficult due to their short residence time in combustor. In an experimental study, Brown et al. [1] showed that the spreading rate of a supersonic mixing layer decreased drastically with increasing free stream Mach number. A similar conclusion was drawn by Papamoschou et al. [2] on the basis of a theoretical analysis of shear-layers. Furthermore, they showed that the reduction in spreading rate correlated most closely with the convective Mach number, where convective Mach number is defined as the differential velocity normalized by the speed of sound. An independent linear stability theory analysis of Ragab et al. [3] reached the same conclusion. These investigations showed that difficulty exists in achieving a high degree of mixing in high

Mach number flows. Therefore, it is necessary to investigate all the parameters that affect the mixing of hydrogen in supersonic airstreams. This study is a part of M.Sc. thesis done by Hoque [4]. Here the effect of air stream Mach number on mixing and flame holding capability in supersonic stream is investigated. The geometric configuration of the calculation domain and the inlet conditions of main and injecting flows are shown in Fig.1. The left boundary consists of a backward-facing step of height 5-mm, which was found most efficient in mixing by Ali [5] among the conditions investigated. For this study, the air stream Mach number is varied by taking as 3.00 (Case 1), 3.25 (Case2), 3.50 (Case3), 3.75 (Case4) and 4.0 (Case5). The inlet widths of air and side jet are used as Ali et al. [6], which showed good performance on mixing.

## 2. MATHEMATICAL DESCRIPTION

The flow field is governed by the unsteady, two-dimensional full Navier-Stokes and species continuity equations. The body forces are neglected. With the conservation-law form, these equations can be expressed by

$$\frac{\partial U}{\partial t} + \frac{\partial F}{\partial x} + \frac{\partial G}{\partial y} = \frac{\partial F_v}{\partial x} + \frac{\partial G_v}{\partial y}$$

Where

$$U = \begin{pmatrix} \rho \\ \rho u \\ \rho v \\ E \\ \rho Y_i \end{pmatrix}, \quad F = \begin{pmatrix} \rho u \\ \rho u^2 + p \\ \rho u v \\ (E+p)u \\ \rho Y_i u \end{pmatrix}, \quad G = \begin{pmatrix} \rho u \\ \rho u v \\ \rho v^2 + p \\ (E+p)v \\ \rho Y_i v \end{pmatrix}$$

$$Fv = \begin{pmatrix} 0 \\ \sigma_x \\ \tau_{xy} \\ \sigma_x u + \tau_{yx} v - q_x \\ -\dot{m}_x \end{pmatrix}, \quad G_v = \begin{pmatrix} 0 \\ \tau_{yx} \\ \sigma_y \\ \tau_{xy} u + \sigma_{yv} - q_y \\ -\dot{m}_x \end{pmatrix}$$

$$p = \sum_{i=1}^{ns} \rho_i R_i T = \sum_{i=1}^{ns} \rho_i \frac{R}{W_i} T,$$

$$E = \sum_{i=1}^{ns} \rho_i C_{pi} T - \sum_{i=1}^{ns} \rho_i \frac{R}{W_i} T + \frac{\rho}{2}\left(u^2 + v^2\right)$$

$$\sigma_x = \lambda\left(\frac{\partial u}{\partial x} + \frac{\partial v}{\partial y}\right) + 2\mu\left(\frac{\partial u}{\partial x}\right), \quad \sigma_y = \lambda\left(\frac{\partial u}{\partial x} + \frac{\partial v}{\partial y}\right) + 2\mu\left(\frac{\partial v}{\partial y}\right), \quad \tau_{xy} = \tau_{xy} = \mu\left(\frac{\partial u}{\partial y} + \frac{\partial v}{\partial x}\right), \quad \lambda = -\frac{2}{3}\mu$$

## 3. RESULTS AND DISCUSSION

The present study consists of five cases varying air stream Mach number. The results are to be analyzed and discussed under the following contents: (i) The effect of Mach number on penetration and mixing of hydrogen, and (ii) The characteristics of the flow field.

### 3.1 Penetration and Mixing of Hydrogen

Figure 2 shows the penetration and mass concentration of hydrogen in the flow field. Different penetration height can be found at both upstream and downstream of different cases. Cases 1 and 2 show good mixing of hydrogen and oxygen in upstream recirculation region, but penetration height is low. For high Mach number (cases 3 and 4), large and elongated upstream recirculation causes high penetration dominated by convection of recirculation. At the same time due to strong interaction, high gradient of hydrogen mass concentration exists causing high penetration of hydrogen. It can be point out that the increase of Mach number causes higher penetration of hydrogen. This can be explained by the fact that the increase of Mach decreases the air inlet pressure, which helps the expansion of side jet resulting in high penetration. Figure 3 shows the mixing efficiency along the length of physical model for different cases. The figure shows that mixing efficiency increases sharply at injector position for all cases. Generally in upstream region, the increasing rate of mixing is moderate and in downstream it is slow. Individually, case 5 (Mach 4) has the highest increment of mixing efficiency both at the upstream region and injector position due to strong upstream recirculation and high interaction between air stream and side jet. Again case 5 shows that in upstream the increment of mixing along the length of physical model is highest, whereas in downstream the increment of mixing is slow and almost equal for all cases caused by the supersonic nature of flow. On the top of injector the increment of mixing efficiency of case 5 is higher than cases 1~4. Including the effects activated for mixing, case 5 has the highest overall mixing efficiency at the outflow boundary.

### 3.2 Characteristics of the Flow Field

Various characteristics phenomena such as separation shock, bow shock, Mach disk, reattachment shock can be seen in figure 4 (a~e) and 5 (a~e). Figure 4 (a~e) shows the pressure contours by which the pressure distribution and different shocks can be understood. Flow separation is initiated by the backward facing step at left boundary. The deflection angle of air stream increases with the increase of Mach number caused by the decrease of air inlet pressure. The under expanded side jet rapidly expands and forms a Mach disk and a bow shock due to the interaction with main flow. For high Mach number the slope of the bow shock is steeper indicating strong interaction between the main and side jet resulting in the high gradient of mass concentration and consequently high mixing efficiency. The maximum pressure and temperature in the flow field rises immediately behind the intersection of separation shock and bow shock. In the downstream region the reattachment shock is more visible in the pressure contour as shown in Fig. 4 (a~e). The pressure is higher in the upstream recirculation region while it is much lower immediately behind the injector caused by the suction of injection. Figure 5 shows the temperature contours for the cases (Case 1~5). The maximum temperature, found for cases 1, 2, 3, 4 and 5 are 2233, 2335, 2467, 2561 and 2698 K, respectively.  It can be pointed out that case 5 has the highest temperature which is caused by the interaction of side jet with high momentum of main flow. The separation shock, bow shock and Mach disk can also be understood from the Fig.5 (a~e). The temperature is lower at the upper part of the flow field for all cases and at the upper left corner the temperature is the lowest.

### 4.  CONCLUSION

The Mach number of air stream is varied as (3, 3.25, 3.5, 3.75 and 4) to investigate the mixing flow field. High penetration of hydrogen increases the mixing efficiency along the injector position. It is found that strong interaction is occurring between the main and

injecting flows for high Mach number (M=4). High Mach number increases both the mixing efficiency and flame holding capability. So air stream in supersonic flow having Mach number 4 might act as a good flame holder and become efficient in mixing.

## 5. FIGURES
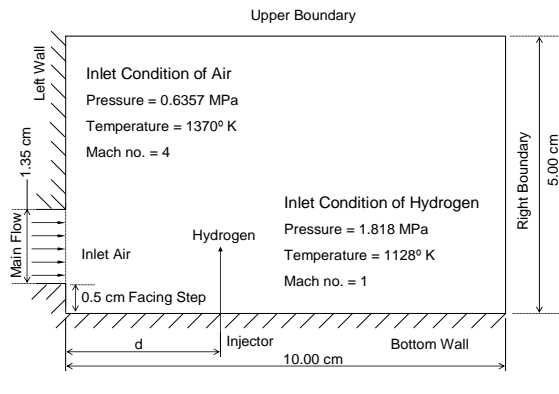


Fig.1 Geometric configuration
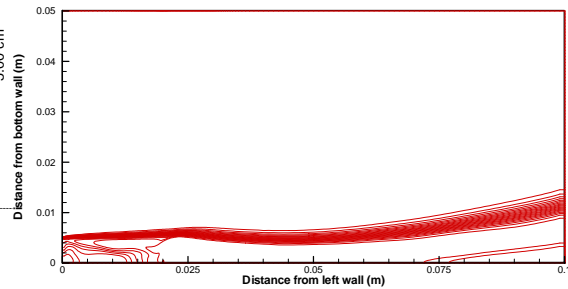


Fig. 2(a) Case-1(Mach No. = 3)
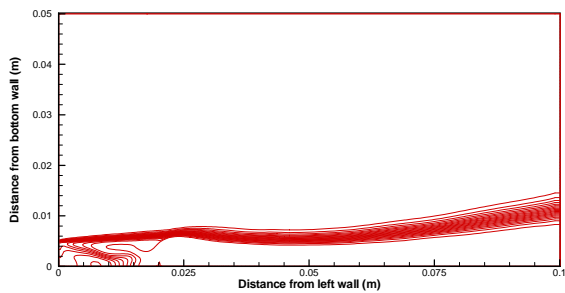


Fig.2(b) Case-2(Mach No. = 3.25)
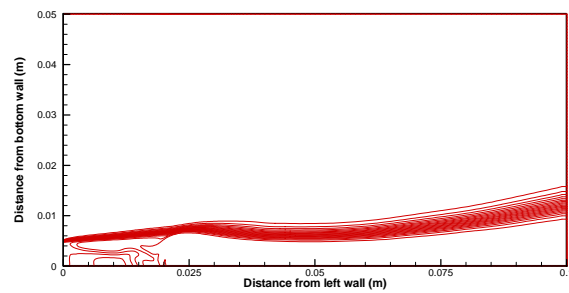


Fig.2(c) Case-3(Mach No. = 3.5)
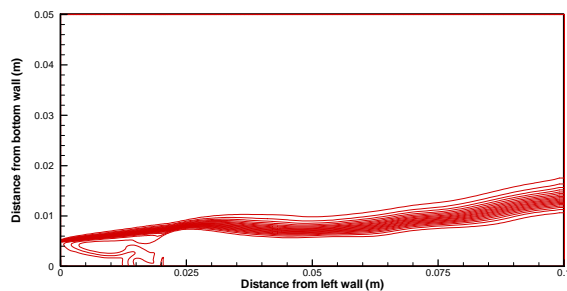


Fig.2 (d) Case-4 (Mach No. =3.75)
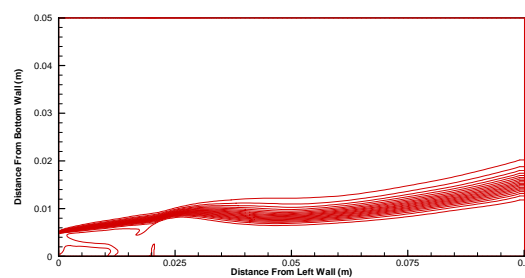


Fig. 2(e) Case-5(Mach No. = 4)

Fig. 2 Mole fraction counter of Hydrogen, Φ(0.05, 1.0, 0.05);
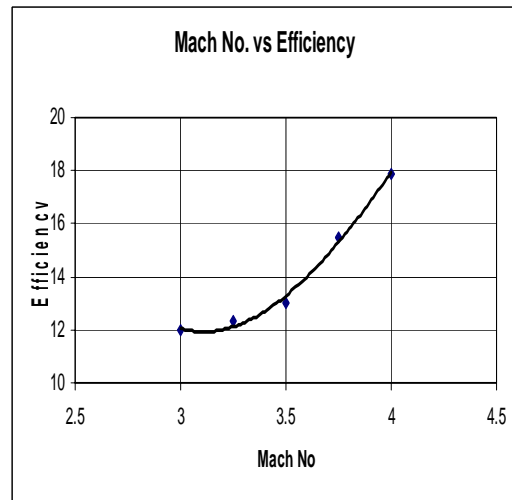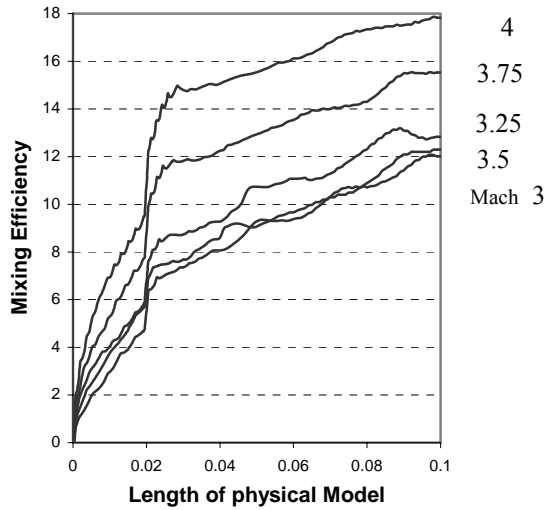
Fig. 3.1 Mixing efficiency along the length of physical model



Fig. 3.2 Mixing efficiency verses Mach Number
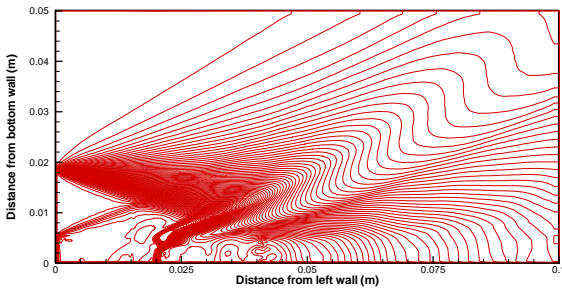


Fig. 4(a) Pressure contour Case-1(Mach No. = 3)
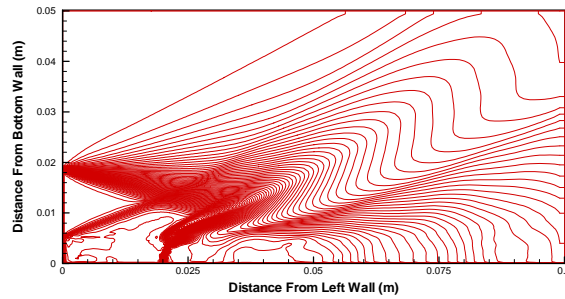


Fig. 4(b) Pressure contour Case-2(Mach No. = 3.25)
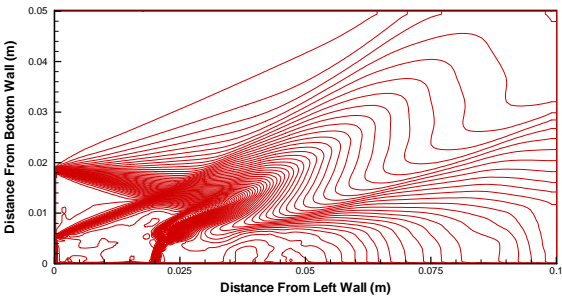


Fig. 4(c) Pressure contour Case-3(Mach No. = 3.5)
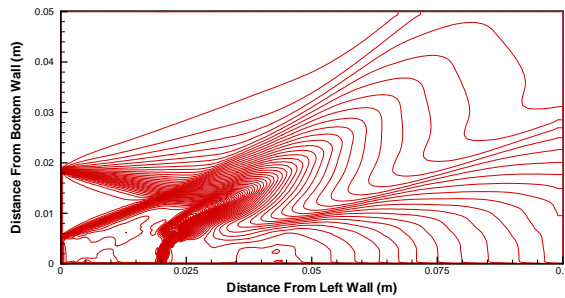


Fig. 4(d) Pressure contourCase-4(Mach No. = 3.75)
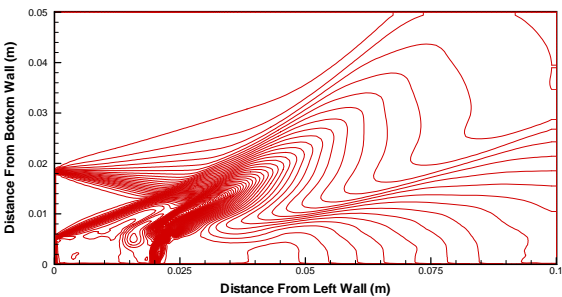


Fig. 4(e) Pressure contour Case-5(Mach No. = 4)
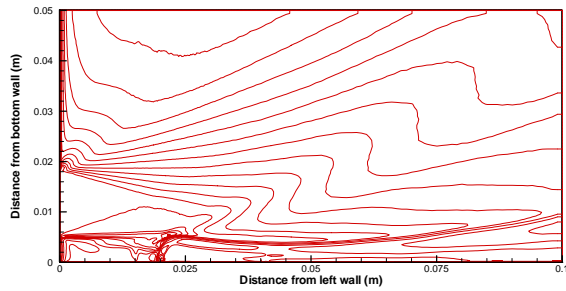
. 5(a) Temperature contour Case-1(Mach No. = 3)    Fig. 5(b) Temperature contour Case-2(Mach No. = 3.25)
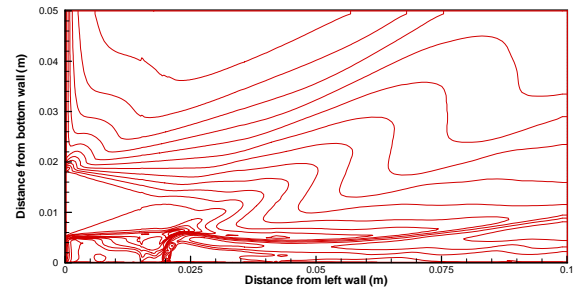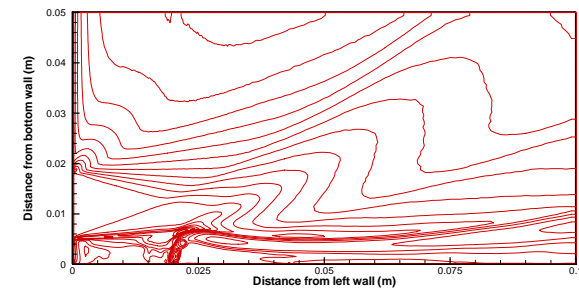


Fig. 5(c) Temperature contour Case-3(Mach No. = 3.5) Fig.5 (d) Temperature contour Case-4(Mach No. = 3.75)
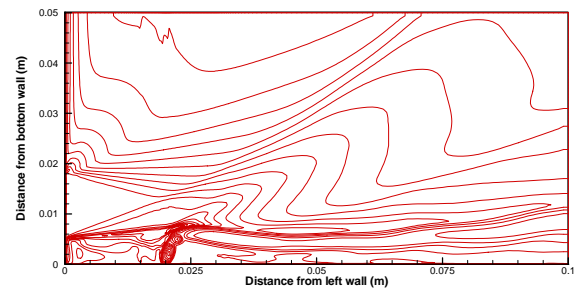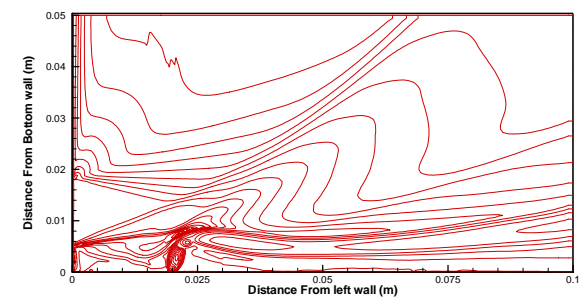


Fig. 5(e) Temperature contour Case-5 (Mach No. = 4)

## 6. REFERENCES

1. Brown, G. L. and Roshko, A.: On Density Effects and Large Structure in Turbulent Mixing Layer, *J.Fluid Mechanics,* Vol. 64, No. 4, pp.775-816, (1974).

2. Papamoschou, D. and Roshko, A.: Observation of Supersonic Free Shear Layers, AIAA Paper 86-0162, January (1986).

3. Ragab, S. A. and Wu, J.L.: Instabilities in the Free Shear Layer Formed by Two Supersonic Streams, AIAA Paper 88-0038, January, 1988.

4. Hoque, M. R.: A Numerical Study on Mixing and Injection Systems in Supersonic Combustors, M.Sc. Engineering thesis BUET, Dhaka, Bangladesh, January, 2004.

5. Ali, M, Physics of Supersonic Mixing and Combustion of a Transverse Jet in Two-Dimensional Finite Stream, Ph. D. Thesis, Nagoya. University, Japan, (1998).

6. Ali, M. and Islam, A.K.M.S.: Effect of Mainflow Inlet Width on Penetration and Mixing of Hydrogen in Scramjet Combustor, Proceedings of the Eighth Asian Congress of Fluid Mechanics, pp. 647–650, December 6-10, Shenzhen, China, (1999).

# EFFECT OF ASPECT RATIO ON ENTROPY GENERATION IN A MICROSTRUCTURE FILLED VENTED CAVITY

Shama Farabi Barna, Arafat Ahmed Bhuiyan, M. H. Banna, A. K. M. Sadrul Islam

Department of Mechanical and Chemical Engineering, IUT,
Board Bazar, Gazipur-1704, Dhaka Bangladesh
Email: farabibd@gmail.com, arafat_iut_mce@yahoo.com

## ABSTRACT

*This study has been conducted considering an enclosure filled with fluid saturated porous medium with adiabatic top wall, bottom wall and right wallThe left wall is assumed to be isothermal. Entropy generation takes place due to mixed Convection. Naatural convection takes place due to the temperature variation between the isothermal wall and the fluid and forced convection is induced by providing an inlet at the bottom surface, and a vent at the top, facing the inlet. The problem is solved using the modified Darcy flow model and energy equation for different Rayleigh Numbers (1, 50, 100, 500, and 1000) and different Pe$^{/}$clet Numbers (0.1, 1, 5, 10, 20, 50 and 100). The equations are solved using standard Finite Element method for considering three different Aspect Ratios of the cavity (AR=H/W=0.5, 1, 1.5). For a particular Aspect Ratio, Inlet Width to Cavity Width Ratio and Inlet Width to Outlet Width Ratio entropy generation rate is the lowest where Rayleigh Number & Pe$^{/}$clet Number both are the lowest.*

**KEYWORD**: *Porous medium, Entropy generation, Aspect Ratio, Rayleigh Number.*

## 1.INTRODUCTION

Fundamental studies related to thermal convection in porous media have increased significantly due to the requirement for energy, the necessity to develop effective technologies for nuclear waste management, transpiration cooling; separation processes in chemical industries, building thermal insulations, and numerous other applications have led to a considerable interest in convective heat transport through porous media. The fundamental nature and the growing volume of works in this area are amply documented in the books by Nield and Bejan [1], Ingham and Pop [2–4]. A large number of important analytical, numerical, and experimental results related to Convective flow inside a square and/or rectangular cavity filled with a fluid-saturated porous medium have been published and they are important to better understand the thermal convection inside porous cavities.

In this study a rectangular enclosure filled with fluid saturated porous medium is considered with adiabatic top-wall, right wall and bottom wall. The left wall is considered as isothermal. Analysis has been done for different aspect ratios of enclosure for different Rayleigh Numbers and Peclet Numbers. The performance of the enclosure is determined by flow visualization and by analyzing different parameters such as Entropy Generation Number, Bejan Number, Nusselt Number.

## 2. BASIC EQUATIONS

In this study we have considered an enclosure filled with fluid saturated porous medium with adiabatic top wall, bottom wall and right wall. The left vertical wall is considered as isothermal at constant temperature, $T_w$. There is an inlet at the left corner of the bottom wall and the vent is on the left corner of the top wall. The widths of the inlet and vent are I and O respectively as shown in figure 1. Buoyancy effects are induced due to the difference in temperature between the left vertical wall, $T_w$, and the through-stream temperature, $T_0$, which has a constant velocity, $V_0$, at the inlet of the enclosure. The inlet forced flow is fixed at the inlet and the temperature difference ($T_w - T_0$) considered here is positive which means it is an aiding flow.

The assumptions made for porous media to prepare mathematical model are: the fluid and the porous medium are in local thermal equilibrium; the properties of the fluid and the porous media are constant; the viscous drag and inertia terms of the momentum equations are negligible, and the Darcy and Boussinesq approximations are valid. Under these assumptions, the conservation equation for mass becomes:

$$\frac{\partial u}{\partial x} + \frac{\partial v}{\partial y} = 0 \qquad \dots \quad \dots \quad \dots \quad \dots \quad \dots \quad \dots \quad \dots \quad (1)$$

The momentum flow inside the enclosure can be modeled by the Darcy flow model [1], by using the assumptions. This constructs a relationship between the flow velocities at a certain direction to the pressure gradient in that direction in vector form is,

$$\mathbf{v} = \frac{K}{\mu}(-\,\mathbf{grad}\,p + \rho\,\mathbf{g}) \qquad \dots \quad \dots \quad \dots \quad \dots \quad \dots \quad \dots \quad \dots(2)$$

Where, $\mathbf{v}, K, \mu, p$, and $\mathbf{g}$ are the velocity vector, permeability, viscosity, pressure, and gravity vector, respectively. Taking **curl** on the both side of Eq. (2) with the assumption, $\mathbf{v} = u\mathbf{i} + v\mathbf{j} + 0\mathbf{k}$ and $\mathbf{g} = 0\mathbf{i} + g_y\mathbf{j} + 0\mathbf{k}$, we can get

$$\frac{\partial u}{\partial y} - \frac{\partial v}{\partial x} = -\frac{g\beta K}{\nu}\frac{\partial T}{\partial x} \qquad \dots \quad \dots \quad \dots \quad \dots \quad \dots \quad \dots \quad \dots \quad \dots \ (3)$$

Where $g = g_y$. Eq. (3.3) has no pressure term. Finally, the energy equation, according to Nield and Bejan [1], is

$$\sigma\frac{\partial T}{\partial t} + u\frac{\partial T}{\partial x} + v\frac{\partial T}{\partial y} = \alpha_m\left(\frac{\partial^2 T}{\partial x^2} + \frac{\partial^2 T}{\partial y^2}\right) \qquad \dots \quad \dots \quad \dots \quad \dots \quad \dots \quad \dots \ (4)$$

Without any external or internal source, the equation of entropy generation according to Mahmud, S., and Fraser, [4-6] is

$$S'''_{gen} = HTI + FFI = \frac{k}{T_0^2}\left[\left(\frac{\partial T}{\partial x}\right)^2 + \left(\frac{\partial T}{\partial y}\right)^2\right] + \frac{\mu}{KT_0}\left(u^2 + v^2\right)\dots \qquad \dots \quad \dots \quad \dots(5)$$

Finally, the equation of energy flux density vector according to Mahmud, S., and Fraser [8] is

$$\mathbf{E} = E_x\mathbf{i} + E_y\mathbf{j} = \rho\mathbf{v}\left[\frac{1}{2}|v|^2 + C_P\,(T\text{-}T_0)\ \right] - k\,\mathbf{grad}(T)\dots \quad \dots\dots \quad \dots \quad \dots \quad \dots\dots(6)$$

We define the stream function, $\psi$, in the usual way as: $u = \dfrac{\partial \psi}{\partial y}$, $v = -\dfrac{\partial \psi}{\partial x}$ ….. ….(7)

Substituting Eqs. (7) into Eqs. (3) and (4), the following equations are obtained:

$$\frac{\partial^2 \psi}{\partial x^2} + \frac{\partial^2 \psi}{\partial y^2} = -\frac{g\beta k}{\nu}\frac{\partial T}{\partial x} \qquad \ldots \quad \ldots \quad \ldots \quad \ldots \quad \ldots \quad \ldots \quad \ldots \quad \ldots \quad (8)$$

$$\frac{\partial T}{\partial t} + \frac{\partial \psi}{\partial y}\frac{\partial T}{\partial x} + \frac{\partial \psi}{\partial x}\frac{\partial T}{\partial y} = \alpha_m\left(\frac{\partial^2 T}{\partial x^2} + \frac{\partial^2 T}{\partial x^2}\right) \ldots \quad \ldots \quad \ldots \quad \ldots \quad \ldots \quad \ldots(9)$$

Where Ra and Pe are the Rayleigh and Pe´clet numbers for a porous medium which are

defined by, $Ra = \dfrac{gK\beta(T_w - T_0)H}{\alpha_m \nu}$, $\qquad Pe = \dfrac{V_0 H}{\alpha_m}$ $\qquad \ldots \quad \ldots \quad \ldots \quad \ldots \quad \ldots$ (10)

The boundary conditions of Eqs. (8) and (9) are

Left isothermal wall: $\psi = 0$, $\qquad T = T_w = 1$ on $x = 0$, $\quad 0 \le y \le H$, … … 11(i)

Inlet: $\qquad\qquad \psi = -xV_0$, $\quad T = T_0 = 0$ on $y = 0$, $\quad 0 \le x \le I$,… … 11(ii)

Bottom Adiabatic wall: $\psi = -I \times V_0$, $\dfrac{\partial T}{\partial y} = 0$ on $\qquad y = 0$, $\quad I \le x \le W$,… … 11(iii)

Right Adiabatic wall: $\psi = -I \times V_0$, $\dfrac{\partial T}{\partial x} = 0$ on $\qquad x = W$, $\quad 0 \le y \le H$, … … 11(iv)

Top Adiabatic wall: $\quad \psi = -I \times V_0$, $\dfrac{\partial T}{\partial y} = 0$ on $\qquad y = H$, $\quad O \le x \le W$,…… 11(v)

Outlet: $\qquad\qquad\qquad \dfrac{\partial \psi}{\partial y} = 0$, $\dfrac{\partial T}{\partial y} = 0$ on $\qquad y = H$, $\quad 0 \le x \le O$ … …. 11(vi)

## 3. VALIDATION

For validity we have compared our domino effect with Mahmud and Pop [7]. The data are taken from the Table 4 of this paper which represents the value of Average Nusselt Number for adiabatic aiding flow circumstances where the aspect ratio is 1, inlet width to cavity width ratio is 0.25 and the inlet width to outlet width ratio is 1. From the figure 2 it appears that the numerical analysis done in our study produces such outcome which is almost identical to the results of Mahmud & Pop.
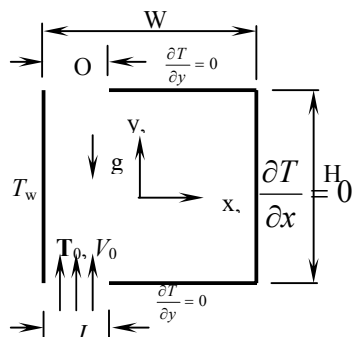


Fig. 1: Physical model and the coordinate system of the cavity
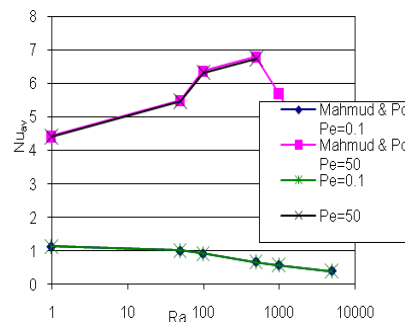
Fig.2: Variation Nu$_{av}$ with Ra for different Pe/clet Numbers (Adiabatic Aiding Flow, AR=1, I/W=0.25, I/O=1)

## 4. RESULTS AND DISCUSSION

Figure 3 shows the isothermal lines for Ra=50, Pe=10. The deviation of isothermal line with the transform of aspect ratio is observed. It can be observed from the figure that near the isothermal wall the isothermal lines are denser as the aspect ratio reduces and the spread of isothermal lines increases with the increase of aspect ratio. Thus it can be accomplished that the temperature gradient near the isothermal wall decreases with the increase of aspect ratio.



| AR=.5 | AR=1 | AR=1.5 |
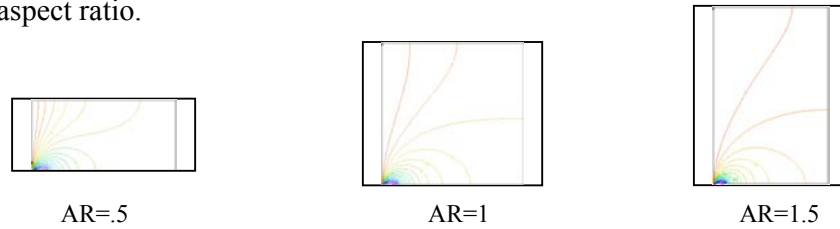
**Fig. 3: Isothermal Line for Ra=50, Pe=10**

Figure 4 shows the streamlines for Ra=50, Pe=10. The variation of streamline with the change of aspect ratio is observed. It is found from the figure that the streamlines are dense near the isothermal wall for low aspect ratio and it spreads with the increase in the aspect ratio. There is another phenomenon observed which is, a vortex is shaped at the top right corner of the cavity.



| AR=.5 | AR=1 | AR=1.5 |
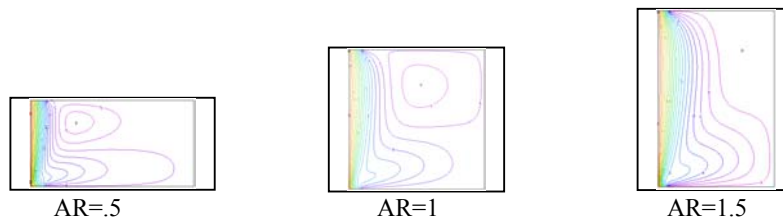
**Fig. 4: Streamline for Ra=50, Pe=10**

Figure 5 shows the constant Bejan Number line for I/W=0.1, I/O=1, Ra=50, Pe=10. These figures show the variation of Bejan number with aspect ratio. From the figure it can be assumed that as the AR increases, the Bejan contour increases and for dissimilar inlet width it varies considerably.



| AR=.5 | AR=1 | AR=1.5 |
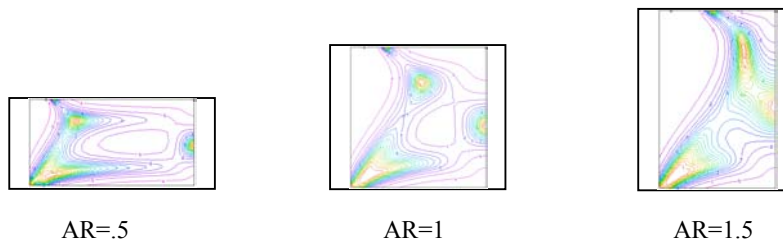
**Fig. 5: Constant Bejan Number Line for I/W=0.1, I/O=1, Ra=50, Pe=10**

Figure 6 to 9 show the variation of Average Entropy Generation Number with Aspect Ratio for different Pe= 0.1, 1, 5, 10, 20, 50, 100 with Rayleigh Number equals to 1.0, 50, 100 and 500, when AR increases from 0.5 to 1.5 for I/W=0.1, I/O=0.5 and is given in Table 1. For a particular Inlet Width to Cavity Width Ratio, Inlet Width to Outlet Width Ratio, Rayleigh Number and Pe$^/$clet Number, Entropy Generation rate increases with the increase of Aspect Ratio.

**Table 1: Percentage of Increase of Entropy Generation Number with the increase of aspect ratio for different Rayleigh Number & Peclet Number**

| Peclet Number | Rayleigh Number | | | |
|---|---|---|---|---|
| | 1.0 | 50 | 100 | 500 |
| 0.1 | 184% | 165% | 162.2% | 157.30% |
| 1 | 166.27% | 162% | 159.20% | 155.08% |
| 5 | 88.23% | 140% | 140.67% | 143.41% |
| 10 | 73.42% | 109% | 112.95% | 126.17% |
| 20 | 69.05% | 69% | 70.57% | 91.09% |
| 50 | 67.88% | 57% | 43.14% | 30.97% |
| 100 | 67.74% | 77% | 74.50% | 18.35% |
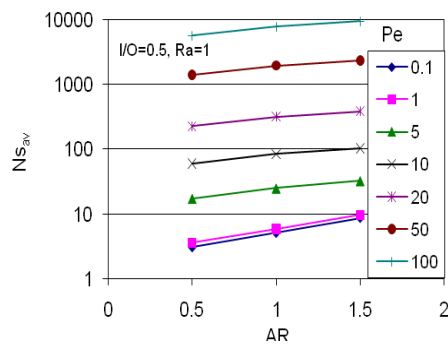


**Fig. 6: Variation of Ns$_{av}$ with Aspect Ratio (AR) for different Pe for I/W=0.1,I/O=0.5, Ra=1**
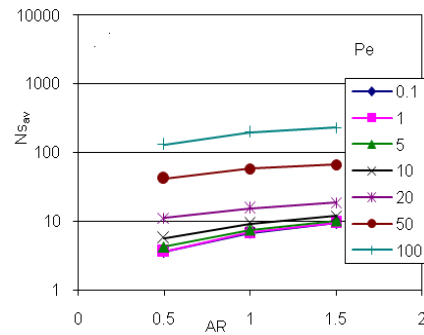


**Fig. 7: Variation of Ns$_{av}$ with Aspect Ratio (AR) for different Pe for I/W=0.1, I/O=0.5, Ra=50**
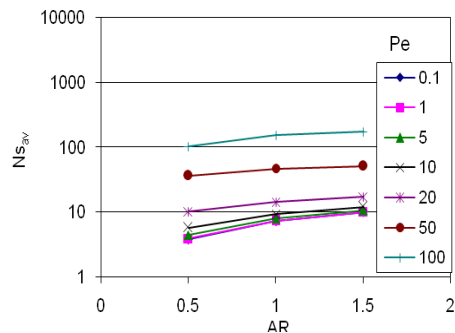


**Fig. 8: Variation of Ns$_{av}$ with Aspect Ratio (AR) for different Pe for I/W=0.1, I/O=0.5, Ra=100**
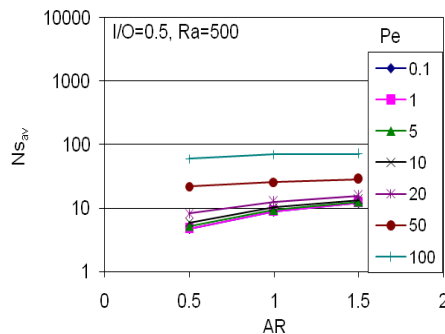


**Fig. 9:Variation of Ns$_{av}$ with Aspect Ratio (AR) for different Pe for I/W=0.1, I/O=0.5, Ra=500**

Figure 10 and 11show the variation of Average Entropy Generation Number with Aspect Ratio for different Ra. It is obvious from these figures that $Ns_{av}$ increases with the increase of Aspect Ratio. From figure 10 it is observed that the value of $Ns_{av}$ increases by184.40%, 165.26%, 159.84%, 157.30%, 158.43%, 161.34% for Ra= 1, 50, 100, 500, 1000, 5000 respectively when AR increases from 0.5 to 1.5  for I/W=0.1, I/O=0.5, Pe=0.10. From figure 11 it is observed that the value of $Ns_{av}$ increases by 67.88%, 57%, 39.66%, 30.97% for Ra= 1, 50, 100, 500 respectively when AR increases from 0.5 to 1.5 for I/W=0.1, I/O=0.5, Pe=50
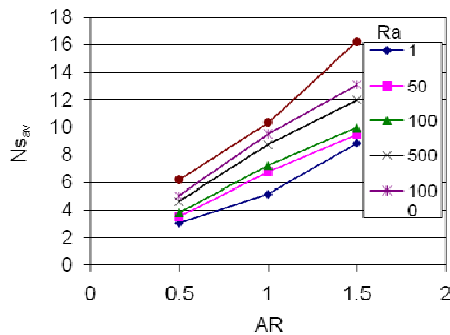


**Fig. 10: Variation of $Ns_{av}$ with Aspect Ratio for different Ra( I/W=0.1, I/O=0.5, Pe=0.1)**
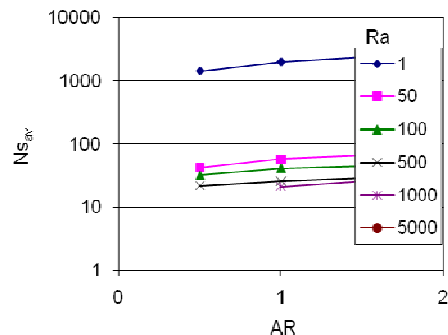


**Fig. 11: Variation of $Ns_{av}$ with Aspect Ratio for different Ra (I/W=0.1, I/O=0.5, Pe=50)**

Figure 12 show the variation of Average Energy Flux Density with Aspect Ratio for different Pe. It is evident from these figures that $E_{av}$ decreases with the increase of Aspect Ratio. It is observed from figure 11 that the value of $E_{av}$ decreases by 42%, 43%, 47%, 49%, 56%, 77% and 86% for Pe= 0.1, 1, 5, 10, 20, 50 and 100 respectively when AR increases from 0.5 to 1.5  for I/W=0.1, I/O=0.5, Ra=50.
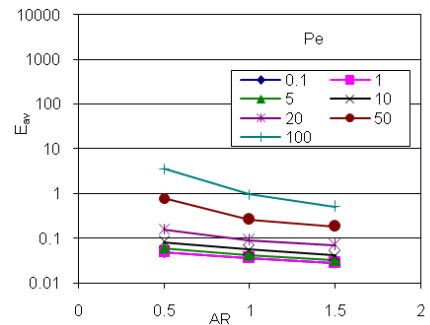


**Fig. 12: Variation of Eav with aspect ratio (AR) for different Pe for I/W= 0.1, I/O=0.5, Ra=50**

## 5. CONCLUSION

The following conclusions can be drawn from this investigation:

1.  The data obtained from the numerical analysis were found to be in satisfactory agreement with the well established journal paper.
2.  For a particular Aspect Ratio, Inlet Width to Cavity Width Ratio and Inlet Width to Outlet Width Ratio, heat flux is the most when both the Pe'clet Number and Rayleigh Number are the highest.

3. For a particular Aspect Ratio, Inlet Width to Cavity Width Ratio and Inlet Width to Outlet Width Ratio entropy generation rate is the lowest where Rayleigh Number & Pe$^/$clet Number both are the lowest.

4. For a particular Aspect Ratio, Inlet Width to Cavity Width Ratio and Rayleigh Number, heat flux increases with the increase of Inlet Width to Outlet Width Ratio.

5. For a particular Aspect Ratio, entropy generation rate increases with the increase of Inlet Width to Outlet Width Ratio for high Pe$^/$clet Number and low Rayleigh Number and for low Inlet Width to Cavity Width Ratio with negligible effect for lower Pe$^/$clet Number. But for high Inlet Width to Cavity Width Ratio the entropy generation rate reduces for low Pe$^/$clet Number.

6. For a particular Inlet Width to Cavity Width Ratio, Inlet Width to Outlet Width Ratio, Rayleigh Number and Pe$^/$clet Number, Heat Flux decreases with the increase of Aspect Ratio and

## ACKNOWLEDGMENTS

## REFERENCES

[1] D.A. Nield, A. Bejan, Convection in Porous Media, second ed Springer, New York,.

[2] D.B. Ingham, I. Pop (Eds.), Transport Phenomena in Porous Media, Pergamon, Oxford, 1998

[3] D.B. Ingham, I. Pop (Eds.), Transport Phenomena in Porous Media, Pergamon, Oxford, 2002

[4] D.B. Ingham, I. Pop (Eds.), Transport Phenomena in Porous Media, Elsevier, Oxford, 2005

[5] S. Mahmud, and R.A. Fraser, 2004, "Magnetohydrodynamic Free Convection and Entropy Generation in a Square Porous Cavity", Int. J. Heat Mass Transfer, vol. **47**, pp. 3245–3256.

[6] S. Mahmud, and R.A. Fraser, 2005, "Flow, Thermal, and Entropy Generation Characteristics inside a Porous Channel with Viscous Dissipation Effect", Int. J. Thermal Sciences, vol. 44, pp. 21–32.

[7] S. Mahmud and I. Pop, 2006, "Mixed convection in a square vented enclosure filled with a porous medium", International Journal of Heat and Mass Transfer vol. 49 (2006), pp. 2190–2206

[8] S. Mahmud, and R.A. Fraser, 2005, "Flow, Thermal, and Entropy Generation Characteristics inside a Porous Channel with Viscous Dissipation Effect", Int. J. Thermal Sciences, vol. 44, pp. 21–32

# NUMERICAL ANALYSIS ON MIXED CONVECTION THROUGH AN ADIABATIC ENCLOSURE FILLED WITH FLUID SATURATED POROUS MEDIUM

Arafat Ahmed Bhuiyan, Shama Farabi Barna, M H Banna, A. K. M. Sadrul Islam

Department of Mechanical and Chemical Engineering, IUT,
Board Bazar, Gazipur-1704, Dhaka Bangladesh

Email: arafat_iut_mce@yahoo.com

## ABSTRACT

*In this study, an enclosure filled with fluid saturated porous medium is considered. The observations are carried out taking left wall is isothermal and remaining walls are adiabatic. Natural convection takes place due to the temperature difference between the isothermal wall and the fluid. Forced convection is induced by providing an inlet at the bottom surface and a vent at the top, facing the inlet. The problem is solved using the modified Darcy flow model and energy equation for different Rayleigh Numbers (1, 50, 100, 500, and 1000) and different Peclet Numbers (0.1, 1, 5, 10, 20, 50 and 100). The equations are solved using standard Finite Element method for considering three different Aspect Ratios of the cavity.*

**KEYWORDS:** *Mixed Convection, Aspect ratio, Rayleigh Number, Peclet Number, Bejan Number*

## 1. INTRODUCTION

Heat transfer by mixed convection in saturated porous media has attracted worldwide attention owing to its fundamental importance & wide range of applications. The overgrowing requirement for energy, the necessity to develop effective technologies for nuclear waste management, transpiration cooling, separation processes in chemical industries, building thermal insulations, winding structure for high-power density in electric machines, packed-bed catalytic reactors and numerous other applications have led to a considerable interest in convective heat transport through porous media.

A number of important analytical, numerical, and experimental results have been demonstrated in the books by Nield and Bejan [1], Ingham and Pop [2–4], Vafai [5,6], Pop and Ingham [7], Bejan and Kraus [8], Ingham et al. [9] and Bejan et al. [10], and the review articles by Hadim and Vafai [11], and Vafai and Hadim [12]. The technical issues of mixed convection flow in porous media have been concerned mainly with situations in which buoyancy effects are substantial, if not entirely dominant.

In this paper our attention has been focused on a problem of mixed convection. By providing an inlet and a square vent, forced convection condition can be imposed inside an enclosure filled with porous medium. The analysis is carried out keeping only the left wall isothermal, remaining walls are adiabatic. The interaction between the buoyancy stemming from one or more heated elements inside the enclosure and the imposed forced flow forms the topic of our investigation.

## 2. BASIC EQUATIONS

At first, fluid flow are considered to take place through an enclosure where left walls are isothermal at a temp $T_w$ (Fig.1)and all are adiabatic. There is an inlet at the left corner of the bottom wall and the vent is on the left corner of the top wall. The widths of the inlet and vent are I and O respectively as shown in Fig. 1, and in this study we have considered I/O=0.5. Buoyancy effects are induced due to the difference in temperature between the left vertical wall, $T_w$, and the through-stream temperature, $T_0$, which has a constant velocity, $V_0$, at the inlet of the enclosure. The inlet forced flow is fixed at the inlet and the temperature difference ($T_w - T_0$) considered here is positive which means it is an aiding flow.



**Fig. 1: Physical model and the coordinate system of the cavity**

To prepare mathematical model, the assumptions made for porous media are: the fluid and the porous medium are in local thermal equilibrium; the properties of the fluid and the porous media are constant; the viscous drag and inertia terms of the momentum equations are negligible, and the Darcy and Boussinesq approximations are valid. Under these assumptions, the conservation equation for mass becomes:

$$\frac{\partial u}{\partial x} + \frac{\partial v}{\partial y} = 0 \qquad \dots \quad \dots \quad \dots \quad \dots \quad \dots \quad \dots \quad \dots \quad \dots (1)$$

The momentum flow inside the enclosure can be modeled by the Darcy flow model [1], by using the assumptions. This constructs a relationship between the flow velocities at a certain direction to the pressure gradient in that direction in vector form is,

$$\mathbf{v} = \frac{K}{\mu}(-\mathbf{grad}\, p + \rho\, \mathbf{g}) \qquad \dots \quad \dots \quad \dots \quad \dots \quad \dots \qquad (2)$$

Where, $\mathbf{v}, K, \mu, p$, and $\mathbf{g}$ are the velocity vector, permeability, viscosity, pressure, and gravity vector, respectively. The permeability $K$ is an empirical constant which may define a length scale squared of pores. The Darcy flow model is applicable where the order of magnitude of the local pore Reynolds number, based on the local volume averaged speed ($|\mathbf{v}|^{1/2}$) and $K^{1/2}$ is smaller than 1. Taking **curl** on the both side of Eq. (2) with the assumption,

$\mathbf{v} = u\boldsymbol{i} + v\boldsymbol{j} + 0\mathbf{k}$ and $\mathbf{g} = 0\boldsymbol{i} + g_y\boldsymbol{j} + 0\boldsymbol{k}$,

we can get

$$\frac{\partial u}{\partial y} - \frac{\partial v}{\partial x} = -\frac{g\beta K}{\nu}\frac{\partial T}{\partial x} \qquad \ldots \quad \ldots \quad \ldots \quad \ldots \quad \ldots \quad \ldots \quad \ldots \qquad (3)$$

where $g = g_y$. Eq. (3) has no pressure term. Finally, the energy equation, according to Nield and Bejan [1], is

$$\sigma\frac{\partial T}{\partial t} + u\frac{\partial T}{\partial x} + v\frac{\partial T}{\partial y} = \alpha_m\left(\frac{\partial^2 T}{\partial x^2} + \frac{\partial^2 T}{\partial y^2}\right) \qquad \ldots \quad \ldots \quad \ldots \quad \ldots \quad \ldots \qquad (4)$$

Without any external or internal source, the equation of entropy generation according to Mahmud, S., and Fraser, is

$$S_{gen}''' = HTI + FFI = \frac{k}{T_0^2}\left[\left(\frac{\partial T}{\partial x}\right)^2 + \left(\frac{\partial T}{\partial y}\right)^2\right] + \frac{\mu}{KT_0}\left(u^2 + v^2\right) \ldots \quad \ldots \quad \ldots \quad .. \ (5)$$

where, $HTI = \frac{k}{T_0^2}\left[\left(\frac{\partial T}{\partial x}\right)^2 + \left(\frac{\partial T}{\partial y}\right)^2\right] \qquad \ldots \quad \ldots \quad \ldots \quad \ldots\ldots \quad .. \ (6)$

and $FFI = \frac{\mu}{T_0 K}\left(u^2 + v^2\right) \ldots\ldots \quad \ldots \quad \ldots \quad \ldots \quad \ldots \quad \ldots \quad \ldots \quad . \ (7)$

Finally, the equation of energy flux density vector according to Mahmud, S., and Fraser is

$$\mathbf{E} = E_x\mathbf{i} + E_y\mathbf{j} = \rho\mathbf{v}\left[\frac{1}{2}|v|^2 + C_P\,(T-T_0)\ \right] - k\,\mathbf{grad}(T)\ldots\ldots \quad \ldots \quad \ldots \quad \ldots \qquad .(8)$$

where $x, y$ are the Cartesian coordinates measured in the horizontal and vertical directions, $u, v$ are the velocity components along $x$- and $y$-axes, and $T$ is the fluid temperature, respectively,

We define the stream function, $\psi$, in the usual way as

$$u = \frac{\partial \psi}{\partial y} \qquad \ldots \quad \ldots\ldots \quad \ldots .. (9),\quad v = -\frac{\partial \psi}{\partial x} \quad \ldots \quad \ldots \quad \ldots \quad \ldots \qquad (10)$$

Substituting Eqs. (9) and (10) into Eqs. (3) and (4), the following equations are obtained:

$$\frac{\partial^2 \psi}{\partial x^2} + \frac{\partial^2 \psi}{\partial y^2} = -\frac{g\beta k}{\nu}\frac{\partial T}{\partial x} \qquad \ldots \quad \ldots \quad \ldots \quad \ldots \quad \ldots \quad \ldots \quad \ldots \qquad (11)$$

$$\frac{\partial T}{\partial t} + \frac{\partial \psi}{\partial y}\frac{\partial T}{\partial x} + \frac{\partial \psi}{\partial x}\frac{\partial T}{\partial y} = \alpha_m\left(\frac{\partial^2 T}{\partial x^2} + \frac{\partial^2 T}{\partial x^2}\right) \ldots \qquad \ldots \quad \ldots \quad \ldots \quad \ldots \qquad (12)$$

where Ra and Pe are the Rayleigh and Pe´clet numbers for a porous medium which are defined by

$$Ra = \frac{gK\beta(T_w - T_0)H}{\alpha_m\nu},\qquad Pe = \frac{V_0 H}{\alpha_m} \qquad \ldots \quad \ldots \quad \ldots \quad \ldots \quad \ldots \qquad (13)$$

## 2.1 Boundary Conditions

It is mentioned before that the temperature of the isothermal walls, $T_w$ is assumed to be 1K. The temperature of the flow passing through the inlet, $T_0$, is considered to be 0K above the freezing point of water. So, the boundary conditions of Eqs. (11) and (12) are

Boundary Condition for left wall being isothermal, all the walls are adiabatic.

Left isothermal wall:     $\psi = 0$,  $T = T_w = 1$ on $x = 0$, $0 \leq y \leq H$,     …     …     …14

It should be noticed that the vertical velocity component, $v$, is numerically equal to $V_0$ at the inlet. Hence the stream-function value at the inlet can be obtained by integrating $v$ from Eq. (10) with respect to $x$ between the limits 0 and I/W.
The assumption of outlet boundary condition is not easy. Convection is assumed to be dominant in the outflow through the vent. The conduction through the outlet will then be almost negligible. Hence the temperature gradient is assumed to be zero at the outlet.

## 2.2 Physical Quantities of Interest

The physical quantities of interest in this problem are the local Nusselt number, Local Entropy generation number, Bejan Number and Energy Flux Density. The local Nusselt Number along the isothermal wall is defined by

$$Nu_{x=0} = -\frac{H}{\Delta T}\left(\frac{\partial T}{\partial x}\right) \quad \dots \quad \dots \quad \dots \quad \dots \quad \dots \quad \dots \quad \dots \quad \dots \quad (15)$$

and the average Nusselt number along the hot wall is defined as

$$Nu_{av} = \frac{\int_0^H |Nu_{x=0}|\,dy}{\int_0^H dy} \quad \dots \quad \dots \quad \dots \quad \dots \quad \dots \quad \dots \quad \dots \quad (16)$$

The local Entropy Generation Number is defined by

$$Ns = \frac{S_{gen}'''}{S_0'''} = \left[\left(\frac{\partial T}{\partial x}\right)^2 + \left(\frac{\partial T}{\partial y}\right)^2\right] + \frac{Ec \times Pr}{\frac{\Delta T}{T_0}}\left[\left(\frac{\partial \psi}{\partial x}\right)^2 + \left(\frac{\partial \psi}{\partial y}\right)^2\right] = Ns_\tau + Ns_F \quad \dots \quad (17)$$

## 3. RESULTS AND DISCUSSION

When left wall is isothermal and remaining walls are adiabatic; Fig. 2 shows the isothermal lines for different Aspect Ratio, I/W=0.25, I/O=0.5 Ra=1 and Pe=0.1. The variation of isothermal lines with the change of aspect ratio is observed. It is evident from the figure that initially the isothermal lines are well spread towards right wall but gets confined near the left isothermal wall as   aspect ratio (AR=1.5) increases. Thus it can be concluded that the rate of change of temperature increases with increasing of aspect ratio & decreases with decreasing of aspect ratio. Again the isothermal lines cover most of area of the porous media as aspect ratio increases.

AR=0.5       AR=1       AR=1.5
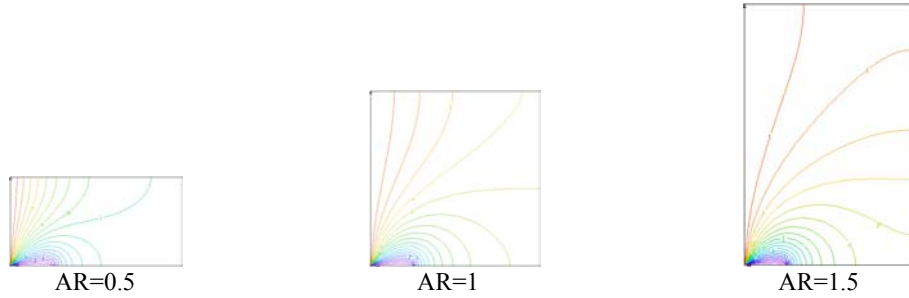
Wall condition: Left wall is Isothermal, remaining walls are adiabatic

**Fig. 2: Isothermal Line for I/W=0.25, I/O=0.5, Ra=1 and Pe=0.1**

Fig. 3 shows the streamlines for I/W=0.4, I/O=0.5, Ra=1 and Pe=0.1. The variation of streamline with the change of aspect ratio is observed when left wall is isothermal and remaining walls are adiabatic. The streamlines at the left wall are dense. As the aspect ratio increases, consequently density of streamlines at the right wall decreases. At low aspect ratio, the fluid flow continues with formation of vortices .The vortex size decreases as the aspect ratio increase and thus facilitates heat transfer & recovering of lost energy.



AR=0.5       AR=1       AR=1.5
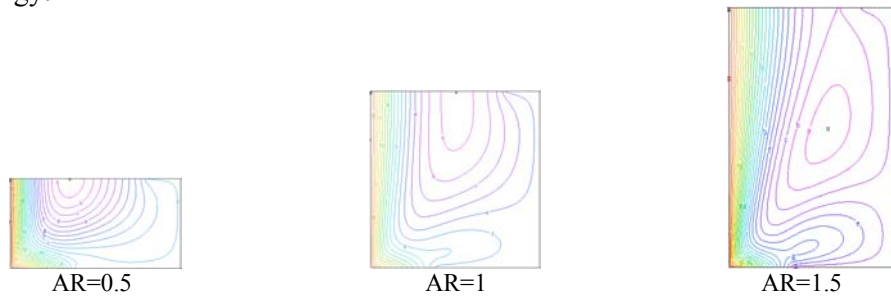
Wall condition: Left wall is Isothermal, remaining walls are adiabatic

**Fig. 3: Streamline for I/W=0.4, I/O=0.5, Ra=1 and Pe=0.1**

Observation on the constant Bejan Number line for different aspect ratio, I/W=0.5,I/O=0.5, Ra=1 and Pe=0.1 has been depicted in Fig. 4. Constant Bejan number does not show any significant change with variation of aspect ratio.



AR=0.5       AR=1       AR=1.5
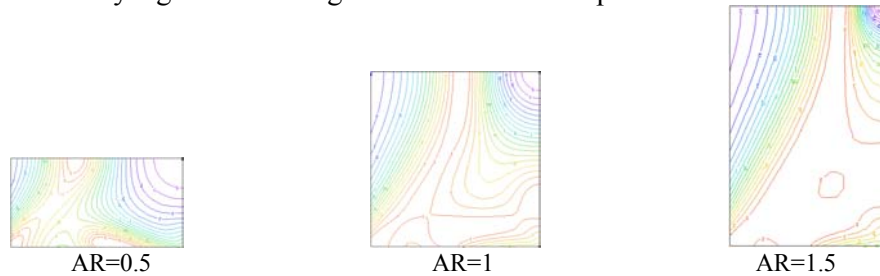
Wall condition: Left wall is Isothermal, remaining walls are adiabatic

**Fig. 4: Constant Bejan Number line for I/W=0.5, I/O=0.5, Ra=1 and Pe=0.1**

On the other hand , for different aspect ratio, I/O=0.5, different Rayleigh number and Peclet number, Average Entropy Generation Number $Ns_{av}$ increases with the increase of Aspect Ratio & moves towards a steady value. From Fig. 5 it is observed that the value of $Ns_{av}$ increases by 210% , 243.2% 200.6% ,212.28%, 141.936% ,74.6% , 58.55% for Pe= 0.1, 1, 5, 10, 20, 50, 100 respectively when aspect ratio increases from 0.5 to 2 for I/W=0.1, I/O=0.5, Ra=100.
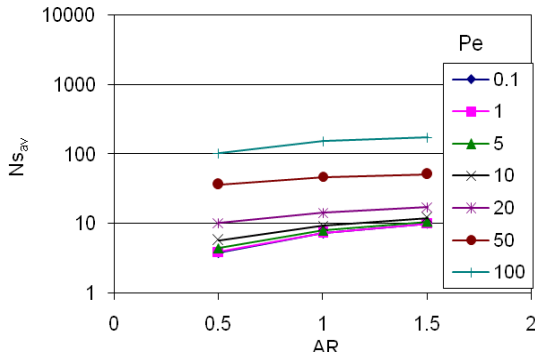


**Fig. 5: Variation of $Ns_{av}$ with Aspect Ratio (AR) for different Pe for I/W=0.1, I/O=0.5, Ra=100**
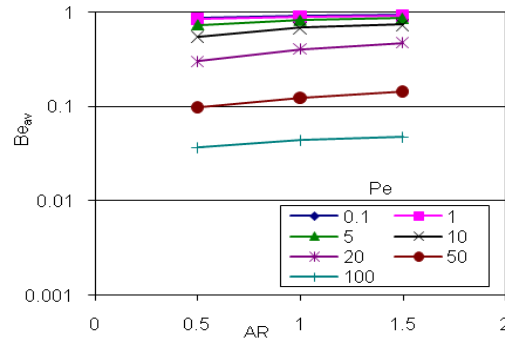
**Fig.6: Variation of $Be_{av}$ with Aspect Ratio (AR) for different Pe for I/W=0.1, I/O=0.5, Ra=50**

Fig. 6 shows the variation of Average Bejan Number with aspect ratio for different Pe. It is evident from this figure that $Be_{av}$ increases with the increase of aspect ratio. It is observed from Fig. 10(a) that the value of $Be_{av}$ increases by 4.03%, 3.75%, 7.4%, 15.58 %, 33.16%, 42.82%, 20.46% for Pe= 0.1, 1, 5, 10, 20, 50, 100 respectively when aspect ratio increases from 0.5 to 2 for I/W=0.1, I/O=0.5, Ra=50.

Fig. 7 demonstrates variation of Average Energy Flux Density with Aspect Ratio for different Pe. $E_{av}$ decreases significantly with the increase of aspect ratio. The decrease rate is higher at low aspect ratio but slows down at high AR. Referring to Fig. 11(a), value of $E_{av}$ decreases by 72.3%, 71.3% ,66.6%, 64.7%, 66.7%, 78.9%, 89.16% for Pe= 0.1, 1, 5, 10, 20, 50 and 100 respectively when aspect ratio increases from 0.5 to 2 for I/W=0.1, I/O=0.5, Ra=100.
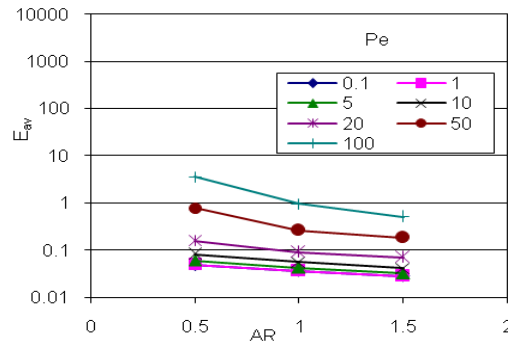


**Fig. 7: Variation of Eav with aspect ratio (AR) for different Pe for I/W= 0.1, I/O=0.5, Ra=50**

## 5. CONCLUSION

The present numerical study examined and explained two-dimensional, steady mixed convection flow in a porous square vented cavity for two different boundary conditions; all walls being adiabatic except left vertical wall is isothermal. The transformed equations of Darcy and energy in non-dimensional form have been solved numerically using the finite element method. Governing parameters chosen are Pe , Ra, I/W, AR which are varied in the range $0.1 \le Pe \le 100$ , $1 < Ra < 5000$, $0.1 \le$ I/W $\le 0.5$, $0.5 \le$ AR

646

$\leq 2$ .It is clear from the results that aspect ratio has considerable influence on the flow and heat transfer characteristics in the cavity. Isotherms, streamlines show substantial variation in their pattern or magnitude favoring convection for increasing values of aspect ratio whereas constant Bejan Number lines remain unaffected. Average Nusselt Number, average entropy generation number, average Bejan Number, average energy flux density either increases or decreases with changing AR. These fluctuations also vary for different Rayleigh or Peclet numbers.

# 6. ACKNOWLEDGEMENTS

# 7. REFERENCES

[1] D.A. Nield, A.Bejan, Convection in Porous Media, second ed., Springer, New York, 1999.
[2] D.B.Ingham,I.Pop (Eds.),Transport Phenomena in Porous Media, Pergamon, Oxford, 1998.
[3] D.B.Ingham,I.Pop (Eds.),Transport Phenomena in Porous Media, Pergamon, Oxford, 2002.
[4] D.B. Ingham, I.Pop (Eds.), Transport Phenomena in Porous Media, Elsevier, Oxford, 2005.
[5] K. Vafai (Ed.), Handbook of Porous Media, Marcel Dekker, NewYork, 2000.
[6] K.Vafai (Ed.), Handbook of Porous Media, second ed.,Taylor & Francis,New York, 2005.
[7] I. Pop, D.B. Ingham, Convective Heat Transfer: Mathematical and Computational Modeling of Viscous Fluid Porous Media, Pergamon, Oxford, 2001.
[8] A. Bejan,A.D. Kraus (Eds.), Heat Transfer Handbook, Wiley, New York, 2003.
[9] D.B. Ingham, A. Bejan, E. Mamut, I. Pop (Eds.), Emerging Technologies and Techniques in Porous Media, Kluwer, Dordrecht, 2004.
[10] A. Bejan, I. Dincer, S. Lorente, A.F. Miguel, A.H. Reis, Porous and Complex Flow Structures in Modern Technologies, Springer, New York, 2004.
[11] H. Hadim, K. Vafai, Overview of current computational studies ofheat transfer in porous media and their applications—forcedconvection and multiphase heat transfer, in: W.J. Minkowycz, E.M.Sparrow (Eds.), Advances in Numerical Heat Transfer, vol. II, Taylorand Francis, New York, 2000, pp. 291–329.
[12] K. Vafai, H. Hadim, Overview of current computational studies ofheat transfer in porous media and their applications-natural and mixed convection, in: W.J. Minkowycz, E.M. Sparrow (Eds.),Advances in Numerical Heat Transfer, vol. II, Taylor and Francis, NewYork, 2000, pp. 331–369.

# MODELLING AND SIMULATION OF PARTICLE TRAJECTORY INSIDE AN ELECTROSTATIC PRECIPITATOR

Shah M E Haque[1], M G Rasul[2] and M M K Khan[2]

[1]Process Engineering & Light Metals (PELM) Centre
Faculty of Sciences, Engineering and Health
Central Queensland University, Gladstone, QLD 4680, AUSTRALIA

[2]College of Engineering and the Built Environment
Faculty of Sciences, Engineering and Health
Central Queensland University, Rockhampton, QLD 4702, AUSTRALIA

E-mail: s.haque@cqu.edu.au

## ABSTRACT

*This paper presents a Computational Fluid Dynamics (CFD) model for particle trajectory inside a wire-plate electrostatic precipitator (ESP). The turbulent gas flow and the particle motion under electrostatic forces were modelled using CFD code 'FLUENT'. Reynolds-averaged Navier-Stokes equations were solved numerically for predicting the gas flow. The turbulence was modelled using the realizable k-ε turbulence model. The effect of electric field had been captured by adding a source term in the momentum equation. This additional source term was obtained by solving a coupled system of the electric field and charge transport equations. The particle phase was simulated by using Discrete Phase Model (DPM). The results of the simulation showed that particle trajectory depends on the size of the particle diameter. The larger the diameter, the more efficient was the particle collection due to the higher particle charging. This study gives an insight into the particle dynamics and its collection inside any industrial ESP.*

**Keywords:** *Electrostatic precipitator, Modelling and simulation, Particle trajectory.*

## 1. INTRODUCTION

Electrostatic precipitators (ESP) are the most common, effective and reliable particulate control devices. The performance of an ESP can be optimized by simulating the flow field and particle trajectories inside the ESP. The ESP of the local power plant consists of a series of parallel collection electrodes (CE), spaced 400 mm apart, oriented along the direction of the flue gas flow. A number of thin discharge electrodes (DE) are suspended vertically between these plates. The precipitation process involves charging particles of the flue gas by applying high negative voltage to the discharge electrodes and driving the charged particles towards the grounded CE by the electric field produced. The collected particles are then removed from the collection electrodes by rapping process. The negligible change of the electric field in the vertical direction justifies a two-dimensional approach of this study.

There is limited research found in the literature on ESP simulation. Most researches simplified their model by creating a single wire ESP configuration (e.g. Lami *et al.* [1], Zhao *et al.* [2], Park and Kim [3], Anagnostopoulos and Bergeles [4]). An ESP model developed by Suda et al [5] consists of seven wires to analyse the gas flow field. But they considered only single wire segment for their ionic wind analysis. Single wire model may not be capable of

capturing the wake of the wires properly and it can not be assumed that the particle motions will be repeated in the gas flow direction. Hence three wires have been taken into consideration for the development of a representative numerical model of ESP. It is noted that only a limited research [6 - 8] is found in the literature where three wires have been considered for modelling an ESP channel.

The present study attempts to provide a more realistic prediction of gas, ion and particle dynamics inside an ESP channel using a CFD model. The gas flow inside the ESP has been modelled by using the two-dimensional Navier–Stokes equations. Lagrangian approach has been adopted to calculate the trajectory of particles with different diameters.

## 2.  GEOMETRY CONFIGURATION

Two collection electrodes and three discharge electrodes was considered for creating the geometry of an ESP channel. Discharge electrodes were placed in between these two collection electrodes. Due to the symmetry of the geometry only half of a channel was modelled in this study. The configuration and the dimensions of the ESP are shown in Fig. 1. The Fluent Inc. geometry and mesh generation software "GAMBIT" was used as a pre-processor for geometry development and fluid domain discretization purposes. The computational mesh consists of 15000 cells and is shown in Fig. 2. It also shows the boundary conditions that were used in this study for solving the problem.
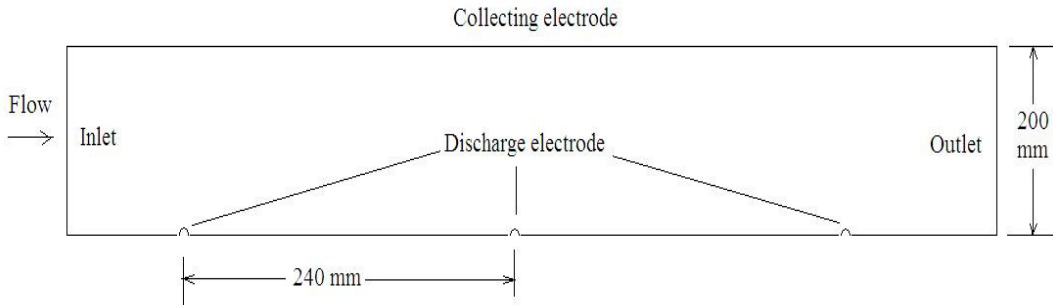


Fig. 1 2D geometry configuration
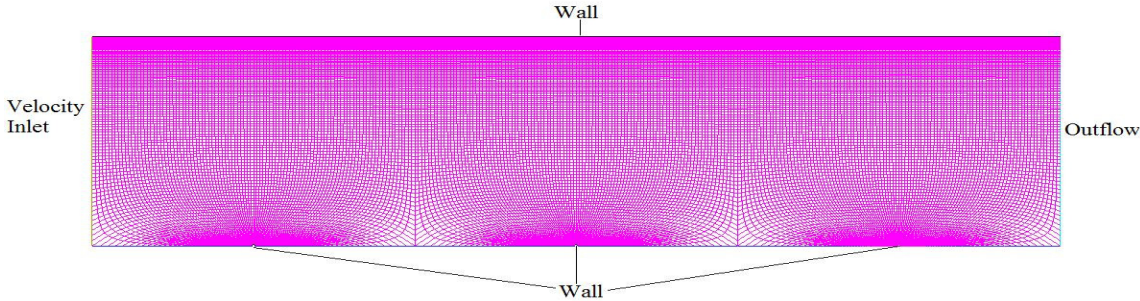


Fig. 2 Computational mesh

## 3.  NUMERICAL APPROACH

Numerical calculations for the gas flow were carried out by solving the Reynolds-averaged Navier-Stokes equations. An additional source term was added to the gas flow equation to introduce the electric field inside the ESP channel. The particle phase was simulated by using Discrete Phase Model (DPM).

### 3.1 Gas Dynamics

The air inside the ESP is treated as incompressible Newtonian fluid due to the small pressure drop across the ESP. The flow can be described by the Conservation of mass equation [9]

$$\frac{\partial \rho}{\partial t} + \vec{\nabla} \cdot (\rho \vec{V}) = 0 \tag{1}$$

and the Momentum equation known as Navier-Stokes equation [9]

$$\frac{\partial \vec{V}}{\partial t} + \vec{V}.\vec{\nabla}\vec{V} = -\frac{\vec{\nabla}p}{\rho} + v\vec{\nabla}^2\vec{V} + S \tag{2}$$

Where $\rho$ is the fluid density (kg/m³), $v$ is the kinemetic viscosity (m²/s) of the fluid, $p$ is the fluid pressure (Pa) and $\vec{V}$ is the fluid velocity (m/s). $S$ is the source term, which expresses the momentum force (N/m²) on the gas flow due to the electric field and can be expressed as [6]

$$S = \rho_{ion}\vec{E} \tag{3}$$

Here $\rho_{ion}$ is the ion charge density (C/m³) and $\vec{E}$ is the electric field intensity (V/m).

The realizable $k-\varepsilon$ model is used in this study to capture the turbulent behaviour of flow inside the ESP.

### 3.2 Electrostatic Field

A high voltage was applied to the DE to generate the electrostatic field between the DE and the grounded CE. The electric field intensity $\vec{E}$ inside the ESP can be described by the Gauss's law equation [10]

$$\nabla.\vec{E} = \frac{\rho_{ion}}{\varepsilon_0} \tag{4}$$

where $$\vec{E} = -\nabla\phi \tag{5}$$

Combining Equations (3) and (4) gives the well known Poisson equation which is defined as

$$\nabla^2\phi = -\frac{\rho_{ion}}{\varepsilon_0} \tag{6}$$

where $\vec{E}$ is the electric field intensity (V/m), $\phi$ is the electric potential (Volt) and $\varepsilon_0$ is the permittivity of the free space.  Under stationary conditions, the electrical flux density is divergence-free and can be written as [11]

$$\nabla.\vec{J} = 0 \tag{7}$$

where $\vec{J}$ is the density of ionic current.

Assuming ion diffusion is of negligible importance compared to conduction [1, 11]), $\vec{J}$ can be expressed as

$$\vec{J} = \rho_{ion}b_{ion}\vec{E} \tag{8}$$

where $b_{ion}$ is the ion mobility.

Combining Equation (7) and (8) gives the following expression

$$\nabla.(\rho_{ion} b_{ion} \nabla \phi) = 0 \tag{9}$$

With the boundary conditions of Table 1 and an appropriate solution method, two transport variables $\phi$ and $\rho_{ion}$ can be numerically calculated.

## 3.3 Particle Dynamics

The trajectory of the particles was predicted by **FLUENT** after integrating the force balance on the particles, which was expressed in a Lagrangian reference frame. This force balance equates the particle inertia with the forces acting on the particle, and can be written as [12])

$$\frac{d\vec{u}_{p,i}}{dt} = F_D(\vec{u}_i - \vec{u}_{p,i}) + \frac{g_i(\rho_p - \rho)}{\rho_p} + \vec{F}_i \tag{10}$$

Where,

$$\frac{dx_i}{dt} = u \quad ; \quad i = x, y \tag{11}$$

Where $\rho_p$ and $u_{p,i}$ denote particle density and velocity respectively. $\vec{F}_i$ corresponds to external forces exerted on the particle that, in the present study, are the electrostatic forces:

$$\vec{F}_i = \frac{\vec{E}_i q_p}{m_p} \tag{12}$$

Where $\vec{E}_i$ is the electric field intensities (V/m), $q_p$ and $m_p$ denote the electric charge (C) and mass (kg) of the particle respectively.

$F_D(\vec{u}_i - \vec{u}_{p,i})$ is the drag force per unit particle mass, where

$$F_D = \frac{3\mu C_D \operatorname{Re}}{4\rho_p d_p^2} \tag{13}$$

Here, $\vec{u}_i$ is the fluid phase velocity (m/s), $\mu$ is the molecular viscosity of the fluid (N.m/s), $\rho$ is the fluid density (kg/m$^3$) and $u_{p,i}, d_p$ and $\rho_p$ denote the velocity (m/s), diameter (m) and density (kg/m$^3$) of the particle respectively. Re is the relative Reynolds number, which is defined as

$$\operatorname{Re} \equiv \frac{\rho d_p |\vec{u}_{p,i} - \vec{u}_i|}{\mu} \tag{14}$$

The drag coefficient $C_D$ can be calculated from the following equation [13]:

$$C_D = \frac{24}{\operatorname{Re}}(1 + b_1 \operatorname{Re}^{b_2}) + \frac{b_3 \operatorname{Re}}{b_4 + \operatorname{Re}} \tag{15}$$

Where

$$b_1 = \exp(2.3288 - 6.4581\phi + 2.4486\phi^2)$$
$$b_2 = 0.0964 + 0.5565\phi$$
$$b_3 = \exp(4.905 - 13.8944\phi + 18.4222\phi^2 - 10.2599\phi^3)$$
$$b_4 = \exp(1.4681 + 12.2584\phi - 20.7322\phi^2 + 15.8855\phi^3)$$

$$\tag{16}$$

The shape factor, $\phi$, is defined as

$$\phi = \frac{s}{S} \tag{17}$$

Where $s$ is the surface area of a sphere having the same volume as the particle, and $S$ is the actual surface area of the particle. The Reynolds number Re is computed with the diameter of a sphere having the same volume.

## 3.4 Particle Charge

The charge, $q_p$, which is acquired by a spherical dielectric particle with radius $r_p$ and relative permittivity $\varepsilon_r$ exposed to an ion flux in a field E can be calculated in the Lagrangian framework by the following Pauthenier equation [14, 15]):

$$q_p = [1 + 2(\frac{\varepsilon_r - 1}{\varepsilon_r + 1})]4\pi r_p^2 \varepsilon_0 |\vec{E}| \frac{t}{(t + \tau)} \tag{18}$$

Where $\varepsilon_r$ is the relative permittivity of the gas, $t$ is the resident time of the particle and $\tau$ is the charging time constant which can be defined by the following expression

$$\tau = \frac{4E}{J} \tag{19}$$

## 4. SIMULATION PROCEDURE

The geometry developed by GAMBIT was exported to FLUENT solver to specify the flow properties, solve the problems and analyse the results. The finite volume methods were used to discretise the partial differential equations of the model using the SIMPLEC method for pressure–velocity coupling and the second order upwind scheme to interpolate the variables on the surface of the control volume. The segregated solution algorithm was selected to solve the governing equations sequentially. Non-equilibrium wall functions were applied to bridge the viscosity-affected region between the wall and the fully-turbulent region.

The electric potential on the collection plates was zero whereas at the discharge electrode surface the value is 70 (kV). The charge density $\rho_0$ at the discharge electrode can be approximately calculated by [15]:

$$\rho_0 = -\frac{\varepsilon(E - E_0)}{ds} \tag{20}$$

where $E$ is the field strength in the cell adjacent to the emitting electrode, $ds$ is the distance between the cell and the electrode surface. The corona onset field $E_0$ along the corona-emitting surface is assumed constant, and it can be obtained according to Peek's law [16]:

$$E_o = E_{Peek} = 3.1X10^6 \delta(C_1 + C_2/\sqrt{\delta r}) \tag{21}$$

where $E_{Peek}$ is the ion current threshold value for an electrode of radius $r$ and $C_1 = 1$ V/m and $C_2 = .031$ V/√m in air of relative density $\delta$ with respect to the normal temperature and pressure conditions.

A number of subroutines have been written and compiled by using User-Defined-Functions (UDF) compatible with FLUENT. The UDFs are then linked to the standard fluid model to solve the Poisson's equation and the charge density equation.

The operating gas was ambient air while the particles were assumed to be ash with density equal to 600 kg/m$^3$. Two sets of particle with the size of 1 (mm) and 1 (μm) have been selected for this study. All particles were injected from the inlet surface with 0.245 kg/s mass

flow rate. Turbulent intensity at the inlet was 5%. Boundary conditions used to solve this problem are summarised in Table 1. The numerical prediction of the model was validated with the result of Choi and Fletcher [6] and was reported elsewhere [17].

Table 1. Boundary conditions applied to the ESP model

| | Gas dynamics | Electric potential | Ion charge density | Particle dynamics |
|---|---|---|---|---|
| Velocity Inlet | $u_x = 1.0 m/s$ <br><br> $u_y = 0.0 m/s$ | $\nabla \phi = 0$ | $\nabla \rho_{ion}$ $= 0$ | $u_{p_x} = 1.0 m/s \; u_{p_y} = 0.0 m/s$ <br><br> Escape |
| Outflow | Mass conservation | $\nabla \phi = 0$ | $\nabla \rho_{ion}$ $= 0$ | Escape |
| Wall-Collecting electrode | No slip | $\phi = 0$ | $\nabla \rho_{ion}$ $= 0$ | Trap |
| Wall-Discharge electrode | No slip | $\phi = 70 kV$ | Peek law | Reflect |

## 5. RESULTS AND DISCUSSION

A velocity contour of the gas field is shown in Fig. 3. A boundary layer, which starts along the collection electrode, was found to suppress the flow separation that occurs after the discharge electrode.  Fig. 4 shows the contours of the electric potential where the potential field forms an elliptical region around the discharge wires. Fig. 5 shows the contours of ion charge density where an initial value of $10^{-7}$ C/m$^3$ is used on the surface of the discharge electrode [15]. 50 particles were injected from the inlet surface to follow their trajectory inside the ESP channel. Fig. 6 shows the trajectory of the particles with 1 (mm) of diameter where particles were found to deviate from their straight path towards the collecting plates as they approached to the wires. The trajectory of the particles with 1 (μm) of diameter is shown in Fig. 7, where almost no deviation of the straight path was observed. It is evident from Fig. 6 and Fig. 7 that the trajectory of the particle depends on its size. The large particle acquires more charge than the small one due to its larger surface area. Highly charged particle was then moved towards the collection electrode for deposition.
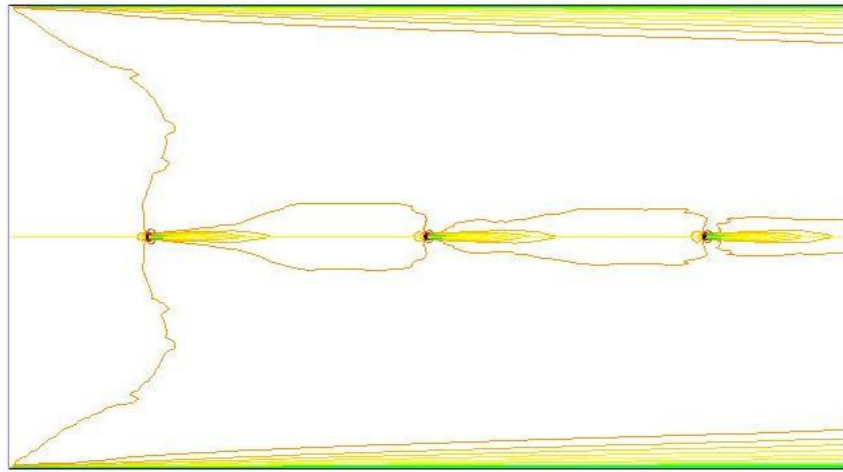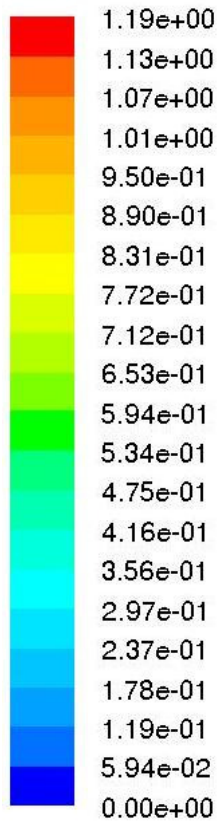
Fig. 3 Contours of gas velocity magnitude (m/s)
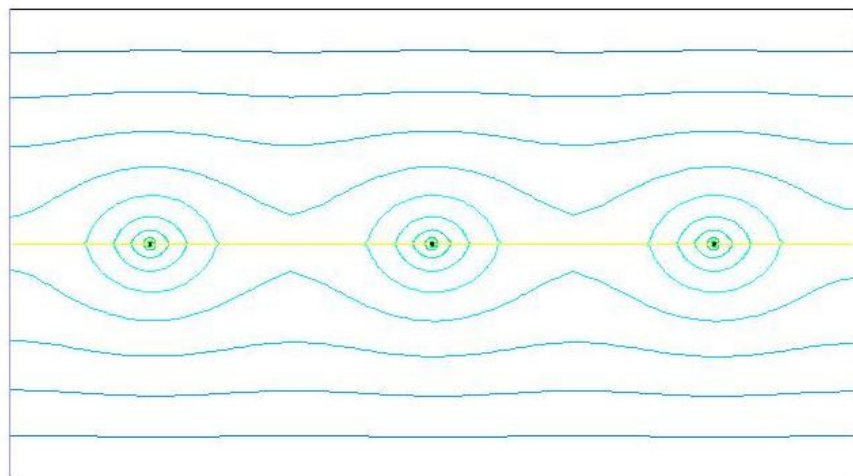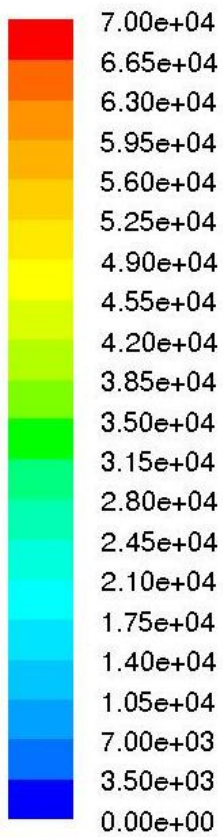


Fig. 4 Contours of electric potential (Volt)
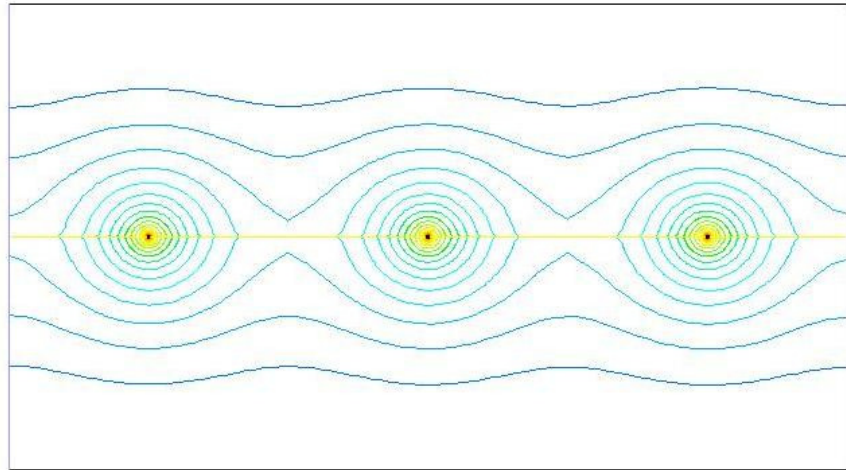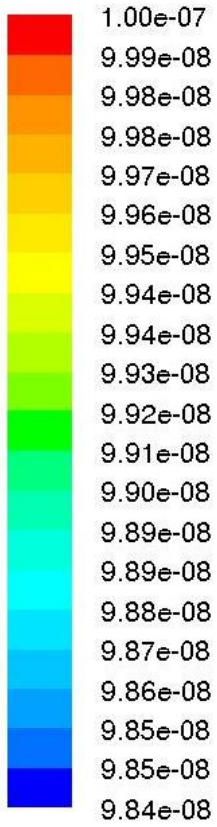
Fig. 5 Contours of ion charge density (C/m$^3$)
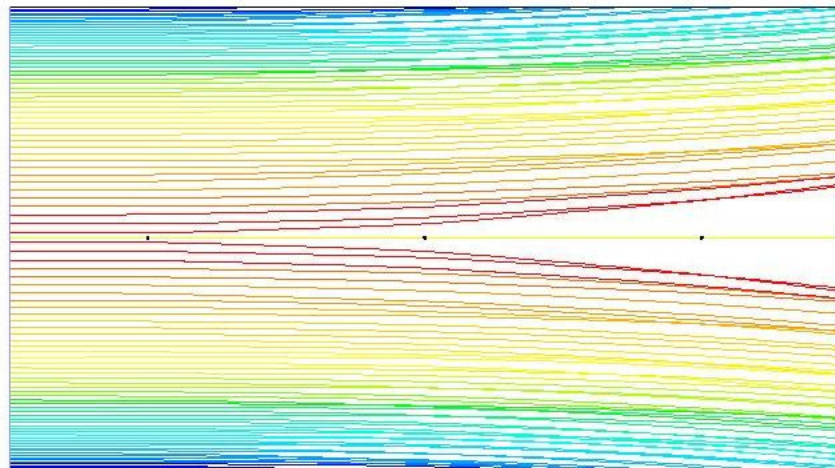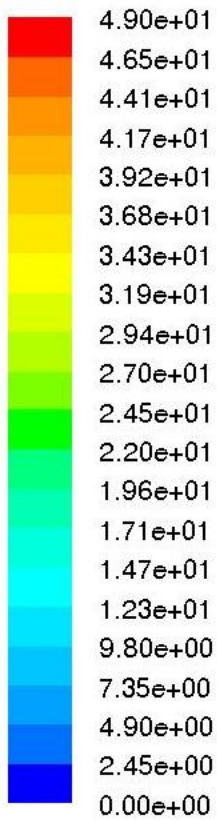


Fig. 6 Trajectory of the particles with 1 (mm) of diameter
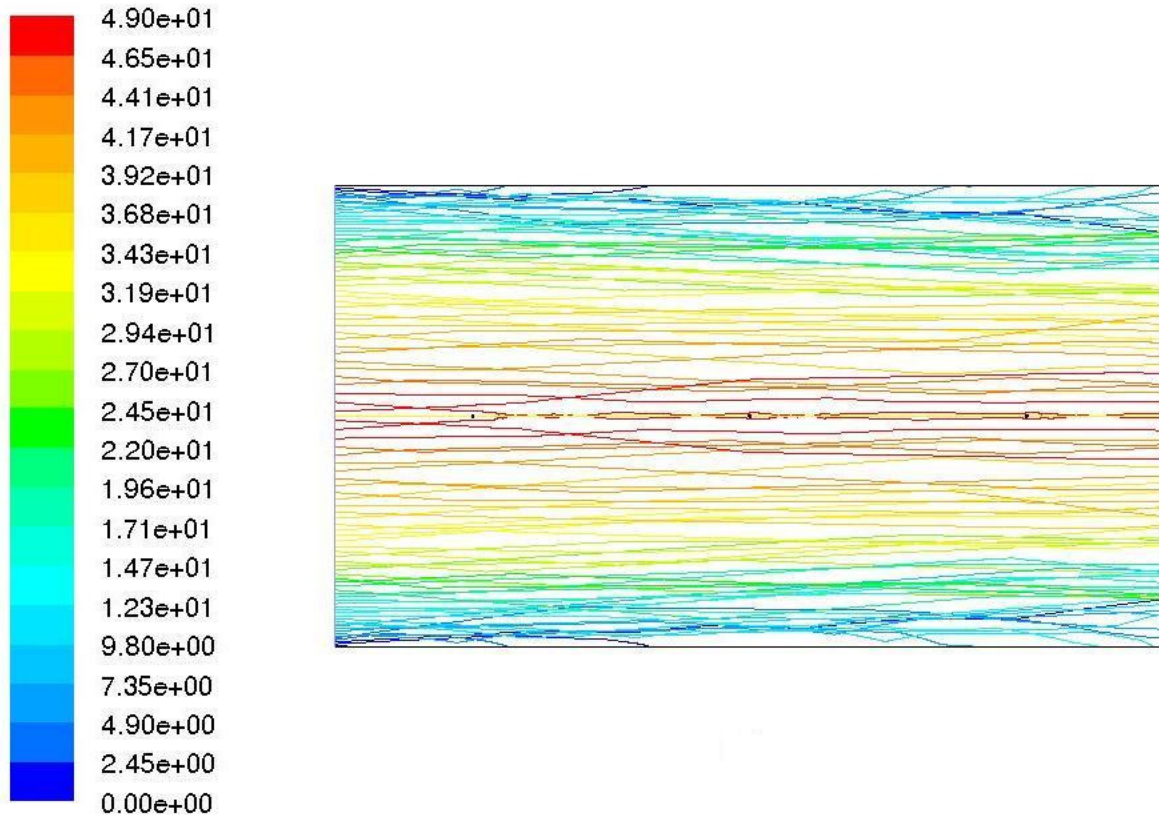
Fig. 7 Trajectory of the particles with 1 (μm) of diameter

## 6. CONCLUDING REMARKS

A two dimensional numerical model for an ESP was presented which considers electrostatic force as an additional force to the standard fluid model. The electrostatic field was solved through writing and compiling a number of subroutines using User-Defined Functions (UDF) of FLUENT. The DPM model was used to simulate the trajectory of particles with different diameters. The study revealed that the particle collection and its movement depend on the size of the particle. Small particles were found difficult to capture as most of them escaped from the collection chamber, whereas significant number of large particles were trapped on the collection wall of this model. This was due to the higher particle charging of the large particles which force them towards the collection electrode for deposition. The larger the diameter of the particle, the higher was the charge and the more efficient was the particle collection. The computational procedure and the model developed can be applied to any geometrical and electrical configuration in identifying options for improving performance of the industrial electrostatic precipitator.

## REFERENCES

[1]   E. Lami, F. Mattachini, I. Gallimberti, R. Turri, and U. Tromboni, A numerical procedure for computing the voltage-current characteristics in electrostatic precipitator configurations, *Journal of Electrostatics*, Vol. 34, pp. 385-399, 1995.
[2]   L. Zhao, E. Dela. Cruz, K. Adamiak, A. A. Berezin, J.S. Chang. A numerical model of a wire-plate electrostatic precipitator under electrohydrodynamic flow conditions, *The 10th International conference on electrostatic precipitator*, Australia. 2006.

[3] Seok. Joo Park & Sang. Soo. Kim, Effects of electrohydrodynamic flow and turbulent diffusion on collection efficiency of an electrostatic precipitator with cavity walls, *Aerosol Science and Technology*, Vol. 37, pp. 574-586, 2003.

[4] J. Anagnostopoulos & J. Bergeles, Corona discharge simulation in wire-duct electrostatic precipitator, *Journal of Electrostatics*, Vol. 54, pp. 129-147, 2002.

[5] Suda, J. M., Ivancsy, T., Kiss, I. and Berta, I., Complex analysis of ionic wind in ESP modeling, *The 10th International conference on electrostatic precipitator*, Australia. 2006.

[6] B. S. Choi, and C. A. J. Fletcher, Turbulent particle dispersion in an electrostatic precipitator, *Applied mathematical modeling*, Vol. 22, pp. 1009-1021, 1998.

[7] K.S.P. Nikas, A.A. Varonos and G.C. Bergeles, Numerical simulation of the flow and the collection mechanisms inside a laboratory scale electrostatic precipitator, *Journal of electrostatics*, Vol. 63, pp. 423-443, 2005

[8] Walter. Egli, Ulrich. Kogelschatz, Edgar. A. Gerteisen, and Ralf. Gruber, 3D computation of corona, ion induced secondary flows and particle motion in technical ESP configurations, *Journal of electrostatic*, Vol. 40&41, pp. 425-430, 1997.

[9] B.R. Munson, D.F. Young, T.H. Okiishi, Fundamentals of fluid mechanics, 4th ed., John Wiley & Sons Inc., NY, 2002.

[10] Gregory A. Kallio and David E. Stock, Computation of electrical conditions inside wire-duct electrostatic precipitators using a combined finite-element, finite-difference technique, *Journal of Applied Physics*, Vol. 59 (6), pp. 1799-1806, 1986.

[11] Marc. Poppner, Rainer. Sonnenschin and Jorg. Meyer, Electric fields coupled with ion space charge. Part 2: computation, *Journal of electrostatics*, Vol. 63, pp. 781-787, 2005.

[12] Fluent Inc. Fluent 6.2 User's Guide, 2005.

[13] A. Haider and O. Levenspiel, Drag coefficient and terminal velocity of spherical and nonspherical particles. *Powder Technology*, Vol. 58, pp. 63-70,1989

[14] C.U. Bottner and M. Sommerfeld , Euler/Lagrange calculations of particle motion in turbulent flow coupled with an electric field. *Proceedings of ECCOMAS Computational Fluid Dynamics Conference,* 2001.

[15] Q. Ye, and J. Domnick, On the simulation of space charge in electrostatic powder coating with a corona spray gun, *Powder technology*, Vol. 135-136, pp. 250-260, 2003

[16] F.W. Peek, Determination Phenomena in High Voltage Engineering, McGraw-Hill, New York, 52-80, 1929.

[17] Shah. M. E. Haque, M. G. Rasul, M. M. K. Khan, A. V. Deev, and N.Subaschandar, A Numerical Model of an Electrostatic Precipitator , *16th Australasian Fluid Mechanics Conference*, Crown Plaza, Gold Coast, Australia, 2-7 December, 2007

# NUMERICAL SIMULATION OF THE TRANSIENT FLOW IN A ROCKET PROPULSION NOZZLE USING AUSMDV SCHEME

Suryakant Nagdewe, H. D. Kim and T. Setoguchi[*]

School of Mechanical Engineering, Andong National University,
388 Songchun-dong, Andong Gyeonbuk 760-749 Korea
[*]Department of Mechanical Engineering, Saga University,
1 Honjomachi, Saga-Shi, 849-8502, Japan
Email: surya@anuis.andong.ac.kr

## ABSTRACT

*Highly over-expanded nozzle of the rocket engines are excited by non-axial forces due to flow separation at sea level operations. Since rocket engines are designed to produce axial thrust to power the vehicle, non-axial static and/or dynamic forces are not desirable. Several engine failures were attributed to the side loads. Present work investigates the unsteady flow in an over-expanded rocket nozzle in order to estimate side load during a shutdown/starting. A numerical computation has been carried out with density based solver on multi-block structured grid. Present solver is explicit in time and unsteady time step is calculated using dual time step approach. AUSMDV is considered as a numerical scheme for the flux calculations to capture complex flow phenomena. One equation Spalart-Allmaras turbulence model is selected. Results presented here is for nozzle pressure ratio i.e. 100 to 2. At 100 NPR, restricted shock separation (RSS) pattern is observed while, 2 NPR shows free shock separation (FSS) pattern. Side load is observed during the transition of separation pattern at different NPR.*

**Key words:** *Free Shock Separation, Restricted Shock Separation, AUSMDV, Nozzle flow.*

## 1. INTRODUCTION

The demand for efficient performance of rocket launchers necessitates the development of nozzles with higher performance by increasing the expansion ratio. However, this may lead to flow separation, asymmetric forces and side-loads, which may cause life-limiting constraints on both the nozzle itself and other engine components [1]. These large side load, which generate in rocket nozzle during startup and shutdown transients cause not only serious trouble at launch but also destroy the engine hardware. In order to avoid the destructive side-load, much work have been done experimentally and numerically to clarify the origin of the side load generation.

Frey and Hagemann [2] conducted numerical computations of flows in a conical nozzle and a nozzle proposed by Rao. They have studied the separation position of the flow in nozzle and the parameters affecting the separation point. Onifri et al. [3] has numerically investigated the flow separation in the nozzle with over-expansion condition. Their results show two flow patterns called FSS (Free Shock Separation) and RSS (Restricted Shock Separation) as shown in Fig. 1 and Fig. 2. FSS is a normal type of the separation pattern and the separated free jet does not reattach to nozzle wall. In FSS, incoming flow separates due to adverse pressure gradient and after the separation an oblique shock wave and a recalculating flow region are observed. FSS can be observed in various types of nozzles such as conical contour nozzles used for solid rocket boosters and bell type nozzles including TP (Truncated Perfect), CTP (Compressed Truncated Perfect) and TO (Thrust Optimized) nozzles. RSS is a peculiar type of the separation pattern and has been observed only in TO nozzle and CTP nozzles [4]. In RSS condition, internal shock wave and Mach disc, which are generated in the nozzle, interact each other and induce shock wave/boundary layer interaction. An incoming boundary layer separates and reattaches. Also a recirculation flow region is formed between separation point and reattachment point. Shock waves cause local high temperature regions as a cause of the heat load around the reattachment point. This heat load

reduces the life of the components. The pressure increase in the separated region of RSS is much higher than that of FSS and sometimes much higher than the ambient pressure [5].

Many researches had been conducted to reveal the mechanism of the generation of the significant lateral force. However, the detailed flow structure and flow mechanism have not been understood sufficiently to enhance the reliability of rocket engines. Present study numerically investigates the unsteady lateral side forces on the nozzle wall.
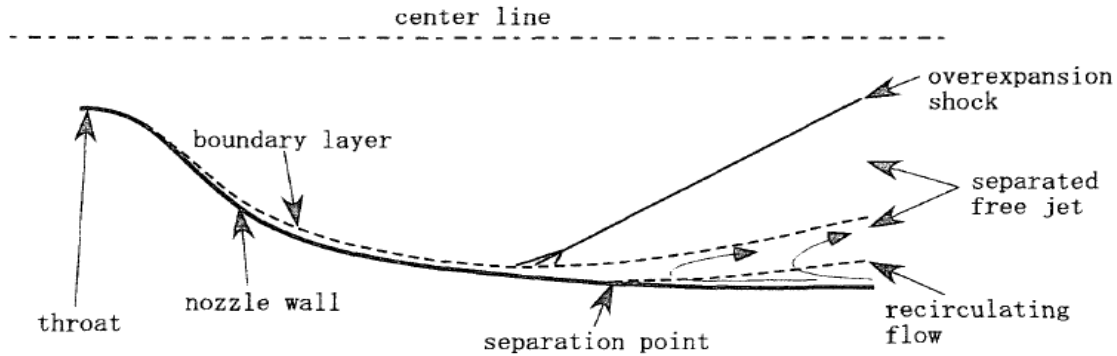


**Fig. 1 Flow pattern of FSS (Free Shock Separation)**
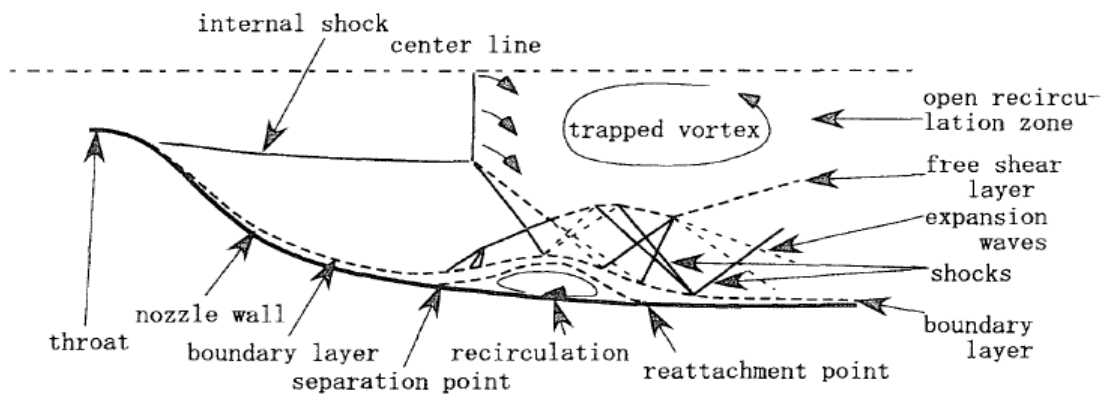


**Fig. 2 Flow pattern of RSS (Restricted Shock Separation)**

## 2. NUMERICAL MODELING

Present solver is a three dimensional finite volume code written for structured multi-block meshes. This code can be configured as Euler, Laminar and Reynolds Averaged Navier Stokes (RANS) solver for solving 2D, axisymmetric or three dimensional problems. The code uses explicit time marching scheme and calculates numerical fluxes using AUSMDV scheme. Second order accuracy is achieved by calculating variables reconstructed by using MUSCL (Monotonic Upwind Scheme for Conservation Laws) approach and limiting fluxes by min-mod limiter. The code is capable of supporting a number of boundary conditions including adiabatic and isothermal walls. Second order central difference scheme is used for viscous term. Viscous coefficient and thermal conductivity is calculated by Sutherland's formula. The time step is calculated using the CFL (Courant-Friedrichs-Lewy) number. Dual time stepping is used for marching the time.

The computational grid used in present study is shown in Fig. 3. A configuration of a Compressed Truncated Perfect Nozzle [4] is selected as shown in Fig. 3. The computational grid consists of 298 points in the axial direction (230 points inside the nozzle) and 101 points in radial direction. Non-slip boundary condition is assumed on the nozzle wall. The total pressure and total temperature are assumed at the inlet of nozzle and static pressure at the external exit of nozzle.
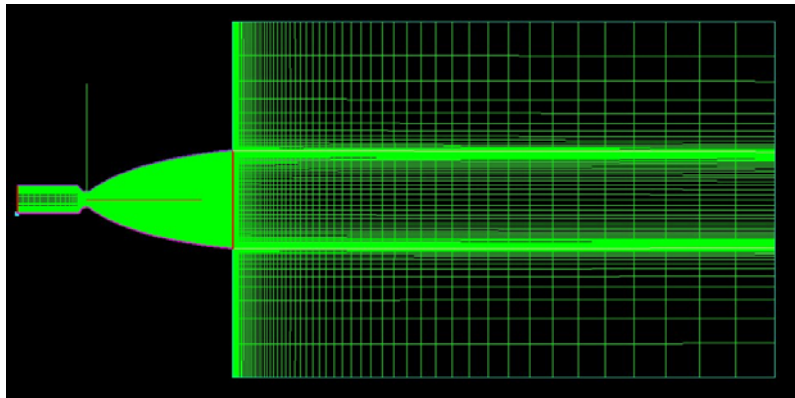
**Fig. 3 Computational domain**

## 3. RESULTS AND DISCUSSION

Computational domain was set to a pressure of 1 atm, a temperature of 290K and a velocity of zero as a initial condition. At inlet, 100 times the atmospheric pressure was set. Static pressure of 1 atm was given as back pressure and varied to 5 times to atm pressure. Pressure at the inlet is decrease from 100 NPR to 2 for the shutdown and 2 to 100 NPR for starting process.

Fig. 4 (a) show Mach contour plot for NPR 2. This shows the RSS separation pattern as explained in introduction. All the nozzle flow physics is captured. Fig. 4 (i) shows the Mach number plot for NPR of 100. At the NPR of 100, the separation pattern is FSS and the separated jet is symmetric. The incoming flow separates due to adverse pressure gradient and after the separation an oblique shock wave and recirculation flow region is observed. Mach color plots for NPR 60, 80 and 100 are shown in Fig. 4 (g), (h) and (i).
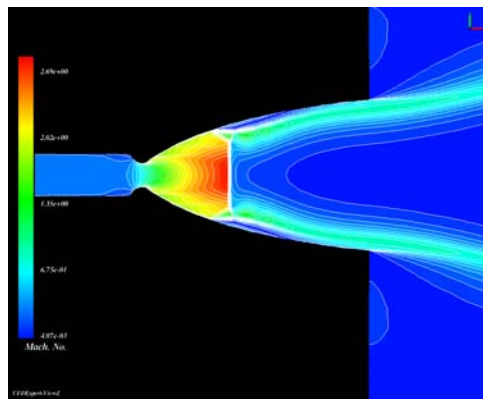


**(a) NPR 2**
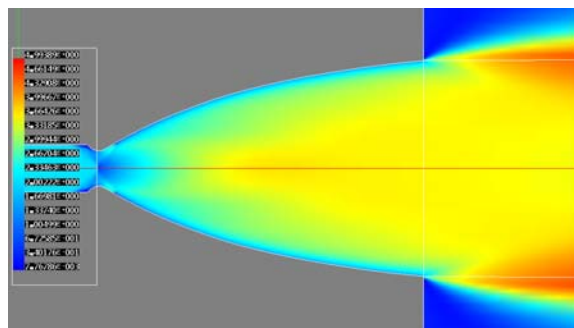


**(b) NPR 10**
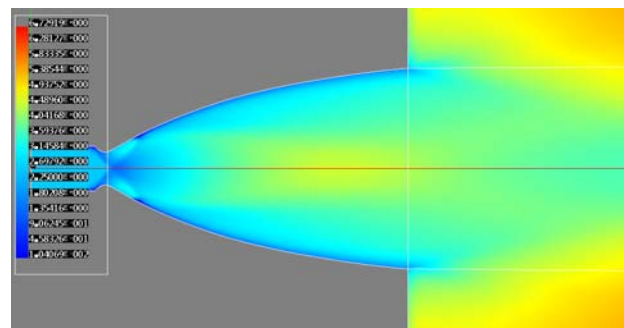


**(c) NPR 20**

660
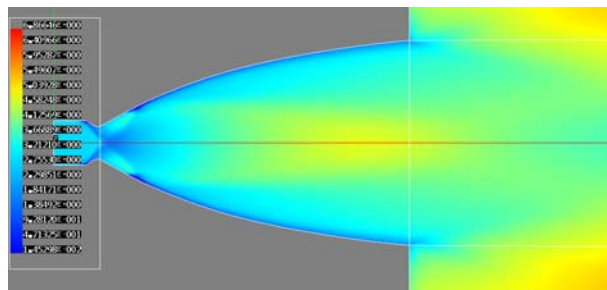
**(d) NPR 30**
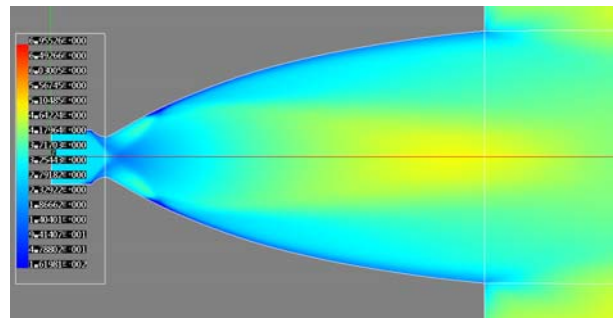


**(e) NPR 40**
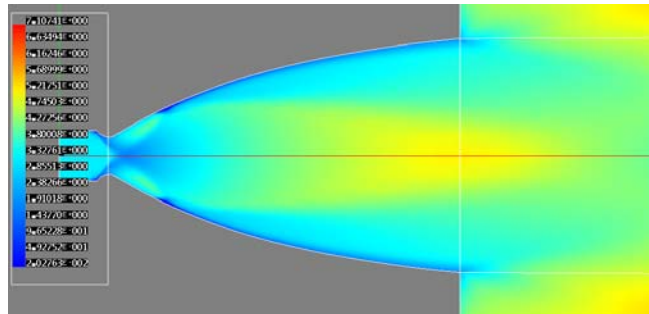


**(f) NPR 50**
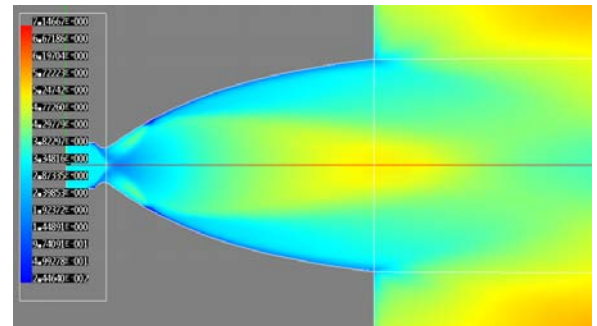


**(g) NPR 60**
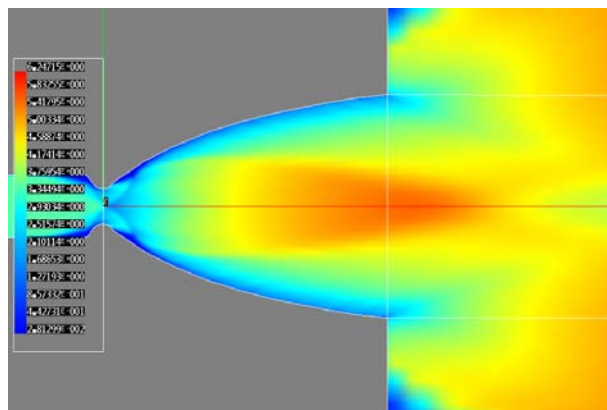


**(h) NPR 80**
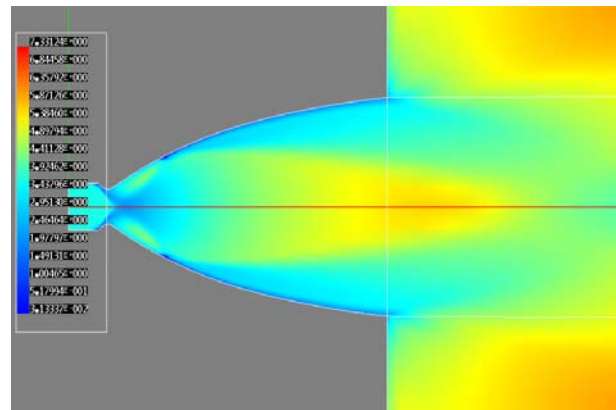


**(i) NPR 100**

**Fig. 4 Mach number color plot for nozzle pressure ratios (2 to 100 NPR)**

Mach color plot for the NPR 10 to 50 are shown in Fig. 4 (b) to (f) respectively. Results shows increase in Mach number for every increment in NPR. Cumulative force (upward) on nozzle wall at different nozzle pressure ratios is shown in Fig. 5. Lateral force on nozzle wall increases as NPR increases. The magnitude of force in y-direction is found to be more than the x-direction (axial). Fig. 5 shows the rise in magnitude of side force on the nozzle wall in very small time. This large side force on nozzle wall has destroyed the engine hardware during launching operation.
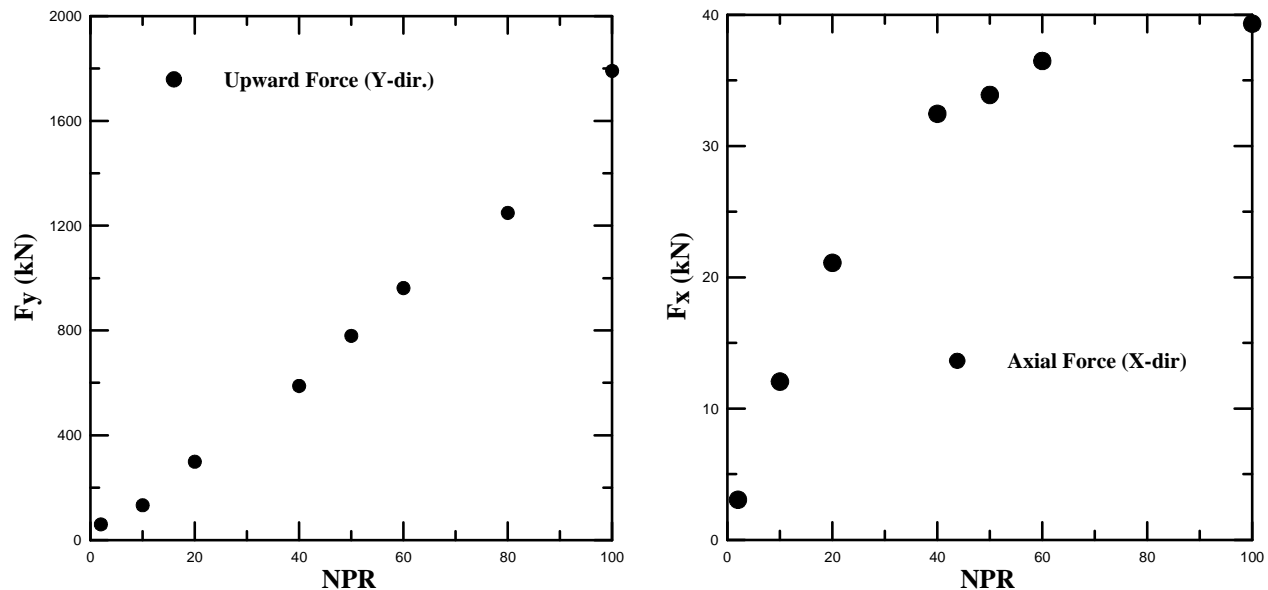
**Fig. 5 Cumulative force on nozzle wall at different nozzle pressure ratios.**

## 4.  CONCLUSIONS

Rocket engines are designed to produce axial thrust to power the vehicle. Several engine failures were attributed to non-axial static and/or dynamic forces (side load). Present work investigates the unsteady flow in an over-expanded rocket nozzle during a shutdown/starting process. The aim of present study is to investigate the lateral side load during the nozzle shutdown or starting condition using computation methodology. The present numerical computations have been carried out with density based solver on multi-block structured grid. Present study considers nozzle pressure ratio i.e. 100 to 2. At 100 NPR, restricted shock separation (RSS) pattern is observed while, 2 NPR shows free shock separation (FSS) pattern. Side load is observed during the transition of separation pattern at different NPR.

## 5.  REFERENCES

[1] Ostlund, J., Flow Processes in Rocket Engine Nozzles with Focus on Flow Separation and Side Loads, PhD Thesis, 2002.
[2] Frey, M., Hagemann, G., Restricted Shock Separation in Rocket Engines, *Journal of Propulsion and Power*, 16 (2000), 4, pp. 478-484.
[3] Onofri, M., Nasuti, F., The Physical Origins of Side Loads in Rocket Nozzles, AIAA 99-2587, 1999.
[4] Yonezawa, K., Morimoto, T., Tsujimoto, Y., Watanabe, Y., Yokota, K., A study of an Asymmetric Flow in an Overexpanded Rocket Nozzle, *Journal of Fluid Science and Technology*, 2 (2007), 2, pp. 400-409.
[5] Sugimoto K., Aso, S., A Study on Unsteady Flow Characteristic and Lateral Force of Conventional Bell-type Nozzle, Memoirs of the faculty of Engineering, Kyushu University, 63 (2003), 2.

# FORCES ON A FREELY FLOATING SHIP WHILE OTHER SHIP PASSING NEARBY

**Islam  M. Rafiqul, Omar Yaakob & Adi Maimun**

**Faculty of Mechanical Engineering**
**University Technology Malaysia**
**Johor, Malaysia**
**e-mail: rafiqulis@fkm.utm.my**

## ABSTRACT

*When a vessel travels nears a freely floating body, it generates waves along the length of the vessel. The pressure rises at the bow and stern and drops along the midsection. These pressure gradients, in turn, generate a set of waves that propagate out from the vessel bow and another generally lower set of waves that propagate out from the vessel stern. The pressure distribution along the hull of a vessel significantly causes lateral forces and horizontal moments to act on the vessel when it passes another vessel in close proximity to other structure. Also the scattered waves from the incoming incident waves cause additional forces on the freely floating or moored vessel in offshore areas. These forces and moments depend on hull sizes, vessel speeds, incident wave directions, lateral separations; and water depths. In this paper, mathematical model is derived considering the dynamic interaction between two vessels using linear wave theory. The mathematical model is then numerically solved by 3D source distribution technique. A general overview and findings of some numerically computed hydrodynamic forces / moments of a ship moving to close proximity of a freely floating body is presented in this paper.*

*KEYWORDS: Wave exciting forces /moments, Linear Wave Theory, 3D source distribution technique, Velocity Potential, Green function*

## 1. INTRODUCTION

Nowadays there are growing public concern on passing effects on a freely floating or moored vessel especially in the offshore area. Ships floating freely are subjected to hydrodynamic forces due to other ships passing nearby. Such forces may induce high forces and unacceptable motions and if it is moored ship then it hinder the loading and unloading operations or cause damage to the hull and mooring systems. Due to generated waves of the passing ships, the moored vessel experiences a motion which may affect the mooring line forces and may damage the hull of the ship and in extreme condition; mooring lines of ships may damaged. Very few research works were carried out on the effect of passing vessel on a freely floating or moored vessel. Some of the researches were carried out where the interaction effect is partially accounted i.e. the presence of the free floating ship does not affect the passing ship. Some of the works were carried out on vessel interaction without speed effect.

The interactions of forces and moments between three ships meeting simultaneously in confined waters were numerically studied by Varyani et al. [1] using discrete vortex distribution method. In addition, the hazards involved in the variation of certain parameters while navigating in crowded waterways were studied. Chen and Fang [2] studied the problems between two moving ships in waves using Three-dimensional potential-flow theory based on the source distribution technique. The numerical solution was compared with experimental results and strip theory. Pinkster and Naaijen [3] studied the effects of passing ships taking free surface effects into account for both of slow and fast moving ships. In case of large and slow moving ships, free surface effects are due to the surrounding harbor geometry. In case of fast moving ships, free surface effects are due to the wash waves generated by the passing ship that propagate into the harbor creating more or less complicated incoming wave system for the moored ship.

The effect of passing vessels on moored vessels and the vessels that are in the process of mooring at quay were studied by Pinkster et al [4]. The effects were studied by using a mathematical model (DELPASS) that used a double body method to describe the effects of passing vessel. Time dependent fluid potential was transformed to frequency domain and it was solved by means of 3D-diffraction method for multiple bodies. But the emphasis was given on soliton waves for restricted water. Islam et al. [5] carried out research on hydrodynamic interaction of two vessels with forward speed. In their work, the authors used linear wave theory and by applying the 3D source distribution technique. The present work is the extension of previous work and is applicable for finite depth and open water and in frequency domain only.

## 2. MATHEMATICAL MODELING

The individual ship is treated as a rigid body having six degrees of freedoms. The ship is subjected to hydrodynamic forces due to incident waves and radiated and diffracted waves due to other ship(s). Two right hand coordinate systems are defined in Figure 1. One is fixed to the space and other one is fixed to the bodies.
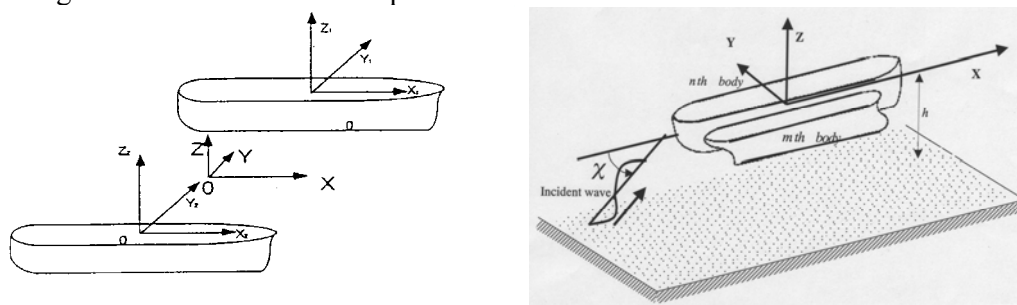


Fig. 1: Definition of multi-body co-ordinate system

The fluid is assumed to be incompressible, inviscid and irrotational and the vessel is assumed to be freely floating in open water. Then there exists a velocity potential satisfying Laplace equation together with boundary conditions on the free surface, on the body, and at the bottom, and the radiation condition in the far field. The time dependence of the fluid motion to be considered here is restricted to simple

harmonic motion and accordingly the flow filed can be characterized by the following velocity potential:

$$\Phi(x, y, z, t) = -\overline{U}x + \phi_s + \phi \quad \dots\dots\dots\dots\dots\dots\dots\dots\dots \quad (1)$$

where, $\phi_s$ = steady velocity potential due to mean forward speed of the ship

and $\phi = \phi_0 e^{-i\omega_e t} + \phi_7^m e^{-i\omega_e t} + \sum_{n=1}^{N}\sum_{j=1}^{6} -i\omega_e X_j^m \phi_j^m \quad \dots\dots\dots\dots \quad (2)$

$\phi_0$ =incident wave potential, $\phi_7^m$ =diffraction wave potential on body

$\phi_j^m$ = potential due to motion of the body in j-th mode , $X_j^m$ = motion amplitude of the body in j-th mode, $\omega_e$ = encountering frequency and is defined as:

$$\omega_e = \omega - \frac{\omega^2 \overline{U}}{g}\cos\chi$$

$\omega$= circular frequency of incident wave

The incident wave potential is defined as follows:

$$\phi_0 = \frac{-ig\zeta_a}{\omega}\frac{\cosh[k(z+h)]}{\cosh kh}e^{ik(x\cos\chi + y\sin\chi)} \quad \dots\dots \quad (3)$$

where, $\zeta_a$ = incident wave amplitude, $\chi$ = wave heading angle from X -axis

The differential equation governing the fluid motion follows from the application of the continuity equation which yields the Laplace equation. The individual potentials are the solutions of the following Laplace equation:

$$\nabla^2\phi = 0 \quad \dots\dots\dots\dots\dots\dots\dots\dots\dots\dots\dots\dots \quad (4)$$

**2.1 Boundary condition**

On the mean wetted surface area of each body S, the above linear velocity potentials must satisfy the Laplace equation and also the following boundary conditions:

-The steady motion potential:

$$\overline{W}.n = 0 \text{ on S} \quad \dots\dots\dots\dots\dots\dots\dots\dots\dots\dots\dots\dots.(5)$$

where $\overline{W}.n = \overline{U}\nabla(\phi - x)$ and $\overline{U}\phi = \phi_s$

-linearised free surface condition:

$$[(i\omega_e - U\frac{\partial}{\partial x})^2 + g\frac{\partial}{\partial z}]\phi = 0 \text{ at } z = 0 \quad \dots\dots\dots\dots\dots\dots\dots \quad (6)$$

-boundary condition on the sea floor :

$$\frac{\partial\phi}{\partial z} = 0 \quad \text{on } z = -h \quad \dots\dots\dots\dots\dots\dots\dots\dots\dots\dots.(7)$$

-and the boundary conditions on the wetted surface of the floating bodies. Due to linearization, this boundary condition may be applied on the wetted surface of the floating bodies in their equilibrium position

$$\frac{\partial\phi_0}{\partial n} + \frac{\partial\phi_7^m}{\partial n} = 0 \quad \text{on } S^i \text{ and } i = 1...N \quad \dots\dots\dots\dots\dots\dots.(8)$$

$$\frac{\partial\phi_j^m}{\partial n} = -i\omega_e n_j^m + \overline{U}M_j^m \quad \text{on } S^m \quad \dots\dots\dots\dots\dots\dots\dots\dots.(9)$$

$$\frac{\partial \phi_j^m}{\partial n} = 0 \quad , \qquad \text{on} \qquad S^i \ {\scriptstyle (i \neq m)}.$$

………………………………………………..(10)

In which $n_j^m$ is the direction cosine on the surface of the body '$m$' in the j-th mode of motion and has the following form :

$n_1^m = \cos(n^m, x^m)$, $n_2^m = \cos(n^m, y^m)$, $n_3^m = \cos(n^m, z^m)$,

$n_5^m = (z^m - z_G^m)n_1^m - (x^m - x_G^m)n_3^m$, $n_6^m = (x^m - x_G^m)n_2^m - (y^m - y_G^m)n_1^m$,

And $M_1^m = M_2^m = M_3^m = M_4^m = 0$ , $M_5^m = n_3^m, M_6^m = -n_2^m$

where $x_G^m, y_G^m$ and $z_G^m$ are the co-ordinate of the centre of gravity of the body '$m$' and $x^m$, $y^m$, $z^m$ are the investigating point on the wetted surface of the body '$m$'.

-The radiation condition of the potentials $\phi_j^m$, in which in polar co-ordinate:

$$\lim_{r \to \infty}(r^{\frac{1}{2}}(\frac{\partial \phi}{\partial r} - i(\frac{\omega^2}{g})\phi)) = 0, \qquad …………………………….. \quad (11)$$

## 2.2 Velocity Potentials

However, there is no analytical solution for $\phi_7^m$ and $\phi_j^m$, so the problem should be solved numerically. According to the 3-D source sink method, the potentials $\phi_7^m$ and $\phi_j^m$ can be expressed in terms of well known Green functions that can be expressed by the following equation [6].

$$\phi_j^m(x,y,z) = \frac{1}{4\pi}\sum_{n=1}^{N}\iint_s \sigma_j^m(\xi,\eta,\zeta)G(x,y,z;\xi,\eta,\zeta)ds \qquad …………………………….(12)$$

where, $(\xi,\eta,\zeta)$ denotes a point on surface $S$ and $\sigma(\xi,\eta,\zeta)$ denotes the unknown source distribution. The integral is to be carried out over complete immersed surface of the object. The Green function $G$ (source potential) must in order of the representation in equation (12) to be valid, satisfy all the boundary conditions of the problem with the exception of the body boundary conditions and have a source like behaviour. As a result, boundary conditions are reduced only to on wetted surfaces of the bodies. So, the wetted surfaces should be subdivided into panels to transform integral equations to a system of algebraic equations to determine unknown source density over each panel. The appropriate Green function used in this paper to the boundary value problem posed is given by Wehausen and Laitone [7]. After getting the source density, the velocity potentials on each panel can be obtained using the equation (12).

## 2.3 Forces and Moments

Once the velocity potential is obtained , the hydrodynamic pressure at any point on the body can be obtained from the linearized Bernoulli's equation and can be written as:

$$\frac{\partial \Phi}{\partial t} + \frac{1}{2}(\nabla \Phi)^2 + \frac{P}{\rho} + gz = 0 \qquad …………………………….... (13)$$

Now after putting the value of $\Phi$ in the equation (13), the following expression is obtained,

$$-\frac{P}{\rho} = -i\omega_e\phi + \frac{1}{2}\left\{\nabla(-\overline{U}x + \phi_s)\right\}^2 + \nabla(-\overline{U}x + \phi_s).\nabla\phi + \frac{1}{2}(\nabla\phi)^2 + gz \ldots\ldots\ldots.(14)$$

By neglecting the higher order terms, we can write

$$P = \rho\left(\frac{\overline{U}}{2}\frac{\partial\phi_S}{\partial x} - gz\right) + \rho\left(i\omega_e\phi + \overline{U}\frac{\partial\phi}{\partial x}\right) \qquad\ldots\ldots\ldots\ldots.(15)$$

As first part of equation (15) is associated with the hydrostatic and steady forces, so neglecting this part, the first order wave exciting forces or moments and oscillatory forces and moments caused by the dynamic fluid pressure acting on the body can be obtained from the following integrals:

$$F_k^m.e^{-i\omega_e t} = -i\rho\omega_e e^{-i\omega_e t}\int_s\left\{\phi_0 + \phi_7^m - i\frac{\overline{U}}{\omega_e}\left(\frac{\partial\phi_0}{\partial x} + \frac{\partial\phi_7^m}{\partial x}\right)\right\}.n_k^m ds \quad\ldots\ldots(16)$$

$$F_{kj}^m.e^{i\omega_e t} = -\rho e^{-i\omega_e t}\int_s\left\{\omega_e^2\overline{X}_j\phi_j^m - i\omega_e\overline{X}_j\overline{U}\frac{\partial\phi_j^m}{\partial x}\right\}.n_k^m.ds \qquad\ldots\ldots\ldots(17)$$

where,

$F_k^m$ denotes the k-th component of wave exciting forces or moments, $F_{kj}^m$ denotes the k-th component of force arising from the j-th component of motion of the body 'm'. Moreover, it is customary to decompose the hydrodynamic forces resulting from motion of the bodies into components in phase with the acceleration and velocity of the rigid body motions. These yield the added mass and damping coefficients respectively. These coefficients can be expressed from equation as:

$$a_{kj}^{mn} = -\rho.\text{Re}\left[\int_s(\phi_j^m + \frac{\overline{U}}{\omega_e}\frac{\partial\phi_j^m}{\partial x}).n_k^m.ds\right], \qquad\ldots\ldots\ldots\ldots (18)$$

$$b_{kj}^{mn} = -\rho\omega_e.\text{Im}\left[\int_s(\phi_j^m + \frac{\overline{U}}{\omega_e}\frac{\partial\phi_j^m}{\partial x}).n_k^m.ds\right] \qquad\ldots\ldots\ldots\ldots\ldots\ldots(19)$$

## 2.4 Non-dimensionalization

The forces and moments are non-dimensionalized as follows:

Surge: $F_1' = \dfrac{F_1}{\frac{1}{2}\rho g\zeta_a BL}$, Sway: $F_2' = \dfrac{F_2}{\frac{1}{2}\rho g\zeta_a BL}$, Heave: $F_3' = \dfrac{F_3}{\frac{1}{2}\rho g\zeta_a BL}$

Roll: $M_4' = \dfrac{M_2}{\frac{1}{4}\rho g\zeta_a B^2 L}$, Pitch: $M_2' = \dfrac{M_2}{\frac{1}{4}\rho g\zeta_a BL^2}$, Yaw: $M_2' = \dfrac{M_2}{\frac{1}{4}\rho g\zeta_a BL^2}$

## 3. VALIDATION

On the basis of the model outlined above, a computer program has been developed. The computation model is expected to be validated by the model tests. But since the tests have not been carried out yet, the results obtained from computation has been compared with published results; in this case the works of Cheng and Fang [2]. The particulars of the two ships of similar lengths (Table 1) are taken from Cheng and Fang [2]. The first is a Mariner ship designated Ship A, while the second is a Series 60 ship, designated Ship B. the The computation of wave forces /moments of Ship A plying in close proximity of Ship B running in the same direction and speed has been carried out for $F_n = 0.14$. Figure 2 shows a comparison of non dimensional heave forces on Ship A between those given by the current computation program and

those taken from Cheng and Fang [2]. It indicates that the two results are similar in trend. However, the actual values differ and this is may be due to use of different Green function. In their work, Cheng and Fang [2] used zero speed Green function, whereas in the present work green function is computed with speed dependent green function.

Table 1 Principal Particulars of the Ships

| Ship | Mariner ship (Ship A) | Series 60 ship (Ship B) |
|---|---|---|
| Block coefficient | 0.61 | 0.60 |
| LBP (m) | 121.951 | 121.951 |
| B (m) | 17.422 | 16.260 |
| T (m) | 6.859 | 6.504 |
| Displacement Ton | 9065.00 | 7926.19 |
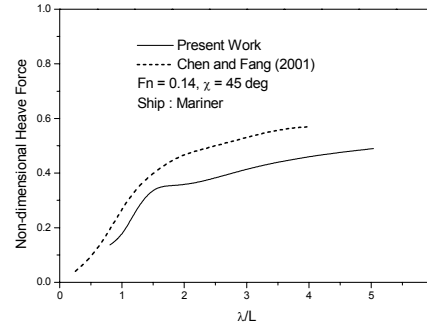


Fig. 2 Comparison of heave force

## 4. RESULTS AND DISCUSSIONS

To examine the effects of passing ship for the wave exciting forces and moments on freely floating ship, computations have been carried out for the pair of ships mentioned above (Table 1) at an angle 45 degree and in a depth of 500 m. Ship A is assumed freely floating ($U = 0$) and Ship B has a forward speed ($F_n = 0.14$). The lateral separation distance (centre line to centre line) is 32.476 m. The non dimensional forces and moments of Ship A are plotted against wave circular frequency in the Figure 3 to 8. In the figures, results for single body means Ship A floating freely on its own and double body means Ship A floating freely in the presence of Ship B which is passing nearby. Fig. 3 shows that, the interaction leads to Ship A experiencing an increase surge forces in the frequency range of 0.5 to 0.9. On the other hand, sway force (Figure 4) on Ship A decreases because the incident waves are obstructed by Ship B as it is in the weather side. The diffraction effect has an adverse effect on heave as seen in Figure 5. The coupling with sway leads to a reduced roll moment (Figure 6). In Figure 7, it is seen that pitch moment increases as it is coupled with heave. Yaw moment increases due to interaction at low frequency region, especially at the frequency ranging from 0.45 to 0.9. The results shown in Figures 3 to 8 indicate that there is significant effect of passing vessel on heave force, pitching moment and yaw moments of the stationary ship. These forces and moments cause excessive motion in the respective mode that increases unacceptable motions and if it is moored ship then it will hinder the loading and unloading operations or cause damage to the mooring systems.
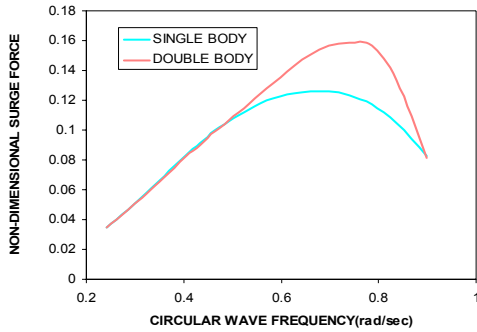
Fig. 3 Non dimensional surge force on freely floating ship
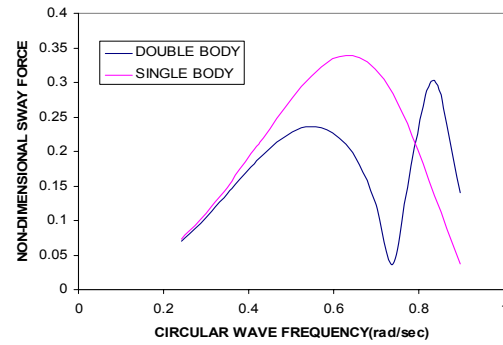

Fig. 4 Non dimensional sway force Freely floating ship
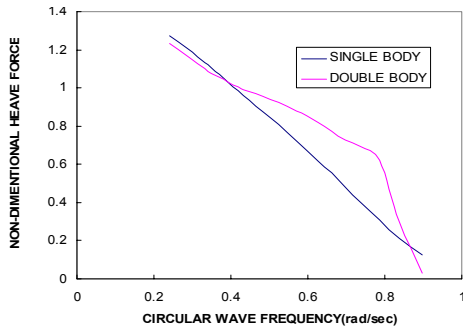

Fig. 5 Non dimensional heave force on freely floating ship
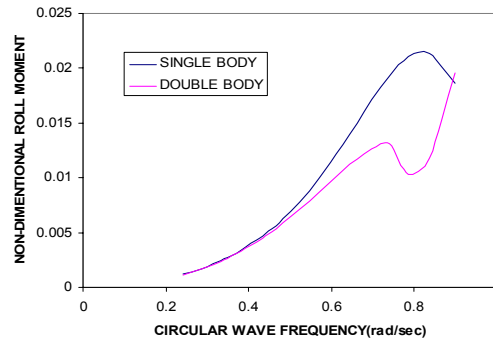

Fig. 6 Non dimensional roll moment on freely floating ship
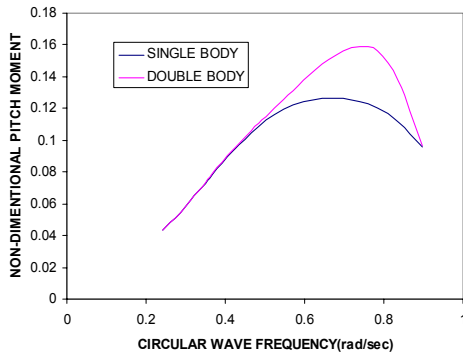

Fig. 7 Non dimensional pitch moment on freely floating ship
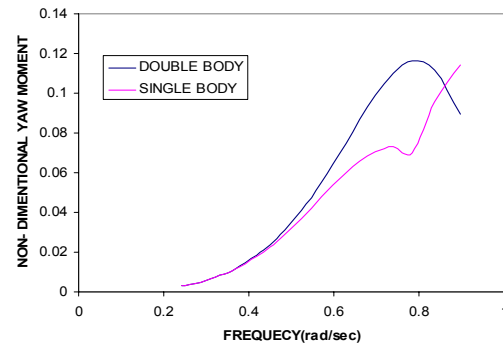

Fig. 8 Non dimensional yaw moment on freely floating ship

## 5. CONCLUDING REMARKS

A method for and results of computational hydrodynamics studies of interaction between two ships have been presented. Preliminary results indicate that the effects of interaction on a freely floating body when another ship passing nearby is quite significant. For such interaction, heave, pitch and yaw moment have significant influence which may hinder loading and unloading operation because of excessive motion in the respective mode. In this paper, the model is validated only with published results with speed but the model need to be validated by model experiment which is next step. Also computations need to be carried out for several separation distances, various depths and different incident angles. However, the program

669

developed for computation of interaction forces and moments for a freely floating ship while other ships passing nearby numerically expected to be able to predict satisfactorily.

## ACKNOWLEDGEMENTS

## References

[1]    K. S. Varyani, R. McGregor  and P. Wold, Interactive forces and moments between several ships meeting in confined waters, *Control Engineering Practice*, Vol. 6, 1998, pp. 635-642.

[2]    Gung-Rong Chen and Ming-Chung Fang, Hydrodynamic interactions between two ships advancing in waves, Ocean Engineering, Vol. 28, 2001, pp. 1053-1078.

[3]    J. A. Pinkster and P. Naaijen, Predicting the effect of passing ships, *International Workshop on water Waves and Floating Bodies*, 2003.

[4]    J. A. Pinkster and Michel N. Ruijter, The influence of passing ships on ships moored in restricted waters, *Offshore Technology Conference*, 2004.

[5]    Islam MR, Islam Nazrul and Maimun Adi, Effect of Vessel Interaction On Hydrodynamic Forces While Advancing Closely In Waves, *Marine Technology Conference* (MARTEC 2008), Indonesia.

[6]    Islam MR, a Study on motios and Non Linear Second Order Forces on Multi-Body Floating system, *Doctoral Thesis, Yokohama National University*, 2001.

[7]    Wehausen and Laitone, Surface Waves, *Encyclopedia of Physics*, Vol-9, Springer-Verlag, Berlin (1960)

# CFD Analysis of Turbidity Spikes Movement for Unsteady Turbulent Flow in a Horizontal Pipe

## By Alamgir Hossain[1] and Jamal Naser[2]

## ABSTRACT

This article presents the hydrodynamics of particles flowing through a horizontal pipe that was performed by using a comprehensive 3D numerical investigation. The particles were introduced in time dependent profile with a reasonable peak load and allowed them to flow in the turbulence flow field. The multiphase mixture model available in Fluent was used in this study. The deposition of particles, along the pipe, has been investigated. The effect of unsteady fluid velocity over particle loads has also been investigated. Results show that after a certain length and time, when the velocity is steady after deceleration period, the shear stress is sufficiently high so that particle re-entrains and deposits or rolls along the bottom surface of pipe wall, which creates a secondary group of particles (called *kink*).

## INTRODUCTION

Deposition of particles from flowing suspensions is an important process in various fields of engineering and in nature. Analyzing deposition of small particles suspended in fluid streams has attracted considerable attention in the past three decades (Anderson and Russell 1970b; Anderson and Russell 1970a; David *at el.* 1987; Swailes and Reeks 1994; Thomson 2003; Laurinat *at el.* 1985; Abuzeid *at el.* 1991; Grainger *at el.* 2003; Hossain *at el.* 2003; Hossain *at el.* peer review). This is because particle deposition plays a major role in a number of industrial processes such as filtration, separation, particle transport, combustion, air and water pollution, and many others.

Modern management of water-distribution systems like South East Water Ltd (SEWL), Melbourne Water, Sydney Water, need simulation models that are able to accurately predict the hydrodynamics of particles behavior that are responsible of turbidity spikes in the water distribution networks.

Turbidity is measured in *Nephelometric Turbidity Units* or NTU, which represents the average volume scattering over a defined angular range. The greater the amount of total suspended solids (TSS) in the water makes the drinking water murkier and turbidity gets the higher measured. Large accumulation of the suspended solids produces turbidity spikes.

## BACKGROUND

A numerical simulation was carried out by Hossain *et al.* (2003), where the circumferential particle deposition in a straight pipe for turbulent flow is presented. The researcher also explained the circumferential deposition for the straight pipe. But these models are for steady flow. This paper investigates the hydrodynamics of particle for time dependent flow and particle load profile associated with turbulence through a horizontal straight pipe.
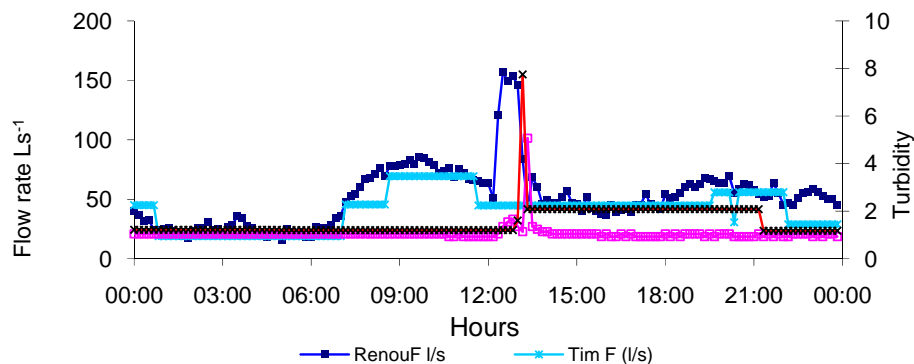


Figure 1: Flow rate and turbidity spikes in a particular day at for two monitoring stations: Renou and Timmothy (Prince *at el.* 2001).

In an online monitoring system installed in the SEWL distribution system, it is possible to pick up thousand of turbidity spikes in a day. Figure 1 represents flow rates and turbidity spikes (taken as turbidity > 2 NTU) at two monitoring points located in a single pipe.

---

[1] Assistant Professor, ME Dept. Military Institute of Science and Technology, Dhaka, Bangladesh. ahossain@mist.edu.bd

[2] Senior Lecturer, Swinburne University of Technology, Hawthorn, VIC 3122, Australia. jnaser@swin.edu.bd

Figure 2: Different arbitrary velocity and particle load profiles for the spike.
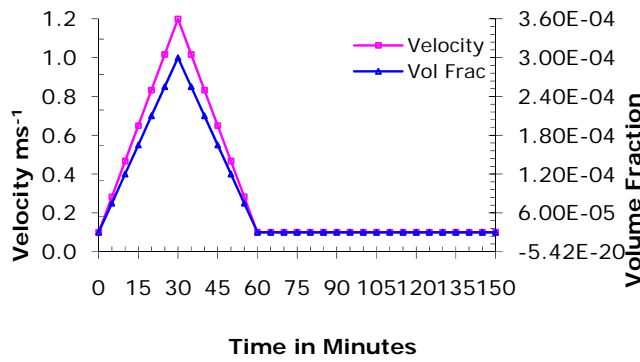
From figure 1 it was understood that numerous numbers of particle load profiles could be generated in a single day. In this article only a single profile has been chosen to understand the hydrodynamic behaviour of particles movements, which is shown in figure 2.

In this model spherical solid 10 μm particles have been used based on Grainger *et al.* (2003). According to SEWL's report (2002), particle specific density 3.0 has been considered.

This profile shown in figure 2 was introduced in FLUENT by a writing subroutine.

The objective for this study is two-fold. First, to analyze the spikes (Figure 2) traveling along the pipe for the particular transient flow profile (figure 2; single spike, similar to what is seen in reality (Prince and McManus 1999; Prince *et al.* 2001)). Second, to investigate the effect of velocity ramp-up (acceleration) and ramp-down (deceleration) on particle movement.
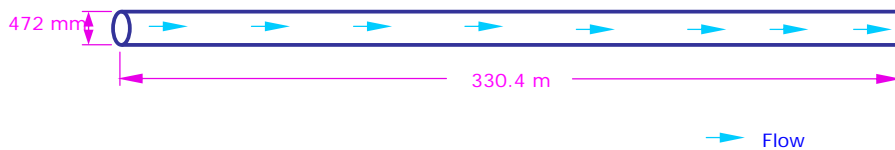


Figure 3: Schematic diagram of the horizontal straight pipe.

Table 1: Physical and hydraulic characteristics of the system used for CFD simulation.

| Characteristics | Description |
|---|---|
| Pipe length (m) | 330.4 |
| Diameter of the pipe D (m) | 0.472 |
| VF of each secondary phase (ppm) | $3\times10^{-4}$ |
| Particle density (kgm$^{-3}$) | 3000 |
| Particles sizes (μm) | 10 |
| No of computational cells | 296540 (produce grid independency results) |
| Inlet velocity and VF profile | see Figures 2 |

In order to study the hydrodynamics of particles behavior in a turbulent flow field numerically: a geometry shown in figure 3 comprising 330.4 m long and 472 mm diameter pipe has been considered as seen at SEWL distribution system. Table 1 shows the boundary conditions that have been implemented for the CFD investigation in this study.

**GOVERNING EQUATIONS**

The Multiphase Mixture Model of FLUENT 6.1 (2001) used in this study solves the continuity and the momentum equation for the mixture. Volume fraction (VF) equations are solved for the secondary phases. The model also solves for the well-known algebraic expressions for the relative velocities for secondary phases (FLUENT INC. 2001 Chapter 20).

Continuity Equation for the Mixture

The continuity equation for the mixture is

$$\frac{\partial}{\partial t}\left(\rho_m\right) + \nabla \cdot \left(\rho_m \vec{v}_m\right) = 0 \tag{1}$$

where $\vec{v}_m$ is the mass-averaged velocity:

$$\vec{v}_m = \frac{\sum_{k=1}^{n} \alpha_k \rho_k \vec{v}_k}{\rho_m} \tag{2}$$

and $\rho_m$ is the mixture density:

$$\rho_m = \sum_{k=1}^{n} \alpha_k \rho_k \tag{3}$$

$\alpha_k$ is the volume fraction of phase $k$.

## Momentum Equation for the Mixture

The momentum equation for the mixture can be obtained by summing the individual momentum equations for all phases. It can be expressed as:

$$\frac{\partial}{\partial t}\left(\rho_m \vec{v}_m\right)+\nabla\cdot\left(\rho_m \vec{v}_m \vec{v}_m\right)=-\nabla p+\nabla\cdot\left[\mu_m\left(\nabla\vec{v}_m+\nabla\vec{v}_m^T\right)\right]+\rho_m \vec{g}+\vec{F}+\nabla\cdot\left(\sum_{k=1}^{n}\alpha_k \rho_k \vec{v}_{dr,k}\vec{v}_{dr,k}\right) \tag{4}$$

where $n$ is the number of phases, $\vec{F}$ is a body force, and $\mu_m$ is the viscosity of the mixture:
$$\mu_m=\sum_{k=1}^{n}\alpha_k \mu_k \tag{5}$$

$\vec{v}_{dr,k}$ is the drift velocity for secondary phase $k$:
$$\vec{v}_{dr,k}=\vec{v}_k-\vec{v}_m \tag{6}$$

## Relative (Slip) Velocity and the Drift Velocity

The relative velocity (also referred to as the slip velocity) is defined as the velocity of a secondary phase ($p$) relative to the velocity of the primary phase ($q$):
$$\vec{v}_{qp}=\vec{v}_p-\vec{v}_q \tag{7}$$

The drift velocity and the relative velocity ($\vec{v}_{qp}$) are connected by the following expression:

$$\vec{v}_{dr,p}=\vec{v}_{qp}-\sum_{k=1}^{n}\frac{\alpha_k \rho_k}{\rho_m}\vec{v}_{qk} \tag{8}$$

The basic assumption of the algebraic slip mixture model is that, to prescribe an algebraic relation for the relative velocity, a local equilibrium between the phases should be reached over short spatial length scales. The form of the relative velocity is given by
$$\vec{v}_{qp}=\tau_{qp}\vec{a} \tag{9}$$

where $\vec{a}$ is the secondary-phase particle's acceleration and $\tau_{qp}$ is the particulate relaxation time. Following Manninen *et al.* (1996) $\tau_{qp}$ is of the form:
$$\tau_{qp}=\frac{\left(\rho_m-\rho_p\right)d_p^2}{18\mu_q f_{drag}} \tag{10}$$

where $d_p$ is the diameter of the particles of secondary phase $p$, and the drag function $f_{drag}$ is taken from Schiller and Naumann (1935):
$$f_{drag}=\begin{cases}1+0.15\text{Re}^{0.687} & \text{Re}\le1000\\0.0183\,\text{Re} & \text{Re}>1000\end{cases} \tag{11}$$

and the acceleration $\vec{a}$ is of the form
$$\vec{a}=\vec{g}-\left(\vec{v}_m\cdot\nabla\right)\vec{v}_m-\frac{\partial\vec{v}_m}{\partial t} \tag{12}$$

## Volume Fraction Equation for the Secondary Phases

From the continuity equation for secondary phase $p$, the volume fraction equation for secondary phase $p$ can be obtained:
$$\frac{\partial}{\partial t}\left(\alpha_p\rho_p\right)+\nabla\cdot\left(\alpha_p\rho_p\vec{v}_m\right)=-\nabla\cdot\left(\alpha_p\rho_p\vec{v}_{dr,p}\right) \tag{13}$$

## Turbulence Model (The Spalart-Allmaras Model)

The model proposed by Spalart and Allmaras (1992) solves a transport equation for a quantity that is a modified form of the turbulent kinematic viscosity $\nu$ for steady state.

$$\frac{\partial}{\partial x_i}\left(\rho_m\tilde{\nu}\vec{v}_m\right)=G_\nu+\frac{1}{\sigma_{\tilde{\nu}}}\left[\frac{\partial}{\partial x_j}\left\{\left(\mu_m+\rho_m\tilde{\nu}\right)\frac{\partial\tilde{\nu}}{\partial x_j}\right\}+C_{b2}\rho_m\left(\frac{\partial\tilde{\nu}}{\partial x_j}\right)^2\right]-Y_\nu+S_{\tilde{\nu}} \tag{14}$$

where $G_\nu$ is the production of turbulent viscosity and $Y_\nu$ is the destruction of turbulent viscosity that occurs in the near-wall region due to wall blocking and viscous damping. $\sigma_{\tilde{\nu}}$ and $C_{b2}$ are constants and $\nu$ is the molecular kinematic viscosity. $S_{\tilde{\nu}}$ is a user-defined source term.

## RESULTS AND DISCUSSIONS

Figures (4a-c) show the particle distribution along the pipe averaged over the unit cross-sectional area. The figures (4a and 4b) represent the particle distribution as a function of time along the pipe for 150 minutes at an interval of 15 minutes. The third figure (4c) represents the average particle volume fraction (VF), which has been computed as a function of time at different cross-sections (at 0, 80, 160, 240, and 330.4 meters) for each inlet profile.

### Particle Distribution along the Pipe

Figure 4a and 4b show the average particle volume fraction over the length of pipe for the profile where both velocity and particle load vary over a period of 1 hour, followed by a steady state condition for another 90 minutes. With time, the peak particle distribution is moving towards the end of the pipe although the movement is slower than the average steady velocity of 0.1 m/s, as expected. This is because of gravitational force, which pulls the particles down to the bottom of the pipe where the velocity is low due to formation of boundary layer. Therefore, most of the particles were either rolling or moving through the lower velocity region, which resulted slower movement of particles. However, after 105 minutes the profiles became distorted and particles accumulated to form a secondary *kink* (a secondary group of particles). The kink can be defined as a group of particles that accumulates and moves/rolls near the bottom region of the pipe wall.
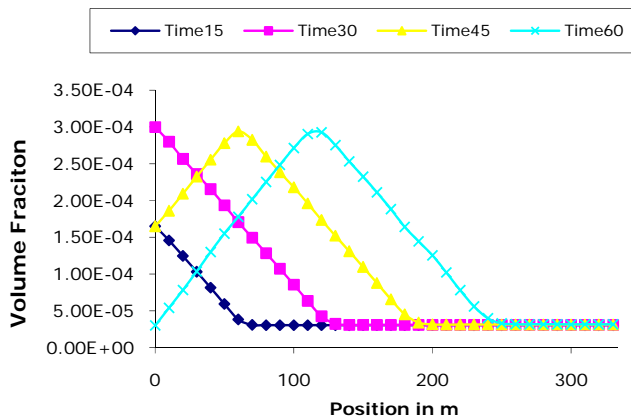


Figure 4a: Average particle distribution along the pipe at different times (0-60 minutes).
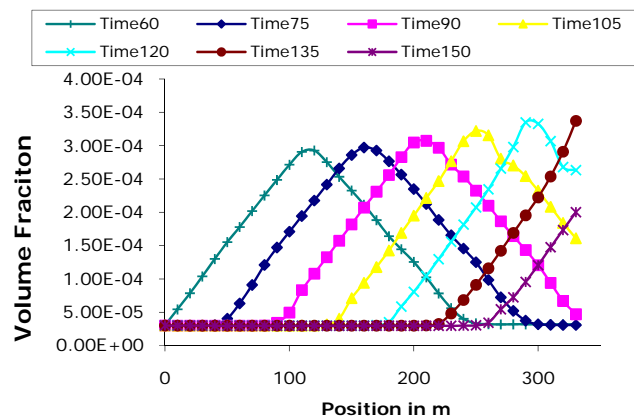
Figure 4b: Average particle distribution along the pipe at different times (60-150 minutes).

### Particle Deposition at Different Planes

Figure 5 shows the particles distribution as a function of time at different cross-sections of the pipe. These 5 planes have been taken at 0 (inlet), 80, 160, 240, and 330.4 (outlet) meters. Figure 5 shows that the sharp peak concentration is smoothed out as particles move further downstream of the pipe.



Immediately after the inlet particles disperse at the development region. The peak particle concentration gets marginally lower before increasing again at the downstream location of pipe (Figure 5). This is because of initial impact of turbulence at developing region, where particles may distribute and results in a lower volume fraction. After that region, some of particles slow down or stop, which results in the marginally higher concentration as particles move downstream.

Figure 5: Average particle volume fraction as a function of time for different cross-sections of pipe along pipe length

### Kink Formation due to Gravity Deposition

Figures 6 [a-c] represent the particle concentration at different depths along the pipe length. Figures 6a-6b show the concentration of particle, which is dispersing along the pipe length of the pipe. At the beginning ( upto 60 mins) the particle profile is similar to that of input. But after 90 mins the particles are dispersing along pipe length as because the velocity gets steady and uniform.
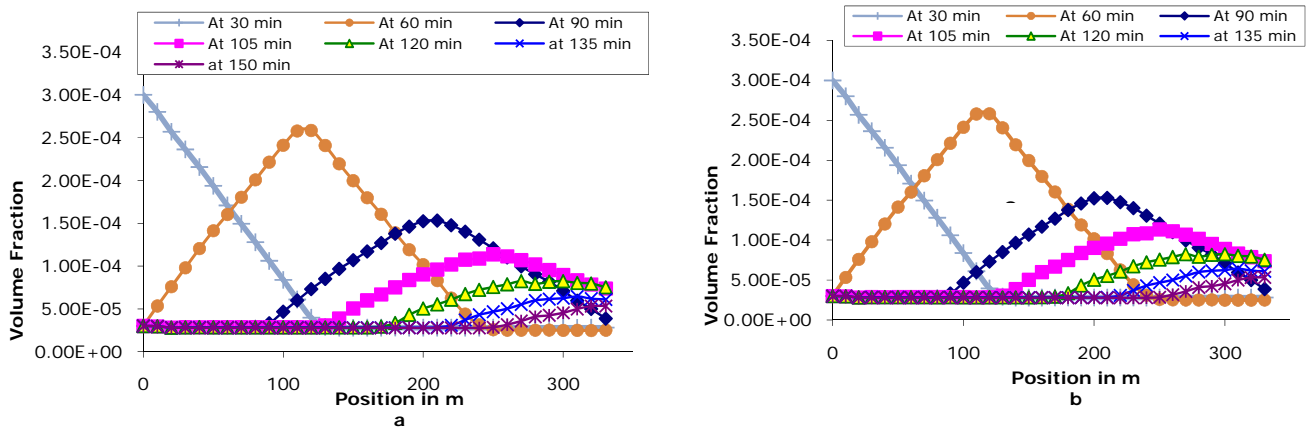
Figure 6: Particle concentration at different depths along the pipe length at different time (a, and b for the top and bottom region of the pipe respectively).



For the understanding of the particle deposition phenomenon the researcher introduced the same particle profile keeping velocity constant and got the figure 7 in which particles look depositing and gets a secondary peak called kink.

The scales for each figure are different so that the volume fraction can be shown clearly. Figure 7 shows the formation of the secondary kink after certain period of time and length of pipe. It was becoming bigger while travelling further downstream of the pipe.

Figure 7: Particle concentration at the bottom for steady flow

The formation of the kink can be explained by the increase in particle accumulation, which is directly related to the shear stress (Prince *et al.* 2003; Boxall *et al.* 2001; Hoven and Vreeburg 1992). This shear stress increases with age of deposition (Mohauas, 1974) and the growth of the deposited layer of particles (Powel, 1982). After a certain length of time this shear stress is sufficiently high due to the depth of the deposited layers to form kinks or groups of particles on the bottom region of pipe wall (Figure 6c).

## CONCLUSION

In this paper unsteady flow inlet conditions have been investigated to explain the turbidity spike movement observed in the water distribution networks. This study provided an opportunity to understand the movement behavior and the distortion phenomenon of turbidity spikes or kinks observed in the water distribution networks. Results show that the particles were settling at the bottom wall of the pipe due to gravity at steady flow. After a certain length of pipe and period of time this deposition became large and dispersed. The deposited particles then split and formed secondary kinks. Depending upon the velocity profiles the kinks were different in shape and size.

## REFERENCES

Abuzeid, S., Busniana, A. A., and Ahmadi, G. (1991). "Wall deposition of aerosol particles in a turbulent channel flow." Journal of Aerosol Science, 22, 43-62.

Anderson, R. J. and Russell, T. W. F. (1970a). "Circumferential variation of interchange in horizontal annular two-phase flow." Ind. Engg. Chem. Fundam., 9, 340.

Anderson, R. J. and Russell, T. W. F. (1970b). "Film formation in two-phase annular flow." AIChE Journal, 14, 626-633.

Boxall, J. B., Skipworth, P. J., and Saul, A. J. (2001). "A novel approach to modelling sediment movement in distribution mains based on particle characteristics." Proceedings of the Computing and Control in the Water Industry Conference UK, De Monfort University, UK, De Monfort University, UK.

David, Y. H. P., Francisco Romay-Novas, and Benjamin Y. H. Liu (1987). "Experimental study of particle deposition in bends of circular cross section." Aerosol Science and Technology, 7, 301-315.

FLUENT. FLUENT INC. 2001. USA.

FLUENT INC. (2001). "FLUENT Manual." USA.

Grainger, C., Wu, J., Nguyen, B. V., Ryan, G., Jayanratne, A., and Mathes, P. (2003). "Part 1: Settling , Re-Suspension and Transport." CRC, CFC, Melbourne, Australia.

Hossain, A., Naser, J., McManus, K., and Ryan, G. (2003). "CFD Investigation of particle deposition and dispersion in a horizontal Pipe." Third International Conference on CFD in the Minerals and Process Industries, CSIRO, Melbourne, Australia, Melbourne, Australia.

Hoven, T. J. J. and Vreeburg, J. H. G. (1992). "Distribution system analysis by continuous monitoring and network calculation." Water Supply, 10, 117-124.

Laurinat, J. E., Hanratty, T. J., and Jepson, W. P. (1985). "Film thickness distribution for gas-liquid annular flow in a horizontal pipe." Phys. Chem. Hydrodynamics, 6, 179-195.

Manninen, M., Taivassalo, V., and Kallio, S. (1996). "On the mixture model for multiphase flow." VTT Publications 288, Technical Research Centre of Finland, Finland.

Prince, R., Goulter, I., and Ryan, G. (2001). "Relationship between velocity profiles anfd turbidity problems in distribution systems." World Water and Environmental Resources Congress, AWWA, Orlando, Florida.

Prince, R., Goulter, I., and Ryan, G. (2003). "What causes customer complaints about discoloured drinking water?" Journal of the Australia Water Association, 30(2), 62-68.

Prince, R. and McManus, K. (1999). "Are dirty water customer complaints an appropriate key performance indicator?" 3rd Annual Australian Environmental Research Event, [CDROM].

Schiller, L. and Naumann, Z. (1935). Z.Ver. Deutsch. Ing., 77, 318.

Spalart, P. and Allmaras, S. (1992). "A one-equation turbulence model for aerodynamic flows." American Institute of Aeronautics and Astronautics.

Swailes, D. C. and Reeks, M. W. (1994). "Particle deposition from a turbulent flow. I. A steady-state model for high inertia particles." Physics of Fluids, 6(10), 3392.

Thomson, D. J. (2003). " Dispersion of particle pairs and decay of scalar fields in isotropic turbulence." Physics of Fluids, 15(3), 801-813.